

NUMERICAL STUDY OF LIQUID SLOSHING
IN LNG TANKS COUPLED WITH SHIP MOTIONS

Liu Xiangbo

B. Eng. SJTU

A THESIS SUBMITTED
FOR THE DEGREE OF DOCTOR OF PHILOSOPHY
DEPARTMENT OF CIVIL AND ENVIRONMENTAL
ENGINEERING
NATIONAL UNIVERSITY OF SINGAPORE

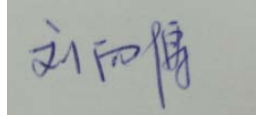
2015

DECLARATION

I hereby declare that the thesis is my original work
and it has been written by me in its entirety.

I have duly acknowledged all the sources
of information which have been used in the thesis.

This thesis has also not been submitted for any
degree in any university previously.

A rectangular box containing a handwritten signature in blue ink. The signature appears to be '刘向博' (Liu Xiangbo).

Liu Xiangbo

2015

Acknowledgments

First of all, I would like to express my sincere gratitude to my supervisor Professor Bai Wei. Since the beginning of my Phd life here in Singapore, he has been supporting me in every aspects of my life. He guided me with skills, patience and care. Whenever I encountered a problem, he has always been there for me. Besides sharing his programming knowledge, research skills and invaluable advice with me, the most important thing he made me learn is how to face the tough aspect of life and be strong. Without him, this thesis would never be possible.

I am also very grateful to my co-supervisor Professor Koh Chan Ghee for his professional guidance and continual support throughout the duration of my PhD. His insights, comments, critical assessments and ideas for improvements always sharpened my views and helped me refine my work.

My special thanks to Professor Ang Kok Keng, Professor Chui Ting Fong and Professor Yuan Jing for their suggestions on my research proposal which helped me greatly to refine my research scope and define the research focus. Thanks to Professor Lee Fook Hou as well for providing me supports during the past few months with an opportunity to learn and share. I also acknowledge the financial support by the National University of Singapore in the form of Research Scholarship.

I am grateful to my colleagues, classmates and friends from NUS, who supported me in many ways, especially Dr. Sun Liang, Dr. Harrif Santo, Dr. Zhang Yang, Dr. Shen Wei, Dr. Chen Mingshen, Dr. Liu Guangliang and Mr. Xu Ming. I also would like to thank my mates in our group, Dr. Gao Mimi, Dr. Mohammed Abdul Hannan, Dr. Luo Min, Mr. Feng Xingya, Mr. Chen Xianglong, Mr. Yan Bin, Ms. Zhang Tong for their insightful discussions and advice.

Last but not least, I would like to express my gratitude from the bottom of my heart to my parents. Thank you so much for your continuous and invaluable support in my life. I could not have finished the whole study without the great love and care from you.

Contents

1	INTRODUCTION	1
1.1	Background	1
1.2	Review of studies on liquid sloshing	3
1.2.1	Analytical methods to study sloshing	3
1.2.2	Experimental investigations on sloshing	5
1.2.3	Numerical modeling of sloshing	7
1.2.3.1	Approaches based on potential flow theory	7
1.2.3.2	Approaches based on viscous flows	8
1.3	Review of studies on interaction between sloshing and ship motions	11
1.3.1	Effects of sloshing on ship motions	12
1.3.2	Effects of ship motions on sloshing	12
1.3.3	Full coupling between sloshing and ship motions	13
1.4	Objective and scope	16
1.5	Organization	18
2	A NUMERICAL MODEL FOR SIMULATION OF FREE SURFACE FLOWS	21
2.1	Mathematical formulation	21
2.1.1	Level Set Method	21
2.1.2	Navier-Stokes equations	26
2.2	Numerical model	26
2.2.1	Solution to the Level-Set equation	26
2.2.1.1	Spatial discretization	26
2.2.1.2	Temporal discretization	29
2.2.1.3	Re-initialization of the Level-Set function	30
2.2.2	Solution to Navier-Stokes equations	32
2.3	Validation of the numerical model	34
2.3.1	Vortex in box	34

2.3.2	Lid-driven cavity flow	38
2.3.3	Free sloshing in a rectangular container	42
2.3.4	Dam break test case	45
2.4	Summary	49
3	LIQUID SLOSHING DUE TO SHIP MOTIONS	51
3.1	Introduction	51
3.2	Forced sloshing	51
3.2.1	Sloshing due to surge motions without breaking waves	53
3.2.2	Sloshing due to pitch motions	59
3.2.3	Sloshing due to surge motions with breaking waves	63
3.3	A study on sloshing induced by ship motions	66
3.3.1	Effects of initial phase differences between each motion	67
3.3.2	Effects of excitation frequency	72
3.3.3	Effects of filling level	76
3.3.4	Effects of external wave height	79
3.3.5	Pressure in the tank	81
3.4	Summary	84
4	AN IMPROVED NUMERICAL MODEL BY HIGH-RESOLUTION CONVECTION SCHEMES	87
4.1	Introduction	87
4.2	The preliminary model : the numerical dissipation issue	87
4.2.1	Nonlinear liquid sloshing under horizontal motions - 1	87
4.3	The intermediate model: a parametric study of the smoothing band in the Level-Set technique	91
4.3.1	Nonlinear liquid sloshing under horizontal motions - 2	91
4.3.2	Sloshing under vertical motions	95
4.3.3	Sloshing under rotational motions	98
4.4	The final model: implementation of high-resolution convection schemes	102
4.4.1	Highly-accurate and bounded convection schemes	102
4.4.1.1	Normalized Variable Diagram	103
4.4.1.2	The Convection Boundedness Criterion	108
4.4.1.3	Composite schemes	111
4.4.2	Validation: lid-driven flow	117
4.4.3	Sloshing under surge motions	119
4.4.4	Wave generation in a wave tank	128

4.5	Summary	135
5	NUMERICAL STUDY ON COUPLING OF SLOSHING AND SHIP MOTIONS	137
5.1	Numerical modeling of ship motions in waves	137
5.1.1	Mathematical formulation	138
5.1.1.1	Model description	138
5.1.1.2	Governing equations and boundary conditions	138
5.1.1.3	Higher-order boundary element method	140
5.1.1.4	Hydrodynamic forces	144
5.1.2	Numerical implementation	146
5.1.2.1	Mesh generation	146
5.1.2.2	Artificial damping layer	147
5.1.2.3	Time stepping scheme	148
5.1.2.4	Algebraic equation solver	148
5.2	A COUPLED numerical model for simulation of the interaction between sloshing and ship motions	149
5.2.1	Mathematical formulation	149
5.2.2	Numerical implementation	150
5.2.3	A preliminary validation of the COUPLED model	151
5.3	A parametric study on the coupling effects between sloshing and ship motions	153
5.3.1	Effects of wave amplitude	153
5.3.2	Effects of wave frequency	164
5.3.3	Effects of the filling level in the water tank	170
5.4	Summary	177
6	CONCLUSIONS AND RECOMMENDATIONS	179
6.1	Conclusion	179
6.2	Recommendations for future research	182
	Bibliography	185

Abstract

Global growing needs for energy lead to the demand for new energy sources. Among them, liquefied natural gas (LNG) plays a more and more important role since it's easier to store and transport. These advantages raise the demand for LNG carriers, LNG floating production, storage and off-loading units (FPSOs), and LNG floating storage and re-gasification units (FSRUs).

For ships carrying liquid cargo, like LNG carriers, motion responses in waves are affected by both external wave excitations and internal sloshing-induced forces and moments. That is, the sloshing flow in a ship cargo, like a LNG tank, is excited by ship motions, but it affects the ship motions in return. This coupling effect is important in the prediction of the ship motion and the sloshing flow. The effect of the liquid sloshing is sometimes critical in ship structural design. Sloshing flows can generate impulsive pressures acting on the internal structure, and this is the potential damage to the structure. Therefore, the study of coupling effects is important to the design of LNG carriers.

In order to study the interaction between liquid sloshing and ship motions in waves, the two problems need to be solved simultaneously and accurately. To investigate sloshing in tanks subjected to large excitations close to the natural frequency of the fluid, it is pertinent to use a surface capturing technique to handle the high surface curvature and breaking fluid. In this study, the Level Set Method, which has been great popular in the simulation of multiphase fluid flows, is applied. The governing equations for the viscous fluid inside the tank are solved by using a finite difference approximation in an arbitrarily moving coordinate system to predict sloshing flows in a two-dimensional rectangular tank under three-degrees-of-freedom excitations. Validation is carried out by reproducing different benchmark sloshing cases and comparing the present numerical result with published data. Good agreement suggests that the numerical model is capable of solving the violent sloshing problem.

Before applying the numerical model to couple with ship motions, a preliminary study is conducted to further demonstrate the capability of the Level-Set numerical model. In this study, the ship motions obtained from a realistic LNG carrier in seas are used to generate the sloshing waves in a full-scale LNG tank. A parametric study regarding wave frequency, amplitude and tank filling levels is performed. Long time

simulations in extreme conditions which involve violent fluid motions such as wave breaking are carried out successfully.

At the same time, a further improvement on the Level-Set based sloshing model is made. A parametric study on the effects of the smoothing band is performed based on the preliminary numerical model. It indicates that the conventional size of the smoothing band may not be suitable when more stable but less accurate fluid solver applied to handle the wave breaking problem. To increase the accuracy and efficiency while keep the stability, high-resolution convection schemes are incorporated. Validation cases with good agreement indicate that the combination of the high-resolution convection schemes with the Level-Set technique is successful, promising and suitable for applying in the coupled program.

To approach real-world situations, nonlinear ship motions in waves are solved based on a nonlinear potential flow model. To obtain the wave forces acting on the LNG carrier, some auxiliary functions are applied. Based on the kinematic and dynamic relations with time marching, the numerical methodology to study the interaction between the sloshing and ship motion in waves is proposed. The COUPLED model is validated by reproducing a benchmark experiment. Finally, a parametric study with regard to wave amplitude and frequency is conducted. Comparison of the ship motions with and without sloshing effects is performed. Sloshing effects on ship motions are further investigated with respect to different tank filling conditions.

List of Figures

1.1	Worldwide growth in LNG demand from Foss (2012).	1
1.2	LNG fleet containment from Foss (2012).	2
1.3	LNG fleet containment - ship orders from Foss (2012).	3
2.1	An illustration of the interface and the Level-Set function.	22
2.2	An example of capturing interface by Level Set Method.	22
2.3	Level Set Method for two-dimensional free surface flows.	24
2.4	Fluid properties in the whole domain.	25
2.5	Demonstration of the two-dimensional staggered grid.	32
2.6	Initial conditions of the vortex in box case.	35
2.7	Comparison between different meshes at $t = 2$ (red dashed line: 100×100 , blue dash-dot line: 200×200 , pink solid line: 400×400 , black solid line: 800×800).	35
2.8	Comparison between different meshes at $t = 4$ (gray dash line: 100×100 , red dash-dot line: 200×200 , blue long dashed line: 400×400 , pink solid line: 800×800 , black dash-dot-dot line: Ideal condition).	36
2.9	Surface profiles at different time instants during the vortex stretch and recover process.	37
2.10	The geometry of the lid-driven cavity.	38
2.11	Comparison between numerical results with different mesh sizes and the benchmark solution for $Re = 100$	39
2.12	Comparison between numerical results with different mesh sizes and the benchmark solution for $Re = 400$	40
2.13	Comparison between numerical results with different mesh sizes and the benchmark solution for $Re = 1000$	41
2.14	A schematic view of the free sloshing case.	42
2.15	Time histories of free surface displacement at the left wall for three mesh sizes.	43

2.16	Time histories of free surface displacement at the left wall for three time intervals.	43
2.17	Comparison of wave profiles between the present numerical results and analytical solutions at different time instants.	44
2.18	A schematic view of the dam break case.	45
2.19	Wave profiles captured by the presented numerical model at different time instants.	46
2.20	Comparison of time histories of the pressure among the present results, Fekken’s numerical results and experimental measurements.	47
2.21	Comparison of the wave height recorded at four probes among the present results, Fekken’s numerical results and experimental measurements.	48
3.1	Definition of the two-dimensional moving coordinate system.	52
3.2	A schematic view of the two-dimensional rectangular tank used in Koh’s experiment.	53
3.3	Convergence test of three mesh sizes.	54
3.4	Convergence test of three time intervals.	55
3.5	Comparison between the present numerical results and Koh’s experimental recordings.	56
3.6	Comparison of wave profile between present numerical results (solid line) and Koh’s experimental data (circle) at different time instants.	57
3.7	Comparison of dimensionless lateral force against T/T_1 among the present numerical result, Faltinsen’s solution and laboratory measurements.	58
3.8	A sketch of the two-dimensional tank used in Chen’s experiment with the rotation axis.	59
3.9	Comparison of time histories of pressure at $\omega = 0.95$ rad/s, among present numerical results, Chen’s SPH results and Chen’s experimental data.	60
3.10	Comparison of time histories of pressure at $\omega = 3.09$ rad/s, among present numerical results, Chen’s SPH results and Chen’s experimental data.	61
3.11	Comparison of time histories of pressure at $\omega = 3.81$ rad/s, among present numerical results, Chen’s SPH results and Chen’s experimental data.	61

3.12	Comparison of time histories of pressure at $\omega = 5.47$ rad/s, among present numerical results, Chen's SPH results and Chen's experimental data.	62
3.13	Comparison of the pressure amplitudes obtained at various excitation frequencies between the present numerical results and Chen's SPH results.	62
3.14	Comparison of maximum wave elevation against the excitation period, between the present numerical results and the experimental results.	64
3.15	Wave profiles captured by the present numerical model at various time instants.	65
3.16	Time histories of free surface elevation on the left wall for various phase differences under the 40% filling level.	68
3.17	Maximum free surface elevations for various phase differences under the 40% filling level.	69
3.18	Comparison of free surface elevation between results for $\alpha_x = 0.75\pi$ and $\alpha_x = 1.25\pi$	69
3.19	Time histories of free surface elevation on the left wall for various phase differences under the 20% filling level.	70
3.20	Maximum free surface elevations for various phase differences under the 20% filling level.	70
3.21	Time histories of free surface elevation on the left wall for various heave phases.	71
3.22	Time histories of free surface elevation under fully coupled and superposed excitations.	72
3.23	Maximum elevation differences at different excitation amplitudes.	72
3.24	Time histories of free surface displacement at four different frequencies.	74
3.25	Maximum elevations at different frequencies.	75
3.26	Time histories of free surface displacement under different filling conditions at the given frequencies.	77
3.27	Maximum elevations under different filling conditions at the given frequencies.	78
3.28	Maximum elevations at various frequencies under five different filling conditions.	78
3.29	Maximum elevations at various frequencies under lower filling conditions.	79
3.30	Time histories of free surface displacement induced by different wave heights.	80

3.31	Maximum wave elevations induced by different wave heights under various filling conditions.	80
3.32	Time histories of pressure at four different frequencies on the left tank wall.	82
3.33	Time histories of pressure under four different filling conditions on the left tank wall.	83
3.34	Time histories of pressure induced by five different wave heights at $y = 6$ m on the left tank wall.	84
3.35	Pressure distribution at the left wall when the sloshing wave just reaches the tank roof for three different cases.	84
4.1	A sketch of the two-dimensional rectangular tank in Liu's work. . . .	88
4.2	Comparison of surface displacement with different mesh sizes for the non-resonance case.	89
4.3	Comparison of surface displacement with different mesh sizes for the resonance case.	90
4.4	Comparison of time histories of surface displacement between numerical results with smoothing sizes varied from $s = 2.0$ to $s = 8.0$	92
4.5	Comparison of time histories of surface displacement between numerical results with smoothing sizes varied from $s = 10.0$ to $s = 16.0$	93
4.6	Comparison of time histories of surface displacement between 190×100 with $s = 2.0$ and 380×200 with $s = 4.0$	94
4.7	Comparison of time histories of surface displacement among the improved numerical prediction, the experimental data and the analytical solution.	95
4.8	A schematic view of the initial conditions of the heave-induced sloshing.	96
4.9	Time histories of wave elevation at the left wall for three mesh sizes.	97
4.10	Time histories of wave elevation at the left wall obtained by different smoothing sizes.	98
4.11	Comparison between Frandsen's results and the present numerical predictions with $s = 4.0$ for the non-resonance case.	98
4.12	A sketch of the water tank used in Akyildiz's experiment.	99
4.13	Comparison of the time histories of pressure at two probes when $\theta_0 = 4^\circ$	100
4.14	Comparison of the time histories of pressure at two probes when $\theta_0 = 8^\circ$	101
4.15	Node variables in a general form.	104
4.16	Node variables in a normalized form.	104

4.17	Classic convection schemes on NVD.	106
4.18	An illustration of interpolative boundedness.	108
4.19	An illustration of the convection boundedness criterion.	111
4.20	MINMOD in the NVD frame.	112
4.21	MUSCL in the NVD frame.	113
4.22	SMART in the NVD frame.	114
4.23	COPLA in the NVD frame.	115
4.24	Comparison between solutions given by the high-resolution convection schemes and the benchmark solution for $Re = 100$	118
4.25	Comparison between solutions given by the high-resolution convection schemes and the benchmark solution for $Re = 1000$	119
4.26	Comparison between numerical results based on classical upwind schemes and Koh's experimental data.	120
4.27	Comparison between numerical results based on high-resolution convection schemes and Koh's experimental data.	121
4.28	Results of the error study for the selected convection schemes.	122
4.29	Time histories of surface displacement predicted by first-order upwind scheme with different s values.	123
4.30	Time histories of surface displacements predicted by MINMOD with different s values.	124
4.31	Time histories of surface displacements predicted by COPLA with different s values.	125
4.32	Comparison of time histories of surface displacement between different s values with two different mesh sizes based on MINMOD.	126
4.33	Comparison of time histories of surface displacement between different s values with two different mesh sizes based on COPLA.	127
4.34	Time history of the velocity of the wave paddle recorded in Gao's experiment.	128
4.35	Comparison of time histories of wave elevation between numerical results with different mesh sizes and Gao's experimental data.	129
4.36	Comparison of time histories of wave elevation between MINMOD results with different s values and Gao's experimental data.	131
4.37	Comparison of time histories of wave elevation between COPLA results with different s values and Gao's experimental data.	132
4.38	Comparison of time histories of wave elevation among the present numerical results, Bai's numerical solutions and Gao's experimental data.	134

5.1	A schematic view of the circular numerical wave tank.	138
5.2	An example of mesh generated on the barge and the free surface. . .	147
5.3	A schematic view of box-shaped hull section used in Rognebakke's experiment.	152
5.4	Comparison of sway amplitude for empty tanks and two tanks filled with $h = 0.186$ m between the present numerical results and Rognebakke's experimental data.	152
5.5	A schematic view of the COUPLED model used in this study.	154
5.6	Time histories of the motion RAOs of the barge with an empty tank for different wave amplitudes.	155
5.7	Time histories of the wave forces on the barge with an empty tank for different wave amplitudes.	156
5.8	Time histories of the motion RAOs of the barge with a filled tank for different wave amplitudes.	157
5.9	Time histories of the wave forces on the barge with a filled tank for different wave amplitudes.	159
5.10	Time histories of the sloshing effects on the barge motions for different wave amplitudes.	160
5.11	Maximum sloshing effects on ship motions under different wave ampli- tudes.	161
5.12	Time histories of the surface displacement at the left wall for different wave amplitudes.	162
5.13	Time histories of pressure at the left wall for different wave amplitudes.	162
5.14	Maximum surface displacements under different wave amplitudes. . .	163
5.15	Maximum pressure under different wave amplitudes.	163
5.16	Time histories of the motion RAOs of the barge with an empty tank at different wave frequencies.	165
5.17	Time histories of the motion RAOs of the barge with a filled tank at different wave frequencies.	166
5.18	Time histories of the sloshing effects on the barge motions at different wave frequencies.	167
5.19	Maximum sloshing effects on ship motions at different wave frequencies.	168
5.20	Time histories of the surface displacement at the left wall at different wave frequencies.	169
5.21	Time histories of pressure at the left wall at different wave frequencies.	170
5.22	Maximum surface displacements at different wave frequencies.	170

5.23	Maximum pressure at different wave frequencies.	170
5.24	Time histories of the barge motions obtained by the COUPLED model under different filling conditions.	172
5.25	Time histories of the sloshing effects on barge motions under different filling conditions.	173
5.26	Time histories of the sloshing effects on barge motions under low filling conditions.	174
5.27	Maximum sloshing effects on barge motions under different filling conditions.	175
5.28	Time histories of the surface elevation at the left wall under different filling conditions.	176
5.29	Time histories of pressure at the left wall under different filling conditions.	176
5.30	Maximum surface elevations under various filling conditions.	177
5.31	Pressure distribution at the left wall under three different filling conditions.	177

List of Tables

3.1	Motion RAOs applied in this parametric study.	73
3.2	Frequency ratios for various filling levels.	76
4.1	Results of the error study for the three convection schemes with different s values.	125
4.2	Results of the error study for MINMOD and COPLA with different mesh sizes.	127

Chapter 1

INTRODUCTION

1.1 Background

The demand for natural gas in the world was boosted in late 1970s by the desire to diversify energy sources in the wake of global oil shocks. Due to the clean environmental advantages of natural gas over other fossil fuels and its superior thermal efficiency when used in power generation, the demand for natural gas is sustained (Foss, 2012). Currently most natural gas is supplied by pipelines where the natural gas resources are near the market. However, there are still large reserves of natural gas existing around the world in areas where there is no significant market, or where natural gas resources far exceed regional demand, or where pipeline options are limited. Then some of the natural gas produced there will be liquefied, in order to ship to areas where usage of natural gas exceeds indigenous supply.

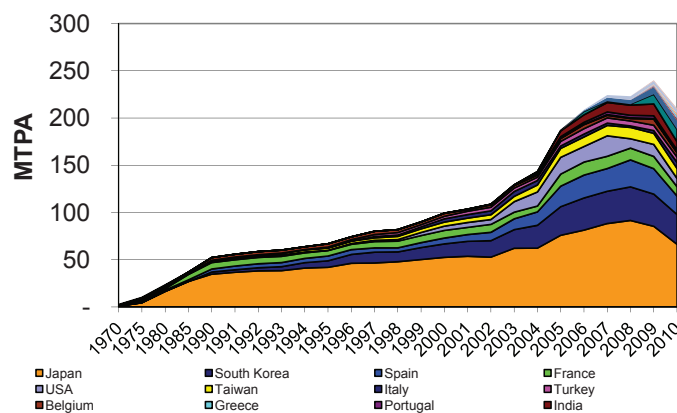


Figure 1.1: Worldwide growth in LNG demand from Foss (2012).

Liquefied natural gas (LNG) is natural gas that has been cooled to the point when it condenses to liquid, which occurs at a temperature of approximately minus 161 degree centigrade at atmospheric pressure. At the liquid state, the volume of gas is reduced by approximately 600 times. This makes it more economical to store natural gas where other forms of storage do not exist and to transport natural gas over long distances while using pipelines is too expensive or not possible. Liquefaction also provides the possibility to store natural gas for use during high demand periods in areas where developing underground storage facilities is not suitable. Therefore, LNG plays a growing role in the global energy future as shown in Fig. 1.1.

Due to the growing LNG market, there is a strong demand for new LNG carriers with larger cargo capacity. Historically, most of the LNG carriers used spherical (Moss) tanks. However, according to Fig. 1.2 and Fig. 1.3, there is a trend toward the newly proposed membrane tanks. This is due to the fact that membrane design utilizes the hull shape more efficiently, and has less void shape between cargo tanks and ballast tanks. Therefore, membrane design is much cheaper than moss design of equal capacity. In addition, the growing energy market also requires that new LNG tanks with larger cargo capacity could be operated under any filling conditions. Thus, LNG sloshing problem, which usually arises in partially filled containers, becomes a design concern for LNG tanks.

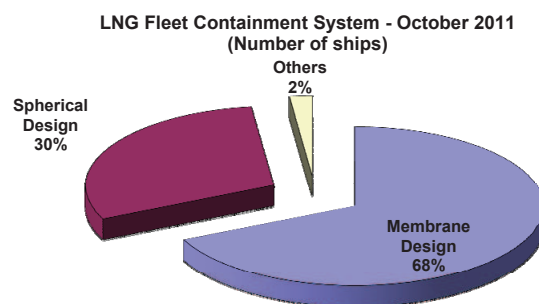


Figure 1.2: LNG fleet containment from Foss (2012).

Under adverse weather condition, violent ship motions caused by sea waves would excite strong sloshing flows inside the LNG tank. In that situation, LNG moves against sides of the tank with an increased wave elevation. This can produce strong impulsive loads on internal tank walls, especially when the tank is large. Furthermore, if the external excitation is close to the natural frequency of the sloshing system, it may lead to structural damage of tank membranes and possibly result in tank rupture.

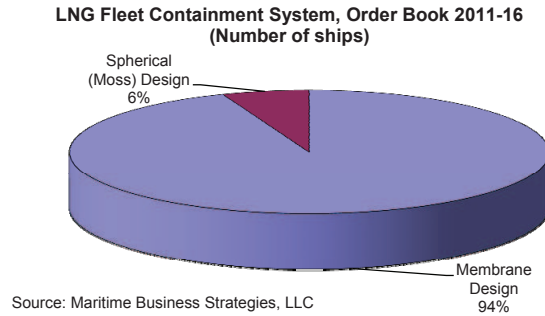


Figure 1.3: LNG fleet containment - ship orders from Foss (2012).

At the same time, sloshing-induced forces and moments would result in significant changes of ship motions, which are crucial to the safety and stability of LNG carriers during delivery and offloading operations. Therefore, study on liquid sloshing and interactions between sloshing and ship motions are of great importance to both the design of LNG carriers and the LNG industry.

1.2 Review of studies on liquid sloshing

As the previous stated significance of study on liquid sloshing, so far, various researchers have devoted efforts to studying liquid sloshing analytically, experimentally and numerically.

1.2.1 Analytical methods to study sloshing

From the mathematical point of view, the sloshing motion is a difficult problem to analyze due to the nonlinear boundary conditions on the free surface and the complex position prediction of the free surface. To develop an analytical solution for the sloshing motion, certain assumptions have been made in the previous work. The general equations of motions for a fluid in closed containers can be simplified by assuming the container rigid and impermeable. In addition, the fluid is assumed inviscid, incompressible and the flow is initially irrotational. Capillary or surface tension effects are also often ignored in a gravitational field.

In early years, Moiseev (1958) presented an analytical investigation and discussed qualitatively some sloshing tests. He used the nonlinear free surface boundary conditions and applied the method presented by Stoker and Lindsay (1958). In this method, the velocity potential and wave height were expanded in a power series in

which each term of the series was represented by a potential function. Abramson (1966) also applied the potential theory to study linear hydrodynamic pressure induced by liquid sloshing. Ockendon and Ockendon (1973) proposed an analytical scheme for resonant sloshing due to external vertical excitations. Later, Faltinsen (1978) developed a linear analytical solution to liquid sloshing problem in a horizontally excited two-dimensional rectangular tank. With the small amplitude and low gravity assumption, Dodge et al. (1991) conducted an analytical analysis on liquid sloshing in axisymmetric containers.

Recently, Faltinsen and Timokha (2001) developed an analytical multi-modal method to describe the nonlinear sloshing flow in a rectangular tank with finite water depth. This method decomposed the free surface elevation to several modes. Subsequently, Faltinsen and Timokha (2012) derived a new Trefftz representation for the sloshing velocity potential in the liquid sloshing problem in a two-dimensional circular tank. This solution included a modified Poisson integral depending on the fully continuous component of strength functions and terms that are proportional to the jumps of the strength function at the tank top. Calculations confirmed that this solution can approximate the natural sloshing modes accurately for all tank fillings. Thus, they concluded that this solution can be used for a numerical study of the limiting case of the completely filled tank. It was also pointed out that their approach could be easily generalized to the arbitrary two-dimensional sloshing problem for a smooth closed tank surface by using conformal mapping. Also based on the multi-modal method, Faltinsen and Timokha (2013) constructed an analytical method of nonlinear sloshing in a spherical tank. By using analytically approximated natural sloshing modes and curvilinear spatial coordinates, general fully nonlinear modal equations, weakly nonlinear modal equations and Moiseev-Narimanov modal system were derived for the spherical shape. The latter was emphasized in this study to construct an asymptotic time-periodic solution and classify the steady-state wave regimes appearing as stable and unstable planar waves and swirling for spherical tanks theoretically.

Besides these, Ikeda et al. (2012) studied nonlinear liquid sloshing in a square tank subjected to obliquely horizontal excitations with an improved model. In their theoretical analysis, five higher sloshing modes were considered by applying Galerkin's method to derive the modal equations of motion. Linear viscous terms were incorporated to consider the damping effects. Van der Pol's method was applied to determine the frequency response. Experiments were conducted to confirm the validity of the theoretical analysis. Since damping effects were taken into account in their study, the obtained frequency response curves can clearly explain the phenomena of nonlinear

sloshing dynamics in real systems. They also found that higher sloshing modes play a significant role in improving the accuracy of the frequency response curves. To study shallow-water sloshing phenomena theoretically, Antuono et al. (2012) proposed a model system starting with a set of Boussinesq-type equations with a linearized dispersive term. Based on a spatial Fourier decomposition, this system employs a spatial modulating term to include the exciting forces and thus is capable of representing a generic two-dimensional motion of the tank. This leads to a formulation that is consistent with the conservation of momentum and energy of the flow. Comparisons with both experimental measurements and numerical simulations validated the capability of their proposed model. They also pointed out that depth-averaged equations can provide a good description of shallow-water sloshing motions with non-breaking waves.

Analytical methods are adequate to study sloshing when the liquid motion is not violent. However, they might not be able to describe strong sloshing involving breaking waves and overturning liquid.

1.2.2 Experimental investigations on sloshing

As a reliable approach to study complex sloshing flows, extensive experimental investigations have been conducted by various researchers in order to better understand sloshing phenomena, and validate analytical and numerical analysis of different sloshing problems.

In early years, Sumner (1965) measured the horizontal slosh force for an excitation frequency equal to the fundamental natural frequency of the liquid free surface at each liquid-depth ratio considered in the tests. Abramson et al. (1974) studied the sloshing in a prismatic tank and measured the wave amplitude near the wall and longitudinal force for large-amplitude steady-state sloshing. Bass et al. (1985) gave the modeling criteria for scaled LNG sloshing experiments.

Later, Hinatsu et al. (2001) carried out experiments to analyze pressures on tank walls for various sloshing arrangements. To define the characteristics of liquid sloshing in cylindrical and rectangular tanks, Madarame et al. (2002) performed an experimental study and found that the induced mode had one diametrical node, which was accompanied by the lateral motion of the swell. The mode was replaced by a lower one as the inlet-surface distance and velocity increase. Akyildiz and Ünal (2005) made an experimental investigation of pressure distributions at different locations and three

dimensional effects on liquid sloshing in a rectangular tank at a scaled model with different filling levels.

Recently, Khezzar et al. (2009) performed an experimental study on water sloshing in a rectangular tank subjected to sudden impact. Different filling ratios and tank accelerations were tested. Ji et al. (2012) studied the nonlinear two-dimensional lateral sloshing experimentally by the aids of the time history of wave elevation recorded at the sidewall, free surface profile captured by high speed camera, and velocity vector flow field obtained by PIV technique. In this study, non-resonant sloshing with deep water condition was considered. Based on the experiments, they found that four regimes of the sloshing waves can be categorized : mild 2-D wave; strongly nonlinear 2-D wave with hydraulic jump-like motion; 3-D wave with regular structure in the longitudinal direction; 3-D chaotic wave. In their study, a comprehensive discussion on strongly nonlinear 2-D wave concluded that this off-resonant sloshing problem can be characterized into a combination of three sloshing motions: 1. standing waves during run-down process similar with linear sloshing; 2. hydraulic jump along the vertical wall during the run-up process; 3. bore motion propagating from the sidewall to interior fluid region like a dam break during stationary process. To measure the impact pressure accurately during the sloshing process excited by sinusoidal motions in the sway direction, Pistani and Thiagarajan (2012) setup a sloshing experiment in a two-dimensional tank. In their study, the artificial pressure spike acquired by the transducer when measuring in the two phase environment was solved by lowering the excitation voltage of sensors. Details of the analysis of characteristics of the pressure traces during the impact of the fluid and their location in the tank were also discussed. In addition, they proposed a strategy for defining a threshold pressure based on the transducer location and sloshing impact time. Kim et al. (2013) build a new experimental facility and performed a series of model tests on sloshing. It was reported that the density ratio of liquid and gas should be carefully handled in sloshing experiment. In their study, a higher density ratio of gas and liquid would generally lead to higher sloshing-induced pressure.

These experiment investigations can help discuss the nonlinear characteristic of sloshing wave, display the complicated sloshing process directly and obtain useful measurements for validating analytical solution and numerical simulations. However, there still are some limitations on this approach. Due to the scaling effects, unmatched parameters like fluid viscosity and compressibility in model tests may produce unexpected results different from the real situation. In addition, errors are possibly encountered in the data processing of experimental measurements. Furthermore, it

is usually time consuming and expensive to conduct experiments that reproduce a real-world situation (like a full-scale LNG tank in realistic sea conditions).

1.2.3 Numerical modeling of sloshing

With the rapid growth of computer power and recent advance in numerical methods, extensive numerical studies on the liquid sloshing problem have been conducted.

1.2.3.1 Approaches based on potential flow theory

Based on potential flow theory, the Boundary Element Method (BEM) could be used to solve liquid flow phenomena with nonlinear free surface behavior inside a tank. The flow variables can be expressed in terms of a velocity potential that satisfies Laplace's equation and free surface boundary conditions in an appropriate tank. In early years, Faltinsen (1978) utilized the BEM to simulate sloshing flows in a two dimensional rectangular tank and validated his numerical method by a linear analytical solution. Nakayama and Washizu (1981) applied the same method to study nonlinear sloshing flows in a container under horizontal, vertical and rotational excitations. Later, with a higher-order BEM, Lee and Choi (1999) investigated the sloshing problem in cargo tanks. Landrini et al. (1999) further applied a B-spline based BEM to study sloshing phenomena. Recently, Huang et al. (2010) developed a time-domain green function based BEM to simulate sloshing flow in tanks with experimental validations.

The Finite Element Method (FEM) is popular in many types of engineering applications and has been used to solve Laplace's equation in sloshing studies. Nakayama and Washizu (1980) analyzed the nonlinear liquid sloshing in a two-dimensional rectangular tank under pitch excitations by applying the FEM. Later, Okamoto and Kawahara (1990) used a Lagrangian finite element method to analyze large amplitude sloshing waves in a container. Wu et al. (1998) applied an inviscid finite element model to study the behavior of non-breaking sloshing waves in three dimensional tanks. They focused on near-resonance cases and reported the effects of three-dimensional motions in comparison with two-dimensional standing waves. In recent years, Kim et al. (2003) developed a three-dimensional finite element model to investigate the impact pressure due to sloshing in LNG tank. The model was validated by comparing sloshing motions and pressure with experimental data. Following Nakayama and Washizu (1980), Cho and Lee (2004) used the nonlinear FEM to analyze large amplitude sloshing flows in two-dimensional tanks. Based on the fully nonlinear potential theory, Wang and Khoo (2005) applied the FEM to investigate nonlinear sloshing

in a two-dimensional rectangular tank under random excitations. They studied the nonlinear effects of the random waves and observed the typical nonlinear feature of sloshing waves.

Meanwhile, the Finite Difference Method (FDM) has also been utilized to solve the governing equations for liquid sloshing in the frame of potential wave theory. For instance, Frandsen (2004) developed a fully nonlinear finite difference model to study sloshing wave in a two-dimensional tank excited by surge and heave motions. Numerical results were compared with analytical solutions. Good agreement was shown for small to steep non-breaking waves and the nonlinear feature was captured. Nevertheless, these mentioned studies based on potential flow theory cannot simulate sloshing wave with viscous effects and wave-breaking features because of the inviscid assumption.

1.2.3.2 Approaches based on viscous flows

To simulate viscous sloshing flow, some other numerical methods have been developed to solve the Navier-Stokes equations. Most of these methods could be categorized as either grid methods or grid-less methods.

Grid-less methods

Recently, Grid-less methods which follow individual fluid particles have been proposed and gained popularity in the simulation of free surface flows. Among them, smoothed particle hydrodynamics (SPH) method proposed by Gingold and Monaghan (1977) has been widely employed to investigate sloshing flows. Souto Iglesias et al. (2004) applied the SPH to perform a numerical simulation of anti-roll tanks and sloshing type problems. Using the same numerical model, Souto-Iglesias et al. (2006) investigated sloshing moment amplitudes in a rectangular tank at different rolling frequencies. Experiments were conducted for validation of the numerical solutions. Later, Colagrossi et al. (2010) implemented the improved SPH method to study violent sloshing wave impacts. Numerical results agreed well with laboratory measurements. The local features of sloshing wave impacts were clearly captured and discussed. Shao et al. (2012) proposed an improved SPH method for modeling liquid sloshing dynamics. In their method, density correction and kernel gradient correction were used to achieve better pressure field. Turbulent model was incorporated into this SPH method. They also proposed a coupled dynamic solid boundary treatment (SBT) algorithm to improve the accuracy near the solid boundary areas. Based on this algorithm, Chen et al.

(2013) proposed a further improved SPH model by applying a smaller acting distance of repulsive boundary particles. They also utilized the Moving Least Squares method in the density reinitialization to obtain better pressure field. Based on their improved SBT, a new pressure measurement method on solid walls was also given, which took a pressure correction term into account. Experiments were conducted and obtained wave pattern and pressure measurements close to their numerical results. Recently, Gotoh et al. (2014) proposed two schemes to improve the ISPH-based methods in simulation of violent sloshing flows with a particular focus on sloshing-induced impact pressure. They comprised a higher-order Laplacian of Poisson Pressure Equation and an Error Compensating Source of PPE to minimize the instantaneous and accumulative projection-based errors. In their study, importance of dynamically adjusted coefficients of error minimizing terms in the source term of PPE was highlighted, which is shown to be superior to a scheme with constant coefficients.

Meanwhile, the moving particle semi-implicit (MPS) method proposed by Koshizuka and Oka (1996) has also been applied to the simulation of sloshing waves. For instance, Yoon et al. (1999) adopted the MPS method to simulate a self-induced sloshing problem. Recently, a new Lagrangian particle method proposed by Koh et al. (2012), called the consistent particle method (CPM) has been employed to investigate sloshing flows in a two-dimensional rectangular tank with various filling levels. This method approximates the partial differential operator in a way consistent with Taylor series expansion and applies a boundary particle recognition method to help define the fluid domain. Good agreement was achieved between the numerical results and experimental data.

Grid methods

When solving the Navier-Stokes equations with grid methods, due to the presence of free surface, additional schemes have to be applied in order to simulate sloshing waves.

One of the commonly applied schemes is the Marker-And-Cell (MAC) method, which was first proposed by Harlow et al. (1965). The MAC method introduces particles which have no mass and are marked as liquid or gas across the interface at the initial time. With time marching, the particles are moved in a Lagrangian way and then recognized as liquid or gas particles in each cell. By this way, the interface is reconstructed. Based on the MAC approach, Feng (1973) investigated liquid sloshing flows in a three-dimensional rectangular tank. Later, Cordonnier (1994) performed a numerical study of sloshing phenomena inside tanks of various shapes based on a

modified MAC method. The impacts on the walls were studied. The comparison with experiments showed a good agreement.

Another scheme that has been widely used is SURF scheme proposed by Hirt et al. (1975). In this approach, the free surface elevation is followed and assumed as a single-valued function of the horizontal tank coordinates. Using SURF to track the free surface, Arai et al. (1992) simulated three-dimensional sloshing flow based on the SOLA, a finite difference scheme introduced by Hirt et al. (1975). Following this SOLA-SURF combination, Kim (2001) studied sloshing flows with impact load in two- and three-dimensional containers. Later, Kim et al. (2004) simulated violent sloshing flows in prismatic tanks and investigated the impact pressure on tank ceiling.

Recently, the Volume of Fluid (VOF) method, which is proposed by Hirt and Nichols (1981), has been extensively employed to capture the free surface when simulating sloshing flows. In this method, a scalar named the volume fraction or the color function is introduced to define the filling degree of each cell in the whole domain. A cell with a volume fraction with zero value is defined as an empty cell, while the one with value of one is defined as a full cell. For those partially filled cells, the volume fraction of the fluid in each cell needs to be computed by solving a transport equation. By tracing the change of the volume fraction, the motion of free surface is captured. In early days, Solass (1995) applied a commercial program FLOW3D to investigate sloshing phenomena. This program utilizes the SOLA scheme for solving the Navier-Stokes equations and the VOF technique for tracking the free boundaries of the fluid. In this study, it was reported that a sensitivity of the results to the choice of numerical parameters and the lack of conservation of fluid mass can cause unphysical sloshing behavior. Later, Van Daalen et al. (2000) applied a Navier-Stokes solver based on the VOF method to simulate the low-filling sloshing flows in an anti-roll tank. Simulated and measured roll moment amplitudes and phases were found to be in good agreement for different sets of motions and various tank parameters. Celebi and Akyildiz (2002) developed a viscous flow solver to capture nonlinear free surface flows using the VOF technique. They simulated two-dimensional sloshing motions in tanks excited by rotational and translational motions. Based on finite volume method (FVM) and VOF scheme, Lee et al. (2007a) conducted a series of parametric sensitivity studies on the LNG sloshing loads. Their results revealed that the liquid turbulence, viscosity and density ratio are not significant to the dimensionless impact pressure. Liu and Lin (2008) developed a numerical model combining the FDM and VOF to investigate three-dimensional nonlinear liquid sloshing with broken free

surfaces. The numerical model was validated by good agreement with experiment measurements of two-dimensional sloshing flow under horizontal excitations.

Another surface capturing technique is the Level Set Method proposed by Osher and Sethian (1988). Because of its capability in handling complex free surface and easy implementation, the Level-Set technique has gained popularity in simulation of free surface flows. In this method, a Level-Set function is defined in the whole domain and typically initialized as the signed distance from the interface to the considered point. Then the liquid and gas interface is captured by locating the zero Level-Set function (when the distance is zero) as a solution of the Level-Set transport equation with time marching. Sussman et al. (1998) developed an improved Level Set Method to study incompressible two-phase flows. Yue et al. (2003) applied the Level Set Method to perform the numerical simulation of unsteady multi-dimensional free surface motions. Colicchio et al. (2005) conducted the Level-Set computations of free surface rotational flows and achieved promising agreement with others' work. These studies indicated that the Level Set Method is robust in capturing the free surface and has the potential to study sloshing flows. Gu et al. (2005) applied the Level Set Method with a finite difference flow solver to study sloshing waves. The accuracy and efficiency of the Level Set Method has been reported. Chen and Price (2009) investigated the liquid sloshing in a rectangular tank with various filling levels based on the Level Set Method with inclusion of compressibility effects. Wang et al. (2011) simulated liquid sloshing inside a two-dimensional rectangular tank by the Level Set Method. Parametric studies regarding excitation frequency, amplitude and viscosity of fluid have been performed.

1.3 Review of studies on interaction between sloshing and ship motions

As described earlier, during transport of LNG through seas, not only the adverse sea conditions would lead to strong sloshing which may result in large impulsive loads on tank walls, but also the sloshing-induced forces and moments on LNG carriers would cause an obvious change of the ship motions in waves. Thus, it is of great importance to study the interactions between sloshing inside tanks and ship motions.

1.3.1 Effects of sloshing on ship motions

Researchers have already considered the effects of sloshing motions inside tanks on the ship motions for a long time. The main concern is to use the sloshing motion inside the tank to stabilize the ship motion. In early years, Watts (1883, 1885) introduced a method of creating a rolling damping moment by water sloshing motions inside rectangular tanks to reduce the roll motions of ships. His studies paved the way for the application of the later proposed anti-rolling tanks which utilizes the similar idea. Vasta et al. (1961) further investigated the effects of tanks with liquid sloshing on the roll motion of ships. Bosch and Vugts (1966) conducted experimental investigation using a rectangular tank with water to reduce the ship rolling. In their study, it was reported that 80% roll reduction in periodic waves and 50% in irregular waves were found. Recently, Ikeda and Yoshiyama (1991) studied the coupling effects of sway and roll motions on the performance of a rectangular anti-rolling tank. Results of the tests showed that the sway motion would lower the reduction of the roll angle by the anti-rolling and would increase the natural period of the tank. Their study extended the sloshing effects on other degrees-of-freedom of ship motions. Later, Bass (1991) conducted full-sea trials of free-surface tanks to investigate the effects of sloshing flows on the ships and understand the behavior of anti-rolling containers. His study provided precious experimental results in the real sea condition.

In these studies, the liquid sloshing occurs in a small special designed tank. However, when considering the liquid sloshing in full-scale LNG tanks, whose volume is much larger, the effects of internal sloshing flows on ship motions should be further explored.

1.3.2 Effects of ship motions on sloshing

External ship motions which are of large amplitude or near the natural frequency of the sloshing system would generate violent internal sloshing which can induce large impact pressure on the structure. In addition, realistic sea waves can generate multiple degrees-of-freedom ship motions which are much more complicated than the excitations with single direction used in the conventional sloshing studies. With the recent higher focus on LNG market and related sloshing motion in larger tanks, the effects of ship motions in seas on liquid sloshing motion inside LNG tanks have also been a concern for researchers.

Mikelis and Journee (1984) investigated the liquid motions and induced pressure in two-dimensional tanks based on a finite difference approach. In their study, the

partially filled tanks were mounted on ships. Experiments were also conducted on scaled tanks and the measurements were compared with corresponding numerical predictions. Their study provided an innovative way to apply the effects of ship motions on sloshing. However, their experimental study was based on scaled tanks, whose accuracy may be limited due to size effects. Lee and Choi (1999) conducted a numerical investigation on the sloshing problem in cargo tanks with a higher-order BEM. A parametric study on the filling level was conducted. It was reported in their study that hydraulic jumps were found when the excitation frequency of ship motions was close to the resonance frequency of the sloshing system for lower filling conditions. For higher filling conditions at the same excitation frequency, large impact pressure was found. Recently, Lee et al. (2011) studied the LNG sloshing motions considering ship movements as excitations in a full-scale tank to verify their finite difference model with a marker-density scheme. However, only three cases have been conducted and limited pressure results have been revealed.

In these studies, liquid sloshing in tanks were excited by ship motions. The effects of inside sloshing motions on external ship motions were not considered in return. However, in practice, impact forces and moments induced by sloshing on tank walls could result in instability of the ship during traveling. As reviewed above, the sloshing effects on ship motions have already been studied for a long time. With a further consideration, researchers have devoted efforts to investigations on the interaction between sloshing motions and ship motions.

1.3.3 Full coupling between sloshing and ship motions

So far, there are some existing studies on the coupling problems. In early days, Dillingham (1981) conducted a coupling investigation for motions of a vessel with a shallow water flow on deck. He used an impulse-response technique to solve the coupled equation. Later, Journée (1997) performed a model test in beam waves using a ship model with liquid cargo tanks. A wide range of filling levels were tested. Experimental measurements were compared with the solution given by the strip theory. In recent years, Wang et al. (2012) investigated the interaction phenomenon of sloshing motions and the global wave loads by seakeeping model tests of a self-propelled LNG ship with a liquid cargo tank under the 30% filling condition. In their study, it was noticed that the existence of liquid in tank will affect the natural rolling period of the ship. The motion period of liquid in the tank depends not only on the inner shape of the tank and the liquid filling level, but also on the wave heading angle and

ship speed. It was also reported that sloshing-induced forces between the tank and the ship hull, are different according to the wave length and traveling speed. The existence of liquid sloshing in the cargo tank might reduce the global wave loads on LNG ships in some degree.

Numerical studies on coupling between sloshing and ship motions can be categorized into two approaches: the frequency-domain approach adopting linear sloshing in the frame of potential flow theory; and the time-domain approach using nonlinear sloshing flow. Some representative studies based on the assumption of linear sloshing flow in the frequency-domain are given as follows. Molin et al. (2002) conducted a three-dimensional potential calculation of the ship motion with a semi-analytical approach for the sloshing flow to model the motions of a barge with a partially filled water tank on deck. Experimental investigations were also conducted and compared with the numerical prediction. Applying the same assumption of Molin et al. (2002), Malenica et al. (2003) adopted the boundary integral equation method to solve both sloshing and seakeeping hydrodynamic part. Their results matched the experimental data given by Molin et al. (2002). Later, Newman (2005) extended an exterior panel code WAMIT to inner tank to perform linear coupling analysis. Recently, Tsai et al. (2013) carried out a numerical seakeeping-sloshing coupling analysis for an 8,000TEU container ship. The simulation was conducted by a hydrodynamic numerical code HydroSTAR in the frequency domain considering the high speed effect. The linear sloshing flow was assumed. In their study, for the request of full load sea trial, particular cargo holds were ballasted with sea water to design draft, analyzing with different ship speed and discussing the effects. It was found that the resonant frequency would occur with full load condition and full ship speed, especially for rolling motion. This resonant activity may cause the structure destruction seriously. The assumption of linear sloshing is adequate when liquid sloshing is not violent and breaking waves are not involved. However, in a real-world situation, during the LNG delivery and offloading process, induced sloshing flows might be very severe and include breaking waves.

According to the existing studies, assuming the sloshing flow is linear and applying a frequency-domain approach are not enough due to the importance of nonlinearities for accurate prediction of sloshing motions. Therefore, a time-domain approach is necessary to accurately model the coupling between sloshing and ship motions. Kim (2002) carried out a computational study with the focus on the anti-rolling tank which was found to have significant coupling effects on both ship motions and

sloshing. The linear ship motion was computed by applying a time-domain panel method called Large-Amplitude Motion Program based on potential flow theory. The three-dimensional viscous sloshing flow was modeled by the finite difference based SOLA-SURF method. Rognebakke and Faltinsen (2003) investigated the interactions between ship motions and sloshing by experimental measurements and numerical modeling. The external ship motion was modeled by using linear potential flow theory. The nonlinear sloshing was simulated by a multi-modal method. Good agreements were obtained between the experimental results and numerical predictions. It was reported that the steady-state ship motion was almost linear and sinusoidal at the frequency of the linear incident wave even though the induced sloshing was violent and nonlinear in the water tank.

Later, Lee et al. (2007b) performed a numerical study of the LNG sloshing effects on the global motion of LNG carriers. The ship motions were simulated by a three-dimensional frequency-domain scheme based on potential flow theory. The nonlinear viscous sloshing flow was adopted and solved by a finite difference method using the SURF scheme to capture the free surface in time domain. To couple the two separate numerical solutions, the convolution integral was used to obtain the corresponding simulations of ship motions in time domain. The coupling numerical model was validated by the experimental results. In their study, it was reported that the pattern of the coupling effects between vessel motions and liquid sloshing appreciably changed with filling levels in the LNG tank. Applying similar ideas of obtaining frequency-domain ship motions prior to conversion to time domain, Kim et al. (2007) investigated the coupling effects between ship motions and sloshing. They adopted an impulse-response-function (IRF) method to solve the linear ship motions in frequency domain. The nonlinear inviscid sloshing flow was governed by the Euler equations and simulated based on a finite difference approximation. Based on their numerical results, they concluded that due to the nonlinearity of the sloshing flow, ship motions showed a strong sensitivity to wave slope. Based on their study, Nam et al. (2009) carried out a series of experiments using a LNG FPSO with two tanks. A fair agreement was observed between the experimental work and the simulation results given by the numerical model used in Kim et al. (2007), showing significant coupling effects on both ship motion responses and the sloshing flows.

Recently, Zhao et al. (2014) developed a two-dimensional coupled model which adopted the nonlinear sloshing flows and the linear ship motions both based on potential flow theory in time domain. Experiments were conducted to validate the numerical model. Good agreement was achieved. Based on the verified model, the

coupling between ship sway motion and internal sloshing was investigated. In this investigation, it was observed that internal sloshing amplitude was nonlinear to the incident wave height. Both the internal sloshing and the ship motion exhibited amplitude modulation phenomena. It was also reported that the sloshing reduction effects on the global motions at the natural frequency was caused by sloshing force being π behind the wave force.

It is obvious that most aforementioned studies consider the linear ship motions. Limited investigations on the interactions between nonlinear ship motions and nonlinear sloshing flows are reported. Recently, Mitra et al. (2012) developed a fully coupled model of nonlinear sloshing and ship motions. The fully nonlinear sloshing motion was studied by a finite element method and the nonlinear ship motion was simulated by a hybrid marine control system. Simulated roll motions were compared with existing results. Fair agreement indicated that the proposed model was expected to be useful in evaluating the coupling effect. In their study, the coupling model also allowed for the effects of wind, wave and current. It was found that the wave height can have large effects on sloshing whereas the current velocities caused fairly marginal effects on the ship motions. However, their nonlinear sloshing flow is based on potential flow theory. Therefore, the violent sloshing including the wave overturning and breaking cannot be handled by this coupling model.

1.4 Objective and scope

As discussed in the previous sections, it is of great importance to study liquid sloshing flows inside LNG tanks considering the coupling effects between internal sloshing motions and external motions of the LNG carrier. Since LNG sloshing in the real-world situation might be violent and lead to breaking waves, the analytical solution is not a feasible approach to this study. It also seems impossible to conduct the investigation on sloshing in a full-scale LNG tank mounted in a carrier in sea waves by an experimental means. Therefore, this study focuses on the numerical investigation of liquid sloshing in LNG tanks coupled with ship motions.

As reviewed in the previous section, most numerical analysis on sloshing flows are confined in a small specially designed tank, whose motions are constrained in a single direction. Limited sloshing studies with respect to multi-excitations are reported, not to mention considering the effects of ship motions.

Numerical investigations on the coupled interaction between liquid sloshing and ship motions are mainly based on two approaches. In the early years, studies based on

the frequency-domain approach have assumed that internal sloshing flows are linear. However, recent studies have shown that linear assumption is not accurate to describe violent sloshing motions inside the tank with strong nonlinearities. Therefore, more recent studies have chosen to apply nonlinear sloshing flows based on the time-domain approach. In most of these coupling models assuming liquid sloshing is nonlinear, ship motions were modeled either by the frequency-domain approach or linear time-domain approach. However, frequency-domain approach can only consider periodic results. The instantaneous interaction between sloshing and ship motions cannot be accurately captured. For ship motions based on the linear time-domain approach, the influence of the nonlinear components are not considered. Thus, to accurately model the ship motions, a nonlinear time-domain approach is necessary.

Currently, there are few numerical models that could simulate the interaction by adopting both nonlinear sloshing flows and nonlinear ship motions. Existing ones have simulated the nonlinear sloshing flow based on potential flow theory. As reviewed in the previous section, the potential flow theory cannot consider the viscous effects in sloshing flows. In addition, these numerical models cannot handle large surface deformations, such as water overturning and wave breaking. Coupled numerical models that can simulate viscous sloshing flows with breaking waves and nonlinear ship motions have barely been found.

In addition, most aforementioned coupling studies focus on the coupling influence on single degree of freedom, such as sway or roll. The coupling effects on multi-degrees of freedom need be further explored.

Therefore, the overall objective of this study is to develop a numerical methodology that can model the coupled interaction between internal viscous sloshing flow with breaking waves and external nonlinear ship motions in time domain, and investigate the coupling effects on sloshing and multi-degrees of ship motions.

To achieve this objective, the scope of this study contains:

- Develop a free surface flow solver that solves Navier-Stokes equations based on the finite difference approximation and captures free surfaces with the aid of the Level Set Method.
- Conduct a comprehensive parametric study on sloshing phenomena in a full-scale LNG tank excited by ship motions.
- Develop a numerical model that can couple the ship motions obtained by nonlinear potential flow theory and the viscous sloshing motion based on the developed free surface flow solver.

- Carry out a parametric study to shed lights on the coupling effects on both external ship motions and internal sloshing motions.

The results of this present study might have significant impact on

- Providing a numerical model that can accurately simulate free surface flows with breaking waves and handle fully coupling between nonlinear viscous sloshing and nonlinear ship motions;
- Understanding sloshing phenomena affected by ship motions and their influence on multi-degrees of ship motions in return.

1.5 Organization

This thesis contains six chapters and is organized as follows.

Chapter 1 first introduces the background of the current LNG market. Then a comprehensive review on the studies of liquid sloshing is given. Analytical and experimental approaches to sloshing motions are discussed. Various numerical methods in this field are introduced. Their applications on sloshing are reviewed and discussed. Following this, a review of the work on the coupling effects between sloshing and ship motions is given with related applications and limitations discussed. Based on the reviews, the objective and scope of the study are presented.

Chapter 2 gives the mathematical formulation of the numerical sloshing model. The general ideas of Level Set Method are introduced first. Then both the Level-Set evolution equations and the Navier-Stokes equations are given. The numerical solution to both equations are also briefed with the details of discretization formulations. The numerical model is then validated by classic tests on fluid solver, pure interface capturing, and free surface flow simulation.

Chapter 3 presents the parametric study on sloshing flows inside a full-scale LNG tank excited by ship motions. First, the simulations of sloshing under excitations in horizontal, vertical and rotational directions are performed. Then the sloshing flow with breaking waves is also reproduced. Finally, the parametric study with respect to excitation amplitudes, frequencies and filling levels is carried out. The effects of the initial phase difference between the ship motions on sloshing are also discussed.

Chapter 4 describes the development of the numerical model for simulation of the sloshing flow in this study. First, the numerical dissipation issue of the preliminary sloshing model is discussed. Second, a parametric study on the smoothing band

in the Level-Set technique is conducted. Based on the findings, the intermediate sloshing model is presented. Finally, the final sloshing model which adopts the high-resolution convection schemes is developed. The details of the convection schemes are introduced. The validation of the final model is also performed by repeating the sloshing and wave generation cases.

Chapter 5 performs the study on the coupling between LNG sloshing and ship motions. First, the numerical model based on nonlinear potential flow theory is described. Then the methodology of coupling the numerical models for ship motions and sloshing motions is developed. After that, a preliminary validation of the COUPLED model is conducted. Finally, coupling effects are investigated by a parametric study regarding wave amplitude, wave frequency and the filling level inside the LNG tank.

Chapter 6 summarizes the findings of the present study. Corresponding conclusions on sloshing simulation and modeling of coupling between ship motions and sloshing are made. The possible future research work is suggested in the end.

Chapter 2

A NUMERICAL MODEL FOR SIMULATION OF FREE SURFACE FLOWS

This chapter first presents a brief introduction to the Level Set Method and the governing equations applied in this study. Following the mathematical formulation of the numerical model, details of the numerical approaches used to solve the Level-Set equation and governing equations are given respectively. In the last section, validation of the present numerical model is carried out by reproducing some benchmark test cases.

2.1 Mathematical formulation

2.1.1 Level Set Method

Fig. 2.1 shows the basic idea of the Level Set Method. Instead of following the interface (the blue circle on the left of Fig. 2.1) directly, the Level Set Method builds it into a surface (the green cone-shaped surface). This is called the Level-Set function, and it intersects the x - y plane where the original curve is. Thus, the interface (blue curve) is called the ‘zero level set’ since it is the set of points that are at height zero.

When trying to find the new locations of the interface with time evolution, the Level Set Method follows the motion of the Level-Set function rather than obtaining the motion of the interface directly. A simple example of a similar process is given in Fig. 2.2.

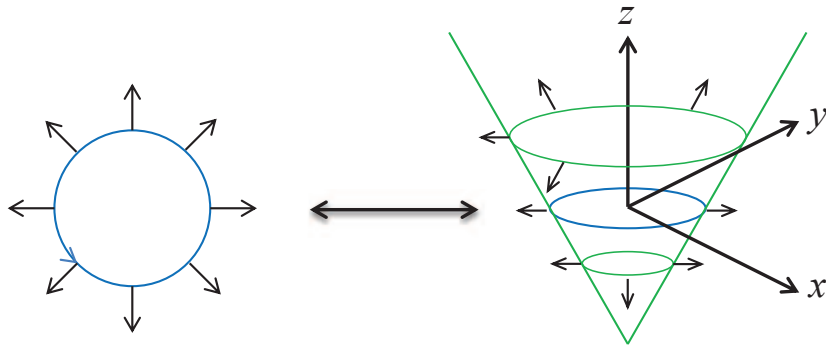


Figure 2.1: An illustration of the interface and the Level-Set function.

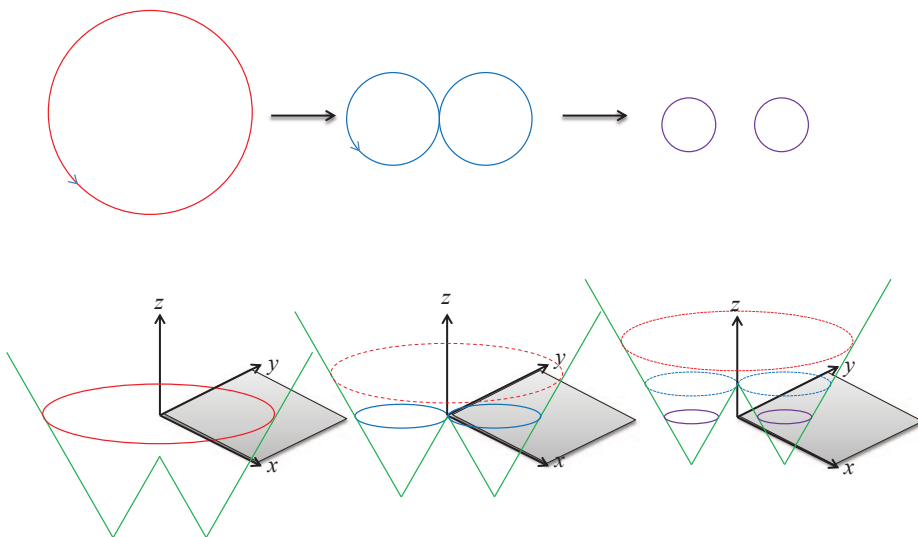


Figure 2.2: An example of capturing interface by Level Set Method.

In the top row of Fig. 2.2, the circle changes its topology by splitting into two. To be more general, if the interface shape is irregular, it is quite difficult to describe this transformation and model this process numerically by parameterizing the boundaries of the shape and following its motion. Doing so requires finding the instant when the shape becomes two parts, and then rebuilding the two shapes with newly solved parameters. On the other hand, it is much easier to find the shape boundary and follow the shape motion through the Level-Set function with its expanding, rising or

falling. For instance, to simulate the process of the first row in Fig. 2.2, directly modeling the splitting of the circle (red line) into two (purple lines) first requires finding the moment the circle splits. The positions of the two circles' centers and their radii at each time instant are also needed to rebuild the two circular shapes. However, one can simulate the process by simply following the falling of the Level-Set function (green line), as shown in the second row of Fig. 2.2. In other words, the interface may get wildly contorted while the Level-Set function can remain well behaved.

To sum up, the original idea behind the Level Set Method is to represent a close curve (the interface) Γ in two dimensions with an auxiliary scalar function ϕ in three dimensions, which is named the Level-Set function. Then the curve Γ is defined as the zero level set of ϕ by,

$$\Gamma = \{(x, y) \mid \phi(x, y, t) = 0\}, \quad (2.1)$$

and thus the curve is determined implicitly after the Level-Set function ϕ is solved in the whole domain. In the original Level Set Method, ϕ is assumed to be positive inside the region bounded by the closed curve Γ and negative outside.

When applying the Level Set Method in modeling a free surface flow, the Level-Set function ϕ defined in the whole computational domain is introduced with the following properties:

$$\phi(x_i, t) \begin{cases} < 0 & \text{if } x_i \in \text{air} \\ = 0 & \text{if } x_i \in \text{interface} \\ > 0 & \text{if } x_i \in \text{water} \end{cases}, \quad (2.2)$$

where x_i is the spatial coordinate. The position of the air-water interface is directly defined by the zero level set $\phi = 0$. In order to satisfy Eq. (2.2), the scalar ϕ can be defined as a signed distance function,

$$|\nabla\phi| = 1 \quad (2.3)$$

which represents the normal positive (in the water phase) or negative (in the air phase) distance of any fluid point \mathbf{P} in the whole domain from the air-water interface. An illustration of the application of the Level Set Method in a two-dimensional free surface flow is given in Fig. 2.3. The interface is the $\phi = 0$ contour. At a certain point \mathbf{P} , its Level-Set value ϕ_P is the shortest distance from its position to the interface

with a negative sign in the air phase and a positive sign in the water phase.

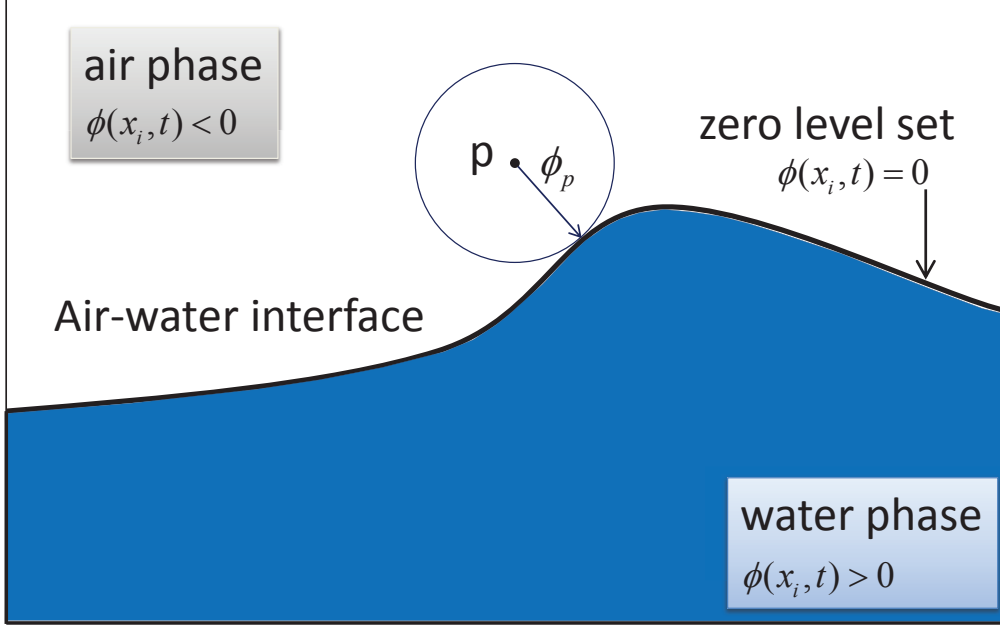


Figure 2.3: Level Set Method for two-dimensional free surface flows.

When a fluid particle in the whole domain is followed, its Level-Set value ϕ does not change with time. In other words, if a fluid particle belongs to the set of points defining the air-water interface, it will always be on the interface. If the free surface is subjected to a velocity field u_i , the Level-Set function is then advected by the following equation:

$$\frac{D\phi}{Dt} \equiv \frac{\partial\phi}{\partial t} + u_i \frac{\partial\phi}{\partial x_i} = 0, \quad (2.4)$$

where D/Dt is the material derivative. Normally, the value of ϕ is known at the initial time $t = t_0$. Then at a certain later time step, based on the known velocity field u_i , the Level-Set function ϕ can be updated by solving Eq. (2.4). Thus, on this way, the air-water interface can be determined by the contour $\phi = 0$ at every time step.

According to the definition, within the whole domain, the fluid properties are: $\rho = \rho_{air}$, $\mu = \mu_{air}$ in the air phase, where the signed distance is negative; and $\rho = \rho_{water}$, $\mu = \mu_{water}$ in the water phase, where the signed distance is positive. However, stability issues may arise at the air-water interface due to the sharp gradient between the two fluid properties, especially when computing viscous flows. Thus, a region of a finite thickness, 2ϵ , called a ‘transition zone’ is introduced around the air-water interface. Over this zone, a smooth but also rapid change of the fluid

properties occurs across the interface from the air domain to the water domain.

Special attention has to be given to proper smoothing of the variables inside the transition zone, since they are linked to those outside the transition zone through the governing equations. Inconsistent smoothing may result in unphysical solutions within the whole domain. The Heaviside-type function is usually employed to smooth the fluid viscosity and density in the transition zone. There are several choices for the Heaviside function. The following is adopted in this study:

$$H(\phi) = \begin{cases} 0 & \text{if } \phi < -\epsilon \\ \frac{1}{2} \left[1 + \frac{\phi}{\epsilon} + \frac{\sin(\pi\phi/\epsilon)}{\pi} \right] & \text{if } |\phi| \leq \epsilon \\ 1 & \text{if } \phi > \epsilon \end{cases} . \quad (2.5)$$

Then the fluid properties in the whole domain can be represented by the following equations:

$$\rho(\phi) = \rho_{air} + H(\phi)(\rho_{water} - \rho_{air}), \quad (2.6)$$

$$\mu(\phi) = \mu_{air} + H(\phi)(\mu_{water} - \mu_{air}). \quad (2.7)$$

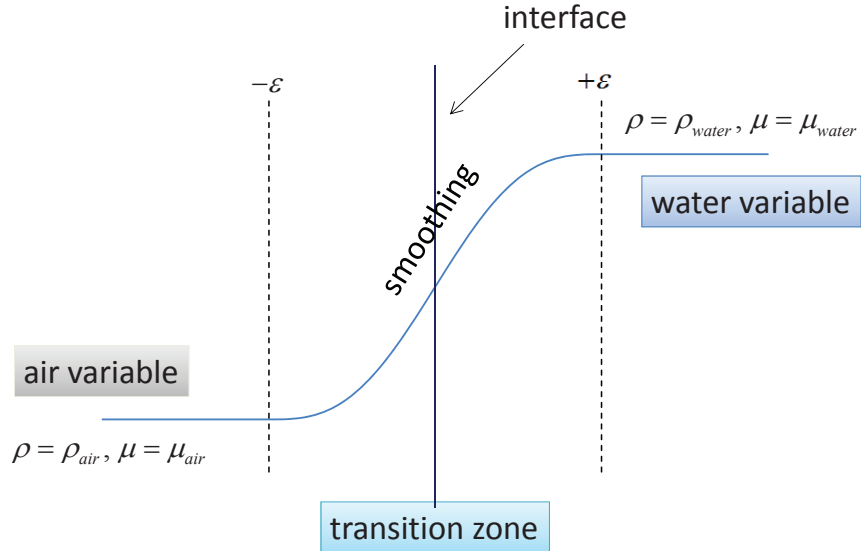


Figure 2.4: Fluid properties in the whole domain.

Fig. 2.4 shows the density and viscosity in the whole domain and the smoothing in the transition zone. With the Heaviside function applied in the transition zone, the air properties are smoothly transformed to water properties across the interface, thus avoiding the sudden jump condition.

2.1.2 Navier-Stokes equations

In this study, we model the water and air phases as two incompressible fluids. Their motions are governed by the Navier-Stokes equations, which represent the conservation of mass and momentum per unit mass:

$$\frac{\partial u_i}{\partial x_i} = 0, \quad (2.8)$$

$$\frac{\partial u_i}{\partial t} + u_j \frac{\partial u_i}{\partial x_j} = \frac{1}{\rho(\phi)} \left(-\frac{\partial p}{\partial x_i} + \frac{\partial \tau_{ij}}{\partial x_j} \right) + f_i, \quad (2.9)$$

where $i, j = 1, 2$ represent the two-dimensional flows, $\rho(\phi)$ is the fluid density in the whole domain defined by Eq. (2.6), p indicates the pressure, f_i denotes the i -th component of the external excitations (including the force due to the gravitational acceleration), τ_{ij} are the viscous stress components given by,

$$\tau_{ij} = \mu(\phi) \left(\frac{\partial u_i}{\partial x_j} + \frac{\partial u_j}{\partial x_i} \right), \quad (2.10)$$

where $\mu(\phi)$ is the fluid viscosity in the whole domain given by Eq. (2.7).

2.2 Numerical model

2.2.1 Solution to the Level-Set equation

2.2.1.1 Spatial discretization

In this study, the fifth order Hamilton-Jacobi Weighted Essentially Non-oscillatory (HJ-WENO) scheme is used to calculate the spatial gradient in Eq. (2.4).

The Essentially Non-oscillatory (ENO) method was first introduced for the numerical solution of conservation law by Harten et al. (1987). Their basic idea was to compute numerical flux functions using the smoothest possible polynomial interpolations. Shu and Osher (1988, 1989) implemented this idea by constructing the numerical flux functions from a divided difference table of the point-wise data. Due

to the fact that the Hamilton-Jacobi equations in one spatial dimension are integrals of conservation laws, Osher and Sethian (1988) extended the ENO method to the Hamilton-Jacobi equations. Since Eq. (2.4) belongs to the category of Hamilton-Jacobi equations, the Level-Set function can be expressed by,

$$\phi(x) = Q_0(x) + Q_1(x) + Q_2(x) + Q_3(x). \quad (2.11)$$

This can be differentiated and evaluated at x_i to find $(\phi_x^+)_i$ and $(\phi_x^-)_i$, which are the forward and backward differences respectively. That is, the following equation:

$$\phi_x(x) = Q'_1(x) + Q'_2(x) + Q'_3(x), \quad (2.12)$$

is applied to define $(\phi_x^+)_i$ and $(\phi_x^-)_i$, where the constant $Q_0(x)$ term vanishes upon differentiation.

Later, Liu et al. (1994) introduced the Weighted ENO method to avoid the overkill problem due to the ENO philosophy of choosing exactly one of the candidate stencils in regions where the data are well behaved. Based on the HJ-ENO scheme, Jiang and Peng (2000) extended the WENO method to the Hamilton-Jacobi equations. This HJ-WENO scheme was found to be of great help in solving the Level-Set evolution equation, Eq. (2.4), since it comes with a higher order of accuracy.

Following the work of Osher and Shu (1991), the details of applying the fifth-order HJ-WENO to calculate the spatial gradient are given as follows. When computing the backward difference $(\phi_x^-)_i$, the third-order HJ-ENO uses a subset of $\{\phi_{i-3}, \phi_{i-2}, \phi_{i-1}, \phi_i, \phi_{i+1}, \phi_{i+2}\}$ and three approximations. By writing

$$\frac{\partial\phi}{\partial x} = \frac{\phi_i - \phi_{i-1}}{\Delta x} \quad (2.13)$$

as $D^-\phi$, we can have following expressions:

$$\nu_1 = D^-\phi_{i-2} \quad (2.14)$$

$$\nu_2 = D^-\phi_{i-1} \quad (2.15)$$

$$\nu_3 = D^-\phi_i \quad (2.16)$$

$$\nu_4 = D^-\phi_{i+1} \quad (2.17)$$

$$\nu_5 = D^-\phi_{i+2}. \quad (2.18)$$

Then the three approximations to $(\phi_x^-)_i$ are defined by,

$$\phi_x^1 = \frac{\nu_1}{3} - \frac{7\nu_2}{6} + \frac{11\nu_3}{6} \quad (2.19)$$

$$\phi_x^2 = -\frac{\nu_2}{6} + \frac{5\nu_3}{6} + \frac{\nu_4}{3} \quad (2.20)$$

$$\phi_x^3 = \frac{\nu_3}{3} + \frac{5\nu_4}{6} - \frac{\nu_5}{6}. \quad (2.21)$$

By weighting the approximations to $(\phi_x^-)_i$, the HJ-WENO scheme combines the above three equations (Eq. (2.19), Eq. (2.20) and Eq. (2.21)) to give

$$\phi_x(x) = w_1\phi_x^1 + w_2\phi_x^2 + w_3\phi_x^3, \quad (2.22)$$

where $w \in [0, 1]$ is the weighting coefficient with

$$w_1 + w_2 + w_3 = 1. \quad (2.23)$$

To reach the fifth-order of accuracy, the optimal combination of the weighting coefficients is $w_1 = 0.1$, $w_2 = 0.6$ and $w_3 = 0.3$. But this optimal approximation is only valid in smooth regions and will yield inaccurate estimations in non-smooth regions. Next, following Jiang and Peng (2000), the weighting coefficients are defined by estimating the smoothness of the stencils in Eq. (2.19), Eq. (2.20) and Eq. (2.21) as,

$$S_1 = \frac{12}{13}(\nu_1 - 2\nu_2 + \nu_3)^2 + \frac{1}{4}(\nu_1 - 4\nu_2 + 3\nu_3)^2 \quad (2.24)$$

$$S_2 = \frac{12}{13}(\nu_2 - 2\nu_3 + \nu_4)^2 + \frac{1}{4}(\nu_2 - \nu_4)^2 \quad (2.25)$$

$$S_3 = \frac{12}{13}(\nu_3 - 2\nu_4 + \nu_5)^2 + \frac{1}{4}(3\nu_3 - 4\nu_4 + \nu_5)^2. \quad (2.26)$$

These estimates are applied to define the following coefficients:

$$\alpha_1 = \frac{0.1}{(S_1 + \epsilon)^2} \quad (2.27)$$

$$\alpha_2 = \frac{0.6}{(S_2 + \epsilon)^2} \quad (2.28)$$

$$\alpha_3 = \frac{0.3}{(S_3 + \epsilon)^2}, \quad (2.29)$$

where,

$$\epsilon = 10^{-6} \max\{\nu_1^2, \nu_2^2, \nu_3^2, \nu_4^2, \nu_5^2\} + 10^{-99}. \quad (2.30)$$

The last term in Eq. (2.30) is used to avoid division by zero, and the first term is a scaling term that aids in transition between HJ-WENO and HJ-ENO. In this study, since the Level-Set ϕ is an approximate signed distance function, the ν that approximates ϕ_x is almost equal to 1. Therefore, ϵ can be set to 10^{-6} . Together with the coefficients defined earlier, the weighting coefficients are finally determined by,

$$w_1 = \frac{\alpha_1}{\alpha_1 + \alpha_2 + \alpha_3} \quad (2.31)$$

$$w_2 = \frac{\alpha_2}{\alpha_1 + \alpha_2 + \alpha_3} \quad (2.32)$$

$$w_3 = \frac{\alpha_3}{\alpha_1 + \alpha_2 + \alpha_3}. \quad (2.33)$$

Calculating the forward difference $(\phi_x^+)_i$ based on the HJ-WENO scheme in the same way, a sub set of $\{\phi_{i-2}, \phi_{i-1}, \phi_i, \phi_{i+1}, \phi_{i+2}, \phi_{i+3}\}$ is used. Similarly, by defining:

$$\nu_1 = D^+ \phi_{i+2} \quad (2.34)$$

$$\nu_2 = D^+ \phi_{i+1} \quad (2.35)$$

$$\nu_3 = D^+ \phi_i \quad (2.36)$$

$$\nu_4 = D^+ \phi_{i-1} \quad (2.37)$$

$$\nu_5 = D^+ \phi_{i-2}, \quad (2.38)$$

Eq. (2.19), Eq. (2.20) and Eq. (2.21) are applied to approximate $(\phi_x^+)_i$. Computing the weights with Eq. (2.31), Eq. (2.32) and Eq. (2.33), the spatial discretization based on the fifth-order HJ-WENO scheme is achieved by applying Eq. (2.22).

2.2.1.2 Temporal discretization

Previous studies suggest that Level Set Method are more sensitive to spatial accuracy, and that temporal truncation errors result in less deterioration of the numerical solution (Osher and Fedkiw, 2006). However, to obtain accurate numerical solutions in this study, it is still necessary to use a higher-order temporal discretization.

Based on the assumption that the spatial discretization can be separated from the temporal discretization in a semi-discrete way that allows the temporal discretization of the PDE to be treated independently as an ODE, Shu and Osher (1988) proposed Total Variation Diminishing Runge-Kutta (TVD-RK) methods to improve accuracy. Unlike some other RK schemes, these TVD-RK schemes produce no spurious oscillations. The existing fourth- and higher-order TVD-RK schemes do not seem to produce a better result when the HJ-WENO scheme is used to calculate spatial

gradients in practical calculations. They only improve the temporal accuracy slightly, but cost more computational time (Osher and Fedkiw, 2006). Due to this fact, the third-order TVD-RK scheme is applied in this study. The details are as follows.

First, an Euler step is applied twice to advance the solution to the time step $t^n + \Delta t$ and then to $t^n + 2\Delta t$, shown as,

$$\frac{\phi^{n+1} - \phi^n}{\Delta t} + u_i^n \cdot \nabla \phi^n = 0 \quad (2.39)$$

$$\frac{\phi^{n+2} - \phi^{n+1}}{\Delta t} + u_{i+1}^n \cdot \nabla \phi^{n+1} = 0. \quad (2.40)$$

Applying the interpolation,

$$\phi^{n+\frac{1}{2}} = \frac{3}{4}\phi^n + \frac{1}{4}\phi^{n+2} \quad (2.41)$$

we can get the approximation to the Level-Set value ϕ at the time step $t^n + \frac{1}{2}\Delta t$. Based on this, taking a further Euler step to advance the solution to $t^n + \frac{3}{2}\Delta t$, we have

$$\frac{\phi^{n+\frac{3}{2}} - \phi^{n+\frac{1}{2}}}{\Delta t} + u_i^{n+\frac{1}{2}} \cdot \nabla \phi^{n+\frac{1}{2}} = 0 \quad (2.42)$$

Similarly, applying the ϕ value at the current time step and time step $t^n + \frac{3}{2}\Delta t$ by the following equation,

$$\phi^{n+1} = \frac{1}{3}\phi^n + \frac{2}{3}\phi^{n+\frac{3}{2}}, \quad (2.43)$$

the third-order accurate approximation to ϕ at the next time step $t^n + \Delta t$ can be produced.

2.2.1.3 Re-initialization of the Level-Set function

As the Level-Set function ϕ is stepped forward in time its distribution throughout the domain may deviate from being a signed distance function (i.e. $|\nabla\phi| \neq 1$), especially for flows undergoing extreme topological changes. Thus, to maintain the signed distance property of the Level-Set function, we need to solve the re-initialization equation given by Sussman et al. (1994),

$$\frac{\partial\phi}{\partial\tau} + S(\phi_0)(|\nabla\phi| - 1) = 0, \quad (2.44)$$

where ϕ_0 denotes the updated ϕ in the current time step. Evolving Eq. (2.44) to the steady state through the fictitious time τ gives us the signed distance function of ϕ .

In the re-initialization equation (Eq. (2.44)), $S(\phi_0)$ is a one-dimensional smeared out function which is continually updated during the calculation using the updated value ϕ_0 by,

$$S(\phi_0) = \frac{\phi_0}{\sqrt{\phi_0^2 + (\Delta x)^2}}. \quad (2.45)$$

In this study, the fast marching method proposed by Sethian (1996) is adopted to perform the re-initialization process. The positive domain (water) and negative domain (air) use the fast marching scheme separately with the same idea. First, all cells are divided and defined as three bands: the accepted band with cells adjacent to the interface, the tentative band with cells close to the accepted band, and the faraway band with all the remaining cells in the corresponding domain. Then, values of Level-Set function ϕ in the accepted band are used to update the value of ϕ in all the tentative cells by solving $|\nabla\phi| = 1$. After the calculation, the tentative cell with the smallest value of Level-Set function is selected and added to the accepted band. In the next step, the ϕ value in the newly accepted cell is used to update the values of ϕ in its neighboring tentative cells by solving $|\nabla\phi| = 1$. Any of its other neighboring cells that are in the defined faraway band are assigned values of updated ϕ at the above step, and are redefined into the tentative band.

Since the cells close to the interface in the first accepted band are not updated by the fast marching procedure, we must specify the values of ϕ in those cells. To achieve this, we adopt the method proposed by Losasso et al. (2006). First, a massless particle is introduced at each cell close to the interface. Using the local properties of ϕ , the particle is transported towards the interface in the local normal direction over a distance equal to its corresponding value of ϕ . Then the normal vector and the value of ϕ are calculated at the new particle location. With the updated information, the particle is propagated again towards the interface. This procedure is continued until the absolute value of ϕ at the particle location is less than a tolerance of the interface,

$$|\phi| < 0.1\Delta x. \quad (2.46)$$

The value of ϕ close to the interface is then updated using the distance from the cell center to the final location of the particle. If the final particle location is not within a tolerance of the interface, the linear interpolation between surrounding cells that cross the interface is applied to update ϕ accordingly.

2.2.2 Solution to Navier-Stokes equations

In this study, the Navier-Stokes equations (Eq. (2.9)) are discretized on a staggered grid with p , ρ and μ defined at grid cell centers, and the velocity u , v at cell faces. An illustration is provided in Fig. 2.5.

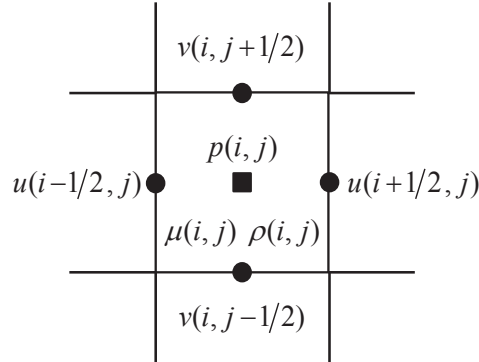


Figure 2.5: Demonstration of the two-dimensional staggered grid.

A two-step scheme by Kim and Moin (1985) is used for the time-advancement of the Navier-Stokes equations. To apply this scheme, the role of pressure in the momentum equations can be interpreted as a projection operator which projects an arbitrary velocity field into a divergence-free field.

Temporal gradients are discretized with a second-order TVD-RK scheme, which performs two Euler time steps. First, Eq. (2.9) is rewritten to obtain a predicted velocity \hat{u}_i^{n+1} at the next time step,

$$\hat{u}_i^{n+1} = \tilde{u}_i^n - \frac{\Delta t}{\rho^n(\phi)} \frac{\partial p^n}{\partial x_i}, \quad (2.47)$$

where the superscript n denotes the current time step and

$$\tilde{u}_i^n = u_i^n + \Delta t \left[\frac{1}{\rho^n(\phi)} \left(\frac{\partial \tau_{ij}^n}{\partial x_j} \right) - u_j^n \frac{\partial u_i^n}{\partial x_j} + f_i \right]. \quad (2.48)$$

In requiring that the predicted velocity field be divergence free, Eq. (2.47) becomes

$$\frac{\partial}{\partial x_i} \left[\frac{1}{\rho^n(\phi)} \frac{\partial p^n}{\partial x_i} \right] = \frac{1}{\Delta t} \left(\frac{\partial \tilde{u}_i^n}{\partial x_i} \right), \quad (2.49)$$

which is a Poisson equation for the unknown pressure field. Applying the second-order central difference scheme to calculate the spatial gradients, (take x -direction as an example),

$$\frac{\partial \tilde{u}}{\partial x} = \frac{u_{i+\frac{1}{2},j} - u_{i-\frac{1}{2},j}}{\Delta x} \quad (2.50)$$

gives the solution to Eq. (2.49). Adding the gradient of the calculated pressure field to Eq. (2.47) obtains a prediction of the new velocity field \hat{u}_i^{n+1} . By solving Eqs. (2.47), (2.48), and (2.49) again with \hat{u}_i^{n+1} , the second prediction for the velocity field at the time step $n+2$ is achieved. By taking an average of the second prediction and the initial velocity field, the velocity field at the time step $n+1$ is given by,

$$u_i^{n+1} = \frac{1}{2} (u_i^n + \hat{u}_i^{n+2}). \quad (2.51)$$

When discretizing the convective term in Eq. (2.9), it is essential to avoid the introduction of numerical instabilities due to the sharp density gradient at the interface. To ensure stability, we employ the first-order upwind scheme in the numerical model at the current stage, which is as follows (take $u \frac{\partial u}{\partial x}$ as an example):

$$u \frac{\partial u}{\partial x} = u_{i+\frac{1}{2},j} \cdot \frac{u_{i+\frac{1}{2},j} - u_{i-\frac{1}{2},j}}{\Delta x}, \quad \text{if } u_{i+\frac{1}{2},j} > 0 \quad (2.52)$$

$$u \frac{\partial u}{\partial x} = u_{i+\frac{1}{2},j} \cdot \frac{u_{i+\frac{3}{2},j} - u_{i+\frac{1}{2},j}}{\Delta x}, \quad \text{if } u_{i+\frac{1}{2},j} < 0. \quad (2.53)$$

To make the numerical model stable, we restrict the time step by the CFL condition and the gravity (Kang et al., 2000). By employing a CFL number of 0.5, the following condition should be satisfied:

$$\Delta t < 0.5 \left[\frac{C_{cfl} + \sqrt{(C_{cfl})^2 + 4(G_{cfl})}}{2} \right]^{-1}, \quad (2.54)$$

where $C_{cfl} = \max(|u|/\Delta x, |v|/\Delta y)$ and $G_{cfl} = g/\Delta y$ and Δx , Δy are the grid increments in the x - and y -directions respectively.

2.3 Validation of the numerical model

The frame of the numerical model described above is based on the work of Archer and Bai (2011). In their work, only a basic free surface flow solver was developed, with a heavy focus on the particle technique applied into the Level Set Method. To make the program suitable for simulations of liquid sloshing, massive revisions and improvements have been made to obtain the present numerical model. In this section, classic test cases are performed to validate the model's capability. To investigate the accuracy of the Level-set algorithm, the vortex in box case, which involves the propagation of an interface in a prescribed velocity field, is studied first. To test the numerical solution to the governing equations of the fluid, the lid-driven cavity flow case, which has been widely used as a benchmark test case, is applied as the second validation case. Since the first two cases are concerned with interface capturing and motion of a single fluid, the free sloshing in a rectangular tank case is performed to test the capability of the combined numerical model for simulation of free surface flows. Finally, an even more difficult test case, the dam break test, is conducted to show the capacity of the present numerical model in modeling the two-phase flows with breaking waves. It is worth mentioning that the tank walls are assumed to be rigid in all the following cases in this thesis.

2.3.1 Vortex in box

The vortex in box test case is a typical test used to access the accuracy of an algorithm in the propagation of an interface. In this case, a circular surface is placed in the velocity field of a constrained vortex. The resulting deformation procedure involves the stretching and restoration of this circular surface.

The velocity field is given by:

$$u = -\sin^2(\pi x) \sin(2\pi y) \cos(\pi t/T) \quad (2.55)$$

$$v = -\sin^2(\pi y) \sin(2\pi x) \cos(\pi t/T), \quad (2.56)$$

where $T = 4.0$ is the total time duration of the simulation. A circular interface with a radius of $r = 0.15$ is placed in a square domain with a size of 1.0×1.0 . The center of the circular interface is located at $(0.5, 0.75)$. Fig. 2.6 shows the initial conditions of this case. According to the given equation of the velocity and simulation time, the flow field will reverse its direction at time $t = 2.0$. At time $t = 4.0$, an accurate algorithm should predict the interface returning to its initial circular shape.

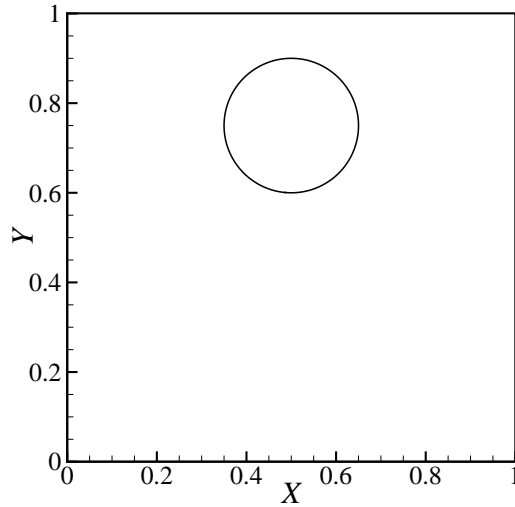


Figure 2.6: Initial conditions of the vortex in box case.

To begin with, four different mesh sizes, 100×100 , 200×200 , 400×400 and 800×800 are applied to test the grid convergence. Fig. 2.7 shows the time instant when the flow stops and begins to reverse its direction. The interface has been stretched into a thin spiraling filament. It can be seen that as the mesh size increases, the difference between the results given by the present model becomes smaller. This indicates a nearly convergent solution is achieved by the mesh of 400×400 .

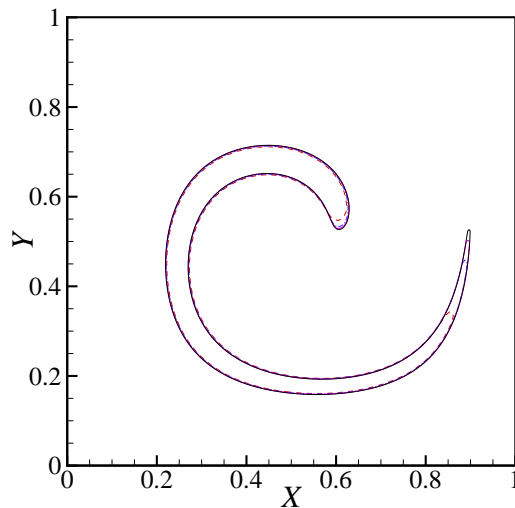


Figure 2.7: Comparison between different meshes at $t = 2$ (red dashed line: 100×100 , blue dash-dot line: 200×200 , pink solid line: 400×400 , black solid line: 800×800).

A comparison is made at time $t = 4.0$ in Fig. 2.8 when the interface is expected

to return and recover its initial circular shape. With the finer mesh size applied, the circular shape obtained is closer to the ideal condition. Same as Fig. 2.7, predictions given by 400×400 and 800×800 are very close to each other, supporting our statement that a convergent solution is achieved by the mesh of 400×400 . In addition, Good agreement between the present solution and the ideal condition validates that the Level-Set algorithm in the present numerical model is capable of capturing the interface with a high degree of accuracy.

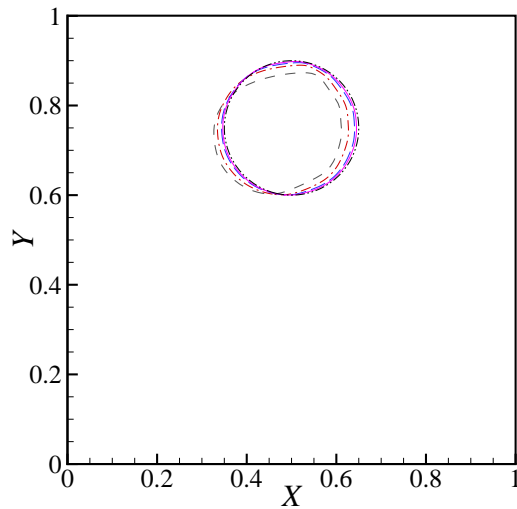


Figure 2.8: Comparison between different meshes at $t = 4$ (gray dash line: 100×100 , red dash-dot line: 200×200 , blue long dashed line: 400×400 , pink solid line: 800×800 , black dash-dot-dot line: Ideal condition).

Fig. 2.9 presents the whole procedure of this vortex box test case with the mesh size of 400×400 . When time $0.0 < t < 2.0$, the circular interface is stretched out while the swirling velocity gradually decreases. At time $t = 2.0$, the flow comes to a stop and starts to reverse its direction. During time $2.0 < t < 4.0$, the reversal of the swirling flow direction gradually drives the stretched interface back. Finally, at time $t = 4.0$, the circular interface is back and has recovered its initial profile as expected. (The captured interface at the time instants $t = 0.0$, $t = 2.0$ and $t = 4.0$ is given in Fig. 2.6, Fig. 2.7 and Fig. 2.8, respectively.)

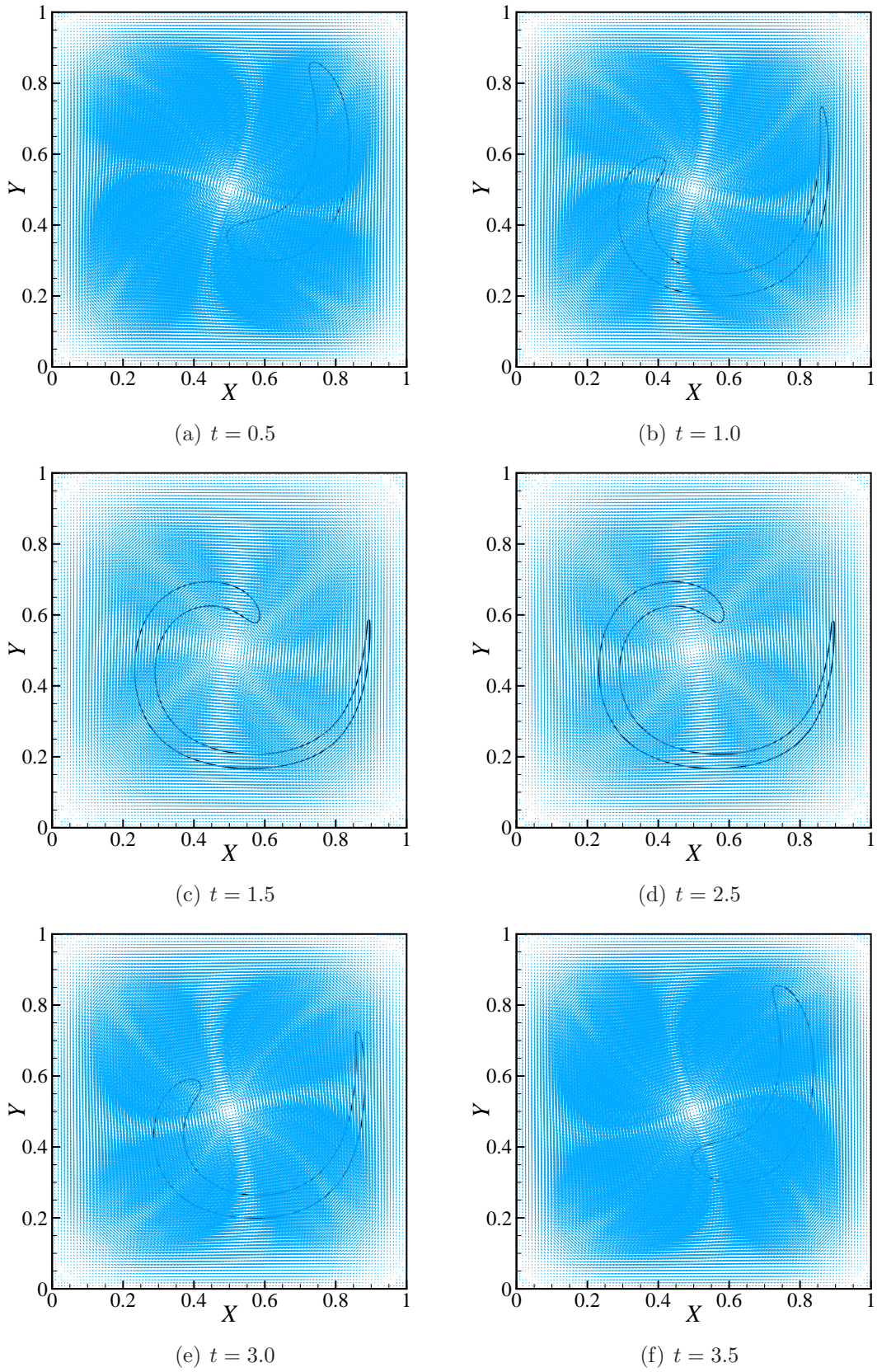


Figure 2.9: Surface profiles at different time instants during the vortex stretch and recover process.

2.3.2 Lid-driven cavity flow

Prior to applying the numerical model to solve the two-phase flow problem, we need to further validate the fluid solver by repeating the well-known lid-driven cavity flow test. As shown in Fig. 2.10, a two-dimensional rectangular cavity with a length of $L = 1$ and a height of $H = 1$ is filled with only one fluid of a fixed density $\rho = 1$. Therefore, the free surface is not of concern here. The top wall moves at a constant velocity $U = 1$ while the other three are stationary. The flows in the cavity with viscosities of $\mu = 1.0 \times 10^{-2}$, 2.5×10^{-3} and 1.0×10^{-3} are simulated. According to

$$Re = \frac{\rho U L}{\mu}, \quad (2.57)$$

the Reynolds numbers are $Re = 100$, $Re = 400$ and $Re = 1000$, respectively.

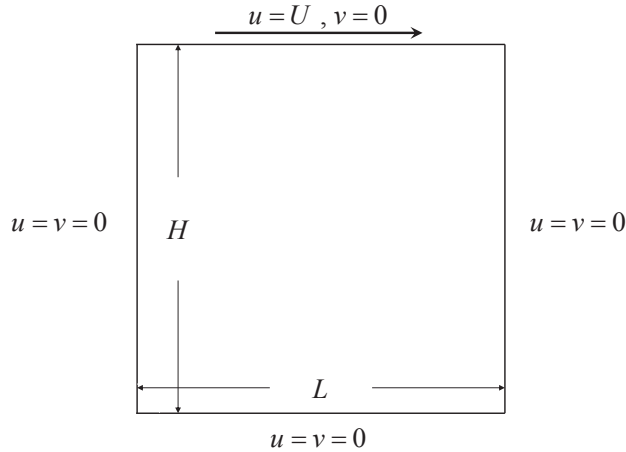
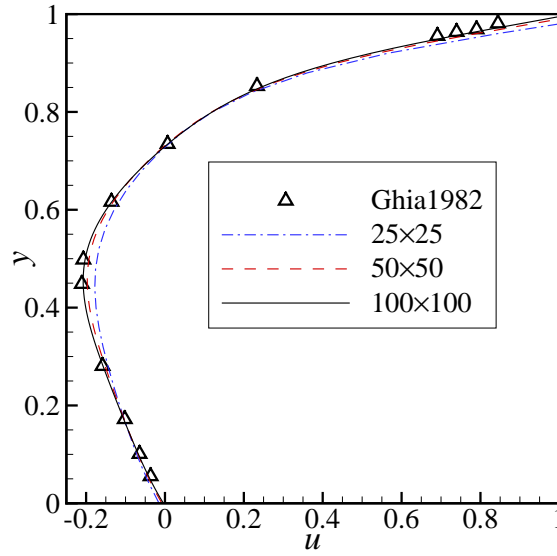


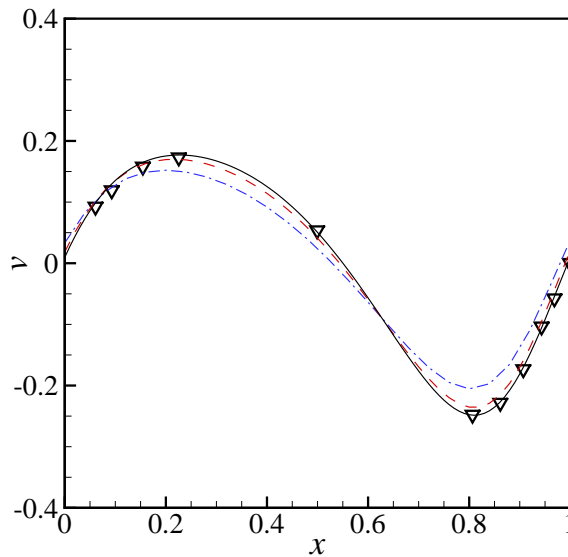
Figure 2.10: The geometry of the lid-driven cavity.

Since there are three different cases with different Reynolds numbers, grid convergence tests are performed for each case. For $Re = 100$, Fig. 2.11 shows the velocity components in the x - and y -directions along the vertical and horizontal centerlines, respectively. The results from the two mesh sizes, 50×50 and 100×100 lie quite close to each other, suggesting a convergent solution is achieved. To validate the accuracy of this solution, the benchmark result of Ghia et al. (1982) is also plotted for the purpose of comparison. The present numerical results agree quite well with the benchmark solution.

Similarly, for $Re = 400$, the mesh size test is also performed. As shown in Fig. 2.12, the numerical results gradually approach the benchmark solution as the mesh



(a) u along the vertical centerline



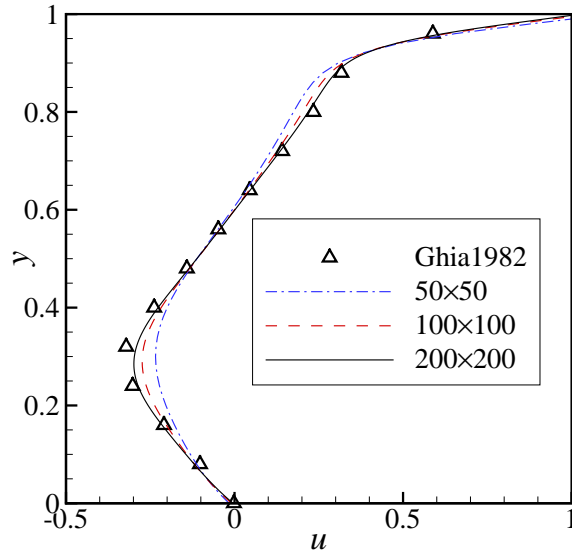
(b) v along the horizontal centerline

Figure 2.11: Comparison between numerical results with different mesh sizes and the benchmark solution for $Re = 100$.

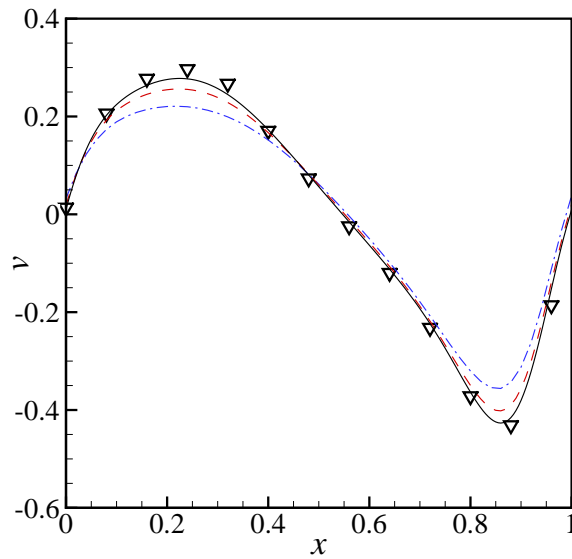
size increases from 50×50 to 200×200 . This suggests that the fluid solver in the present numerical model might need a finer mesh when modeling a challenging case.

Lastly, a further comparison is made for the $Re = 1000$ case, as shown in Fig. 2.13. In this case, an even finer mesh size of 300×300 has to be applied to obtain a satisfying numerical result.

To sum up, as the Reynolds number increases, the numerical modeling of the lid-



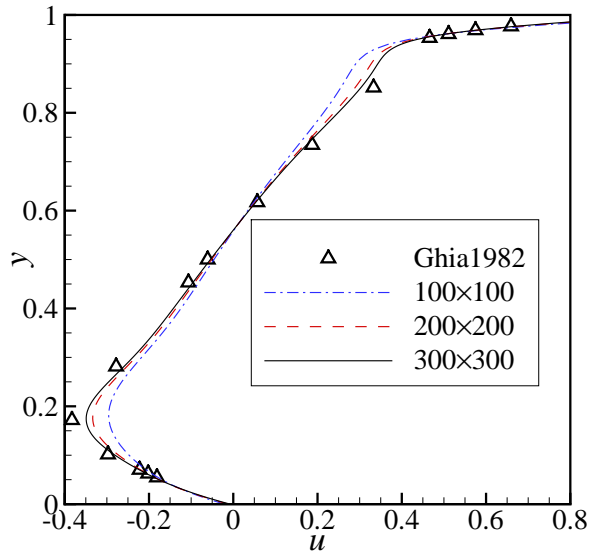
(a) u along the vertical centerline



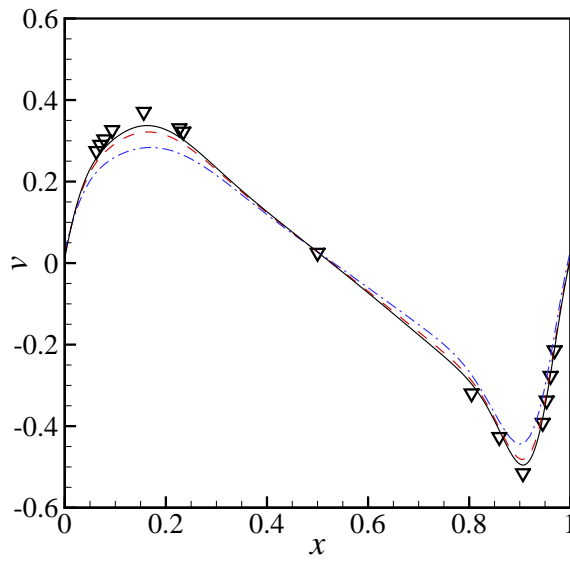
(b) v along the horizontal centerline

Figure 2.12: Comparison between numerical results with different mesh sizes and the benchmark solution for $Re = 400$.

driven cavity flow becomes more challenging. A finer mesh size is required to achieve a more accurate result. Nevertheless, good agreement with the benchmark solution indicates that the present numerical model could solve fluid motions accurately.



(a) u along the vertical centerline



(b) v along the horizontal centerline

Figure 2.13: Comparison between numerical results with different mesh sizes and the benchmark solution for $Re = 1000$.

2.3.3 Free sloshing in a rectangular container

To further validate the present numerical model in modeling fluid motions with a free surface, we shall consider a classic test case for free surface flow problems: wave sloshing in a container under the influence of gravity.

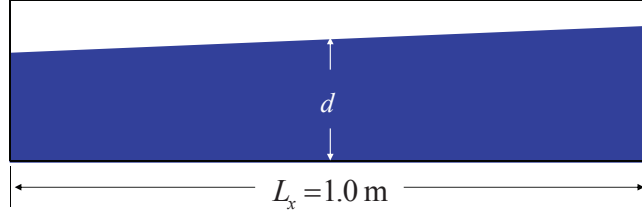


Figure 2.14: A schematic view of the free sloshing case.

As shown in Fig. 2.14, a sloping free surface separating the water phase and air phase is set in a rectangular container. The length of the container is 1 m and the initial slope of the free surface is 0.02 with a still water depth of 0.2 m. Once the fluid begins to move under gravity, there exists an infinite number of standing wave modes in the container. Provided the viscosity is neglected in this case, the analytical solution to this problem can be found based on linear wave theory. The surface displacement η is given by Lin and Li (2002) as,

$$\eta = \sum_{m=1}^{\infty} A_m \sin(k_m x) \cos(\varpi_m t) \quad (2.58)$$

where $k_m = (m\pi)/L_x$ is the wave number, L_x is the length of the water tank, $\varpi_m = \sqrt{gk_m \tanh(k_m d)}$ is the frequency, g is the gravitational acceleration, d is the still water depth and $A_m = SL_x/(m^2\pi^2) [4\sin(m\pi/2) - 2\sin(m\pi)]$ is the amplitude of the m th mode.

To investigate the grid convergence, three different meshes, denoted by Mesh 1, Mesh 2, and Mesh 3, using 40×10 , 160×40 , and 480×120 cells, respectively, are adopted with the time interval of 0.01 s. In Fig. 2.15, time histories of the surface displacement at the left wall of the container obtained with different mesh sizes are compared with the analytical solution. Numerical results with different mesh sizes gradually approach the analytical solution. A convergent solution can be obtained using Mesh 2 in the computational domain.

Further investigations on the convergence of the calculation with three different time intervals are conducted. Fig. 2.16 shows that all the three results obtained by

the chosen time intervals are almost identical, which indicates that the calculations are not very sensitive to the three time intervals as long as the simulation can be completed. Thus, results obtained by Mesh 2 and the time interval of 0.01 s are selected for further comparison.

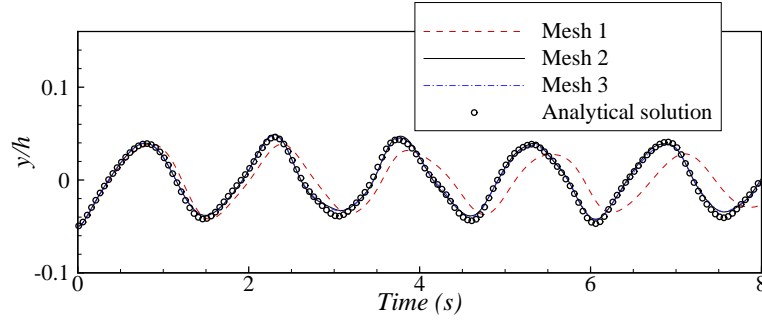


Figure 2.15: Time histories of free surface displacement at the left wall for three mesh sizes.

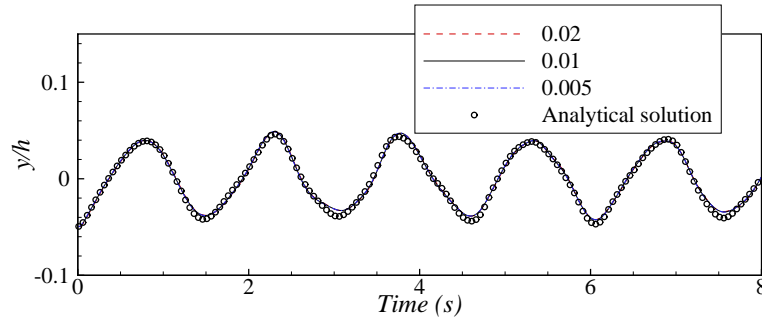
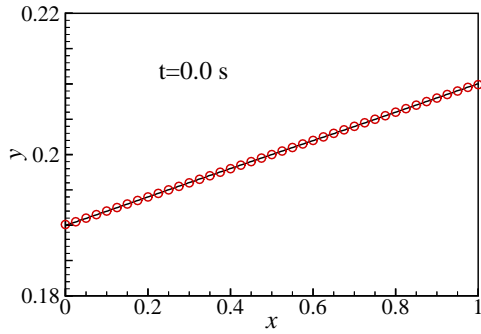
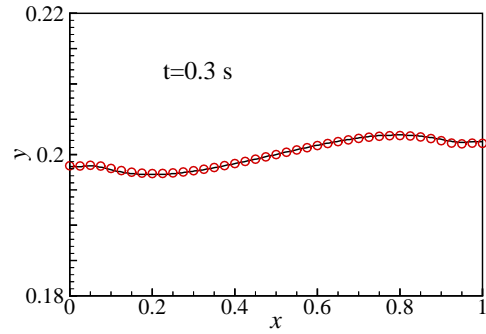


Figure 2.16: Time histories of free surface displacement at the left wall for three time intervals.

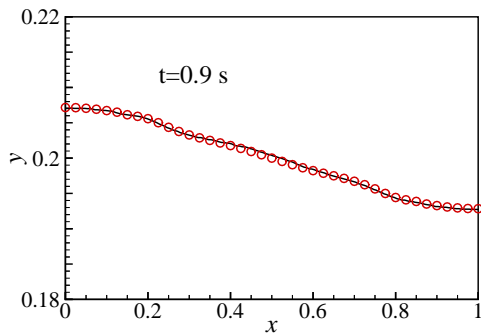
Fig. 2.17 shows the comparison of the wave profiles at six time instants with the corresponding analytical solutions. The first four wave profiles capture the free surfaces during the first wave period for the leading mode, and the last two frames show how the wave behaves after a longer time simulation. From the comparisons, we can see that the numerical predictions agree well with the analytical solution at the beginning, but a slightly larger discrepancy is observed at the last instant of time. This might be caused by the neglect of nonlinear effects in the analytical solution and accumulated errors in the numerical model. Overall, the numerical model at the current phase can accurately simulate the two-phase flows without breaking waves.



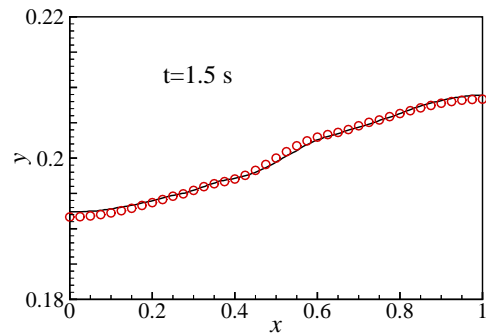
(a)



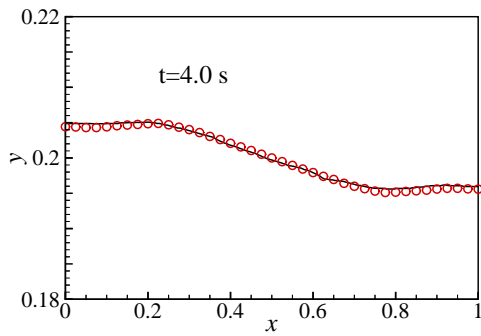
(b)



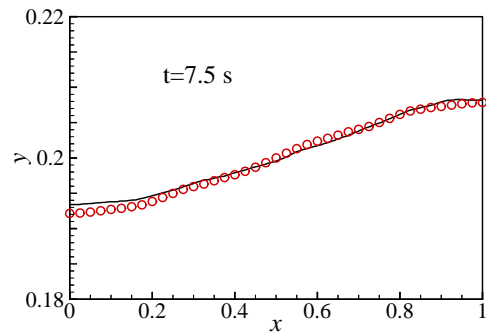
(c)



(d)



(e)



(f)

Figure 2.17: Comparison of wave profiles between the present numerical results and analytical solutions at different time instants.

2.3.4 Dam break test case

In this section, fluid motion with breaking waves is used to test the capability of the present numerical model in handling violent topological changes. The dam break test case has been selected since it involves the following features: free surface splitting, merging, and over turning. In this test case, the sudden collapse of a water column on a rigid horizontal plane is used to simulate the abrupt failure of a dam, where an initially blocked still-water column starts to spread out after the barrier is removed. This test case is a classic validation case and has been the subject of many numerical and experimental studies. Here, the numerical and experimental work of Fekken (1998) is followed.

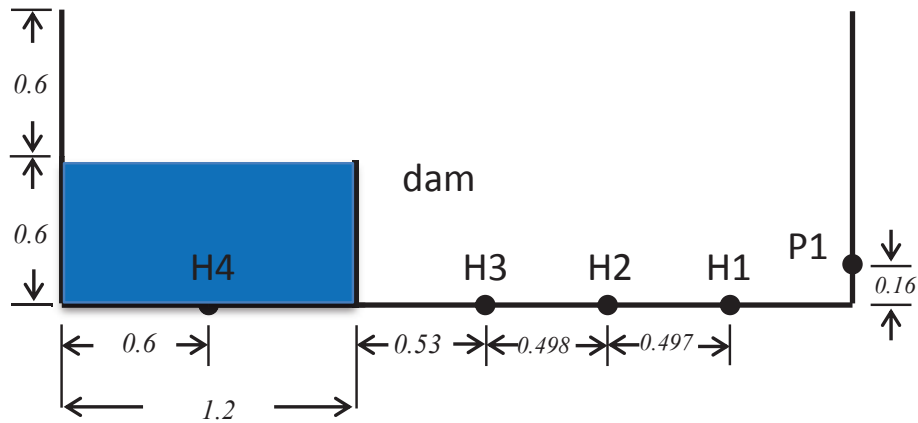


Figure 2.18: A schematic view of the dam break case.

Fig. 2.18 is the schematic view of this dam break case. As shown in this figure, the experiment was conducted in a two-dimensional rectangular tank with a length of $L = 3.332$ m and a height of $H = 1.2$ m. The water column is set on the left side of the wall with a length of $L_w = 1.2$ m and a height of $H_w = 0.6$ m. According to Fekken et al. (1998), the experiment conducted by the Maritime Research Institute Netherlands (MARIN) used four vertical wave probes at position $H1$, $H2$, $H3$, $H4$ and a pressure sensor at position $P1$, as shown in Fig. 2.18, to measure the wave height and pressure.

Following the same procedure of the previous section for the convergence test, the time step $\Delta t = 0.001s$ and mesh size of 216×80 are selected to simulate this test

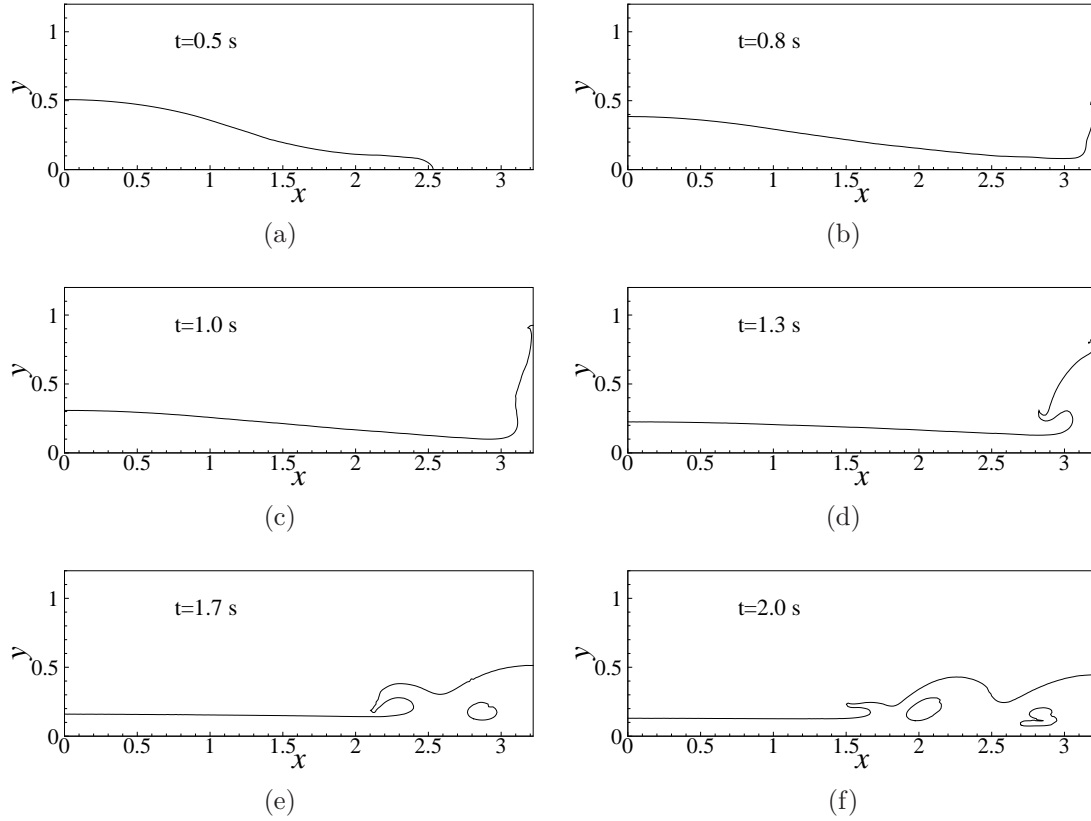


Figure 2.19: Wave profiles captured by the presented numerical model at different time instants.

case. The total simulation time is $t = 4.0$ s. The viscosities of both water and air are neglected. The wave profile obtained by the present numerical model at different time instants are shown in Fig. 2.19. After the vertical barrier is removed at time $t = 0.0$ s, the water column collapses and flows to the right side due to the pressure difference between water and air. When the front of the water hits the wall around $t = 0.6$ s, the kinetic energy of the flow pushes it upwards against the wall. As the water runs up along the right wall, the velocity of the flow decreases gradually due to the energy conversion from kinetic energy to potential energy. Around $t = 1.0$ s, the water front ceases to hit the wall and starts to fall back into the tank due to gravity. Then, the falling water hits the bottom water in the tank at around $t = 1.4$ s. This generates a splash wave traveling to the left with a thin, elongated surge front. The splash falls into the tank and finally the water calms down. It can also be observed that several air bubbles are captured by the present numerical model at around $t = 2.0$ s.

In Fig. 2.20, the comparison of the pressure time history is made among our sim-

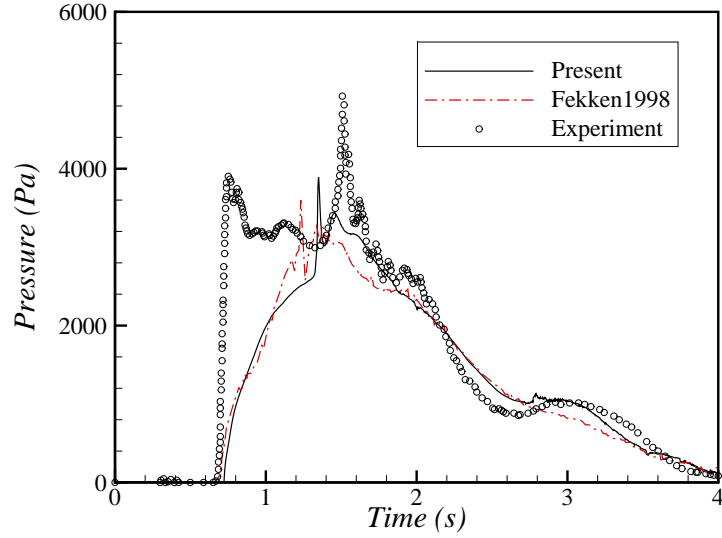


Figure 2.20: Comparison of time histories of the pressure among the present results, Fekken’s numerical results and experimental measurements.

ulation results, the experimental observation of MARIN, and the numerical solutions given by Fekken et al. (1998). To obtain the pressure value at $P1$ in the present numerical model, the values at four neighboring cell centers are identified to perform the interpolation. As shown in Fig. 2.20, both numerical solutions have a similar trend: there are three peaks captured by the two numerical models. The first peak is generated when the water front hits the right wall after the water column collapses. The second one occurs due to the additional induced pressure after the wave front comes to a stop, falls back due to gravity and hits the water in the tank bottom. The third peak is relatively moderate since it occurs when the breaking wave falls down and the water again runs up to the right wall, which results in a pressure increase. However, both numerical solutions have not captured the steep rise in pressure at around time $t = 0.6$ s. One possible reason for this discrepancy is that the slope of the waterfront in the simulation is smaller than that in the experiment just before impact. This difference in the slopes might be due to the fact that both numerical simulations are not exactly equivalent to the experiment. According to Fekken (1998), to represent the dam break in the experiments, a flap was pulled up with a velocity of approximately 4 m/s. As studied in Buchner and van Ballegoyen (1997), the slope of the waterfront may have a big influence on the impact pressure. Thus, the difference in slope of the waterfront leads to the pressure discrepancy around $t = 0.6$ s.

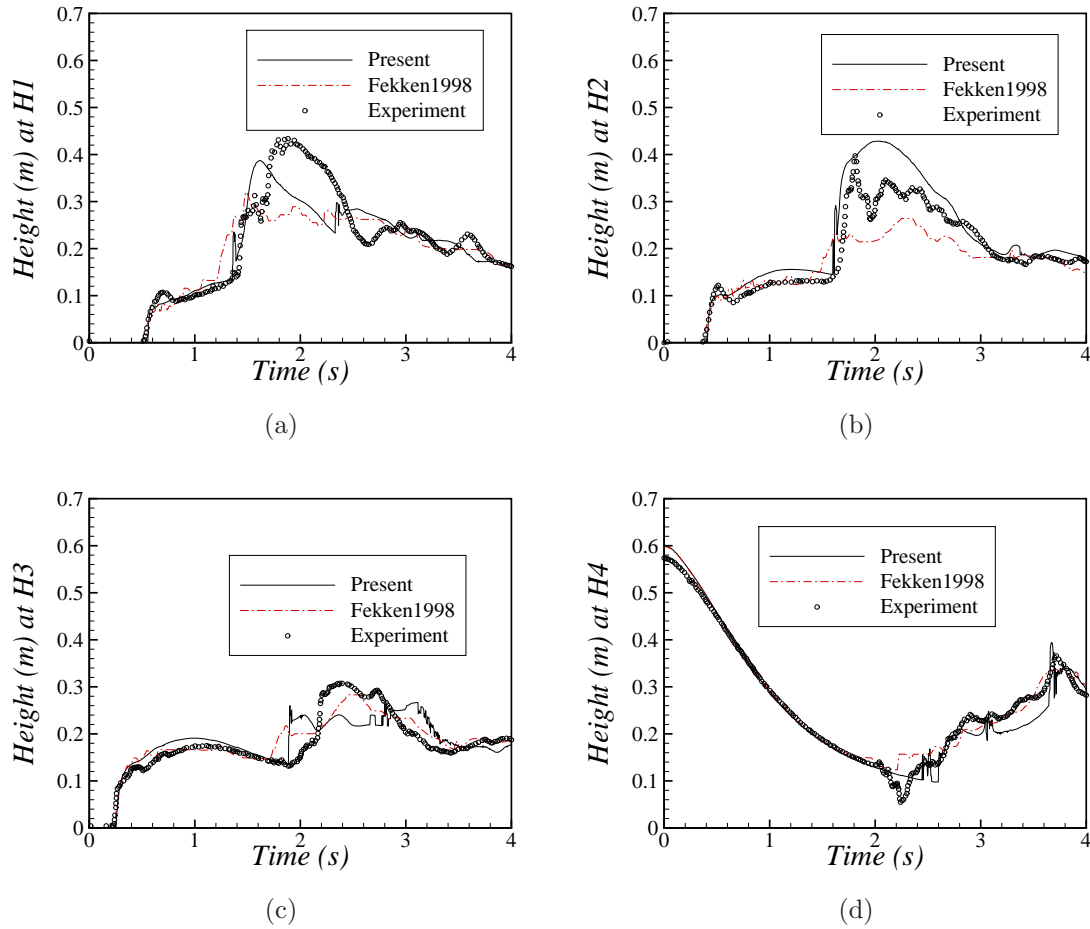


Figure 2.21: Comparison of the wave height recorded at four probes among the present results, Fekken’s numerical results and experimental measurements.

Fig. 2.21 shows the wave heights obtained by the experiment, Fekken’s numerical work and our numerical model at the four measured positions. At the two wave probes nearest to the dam, $H4$ and $H3$, the wave height predicted by both the numerical models are close each other and agree well with the laboratory measurements, except some localized discrepancies, as shown in Fig. 2.21(c) and Fig. 2.21(d). It should be pointed out that, at $t = 0$ s, the wave height should be 0.6 m as correctly given in Fig. 2.21(d) by both numerical results. However, the experimental recording was less than 0.6 m. This height difference could be due to the same reason for the pressure discrepancy mentioned earlier.

However, as the distance from the dam increases, Fig. 2.21(a) and Fig. 2.21(b) show that the wave height at $H2$ and $H1$ generated by the present model diverges from the numerical solution given by Fekken et al. (1998). Although a similar trend of the

two numerical predictions approaching the experimental results could be observed, our results are closer in agreement with the experimental recordings.

2.4 Summary

In this chapter, the numerical model for the simulation of free surface flows applied in the present study was introduced in detail.

The mathematical formulation of the numerical model was given by introducing the basic principle of the Level Set Method capturing the free surface and the Navier-Stokes equations that govern the motions of both the fluids.

To capture the free surface, the Level-Set equation was solved numerically. The fifth-order HJ-WENO scheme was applied to discretize the spatial gradient, while the third-order TVD-RK scheme was employed to calculate the temporal gradient. To maintain the signed distance property of the Level-Set function, the fast marching scheme was adopted for the re-initialization of the Level-Set equation at every time step.

The fluid governing equations were solved using the two-step projection scheme with the second-order TVD-RK scheme to calculate the temporal gradients. The diffusive terms in the Navier-Stokes equations were discretized by the central difference scheme and the convective terms were computed by the first-order upwind scheme.

To test the present numerical model, first, the vortex in box case was studied. With details captured by the Level-Set technique during the vortex deformation and agreement with the ideal conditions at the restoring moment of the vortex, the pure interface capturing part of the present model was validated. Then, the fluid solver of the numerical model was assessed by reproducing the classic lid-driven flow case. Good agreement with the benchmark solutions for different Re numbers indicated the accuracy of the fluid solver used in the present model.

Finally, the free surface flows with and without breaking waves were investigated. In both cases, satisfactory results were achieved. The predictions given by the present model matched the published analytical solutions and experimental data. Thus, the numerical model for the simulation of the free surface flows applied in this study was well verified.

Chapter 3

LIQUID SLOSHING DUE TO SHIP MOTIONS

3.1 Introduction

As described in Chapter 1, sloshing is a motion of a free liquid surface inside a container. It is of great significance with regard to LNG carriers since violent liquid sloshing can lead to structural damage of tank walls. Tank rupture is also a risk if the external excitation is close to the natural frequency of the sloshing system. In addition, to study the interaction between sloshing and ship motions in waves, an accurate prediction of the sloshing flow is required.

In Chapter 2, the numerical model to study free surface flows was discussed and validated by the good agreements obtained with the benchmark results of some classic test cases. In this chapter, the present numerical model is applied to study various sloshing problems. First, the forced sloshing induced by horizontal and rotational motions is investigated. To further validate the capability of the present numerical model, sloshing with breaking waves is also considered. Finally, since the basis of this research is about the interaction between sloshing and ship motions, sloshing in a full-scale tank excited by ship motions encountered in sea conditions is studied.

3.2 Forced sloshing

Forced sloshing in a tank is usually generated by the external tank's motions, which is a problem involving a moving boundary. However, in the numerical simulation, the moving boundary problem is always complicated to solve due to the time vary-

ing computational domain. In order to avoid the complicated boundary conditions imposed on the moving boundary, a coordinate system that moves together with the tank is adopted, as shown in Fig. 3.1. By doing this, the external excitation f_i in Eq. (2.9) can be easily represented by using the tank motion. Thus, f_i consists of the gravitational acceleration, translational and rotational inertia forces and can be expressed in the vector form as (Ibrahim, 2005),

$$\mathbf{f} = \mathbf{g} - \frac{d\mathbf{U}}{dt} - \frac{d\mathbf{\Omega}}{dt} \times (\mathbf{r} - \mathbf{R}) - \mathbf{\Omega} \times [\mathbf{\Omega} \times (\mathbf{r} - \mathbf{R})] - 2\mathbf{\Omega} \times \frac{d(\mathbf{r} - \mathbf{R})}{dt}, \quad (3.1)$$

where \mathbf{g} , \mathbf{U} and $\mathbf{\Omega}$ are the gravitational acceleration, translational velocity and rotational velocity of the moving coordinate respectively. In addition, \mathbf{r} and \mathbf{R} are the position vectors of the considered point in the computational domain and the rotation center respectively, as shown in Fig. 3.1. If no rotational motion is present ($\mathbf{\Omega} = 0$), Eq. (3.1) will be reduced to a simple form with only the first two non-zero terms on the right-hand side of the equation remaining.

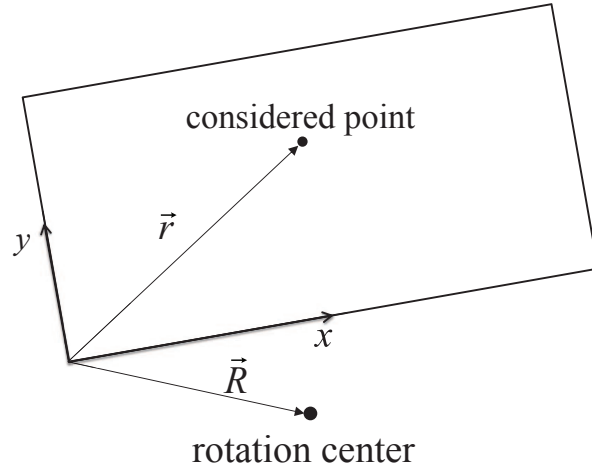


Figure 3.1: Definition of the two-dimensional moving coordinate system.

3.2.1 Sloshing due to surge motions without breaking waves

First, the experiment conducted by Koh et al. (2012) to investigate liquid sloshing in a two-dimensional rectangular tank is reproduced numerically. The tank used in the experiment measures 0.6 m in both the horizontal and vertical directions with a still water depth of 0.3 m. As shown in Fig. 3.2, a wave probe measuring the free surface elevation is located 20 mm from the right wall at point H1, and a pressure sensor is placed on the left wall at point P1, 20 mm above the bottom of the tank.

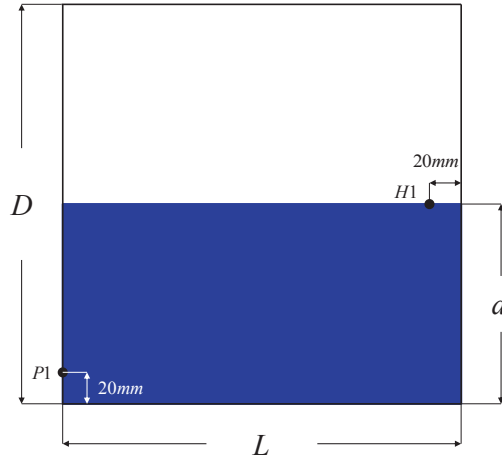


Figure 3.2: A schematic view of the two-dimensional rectangular tank used in Koh's experiment.

The displacement of the tank is governed by,

$$x = A(1 - \cos \omega t), \quad (3.2)$$

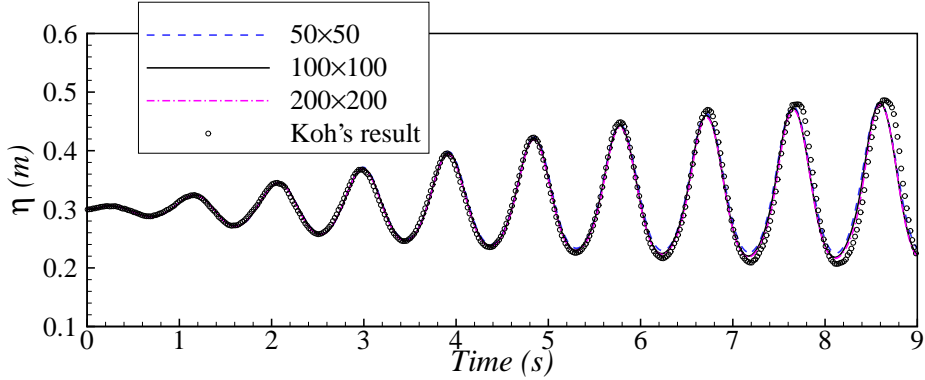
where A is the excitation amplitude set to 5 mm and ω is the excitation frequency chosen to be 6.85 rad/s, the same as the fundamental frequency ω_0 calculated by,

$$\omega_0 = \sqrt{g \frac{\pi}{L} \tanh\left(\frac{\pi}{L} d\right)}, \quad (3.3)$$

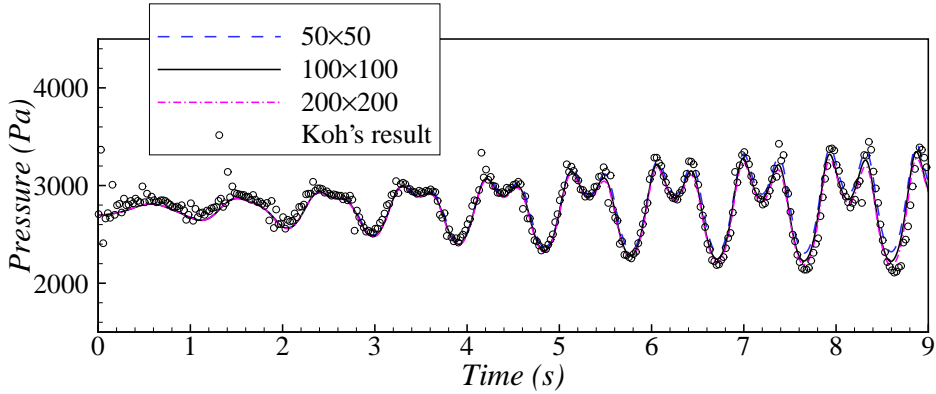
where L denotes the tank length and d is the initial water depth.

To investigate the grid convergence, three different meshes are tested with cell numbers of 50×50 , 100×100 and 200×200 respectively. The time interval is taken as $\Delta t = 0.001$ s. In Fig. 3.3, results of the free surface elevation at point $H1$ and

pressure at point $P1$ are compared with the experimental results. Clearly, numerical results from the different meshes gradually approach the experimental results. The values obtained by the two finer meshes lie close to each other. This suggests that a convergent solution is achieved by the present numerical model and that the mesh size of 100×100 could be used for the following simulations in this section.



(a) Time histories of free surface displacement at point $H1$

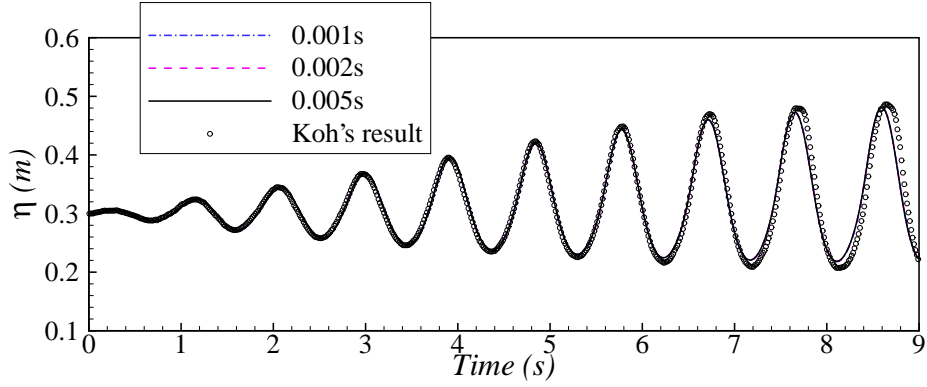


(b) Time histories of pressure at point $P1$

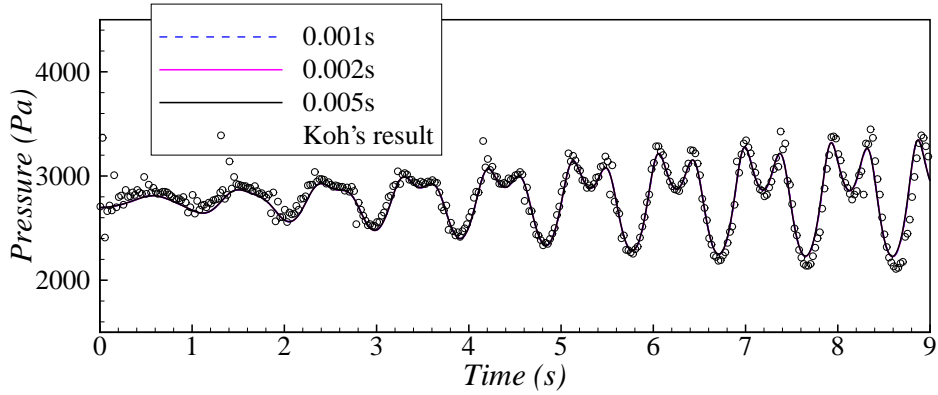
Figure 3.3: Convergence test of three mesh sizes.

We further test the convergence of the calculation with three different time intervals: $\Delta t = 0.001$ s, $\Delta t = 0.002$ s, and $\Delta t = 0.005$ s. Results shown in Fig. 3.4 are almost identical and indicate that the calculations are insensitive to the three time intervals adopted in this case. Thus, a convergent solution can be obtained using the time interval $\Delta t = 0.005$ s. It will be used for the following calculations in this section.

With the chosen mesh and time interval, the time histories of free surface elevation and pressure obtained by the present numerical model are compared with the experimental results in Fig. 3.5.



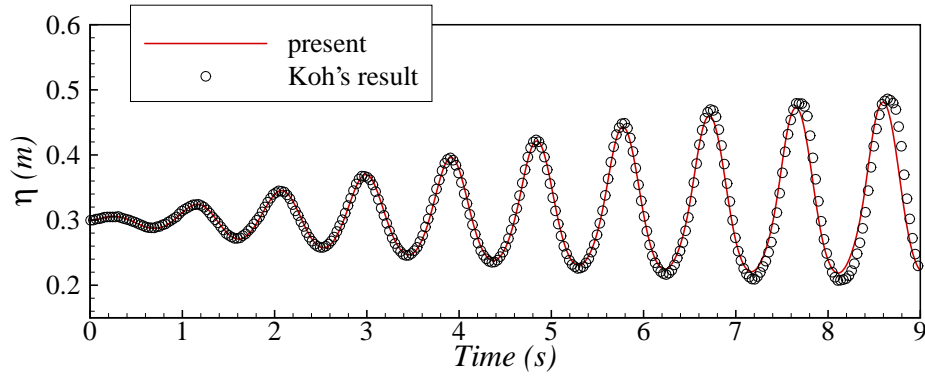
(a) Time histories of free surface displacement at point $H1$



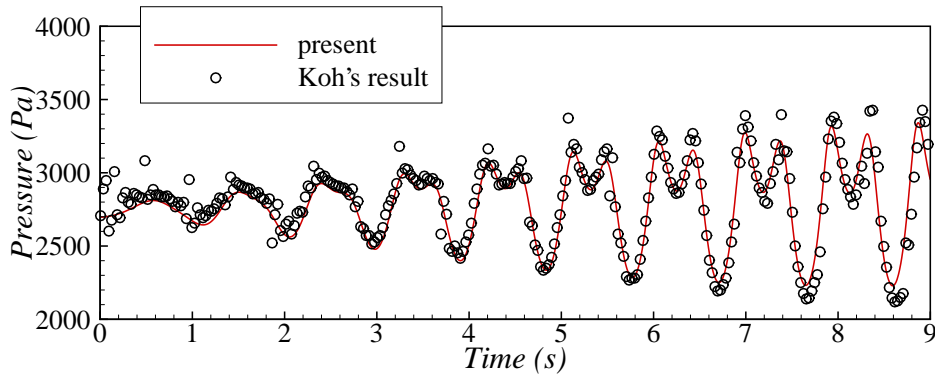
(b) Time histories of pressure at point $P1$

Figure 3.4: Convergence test of three time intervals.

The results show close agreement between the present numerical results and the experimental data in Koh et al. (2012) for both the water surface displacement and the pressure. Resonant phenomenon is clearly observed in Fig. 3.5(a). Note that two successive peaks in each period are captured for pressure after $t = 3$ s in Fig. 3.5(b). As discussed in Peregrine (2003) for wave impact on walls, when water reaches its crest, it is projected upward and it appears to be nearly in free fall. To accelerate the water upward, a higher pressure (the first peak) is required to provide the pressure gradient. At the maximum upward excursion, the water at the crest has little pressure on the water below. When the water falls down after the maximum upward excursion, another higher pressure (the second peak) is needed again to provide the pressure gradient during the deceleration. In addition, a small phase discrepancy is observed after $7s$, which is also reported in the work of Koh et al. (2012). This discrepancy is likely caused by the slight difference in the frequency ratios used between the experiment and the numerical simulation. In order to achieve the resonance in the



(a) Time histories of free surface displacement at point $H1$



(b) Time histories of pressure at point $P1$

Figure 3.5: Comparison between the present numerical results and Koh's experimental recordings.

experiment, the frequency needs to be shifted slightly from the prediction based on linear wave theory.

Fig. 3.6 shows comparisons of the wave profiles at four different time instants with the corresponding experimental data. The wave profiles obtained by the present numerical model agree well with the experimental results. As time elapses, the free surface gradually climbs higher along the side wall. The nonlinear characteristic is observed with the larger upward sloshing amplitude, indicating that the present numerical model can accurately predict nonlinear sloshing motion under horizontal excitations.

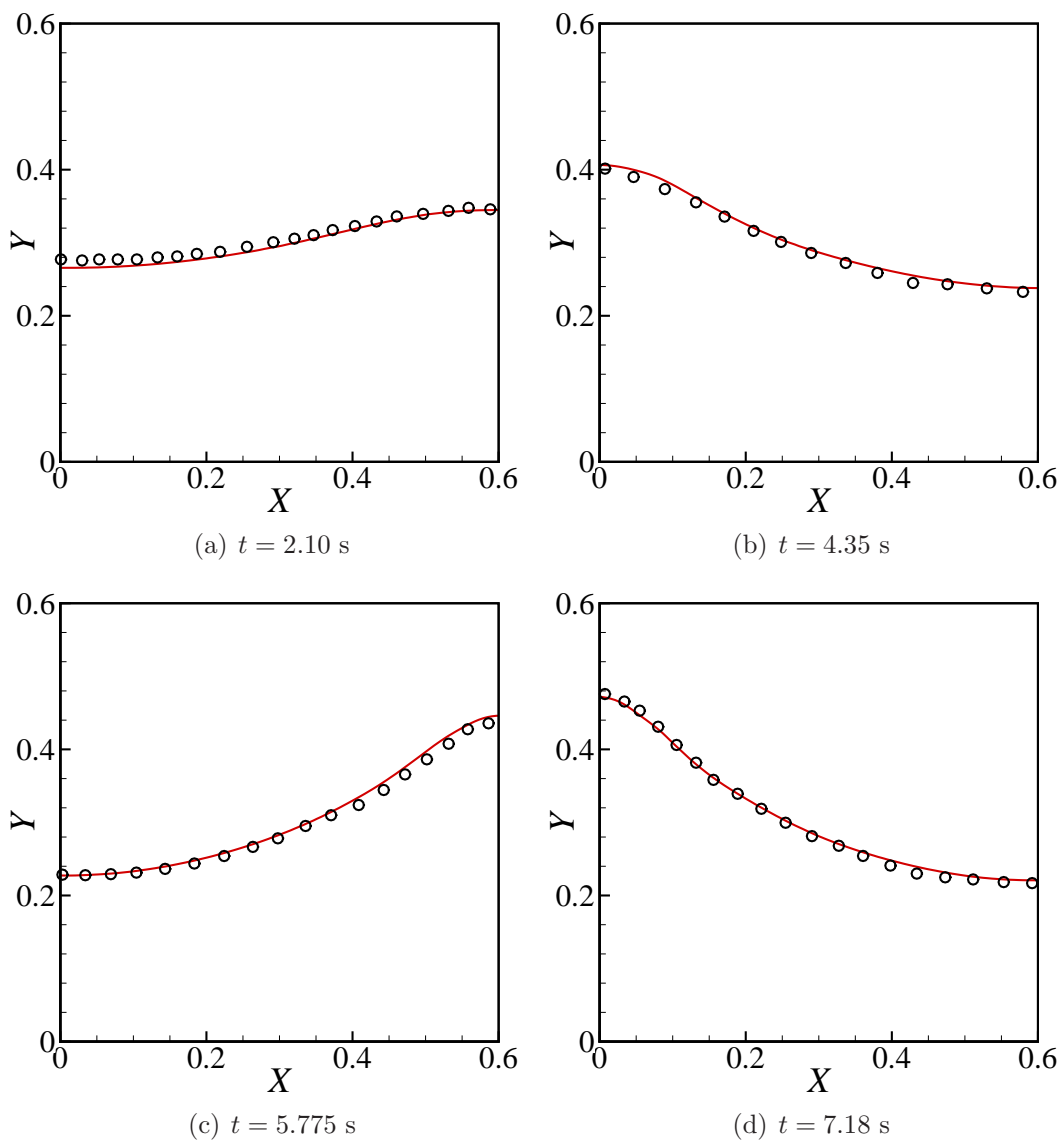


Figure 3.6: Comparison of wave profile between present numerical results (solid line) and Koh's experimental data (circle) at different time instants.

As it is of great importance to predict global sloshing loads on LNG tanks, a further investigation is performed to validate the capability of the present model in modeling sloshing loads. Here, the sloshing excited by horizontal sinusoidal motions in Faltinsen and Timokha (2001) is simulated.

The tank is 1.0 m \times 1.0 m with an initial water depth of 0.35 m, where the highest natural period is $T_1 = 1.2651$ s according to linear wave theory, and the amplitude of the excitation is 0.05 m. The dimensionless lateral forces on the wall, defined as $1000F_x/\rho gl^2b$, are computed by the present numerical model and compared with the analytical solution in Faltinsen and Timokha (2001) and the experimental data in Olsen and Johnsen (1975). The comparison is shown in Fig. 3.7. The shift of the resonant period from T_1 to around $1.1T_1$ is captured by our numerical model and the analytical solution. Good agreement among the present numerical result, the analytical solution and the laboratory recordings is achieved, implying that our numerical model can predict the sloshing loads on the tank wall correctly.

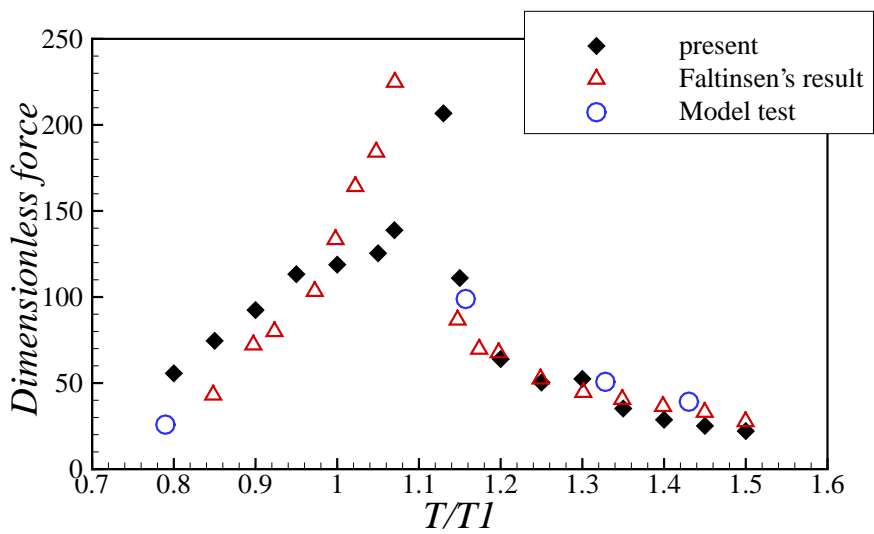


Figure 3.7: Comparison of dimensionless lateral force against T/T_1 among the present numerical result, Faltinsen's solution and laboratory measurements.

3.2.2 Sloshing due to pitch motions

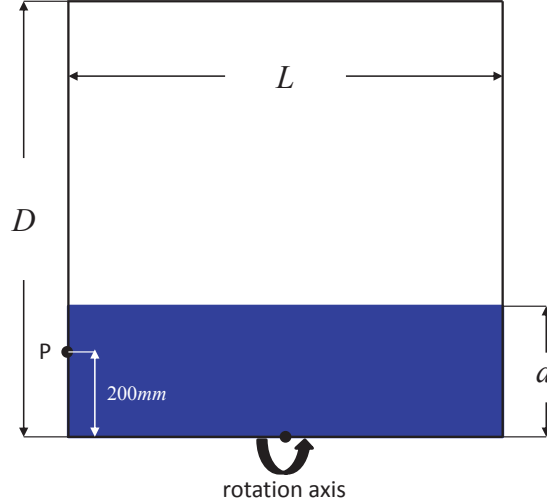


Figure 3.8: A sketch of the two-dimensional tank used in Chen’s experiment with the rotation axis.

In this section, the present numerical model is applied to the analysis of liquid sloshing in a two-dimensional rectangular tank under forced pitch excitations. The experiment conducted by Chen et al. (2013) to investigate the sloshing-induced pressure on solid walls is simulated. Our numerical results are compared with the corresponding experimental data and their numerical results. Fig. 3.8 shows the dimensions of the water tank: $L = 1.0$ m in length, $D = 1.0$ m in height with an initial water depth $d = 0.3$ m. A pressure sensor is placed on the left wall 0.2 m from the bottom of the tank. The tank rolls around the axis at the center of its bottom. The rotational angle of the water tank is given by,

$$\theta = A (\sin \omega t), \quad (3.4)$$

where A and ω represent the pitch excitation amplitude and excitation frequency, respectively. In this case, the rotational excitation amplitude A is equal to 5° . According to Eq. (3.3), the first natural frequency of this sloshing system is $\omega_0 = 4.76$ rad/s. Following the work in Chen et al. (2013), four sloshing cases with different excitation frequencies, chosen according to the first natural frequency, are reproduced numerically here:

- Case 1: $\omega = 0.20\omega_0 = 0.95$ rad/s;

- Case 2: $\omega = 0.65\omega_0 = 3.09$ rad/s;
- Case 3: $\omega = 0.80\omega_0 = 3.81$ rad/s;
- Case 4: $\omega = 1.15\omega_0 = 5.47$ rad/s.

Figs. 3.9 - 3.12 give the time histories of the pressure values obtained in the four cases.

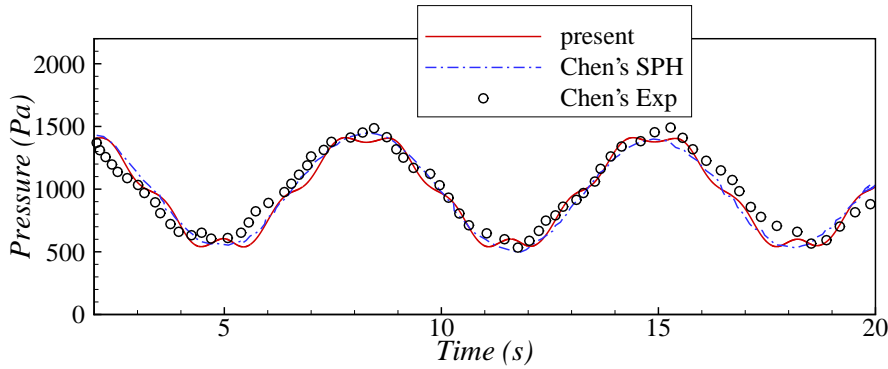


Figure 3.9: Comparison of time histories of pressure at $\omega = 0.95$ rad/s, among present numerical results, Chen's SPH results and Chen's experimental data.

Chen et al. (2013) present the pressure results only after 2 s. This may be due to the transit effect in the experiments. As shown in Fig. 3.9, Case 1 ($\omega = 0.20\omega_0$) simulates the condition when the excitation frequency is much smaller than the natural frequency. Excited by such a relatively low frequency, the free surface oscillates mildly in the tank so that the time history of the pressure obtained on the tank wall varies periodically. The pressure result is approximately sinusoidal with an amplitude of around 500 Pa. This indicates that the hydrostatic pressure is dominant in this case.

In Case 2 ($\omega = 0.65\omega_0$), with a larger excitation frequency that is still not close to the natural frequency, the free surface in the tank climbs higher along the side wall. The pressure result still has a sinusoidal tendency with a larger amplitude of about 800 Pa, as shown in Fig. 3.10. Further, it can be seen that the pressure result becomes asymmetrical with a smaller positive amplitude than the negative one. This suggests that the effect of the dynamic pressure due to the sloshing wave is becoming more evident.

This is validated by Fig. 3.11 and 3.12. Two successive peaks are captured in both plots. Nonlinear characteristics like sharper crests and flatter troughs are also

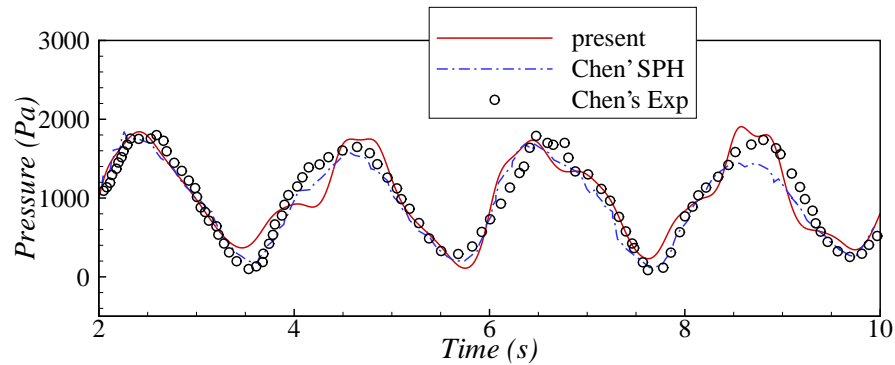


Figure 3.10: Comparison of time histories of pressure at $\omega = 3.09$ rad/s, among present numerical results, Chen's SPH results and Chen's experimental data.

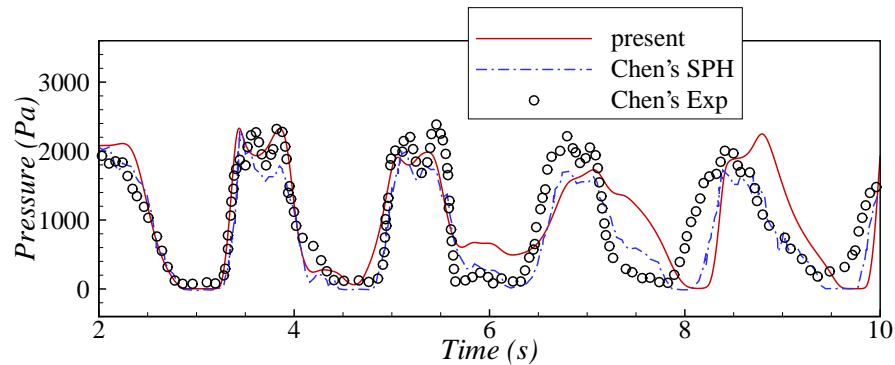


Figure 3.11: Comparison of time histories of pressure at $\omega = 3.81$ rad/s, among present numerical results, Chen's SPH results and Chen's experimental data.

observed. Both cases give a maximum pressure amplitude of around 1200 Pa due to the higher free surface displacement along the side wall. This indicates that the sloshing waves are quite severe in both cases, with excitation frequencies closer to the natural frequency.

However, as the excitation frequency increases, there come some discrepancies between the present numerical result and Chen's work. In Fig. 3.11, there is a phase shift around $t = 8$ s between both the numerical work and experimental result. Apart from the numerical dissipations, the three-dimensional effects in the experiment may also account for this discrepancy. With a larger frequency, the difference in Fig. 3.12 is evident, especially at the early stage $t = 2$ to 4 s. The discrepancy is mainly caused by the unstable movement of the tank during the early acceleration period of the experiment. Nevertheless, the present numerical model provides a closer prediction to the SPH result at that stage. Except for these localized discrepancies, the present

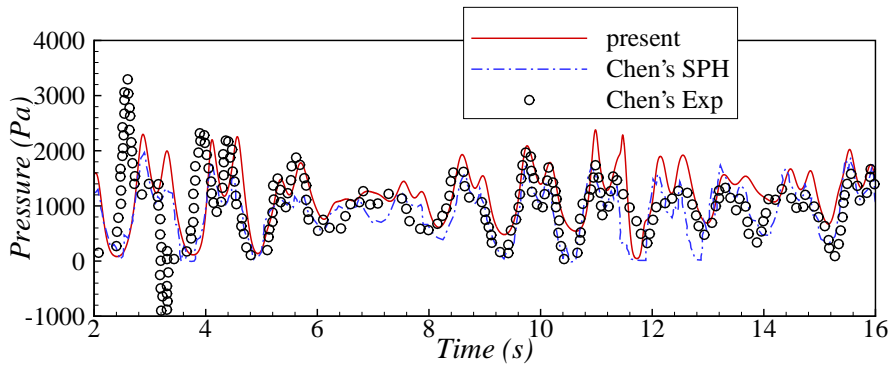


Figure 3.12: Comparison of time histories of pressure at $\omega = 5.47$ rad/s, among present numerical results, Chen's SPH results and Chen's experimental data.

numerical model fits the data of Chen et al. (2013) well.

Fig. 3.13 shows the maximum pressure recorded during the simulation time of 20 s against various excitation frequencies, as well as the comparison with the numerical results in Chen et al. (2013). When the frequency ratio is small, the pressure amplitude gradually increases as the ratio increases. As the ratio approaches 1, the amplitude rises rapidly and then falls quickly while the ratio keeps increasing. A small discrepancy is found around the natural frequency when the sloshing wave in the tank is most severe. Overall, close agreement between the two numerical models is achieved, indicating that the present numerical model can be applied to rotational sloshing simulations.

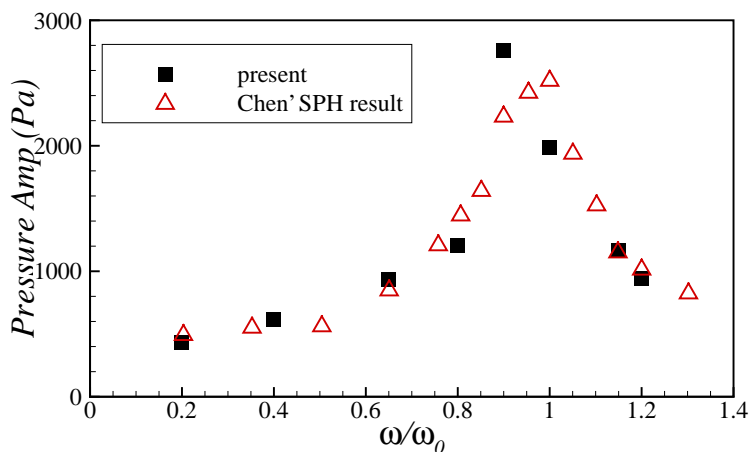


Figure 3.13: Comparison of the pressure amplitudes obtained at various excitation frequencies between the present numerical results and Chen's SPH results.

3.2.3 Sloshing due to surge motions with breaking waves

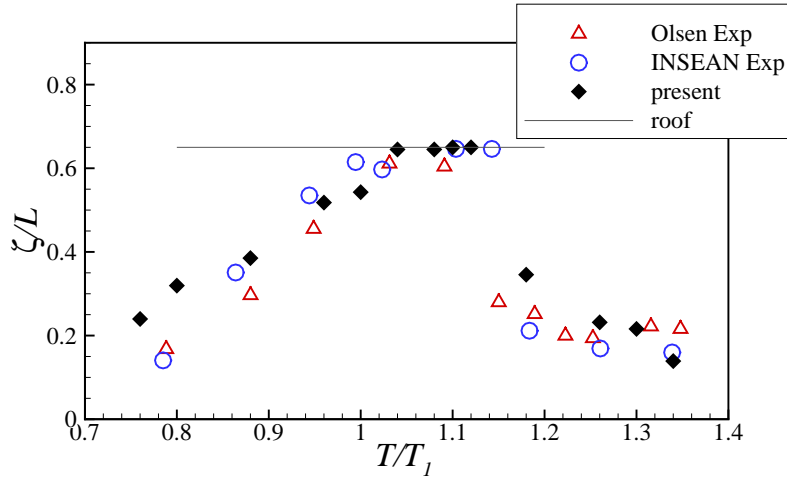
In the first two cases, the good agreement between the experimental results and the numerical results indicates that the present numerical model is able to cope with the two-dimensional sloshing flow in a rectangular tank under surge and pitch motions. However, in these two cases, the excitation is not strong enough to generate breaking waves. In practice, when LNG tanks with various filling levels are being transported under severe sea conditions, strong sloshing flow with breaking waves will likely be induced inside LNG tanks. Therefore, it is necessary to validate the capability of the present numerical model in modeling a sloshing flow with breaking waves. Here, following the experiment conducted by Colagrossi et al. (2004), a series of numerical simulations is performed for severe situations.

In their experiment, a rigid rectangular tank is built with a length of $L = 1$ m, a height of $D = 1$ m and a width of $B = 0.1$ m to model the two-dimensional sloshing flow. A horizontal motion is applied to the tank as the external excitation given by,

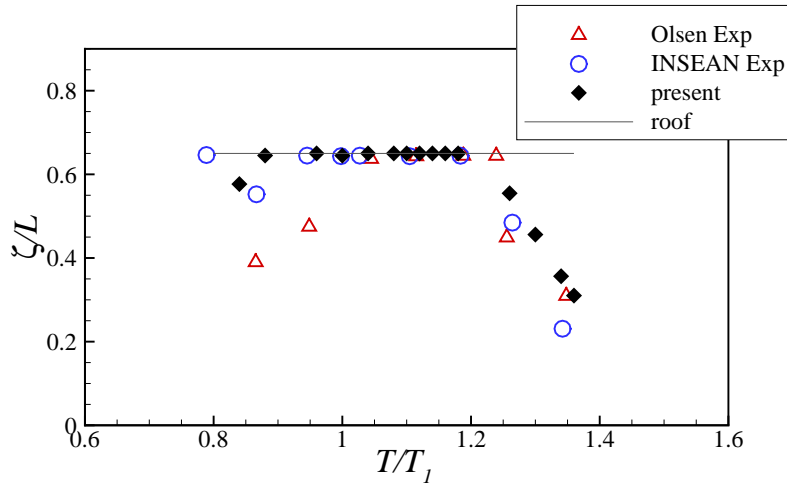
$$x = A \sin(2\pi t/T). \quad (3.5)$$

Here A and T are the excitation amplitude and period, respectively. Since we are exclusively concerned about the sloshing flow with breaking waves, we only reproduce some of their cases, in which the wave impact against the tank roof occurs. Hence, in this study, the tank is filled with water up to $d = 0.35L$, with probes recording the wave elevation at $0.05L$ from the side walls. Two excitation amplitudes $A = 0.05L$ and $A = 0.1L$ are simulated respectively. With various excitation periods ranging from about $T = 0.5T_1$ to $T = 2.0T_1$, the maximum wave elevations in the tank are predicted by the present numerical model. Here T_1 is the natural period of the tank computed by linear wave theory. The simulation time for each case is 30 wave periods, the same as the time used in the experiment. Comparisons with the experimental results in Colagrossi et al. (2004) and Olsen (1970) are shown in Fig. 3.14.

If the ratio of the excitation period to the natural period T/T_1 is smaller than 1, as the period ratio increases, the maximum wave height (ζ) increases accordingly in both $A/L = 0.05$ and $A/L = 0.1$ cases. For the $A/L = 0.05$ case, when the period ratio is around 1.04, the point of ζ value is on the horizontal line, indicating that the sloshing wave eventually hit the tank roof at this excitation period. For the $A/L = 0.1$ case, due to the larger excitation applied, the impact against the tank roof is captured at a smaller period ratio: around 0.9. In this $A/L = 0.1$ case, the range of the period ratio 0.9 to 1.2, at which the wave impact occurs, is also wider than that of 1.04 to



(a) $A = 0.05L$



(b) $A = 0.1L$

Figure 3.14: Comparison of maximum wave elevation against the excitation period, between the present numerical results and the experimental results.

1.14 in the $A/L = 0.05$ case whereby the smaller excitation amplitude is used. When the period ratio keeps increasing, in both cases, the ζ value drops to around $0.2m$ rapidly. As shown in Fig. 3.14, except for some small discrepancies, the numerical results agree well with both experimental results. This validates the capability of the present numerical model in handling sloshing flows with breaking waves.

To better illustrate simulated severe sloshing flow in the tank, we employ one of the simulations as an example to represent the process. In this simulation, the excitation period ratio is $T/T_1 = 1.04$. This, as previously mentioned, is the smallest period ratio in the $A/L = 0.05$ series that captures the impact against the roof with

the filling level $d = 0.35L$. Fig. 3.15 shows the wave profiles at four selected time instants with the chosen parameters. At the initial time around $t = 0.58$ s, the standing wave can be observed. As time elapses, the free surface becomes higher and large volume of water rises up along the side wall, which can be observed in the plot $t = 2.55$ s. Finally, the sloshing wave is strong enough to climb along the right wall and hit the tank roof. At the last time instant, the occasion of the water rolling up along the left wall and the wave overturning before dropping to the tank is captured.

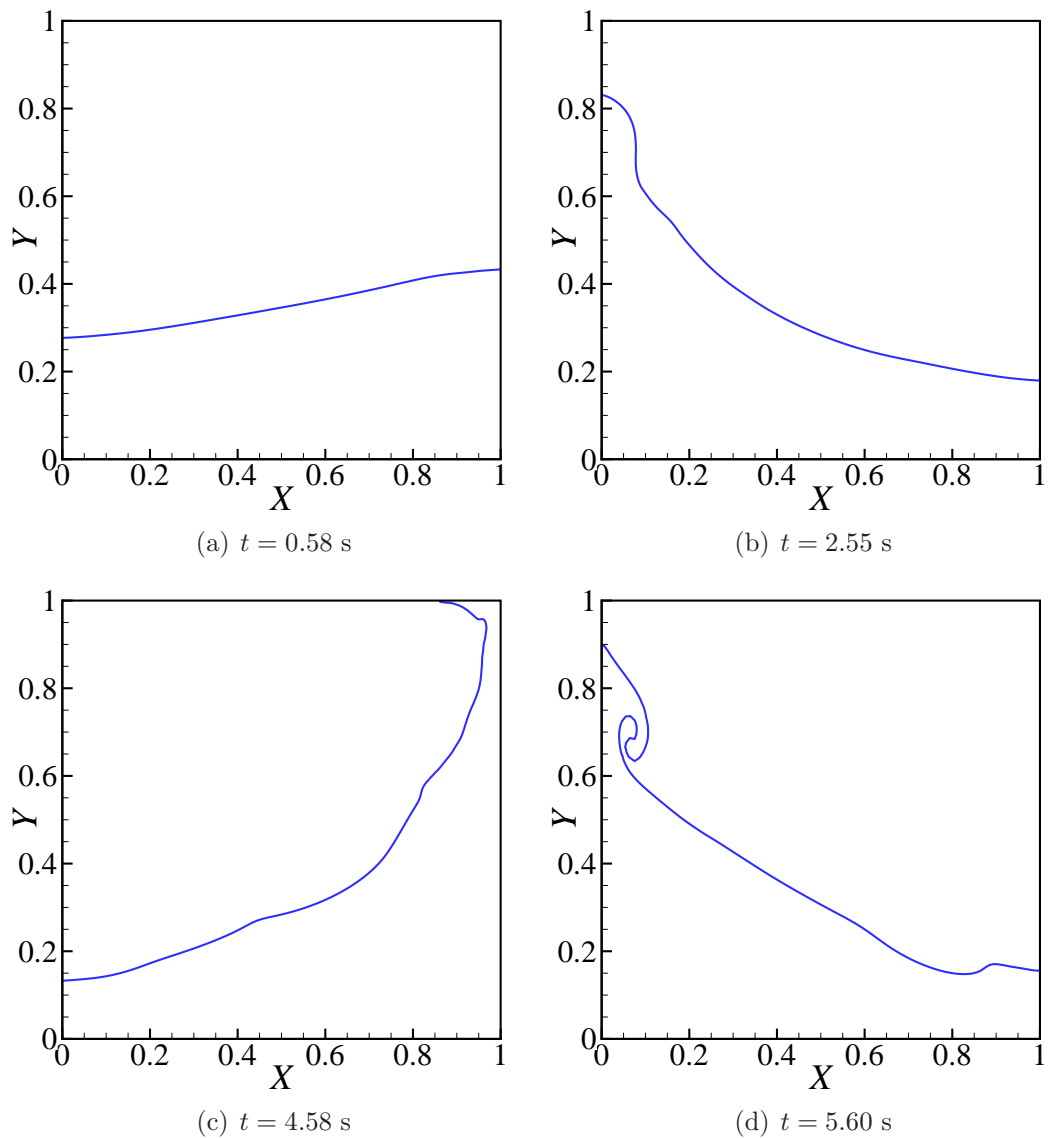


Figure 3.15: Wave profiles captured by the present numerical model at various time instants.

3.3 A study on sloshing induced by ship motions

As reviewed in Chapter 1, most previous studies have focused on sloshing waves in a tank excited by a single translational or rotational motion. However, in a real-world situation, liquid sloshing is usually induced by multi-degrees-of-freedom excitations simultaneously, including surge, sway, pitch, and roll, etc. Chen and Nokes (2005) applied a time-dependent finite difference scheme to analyze the complete two-dimensional sloshing motion in a tank. The coupled surge-heave-pitch excitation was considered and coupling effects were observed when the sloshing flow became non-linear prominent. They also concluded that the coupled motion should be included in the analysis of sloshing inside a tank during an earthquake. Similarly, the sloshing analysis in LNG tanks should also consider this simultaneous coupled motion. In addition, the sloshing wave inside LNG tanks is usually induced by ship motions. Therefore, responses of the LNG carrier excited by sea waves should also be employed in the sloshing analysis to simulate real situations.

Recently, Lee et al. (2011) studied LNG sloshing by considering ship movements in a full-scale tank to verify their finite difference model with a marker-density scheme. However, only three cases have been done and some pressure results have been revealed. Some studies on the coupling effects between internal sloshing flow and external ship motions have naturally used ship responses as excitations of sloshing flow, such as Kim (2002), Rognebakke and Faltinsen (2003), Kim et al. (2007) and Nam et al. (2009). But most of these studies emphasized the sloshing effects on the ship motions and haven't performed a systematic analysis on the internal sloshing under coupling effects.

In this section, the validated numerical model is applied to study LNG sloshing induced by ship motions obtained in sea conditions. A realistic LNG carrier with a length of $L = 270.0$ m, a breadth of $B = 43.4$ m and a depth of $D = 26.0$ m is used. Kim et al. (2008) adopted their WISH numerical program to simulate the dynamic responses of this LNG carrier and a complete Response Amplitude Operator (RAO) was achieved. Since the present numerical model is built in two dimensions, we only consider the head sea condition with the heading angle of the wave $\beta = 180^\circ$. The corresponding surge, heave and pitch RAOs of the LNG carrier obtained by WISH are then applied to excite the LNG tank and induce the internal sloshing waves.

As no information on the LNG tank was provided in Kim et al. (2008), the LNG tank simulated here is assumed to have a length of $L = 50.0$ m and height of $D = 25.0$ m. To further simplify our calculations, the tank is located at the center of the LNG

carrier and the rotational axis is assumed to be through the center of the tank. According to Pérez and Blanke (2002), we employ the following equations,

$$x = A_x \sin(\omega_i t + \alpha_x), \quad (3.6)$$

$$y = A_y \sin(\omega_i t + \alpha_y), \quad (3.7)$$

$$\theta = A_\theta \sin(\omega_i t + \alpha_\theta), \quad (3.8)$$

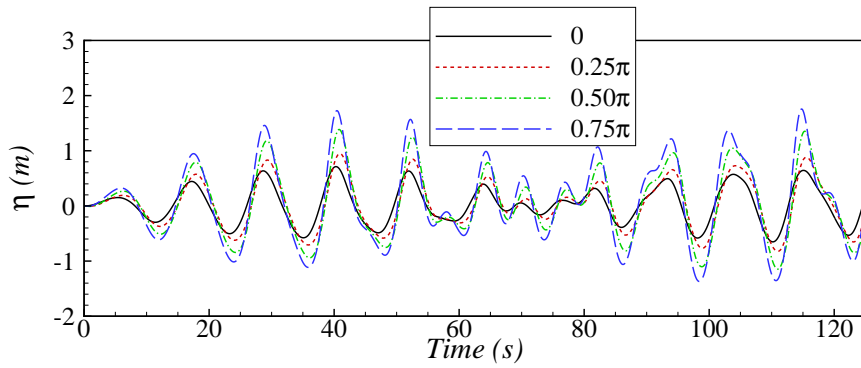
to represent the regular surge, heave and pitch motions of the LNG tank respectively. Here, A_x , A_y , A_θ are the amplitude of each motion defined by the wave height and the corresponding RAO value at a certain frequency ω_i . α_x , α_y , and α_θ denote the random initial phase of each motion.

With the obtained three-degrees-of-freedom RAOs of the LNG carrier, the two-dimensional sloshing flow in the LNG tank is investigated with regard to the excitation frequency, filling level and excitation amplitude (i.e. external wave height), as follows.

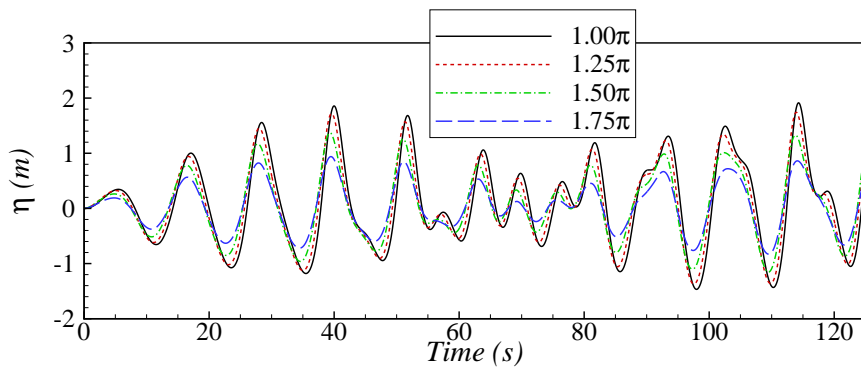
3.3.1 Effects of initial phase differences between each motion

Before we conduct a detailed study of the other factors, it should be noted that in Eqs. (3.6) - (3.8), initial phases are random and undetermined. However, in practice, we are more concerned about the critical condition. Therefore, an investigation into the phase value in each motion is necessary to find the combination that leads to the most severe sloshing inside the tank.

The sloshing wave inside the LNG tank is mainly induced by the horizontal and rotational motions of the LNG carrier. Thus, the investigation starts with the initial phase in the surge motion α_x . Due to the fact that the initial phase in each motion is randomly chosen in the range of $0 - 2.0\pi$, it is better to consider the phase difference between each motion. Here, the phase difference between the surge and pitch motion of the LNG carrier is studied first, while the heave motion is excluded. The phase of pitch motion α_θ is set to be 0. The value of α_x varies from 0 to 1.75π with an interval 0.25π . Thus, 8 cases are conducted in this series with an initial water depth $d = 10.0$ m (40% filling level) and an excitation frequency $\omega = 0.5$ rad/s. According to the RAOs in Kim et al. (2008), at this excitation frequency, the motion amplitudes are $A_x = 0.1054$ m and $A_\theta = 0.5835^\circ$ for the external wave height of 1 m. After the convergence tests, the 200×100 mesh and the time interval $\Delta t = 0.025$ s are utilized in this investigation.



(a) 0 to 0.75π



(b) 1.00π to 1.75π

Figure 3.16: Time histories of free surface elevation on the left wall for various phase differences under the 40% filling level.

Fig. 3.16 gives the time histories of free surface elevation on the left wall for the eight cases. In Fig. 3.16(a), we can observe the trend that as α_x increases from 0 to 0.75π , the predicted surface elevation is raised while all the results have a similar pattern. This demonstrates that the phase differences between the surge and pitch motions have an effect on the induced sloshing flow. Fig. 3.16(b) shows the results obtained for phase differences varying from 1.0π to 1.75π . Contrary to the trend in Fig. 3.16(a), the free surface displacement decreases as the phase difference increases.

The maximum free surface displacements are recorded against the phase difference in Fig. 3.17. The variation of the maximum value corresponds with the observations in the time series. This suggests that when the phase difference is 1.0π , the horizontal component of the pitch motion will enhance the surge motion most and thus induces the most severe sloshing flow. In Fig. 3.17, a symmetrical pattern can be observed. This is further validated by Fig. 3.18. The data for the phase differences $\alpha_x = 0.75\pi$ and $\alpha_x = 1.25\pi$ are almost identical, apart from a phase shift. Since we are concerned

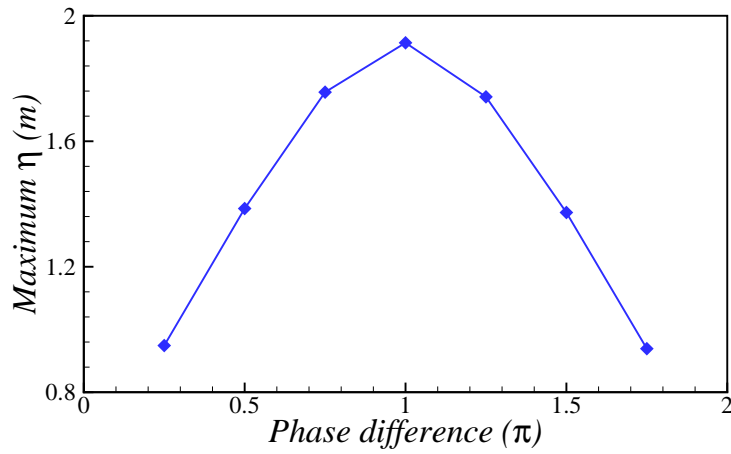


Figure 3.17: Maximum free surface elevations for various phase differences under the 40% filling level.

about the critical condition, in the following cases, the initial phases of surge and pitch are chosen to be $\alpha_\theta = 0$ and $\alpha_x = 1.0\pi$.

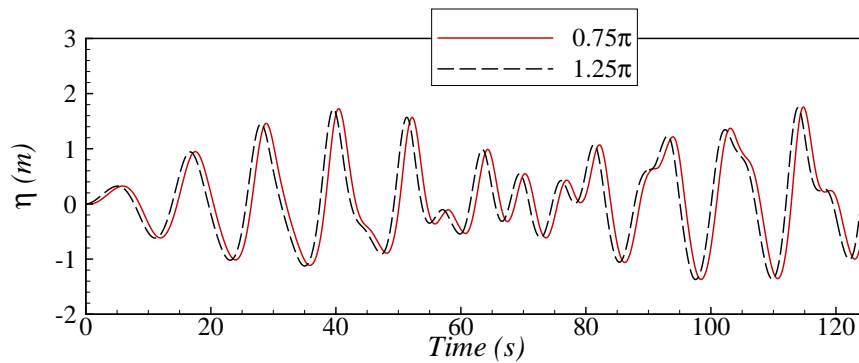


Figure 3.18: Comparison of free surface elevation between results for $\alpha_x = 0.75\pi$ and $\alpha_x = 1.25\pi$.

It is known that a low filling level usually leads to more violent fluid motions in the tank. Therefore, to better understand the effects of the phase difference, the 20% filling level is studied with the same excitation amplitude and frequency used in the previous case. As shown in Fig. 3.19 and Fig. 3.20, the effects of the phase difference between the surge and pitch motions under the lower filling level are similar to those under the 40% filling level. As α_x increases, the surface elevations become larger and reach the maximum value when $\alpha_x = 1.0\pi$. The only difference is the predicted elevations under the lower filling level are generally larger as expected.

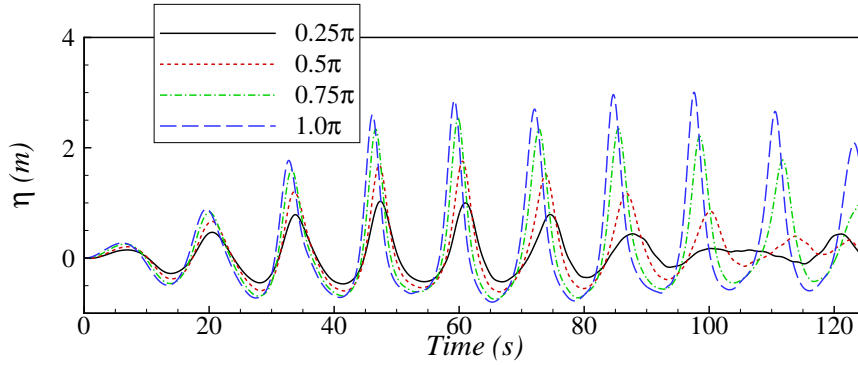


Figure 3.19: Time histories of free surface elevation on the left wall for various phase differences under the 20% filling level.

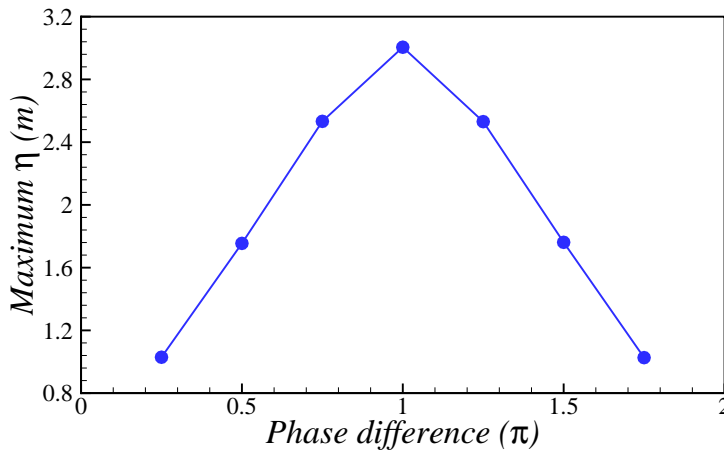


Figure 3.20: Maximum free surface elevations for various phase differences under the 20% filling level.

The tank under pure vertical excitations only causes changes to its gravitational acceleration. This will not lead to a large effect if the free surface of the tank is initially undisturbed. However, during LNG transportation, the tank is usually excited by horizontal, vertical and rotational motions at the same time. In this situation, the free surface will deform due to surge and pitch motions. Thus, the vertical excitation may enlarge the free surface elevation during tank motions (Chen and Nokes, 2005). Hence, an investigation on the random initial phase in the heave motion α_y is further performed.

The determined $\alpha_\theta = 0$ and $\alpha_x = 1.0\pi$ are employed. Due to the likely larger effect of heave motions on free surface displacement, an initial water depth $d = 5.0$ m and

an excitation frequency $\omega = 0.45$ rad/s are used to simulate a strong sloshing flow. Assuming the external wave height is 1 m, the corresponding excitation amplitudes are $A_x = 0.2496$ m, $A_y = 0.3846$ m and $A_\theta = 0.6809^\circ$ according to the RAOs. Fig. 3.21 shows the time histories of free surface elevation on the left wall. All the free surface displacements obtained by varying phases in heave motion are identical. This suggests that the random initial phase of heave motion α_y does not have an apparent effect on the sloshing flow, even though the heave motion would have effects on the deformation of the free surface. The main reason for this negligible effect is that compared to the acceleration of gravity, the change of vertical acceleration is quite small and the difference due to the phase shift is therefore much smaller. Thus, α_y is set to be 0 in all the following cases.

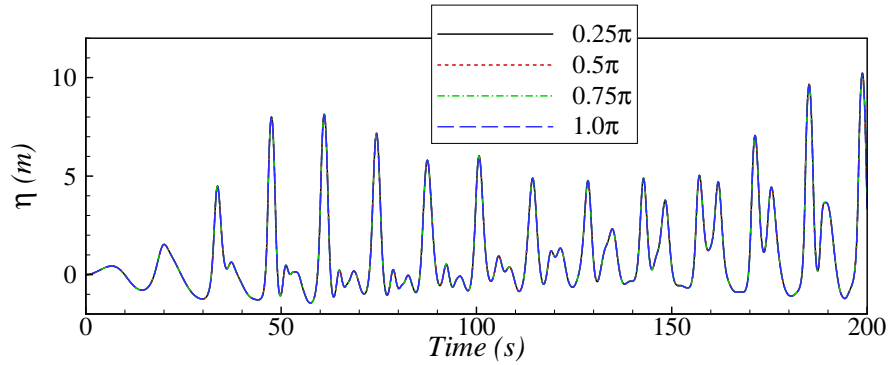


Figure 3.21: Time histories of free surface elevation on the left wall for various heave phases.

Based on the test on the phase difference, to study the necessity of applying the surge-heave-pitch combined excitations to the sloshing study, we also simulate liquid sloshing in the LNG tank excited by each single motion respectively. Since the initial water surface is undisturbed, sloshing waves in the tank cannot be generated by a single heave motion. In this case, only the single surge and pitch motion are considered respectively. The water depth is $d = 10.0$ m and the excitation frequency is $\omega = 0.5858$ rad/s. The corresponding excitation amplitudes are $A_x = 0.041$ m, $A_y = 0.311$ m and $A_\theta = 0.255^\circ$.

Fig. 3.22 shows the time history of the free surface elevation obtained by the fully coupled surge-heave-pitch excitations and surge+pitch superposition with an external wave height $h = 1$ m. It can be observed that the discrepancy becomes more pronounced with time.

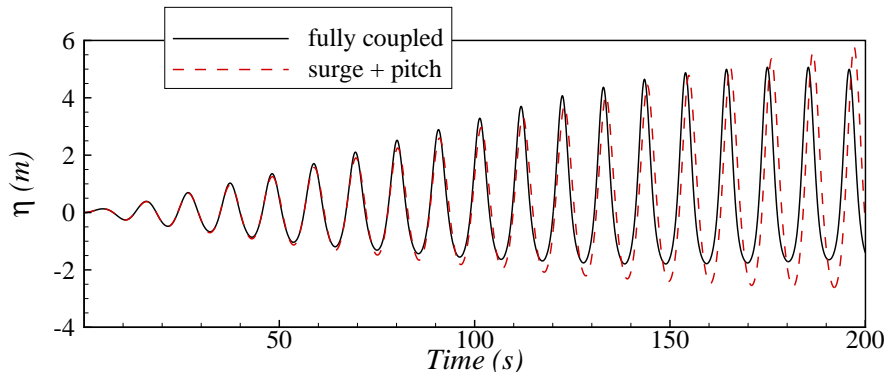


Figure 3.22: Time histories of free surface elevation under fully coupled and superposed excitations.

Fig. 3.23 shows the difference of the maximum elevation as a function of the external wave height. As the the excitation amplitude increases, the difference between the results of the surge-heave-pitch combined excitations and the surge+pitch superposition becomes larger. The predictions given by the fully coupled combination are more conservative. To achieve an accurate simulation of liquid sloshing in LNG tanks, surge-heave-pitch combined excitations that are closer to the real-world situation, are applied in all of the following cases.

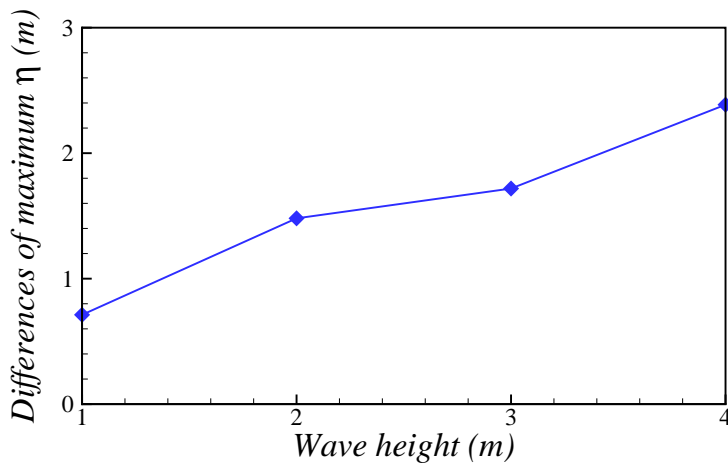


Figure 3.23: Maximum elevation differences at different excitation amplitudes.

3.3.2 Effects of excitation frequency

Various excitation frequencies will excite the sloshing flow in the tank with different levels of severity. It is known that the most severe sloshing is induced when the exci-

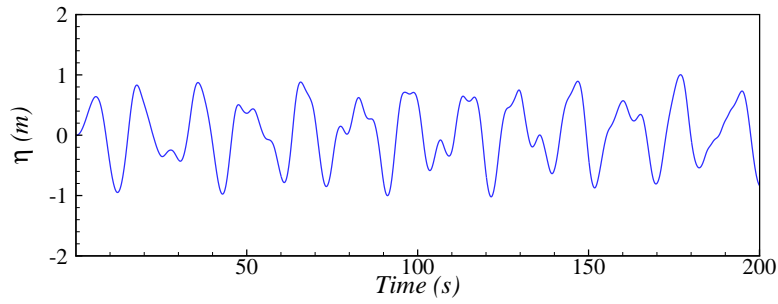
tation frequency is close to the natural frequency of the sloshing system. This leads the free surface displacement to reach its maximum value. Effects of the excitation frequency on the sloshing have been reported (Chen and Nokes, 2005; Wang et al., 2011) where a fixed excitation amplitude is applied to any frequency. However, in realistic seas, the dynamic responses of LNG carriers will vary at different frequencies, indicating that the excitation amplitude at each frequency should be different. In this study, the sloshing wave in a full-scale LNG tank under sea conditions is evaluated, so that the excitation amplitudes are different between each frequency, unlike all previous studies.

According to Kim et al. (2008), the motion RAOs are given with the frequency varying from 0 to 1.4 rad/s. Here, ten different frequencies are selected, shown together with the corresponding RAOs in the three directions in Table 3.1. The RAO values in each motion have an overall trend to decrease as the frequency increases. To better illustrate the effect of the excitation frequency, the 50% filling level is selected, and three more frequencies are added around the resonant frequency at $\omega_0 = 0.635$ rad/s. In addition, all simulations in this and the following sections run for 200 s to provide enough information.

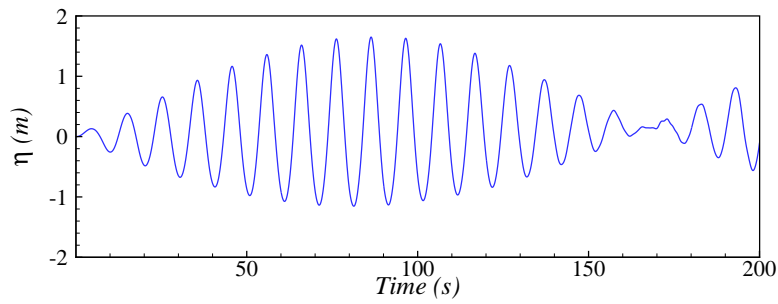
Table 3.1: Motion RAOs applied in this parametric study.

ω	0.2	0.32	0.36	0.4	0.5	0.56	0.6	0.68	0.72	0.8
x	0.8468	0.6313	0.5396	0.4031	0.1054	0.031	0.051	0.037	0.028	0.0201
y	0.9663	0.7917	0.5781	0.5414	0.2582	0.3358	0.2961	0.1278	0.079	0.0357
θ	0.228	0.5302	0.6383	0.6855	0.5835	0.3418	0.201	0.1779	0.1475	0.043

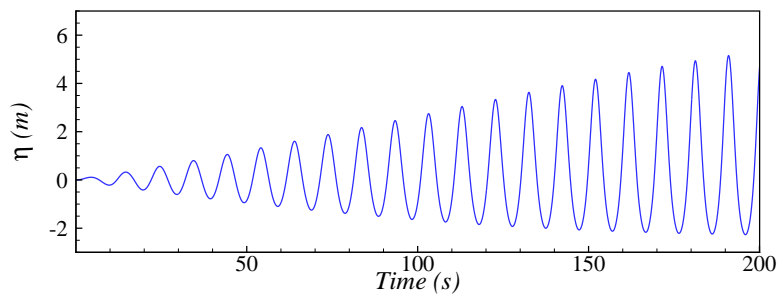
Fig. 3.24 shows the free surface displacement at the left tank wall for 4 typical excitation frequencies $\omega/\omega_0 = 0.629, 0.943, 1.007$ and 1.070 , respectively. As shown in Fig. 3.24(a), when the excitation frequency is relatively far from the resonant value, irregular crests and troughs are observed. Double peaks are also captured, showing that in some instances, the tank cannot catch up with the water movement. As the frequency approaches the natural frequency, the sloshing wave becomes stronger as shown in Fig. 3.24(b). A typical wave envelope is presented, which indicates that a beating phenomenon is captured in this situation. This observation agrees with the conclusion made by Wu et al. (1998). They reported that modulated waves could be obtained when the excitation frequency deviates slightly from the resonant value. Fig. 3.24(c) gives the free surface displacement of the sloshing wave under the excitation



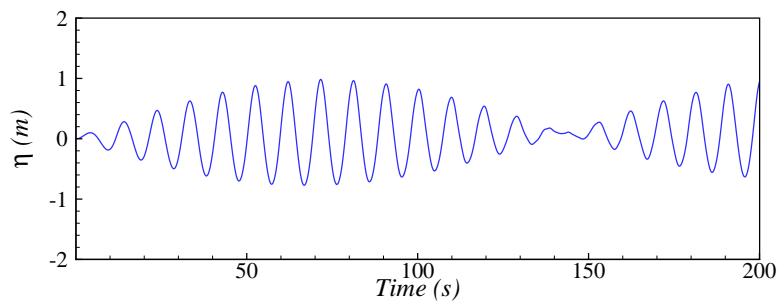
(a) $\omega/\omega_0 = 0.629$



(b) $\omega/\omega_0 = 0.943$



(c) $\omega/\omega_0 = 1.007$



(d) $\omega/\omega_0 = 1.070$

Figure 3.24: Time histories of free surface displacement at four different frequencies.

frequency which is almost equal to the natural frequency. The resonant phenomenon is clearly observed with a much higher surface elevation than the previous two cases. Similar to the case at $\omega/\omega_0 = 0.943$, the free surface elevation at $\omega/\omega_0 = 1.070$ also captures the beating phenomenon in Fig. 3.24(d). Compared with Fig. 3.24(b), the period of the envelope is smaller and the free surface elevation is lower, which is likely due to the larger deviation from the resonant value and smaller RAOs.

The maximum free surface displacement recorded at the left wall during the simulation time is plotted against the excitation frequency in Fig. 3.25. It can be seen that the motion RAOs and the excitation frequency (or the wave frequency) are two competitive factors, and at a certain frequency, the water sloshing in the tank is determined by both the amplitude of RAOs and the deviation of the wave frequency from the resonant frequency of the system. With values close to the resonant condition, the sloshing waves are much higher than those induced by excitations far from the natural frequency, even though the dynamic responses of the tank to waves may be smaller at these wave frequencies. This indicates that the wave frequency is a dominant factor that determines the free surface elevation of the sloshing flow.

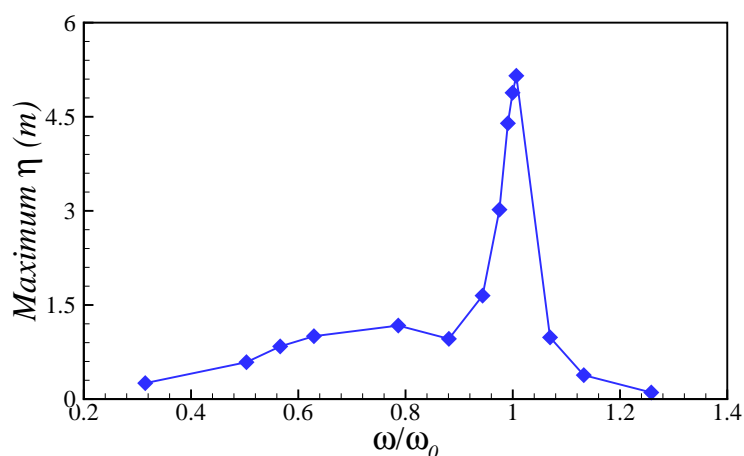


Figure 3.25: Maximum elevations at different frequencies.

3.3.3 Effects of filling level

Due to the growing demand for LNG, newly designed LNG carriers are usually required to have a wide range of filling levels. Thus it is of practical significance to investigate sloshing waves under different filling levels. In this section, five different filling levels as listed in Table 3.2 are utilized to conduct a series of sloshing simulations.

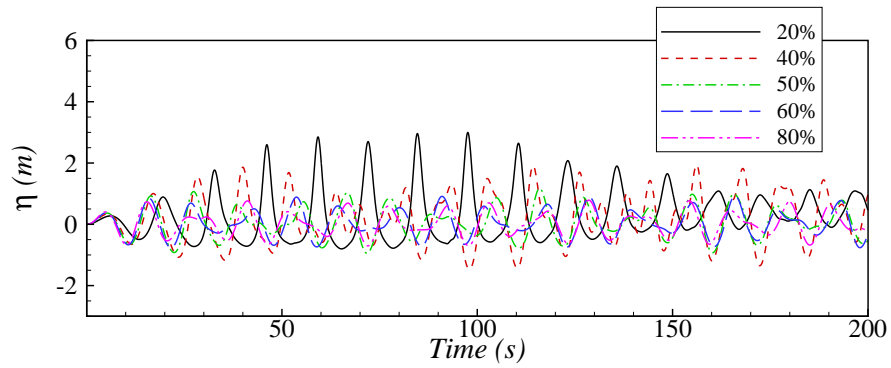
Table 3.2: Frequency ratios for various filling levels.

Filling level	Natural frequency (rad/s)	$0.5/\omega_0$	$0.6/\omega_0$	$0.72/\omega_0$
20%	0.4330	1.1547	1.3856	1.6627
40%	0.5859	0.8534	1.0241	1.2289
50%	0.6358	0.7864	0.9437	1.1324
60%	0.6737	0.7422	0.8906	1.0687
80%	0.7239	0.6907	0.8289	0.9946

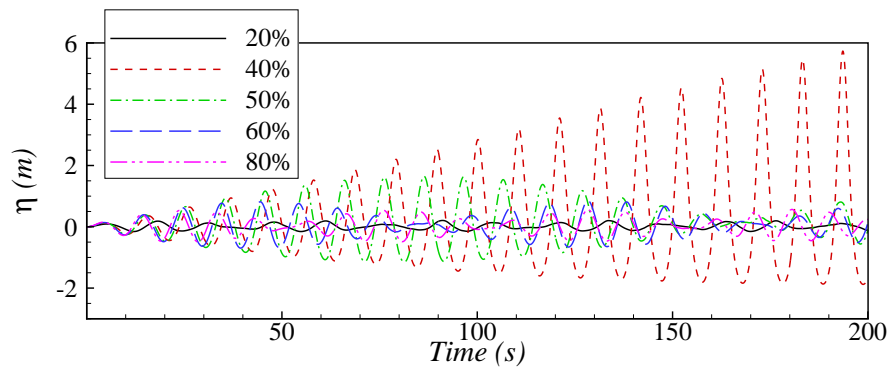
Fig. 3.26 exhibits the free surface displacement with various filling levels at three excitation frequencies, $\omega = 0.5, 0.6$ and 0.72 rad/s. The ratios of these three frequencies to the natural frequency are also shown in Table 3.2. Two resonant results are observed in Figs. 3.26(b) and 3.26(c) for the filling levels of 40% and 80% respectively. This is because the applied frequencies $\omega = 0.6$ and 0.72 rad/s are close to the natural frequencies at these two filling levels. In addition, the beating phenomena are captured for the 50% and 60% filling levels in these two figures, which can be also found in Fig. 3.26(a) for the 20% filling level.

Fig. 3.27 presents the maximum free surface displacement as the function of the filling level. At $\omega = 0.5$, the maximum elevation decreases as the filling level increases from 20% to 80%, while an adverse trend is obtained at $\omega = 0.72$. An intermediate filling level gives the highest free surface elevation when $\omega = 0.6$ is applied. Overall, the effect of the filling depth on the sloshing wave depends on the relation between the selected excitation frequency and the corresponding resonant frequency.

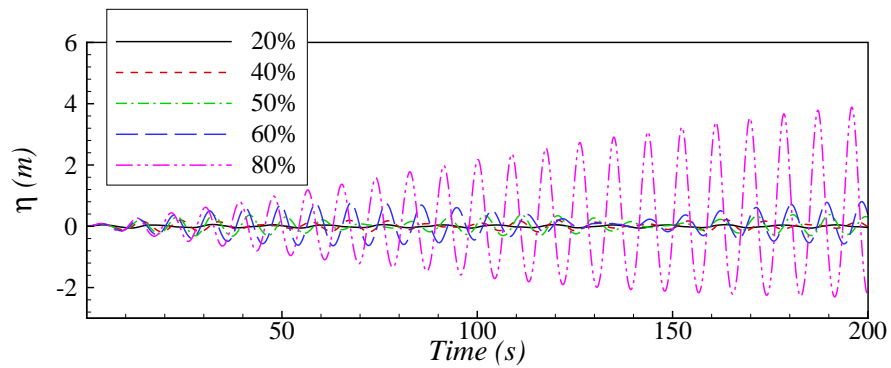
Fig. 3.28 gives the maximum wave elevation at different filling levels over the entire frequency region with the external wave height equal to 1 m. It can be seen that at different filling levels, the maximum sloshing wave always occurs around the corresponding resonant frequency. At the same time, the maximum sloshing wave at most excitation frequencies (between $\omega = 0.2$ and $\omega = 0.5$) happens at the lowest filling level, and lower filling levels generally lead to stronger sloshing flows.



(a) $\omega = 0.5 \text{ rad/s}$



(b) $\omega = 0.6 \text{ rad/s}$



(c) $\omega = 0.72 \text{ rad/s}$

Figure 3.26: Time histories of free surface displacement under different filling conditions at the given frequencies.

To further investigate this, four additional cases with low filling levels of 10%, 15%, 25% and 30% are simulated. Fig. 3.29 shows the maximum wave elevations recorded for the low filling levels against the excitation frequency. We see that the same scenario is also captured for the low filling conditions, where maximum wave elevation occurs around the resonant frequency. It should be noted that in the 10%

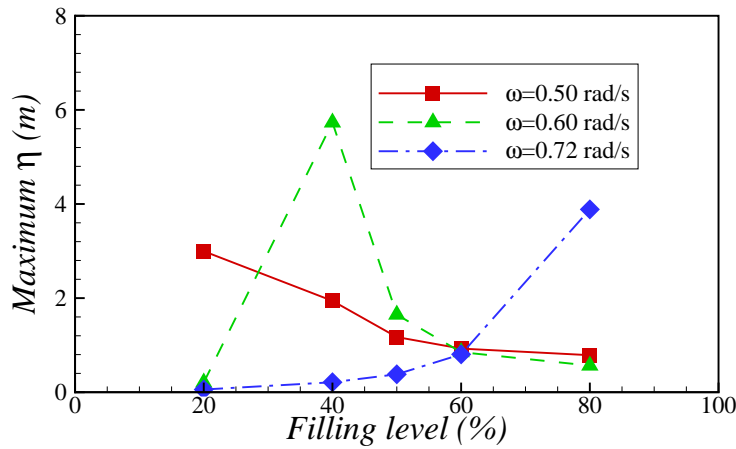


Figure 3.27: Maximum elevations under different filling conditions at the given frequencies.

series, a frequency shift can be clearly observed. It is known that the nonlinearity of sloshing can shift the resonant frequency from the value predicted by linear wave theory. At the very low filling level of 10%, the nonlinearity is expected to be much stronger than at other filling levels. This may be responsible for the frequency shift. As the resonant frequency moves to around $\omega = 0.4$ rad/s and the peak in motion RAOs also occurs around this frequency, the obtained elevation is larger at the filling level of 10% than those at other filling levels.

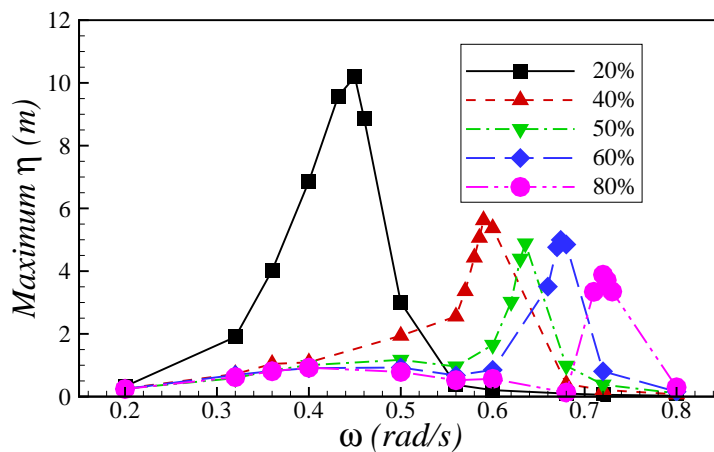


Figure 3.28: Maximum elevations at various frequencies under five different filling conditions.

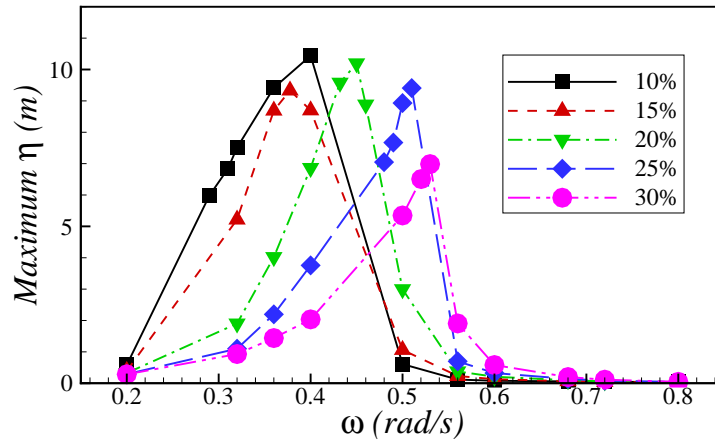


Figure 3.29: Maximum elevations at various frequencies under lower filling conditions.

3.3.4 Effects of external wave height

In all the previous cases, the height of the external sea wave inducing motions of the LNG carrier is assumed to be 1 m in order to focus our study on other factors. In real-world situations, LNG carrier often encounter seas with larger wave heights. Different motion RAOs would thus be obtained because of varying wave heights and have an effect on the sloshing flow in the LNG tank. In this section five different wave heights from $H = 1$ to 5 m are selected, with the filling depth $d = 10$ m and the resonant frequency obtained by applying Eq. (3.3).

Fig. 3.30 shows the time history of the free surface displacement at the left wall with different wave heights. When $H = 1$ m, the resonant phenomenon is captured, while from $H = 2$ m the beating phenomena are observed. As discussed earlier, the beating phenomenon occurs when the excitation frequency is slightly away from the resonant value. Thus, it can be concluded that the frequency obtained by Eq. (3.3) is close to, but not exactly, the real resonant frequency of the sloshing system when the wave height is large. As the wave height increases, the nonlinear characteristics are more evident with sharper crests and flatter troughs. Thus, the increased nonlinear effect results in the shift of the resonant frequency obtained by linear wave theory. In addition, as shown in Fig. 3.30, free surface elevation also becomes larger at the higher wave amplitudes.

Fig. 3.31 shows the maximum sloshing wave elevation with different filling levels excited by various wave amplitudes at the corresponding resonant frequencies. From $H = 2$ m, wave impact against the roof is clearly observed at most filling levels.

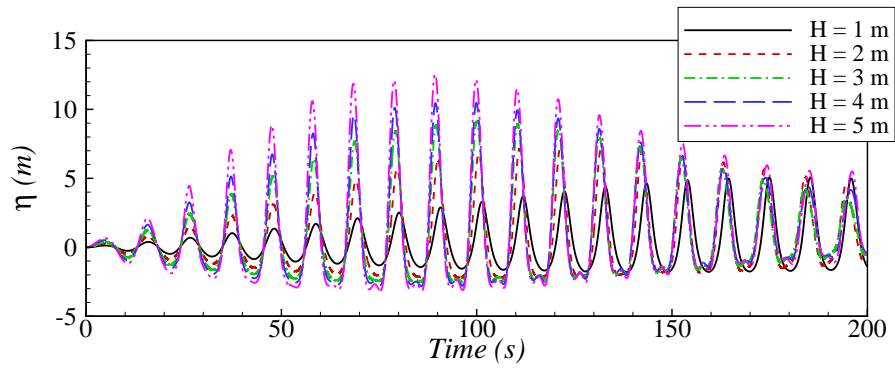


Figure 3.30: Time histories of free surface displacement induced by different wave heights.

The larger increase for the 20% filling level case is clearly noticed when the wave amplitude is larger than 2 m, indicating that the nonlinearity of waves plays a more important role at lower filling levels. Moreover, this figure clearly shows at which wave amplitude the sloshing wave can reach the tank roof at different filling levels.

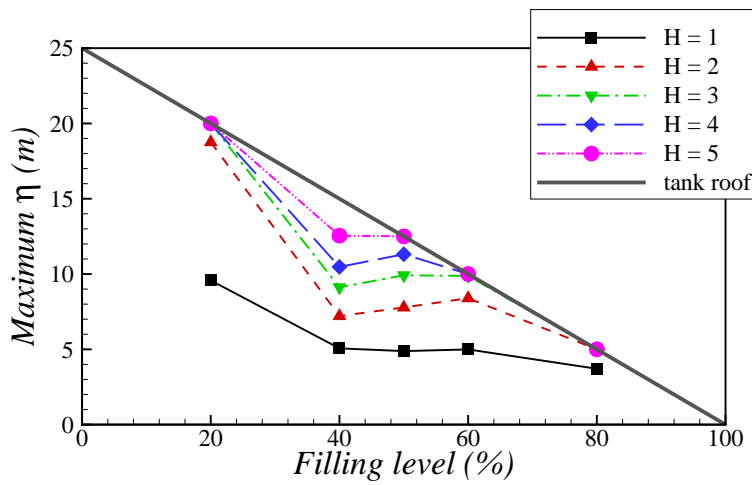


Figure 3.31: Maximum wave elevations induced by different wave heights under various filling conditions.

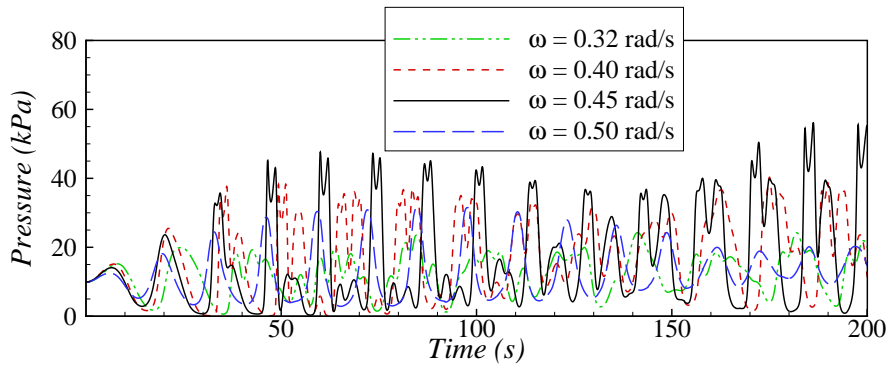
3.3.5 Pressure in the tank

Local pressure is one major concern in the sloshing study. Violent liquid movement can lead to high local pressure in the LNG tank, which may cause brittle damage and consequently, structural failure. Therefore, accurate pressure prediction inside the tank during the sloshing process is of great importance. In this section, pressure on the left tank wall is studied in conjunction with the effects of the excitation frequency, filling depth and external wave height.

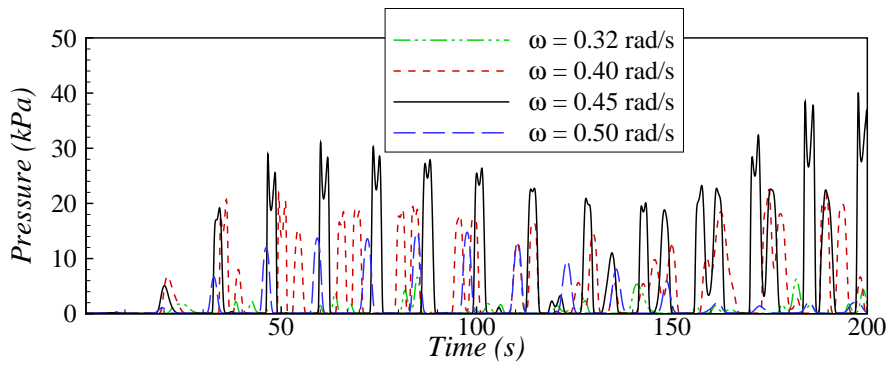
Fig. 3.32 shows the time history of total pressure at three different points $y = 4, 6$ and 8 m respectively on the left tank wall, where y is the distance from the bottom of the tank to the measured point. Four different excitation frequencies, $\omega = 0.32, 0.40, 0.45$ and 0.50 rad/s are used, corresponding to $\omega/\omega_0 = 0.74, 0.92, 1.04$ and 1.15 . The filling depth is fixed at $d = 5$ m in all of the following cases, which corresponds to the 20% low filling condition. The wave amplitude is set to 1 m. As can be seen from the figure, the pressure at $\omega = 0.45$ rad/s is always higher than that at other frequencies. This is because $\omega = 0.45$ is closer to the resonant frequency. From $y = 4$ to 8 m, the pressure decreases due to the hydrostatic effect. At $y = 8$ m, only two results can be recognized, showing that the sloshing wave cannot reach this height along the tank while under the other two excitation frequencies.

Fig. 3.33 shows the time history of pressure at the 20%, 40%, 60% and 80% filling levels. The resonant frequency dependent on the filling depth is applied for each case to simulate the most critical condition. At $y = 6$ m, the pressure shows an increased trend according to the increased filling depth. Except for the 20% filling condition, the pressure oscillates following an approximately sinusoidal pattern, which indicates that hydrostatic pressure dominates in these three filling conditions. The differences in amplitude between different filling levels are due to the different RAO values under corresponding excitation frequencies.

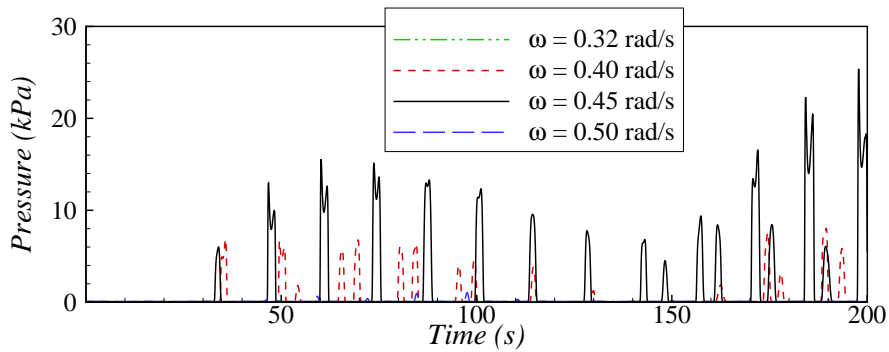
We now consider the effect of external wave height (i.e. the excitation amplitude) on the pressure in the tank. The 40% filling level is used and the wave height varies from 1 m to 5 m. Fig. 3.34 shows the time histories of pressure at $y = 6$ m on the left wall for different wave heights. As the wave height increases, envelopes are gradually formed due to the difference between the real and theoretical resonant frequencies. This is consistent with the variation of free surface elevation excited by different wave heights. In addition, sharper double peaks are gradually formed as larger wave heights are applied, which is not observed in the time history of free surface elevation. This indicates that larger impact pressure on the left wall is produced due to the stronger water movement, even when the free surface is falling down along the left wall. In



(a) $y = 4$ m



(b) $y = 6$ m

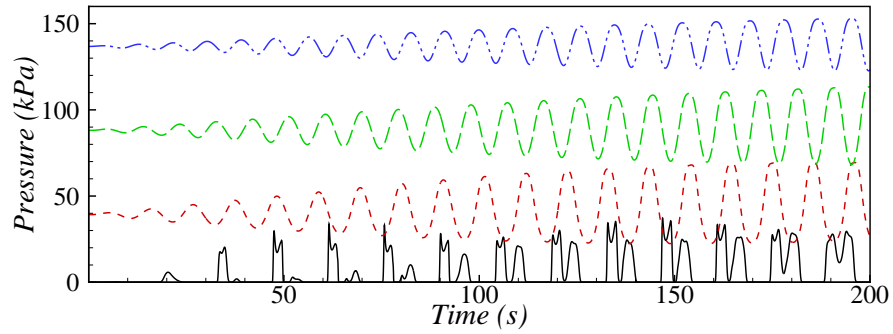


(c) $y = 8$ m

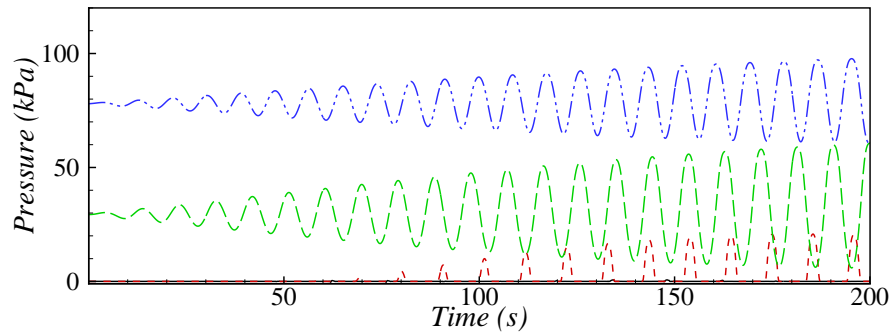
Figure 3.32: Time histories of pressure at four different frequencies on the left tank wall.

other words, larger dynamic pressure is induced at a larger wave height which provides more kinetic energy.

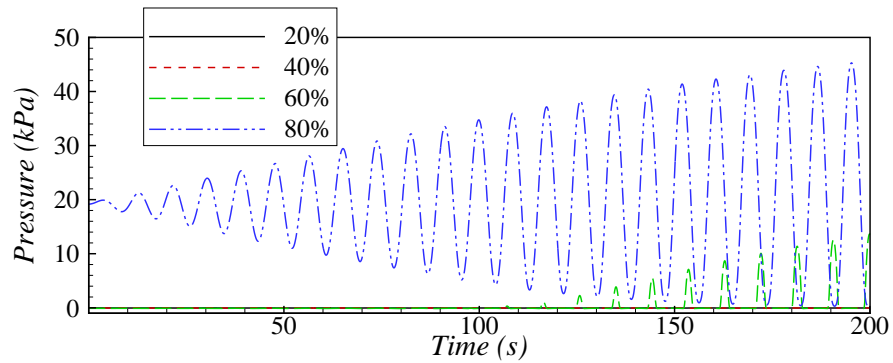
The pressure distributions on the left tank wall when the sloshing wave just reaches the tank roof for three different cases are shown in Fig. 3.35. As the filling depth increases, pressure distribution on the left tank wall gradually becomes linear. This



(a) $y = 6$ m



(b) $y = 12$ m



(c) $y = 18$ m

Figure 3.33: Time histories of pressure under four different filling conditions on the left tank wall.

supports the observation that, of the free surface displacement at various filling depths, the nonlinear sloshing behavior is dominant in lower filling conditions. In Fig. 3.35(a), the increase in the pressure at the top of the tank might be caused by a small volume of the fluid climbing along the tank very rapidly and hitting the top corner like a water jet. In addition, it is interesting to note that negative pressure appears

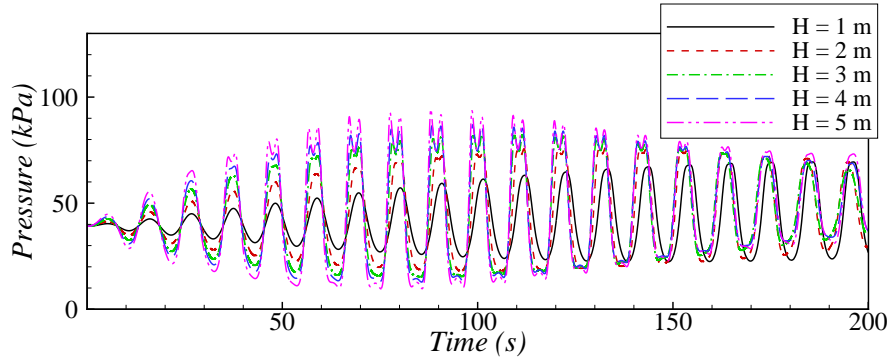


Figure 3.34: Time histories of pressure induced by five different wave heights at $y = 6$ m on the left tank wall.

near the corner at the larger filling levels in Fig. 3.35(b) and Fig. 3.35(c).

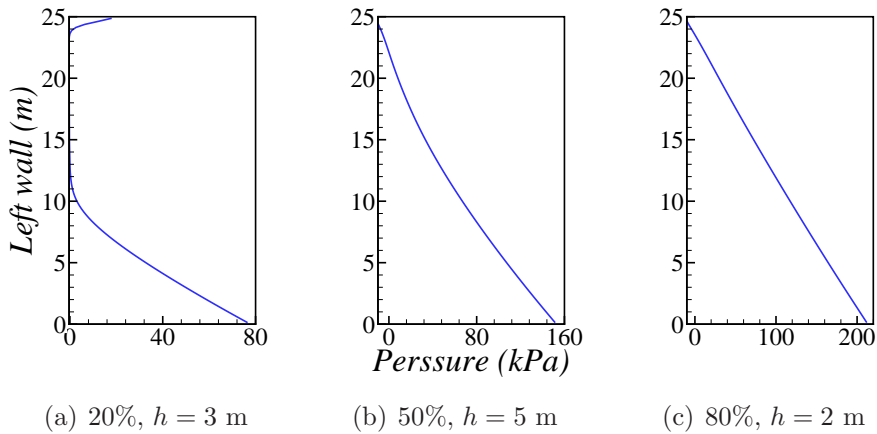


Figure 3.35: Pressure distribution at the left wall when the sloshing wave just reaches the tank roof for three different cases.

3.4 Summary

In this chapter, the numerical model developed in Chapter 2 was applied to the numerical simulation of sloshing flows. By employing the moving coordinate system, the model could easily simulate sloshing waves in a rectangular tank excited randomly by three-degrees-of-freedom motions. First, the developed numerical model was validated by simulating both mild and violent sloshing waves excited by single surge and pitch motions. The present numerical results agreed well with other published exper-

imental and numerical results, indicating the applicability of the present numerical model in complicated sloshing simulations.

Emphasis in this chapter was put on the investigation of sloshing flows in a full-scale LNG tank excited by ship motions in sea conditions. To achieve this, the motion RAOs of a realistic LNG carrier were adopted directly to excite the liquid sloshing in the LNG tank. Based on the parametric study on the effects of excitation frequency, filling level and external wave height, the following conclusions could be made:

1. In head sea conditions, the random initial phase difference between the surge and pitch motions will have definite effects on the induced sloshing waves, and the phase difference of 180° can cause the most violent sloshing.
2. The most critical sloshing wave is generated when the sea wave frequency approaches the resonant frequency of the sloshing system, at which both the pressure and free surface elevation reach the maximum value.
3. As the filling depth increases, the free surface elevation excited by each resonant frequency decreases due to the corresponding smaller RAOs applied. In lower filling level conditions, the nonlinear characteristics of the sloshing wave are more evident.
4. The increase in the external wave height leads to a stronger sloshing wave in the tank due to the larger kinetic energy provided. At a larger wave amplitude, the beating phenomenon can be observed for both the pressure and free surface elevation even at the natural frequency calculated by linear wave theory.

Overall, the external wave height that excites ship motions and the related excitation frequency have a substantial effect on the sloshing wave inside the tank. Since environmental conditions are undetermined during the LNG delivery and a wide range of filling levels are required, the dimensions of the LNG tank should be designed to avoid having a resonant frequency coinciding with the predominant ocean wave frequency and falling within the frequency range in which a large motion RAO of the LNG carrier will be generated.

Chapter 4

AN IMPROVED NUMERICAL MODEL BY HIGH-RESOLUTION CONVECTION SCHEMES

4.1 Introduction

In this chapter, the development of the free surface flow solver is presented in detail. In Chapter 2, the numerical model at the first stage was described comprehensively and validated by classic benchmark solutions. However, the preliminary model would suffer the numerical dissipation issue when considering some challenging sloshing simulations. In this chapter, a detailed description of the issues with the preliminary model is provided, followed by the improvement of the intermediate model (which has been applied in Chapter 3) and the final developed sloshing model.

4.2 The preliminary model : the numerical dissipation issue

4.2.1 Nonlinear liquid sloshing under horizontal motions - 1

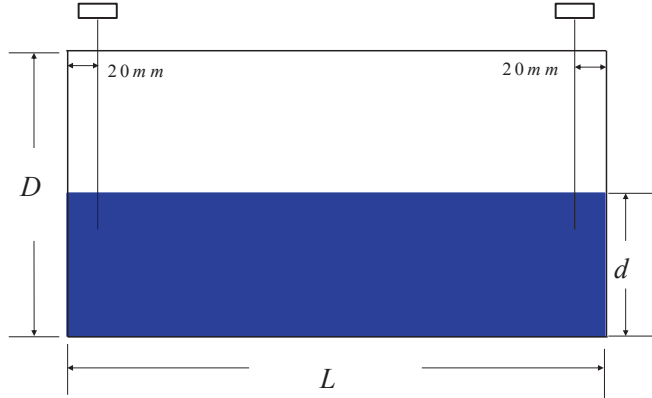


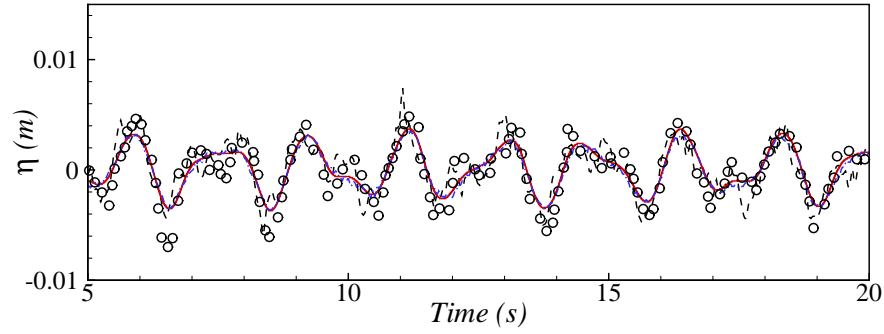
Figure 4.1: A sketch of the two-dimensional rectangular tank in Liu's work.

In order to test the performance of the preliminary model in solving nonlinear waves, we numerically repeat two experiments conducted by Liu and Lin (2008) for both non-resonance and resonance cases. As shown in Fig. 4.1, both cases are performed in a rectangular tank 0.57 m long, 0.31 m wide and 0.3 m high. The initial water depth is 0.15 m, so the lowest natural frequency of the sloshing system is 6.0578 rad/s according to Eq. (3.3).

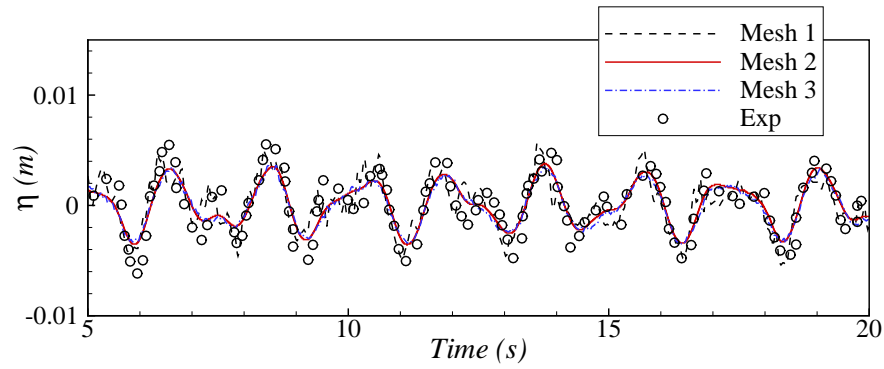
The tank is mounted on a shake table and its motion is governed by a sinusoidal displacement with an amplitude $a = 0.005$ m for both cases. So, in our co-moving system, the acceleration force in the horizontal (x) direction is given by,

$$f_x = -a\omega^2 \sin(\omega t), \quad (4.1)$$

where the excitation frequencies ω are $0.583\omega_0$ and $1.0\omega_0$ for the non-resonance and resonance cases respectively. In both cases, three different meshes are tested, whose cell numbers are 95×50 , 190×100 and 295×150 respectively. A time interval $\Delta t = 0.001$ s is applied.



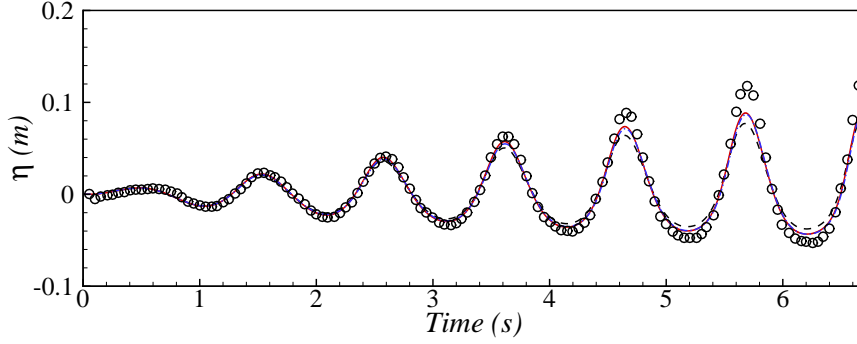
(a) 0.02 m from the left wall



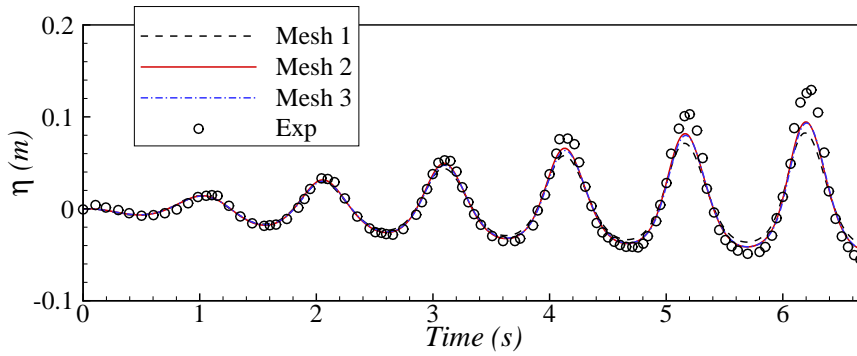
(b) 0.02 m from the right wall

Figure 4.2: Comparison of surface displacement with different mesh sizes for the non-resonance case.

In the first case, the simulation with $\omega = 0.583\omega_0$ runs up to 20 s. In Fig. 4.2, the time evolutions of the surface displacement recorded at 0.02 m from the left- and right-hand side walls are compared with the experimental results. It can be seen that the numerical results gradually achieve a better agreement with the experimental data as the mesh size increases. The values obtained by the two finer meshes lie close to each other at both locations. This suggests that a convergent solution is achieved by the preliminary model. Overall, the numerical results agree with the experimental data.



(a) 0.02 m from the left wall



(b) 0.02 m from the right wall

Figure 4.3: Comparison of surface displacement with different mesh sizes for the resonance case.

In the second case where $\omega = 1.0\omega_0$, the total simulation time is 6.7 s. Fig. 4.3 illustrates the comparison of the time history of the surface displacement. Just like the previous case, Mesh 2 and Mesh 3 give almost the identical results, indicating that a grid-independent solution is achieved. The resonant phenomenon is clearly observed. In addition, nonlinear features of sloshing waves are also captured in Fig. 4.3, which show an asymmetrical wave pattern with a much larger wave crest than trough.

However, in this resonance case, the discrepancy between the experimental data and the results predicted by the preliminary model becomes larger with time. This is mainly due to the accumulation of numerical errors. These errors may be caused by the dissipative nature of the first-order upwind scheme, which is employed to solve the convective terms in the Navier-Stokes equations. But this dissipation is not substantial when linear stationary free sloshing wave and nonlinear sloshing wave under non-resonant excitations are simulated. As described in Chapter 2, the preliminary model consists of a fluid solver and a Level-Set based free surface tracker. In the fluid

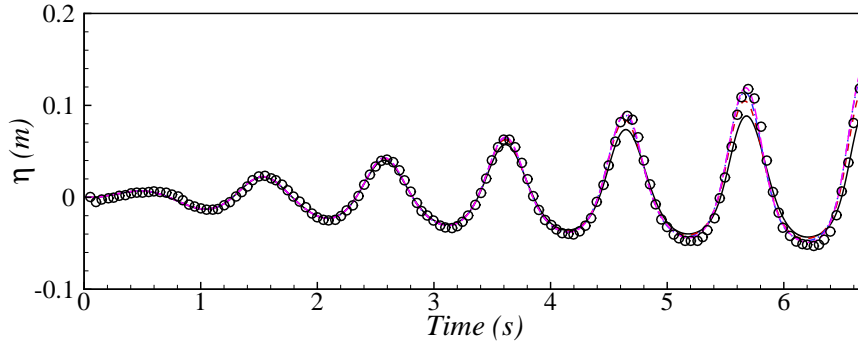
solver, the reason why the first-order upwind scheme is applied is to avoid numerical instability while simulating the two-phase flows. In the Level Set Method, the introduction of the smoothing band also aims to reduce the instability caused by the jump condition from air to water. Therefore, a further parametric investigation on the smoothing band is needed before we exclude the applicability of the first-order upwind scheme in the preliminary numerical model.

4.3 The intermediate model: a parametric study of the smoothing band in the Level-Set technique

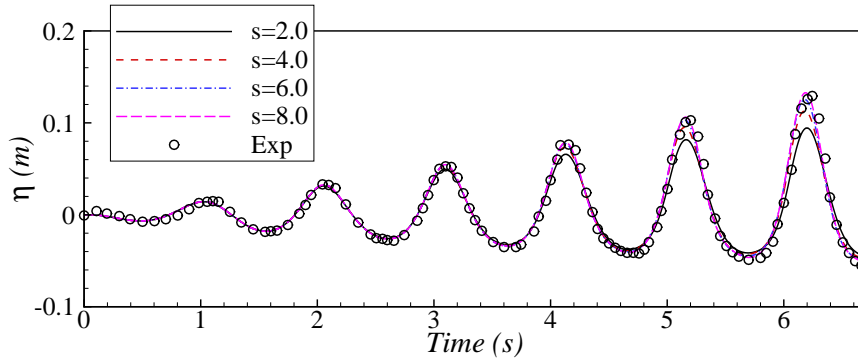
4.3.1 Nonlinear liquid sloshing under horizontal motions - 2

When applying the Level-Set scheme to simulate two-phase flows, a narrow transition zone is usually defined and located around the interface. This avoids introducing numerical instability due to the sharp change of the fluid properties. Smeared functions are thus used to smooth the material properties inside the transition zone. Most studies follow the classical ways of using trigonometric-type Heaviside functions. Some other researchers have also proposed new smoothing functions, such as the exponential-type (Colicchio et al., 2005), to achieve more stable performances. Most of these studies (Gu et al., 2005) adopt the empirical value $\epsilon = 1.5h$ as suggested by Sussman et al. (1994), where h is the minimal mesh size. $\epsilon = 2.0h$ (Wang et al., 2011) or $\epsilon = 3.0h$ (Colicchio et al., 2006) have also been used. However, some other studies have not indicated the size of the smoothing band. Thus, as discussed above, it is essential to study the effects of the size of the smoothing band.

In this section, we continue our numerical simulation of the resonance sloshing experiment by Liu and Lin (2008). Considering that the sharp gradient between air and water may intensify the numerical error, we conduct our study by increasing the size of the smoothing band with an interval $\Delta\epsilon = 2h$. The value $\epsilon = s \times h$ increases from $s = 2.0$ to $s = 16.0$. Following the previous section, the mesh size of 190×100 and a time interval $\Delta t = 0.001$ s are used.



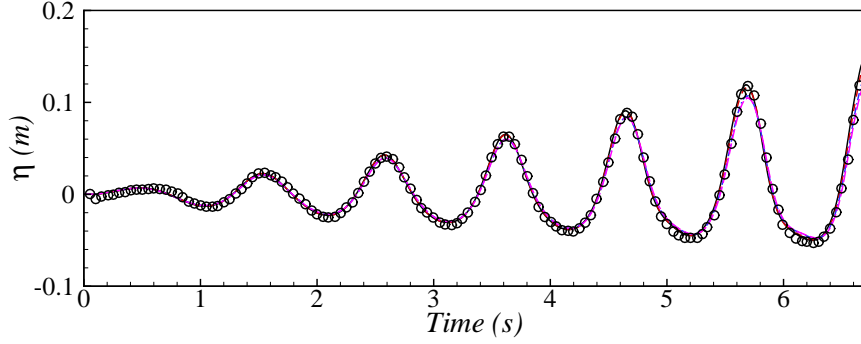
(a) 0.02 m from the left wall



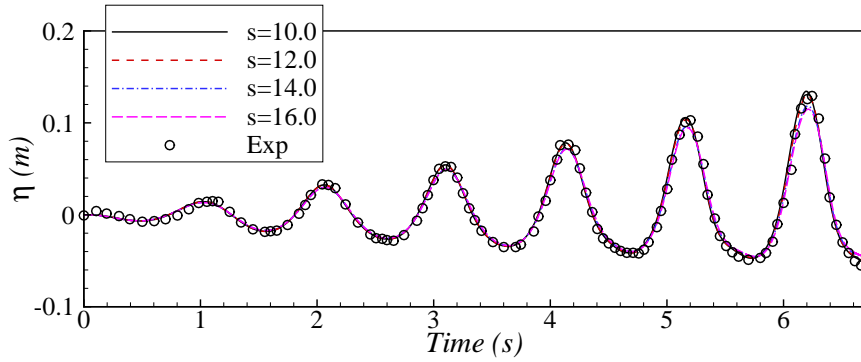
(b) 0.02 m from the right wall

Figure 4.4: Comparison of time histories of surface displacement between numerical results with smoothing sizes varied from $s = 2.0$ to $s = 8.0$.

Fig. 4.4 shows the time history of the surface displacement obtained by the numerical model with $s = 2.0$ to $s = 8.0$. It can be seen that as the smoothing band becomes larger, the wave elevation predicted by the numerical model becomes higher. When comparing the numerical predictions with the experimental measurements, as the s term increases from 2.0 to 4.0, a significant improvement is obtained by the numerical model. For $s = 6.0$ and $s = 8.0$ simulations, the improvement is very limited and the two solutions lie close to each other, which indicates an optimal solution is nearly obtained. In addition, the convergent results obtained by the present model match the experimental recordings well.



(a) 0.02 m from the left wall



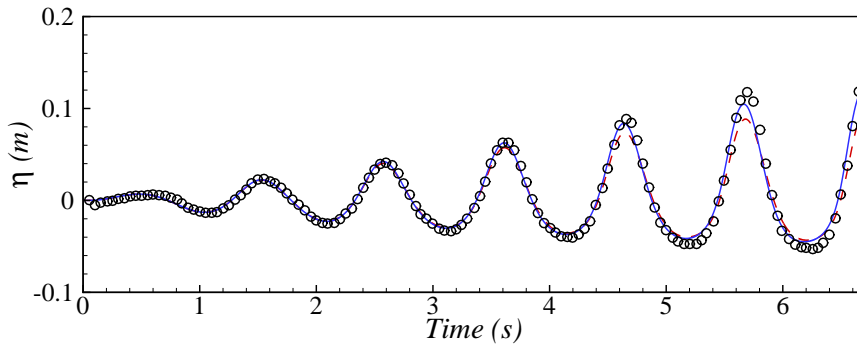
(b) 0.02 m from the right wall

Figure 4.5: Comparison of time histories of surface displacement between numerical results with smoothing sizes varied from $s = 10.0$ to $s = 16.0$.

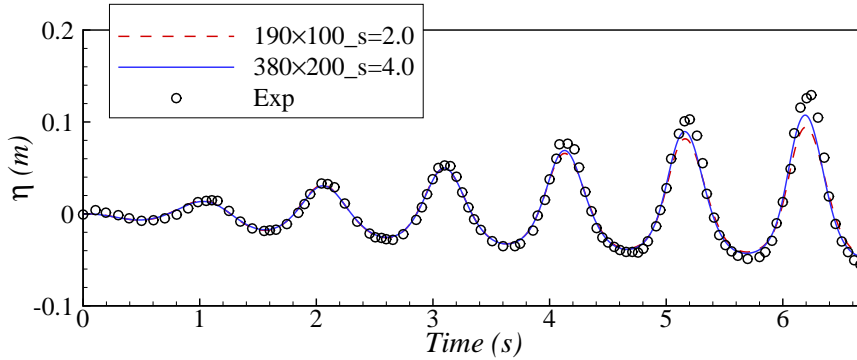
By continuing to enlarge the smoothing band, as shown in Fig. 4.5, the numerical results obtained with $s = 10.0$ to $s = 16.0$ show an opposite trend to those shown in Fig. 4.4: the wave elevations gradually decrease and deviate from the experimental results. This indicates that within a certain range of s values, a convergent solution can be achieved by the current numerical model. Thus, we can say that the size of the smoothing band does have an effect in the present numerical model. But it should also be pointed out that the introduction of the smoothing region around the interface is a numerical technique which aims to reduce the instability caused by the jump condition. In other words, the smoothing region is an artificial area which should be limited to a relatively small size. Therefore, in this study, the maximum size of the smoothing band is limited to 10% of mesh sizes for the whole computational domain. For the resonance case considered in this section, only 10 grid cells can be used as the smoothing band for the mesh size of 190×100 . Thus the maximum s value that can be applied here is 5.0. As shown in Fig. 4.4, the corresponding best simulation

results would be the one given by $s = 4.0$.

To illustrate the applicability of the improved numerical model by increasing the smoothing band, a further comparison is conducted. Two mesh sizes, 190×100 with $s = 2.0$ and 380×200 with $s = 4.0$, are employed respectively to repeat the resonance case. In both simulations, the actual smoothing size is the same, equal to 0.012 m. As shown in Fig. 4.6, even though the physical size is the same, the numerical results obtained with more smoothing grids are closer to the experimental measurements. This indicates that when the smoothing band is properly enlarged, the accuracy of the numerical model is much improved. Therefore, the resultant intermediate model is applicable to deal with violent free surface flows.



(a) 0.02 m from the left wall

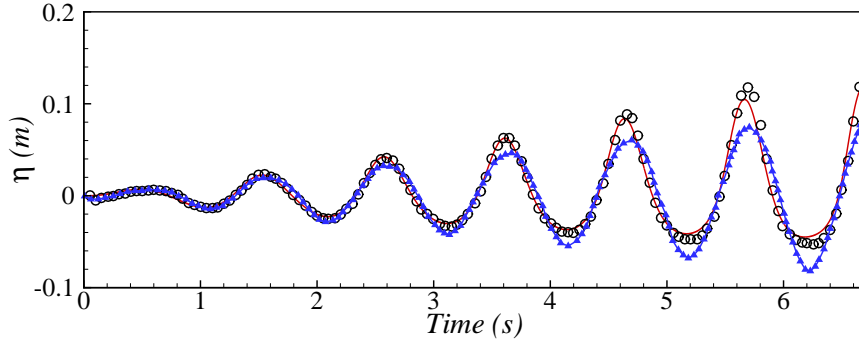


(b) 0.02 m from the right wall

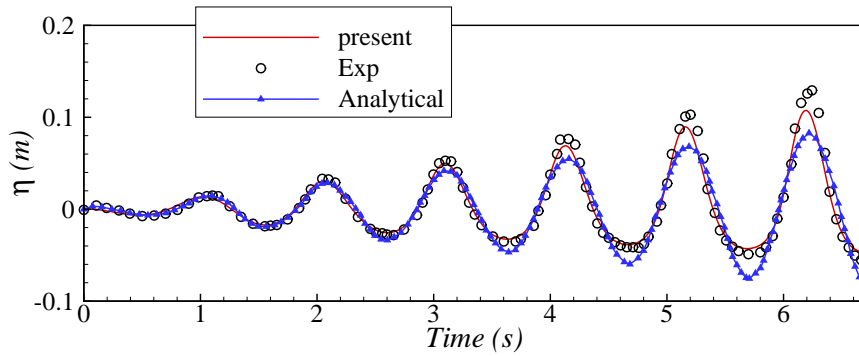
Figure 4.6: Comparison of time histories of surface displacement between 190×100 with $s = 2.0$ and 380×200 with $s = 4.0$.

Further comparison is made and shown in Fig. 4.7. The blue line represents the analytical solution by Faltinsen (1978), which is based on linear potential flow theory without considering the viscous effects. It can be seen that the analytical solution shows a symmetrical wave pattern and fails to match the experimental recordings.

The numerical solution with $s = 4.0$ agrees well with the experiment, suggesting that the intermediate model is capable of accurately simulating nonlinear sloshing motions.



(a) 0.02 m from the left wall



(b) 0.02 m from the right wall

Figure 4.7: Comparison of time histories of surface displacement among the improved numerical prediction, the experimental data and the analytical solution.

4.3.2 Sloshing under vertical motions

Pure vertical excitations on the tank only make changes to its gravitational acceleration. This will not lead to a large effect if the free surface of the tank is initially undisturbed. However, during LNG transportation, the tank may be excited by horizontal, vertical and rotational motions at the same time. In such situations, the free surface will deform due to surge and pitch motions. The vertical excitation would then enlarge the free surface elevation during tank motions (Chen and Nokes, 2005). Thus, it is of importance to validate the improved numerical model in predicting the sloshing under pure vertical excitations.

In this section, we follow the work in Frandsen (2004) and compare the results obtained by the intermediate model with his numerical work. A two-dimensional rectangular tank is used in his simulation and measures 1.0 m in both horizontal and vertical directions. The displacement of the tank is governed by,

$$y = A_y \cos(\omega t), \quad (4.2)$$

where A_y and ω denote the amplitude and frequency of the vertical excitation. The filling water has an average depth $d = 0.5$ m with an initial free surface defined by,

$$\eta_0 = A \cos(\pi x/L). \quad (4.3)$$

Fig. 4.8 provides a schematic view of the computational domain.

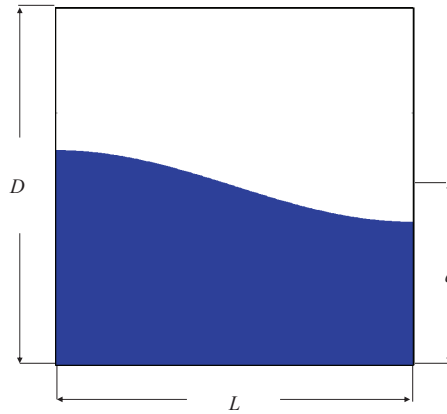


Figure 4.8: A schematic view of the initial conditions of the heave-induced sloshing.

Two cases with different excitations are conducted with the same amplitude of the initial free surface $A = 0.1$ m. In Case 1, the excitation has an amplitude of $A_y = 0.272$ m and a frequency $\omega = 0.798\omega_0$, where $\omega_0 = 5.317 \text{ s}^{-1}$ is the lowest natural frequency of the sloshing system according to Eq. (3.3). The excitation amplitude of Case 2 is $A_y = 0.0668$ m with a frequency $\omega = 1.6102\omega_0$.

To begin with, three mesh sizes, 100×100 , 200×200 and 300×300 , are tested for Case 1. The preliminary numerical model ($s = 2.0$) with a time interval of 0.001 s is used first for the mesh size convergence test. Fig. 4.9 shows the wave elevations at the left wall predicted by the three mesh sizes. The circles are the benchmark solution given by Frandsen (2004). It can be seen that similar results are attained by the preliminary model with the three different mesh sizes at the initial period. As time

elapses, the discrepancy between the results predicted by the coarse mesh and the finer meshes becomes larger due to the accumulation of numerical errors. Conversely, the solutions obtained by the two finer meshes lie close to each other, indicating that a grid-independent solution is achieved. However, even with a convergent solution, in Fig. 4.9, we can see that the preliminary model cannot predict the peak value accurately.

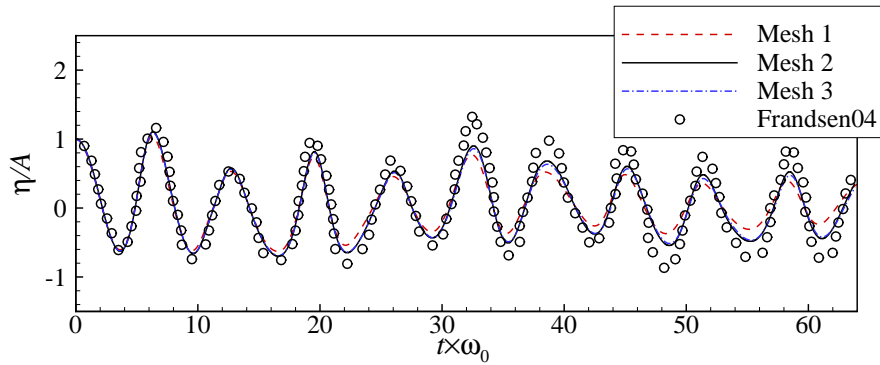


Figure 4.9: Time histories of wave elevation at the left wall for three mesh sizes.

Based on the mesh size convergence test, the mesh size of 200×200 is applied for the following simulations in this section. According to the 10% limitation, a maximum smoothing band of $s = 10.0$ can be applied in the intermediate model. To find the optimal s value for this case, we follow the same process as the previous case, starting from $s = 2.0$ with an interval $\Delta s = 2.0$. In Fig. 4.10, the numerical results with various s values are compared with the benchmark solution. As the s value increases from 2.0 to 4.0, a much better agreement with the benchmark solution can be observed. This indicates that an apparent improvement is achieved by the intermediate model. It should be pointed out that we only increased the s value to $s = 6$ in this case. This is because we find that when increasing s from 4.0 to 6.0, a deviation from the benchmark solution appears, showing that $s = 4.0$ is the optimal s value for this case. Therefore, we stop here since it is impossible to achieve a better result by applying a larger smoothing band than $s = 4.0$.

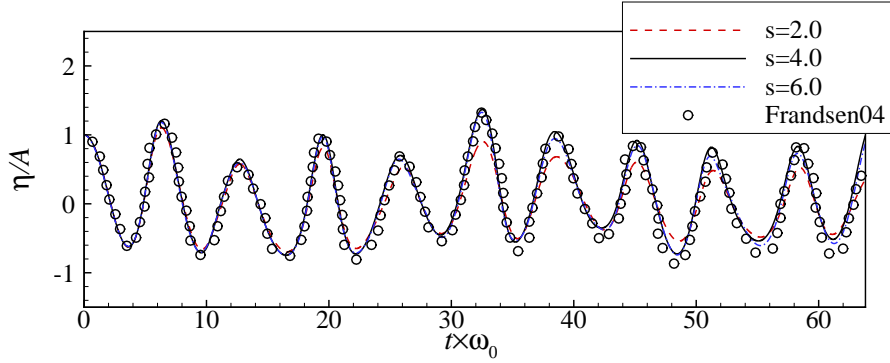


Figure 4.10: Time histories of wave elevation at the left wall obtained by different smoothing sizes.

To further test the optimal s value with the current model, we apply the same mesh size of 200×200 with $s = 4.0$ for Case 2. Fig. 4.11 shows the comparison of the wave elevations at the left wall between the present predictions and the solution given by Frandsen (2004). With a non-resonant frequency applied, random peaks and troughs are generated. Except for some localized discrepancies, the solution attained by the numerical model with $s = 4.0$ is in good agreement with the benchmark solution.

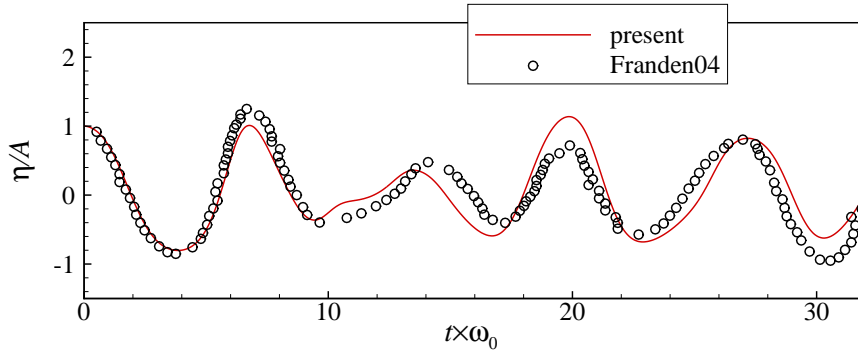


Figure 4.11: Comparison between Frandsen's results and the present numerical predictions with $s = 4.0$ for the non-resonance case.

4.3.3 Sloshing under rotational motions

Besides the translational excitations, rotational motions are the main excitations to cause sloshing phenomena, especially during LNG transportation. In two-dimensional analysis, it is essential to consider the pitch motion in order to perform comprehensive

validation. Thus in this section, besides testing the intermediate model under surge and heave motions, the sloshing in a two-dimensional rectangular tank under forced pitch excitations is also simulated.

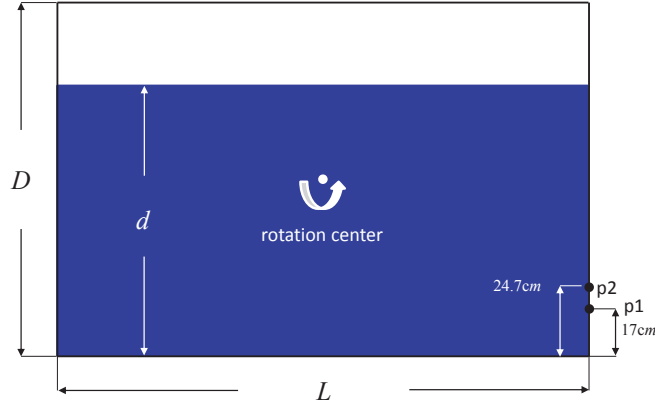


Figure 4.12: A sketch of the water tank used in Akyildiz's experiment.

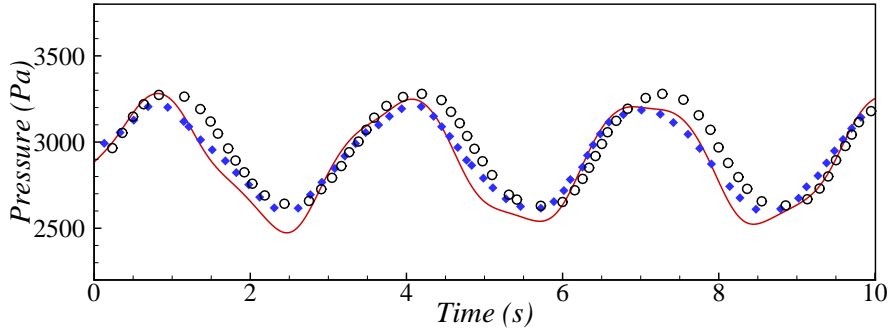
Following the experimental work in Akyildiz and Ünal (2005), as shown in Fig. 4.12, the dimensions of the tank are: length $L = 0.92$ m and height $D = 0.62$ m. The tank is forced to rotate around its center with a motion governed by,

$$\theta = \theta_0 \cos(\omega t + \xi_0), \quad (4.4)$$

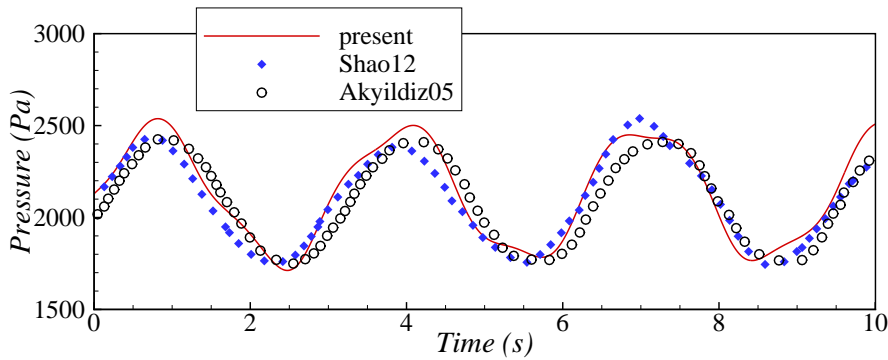
where the excitation frequency is $\omega = 2$ rad/s with $\xi_0 = \pi/2$. The filling ratio is 75% and two pressure probes p1 and p2 are located at the right wall of the tank 17 cm and 24.7 cm from the tank bottom respectively. According to Akyildiz and Ünal (2005), two excitation amplitudes, $\theta_0 = 4^\circ$ and $\theta_0 = 8^\circ$ are applied respectively. After the mesh convergence test, the mesh size of 184×124 is adopted in this case with a time interval of 0.001 s. The s value of 4.0 is chosen as it achieved satisfactory results in the previous validation.

Fig. 4.13 shows the time history of pressure at the two probes for the $\theta_0 = 4^\circ$ case. It can be seen that with the frequency $\omega = 2$ rad/s applied in this case, which is far from the natural frequency $\omega_0 = 5.551$ rad/s according to linear wave theory, the pressure is approximately sinusoidal with an amplitude of around 300 pa. This indicates that the sloshing wave oscillates mildly in the tank and hydrostatic pressure is dominant in this case. In Fig. 4.13, a comparison is also made among the solution by the intermediate model, the numerical result by Shao et al. (2012), and the experimental recording of Akyildiz and Ünal (2005). The time series of Shao

et al. (2012) is predicted by a SPH-based numerical model with improved pressure treatments at the boundary. We can see that the present results are in fair agreement with both results. A small phase difference can be observed between our results and Akyildiz's. However, this phase discrepancy is barely found between our solutions and Shao's.



(a) pressure at p1

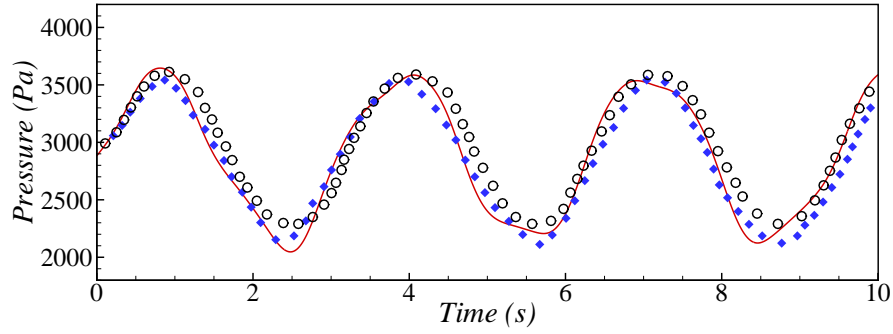


(b) pressure at p2

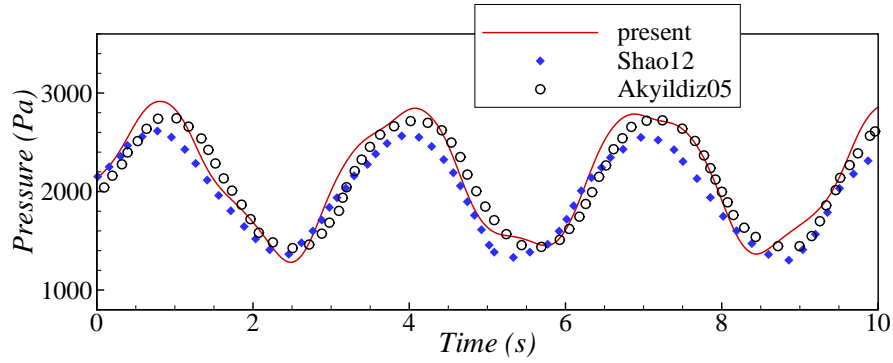
Figure 4.13: Comparison of the time histories of pressure at two probes when $\theta_0 = 4^\circ$.

Similarly, in Fig. 4.14, with a larger excitation $\theta_0 = 8^\circ$ applied at the same frequency, the pressure results are also approximately sinusoidal. But with a larger excitation amplitude, more energy is offered to the sloshing system leading to a larger pressure amplitude of around 600 pa. Except for some local discrepancies, the pressure result predicted by the intermediate model match the data given by both Akyildiz and Ünal (2005) and Shao et al. (2012). This further reveals that the intermediate model, using a finer mesh size and properly larger smoothing band, improves on the accuracy of the preliminary model when dealing with violent free surface flows.

As described above, the first-order upwind scheme is adopted in the preliminary numerical model to calculate the convective term due to the advantage of its numerical



(a) pressure at p1



(b) pressure at p2

Figure 4.14: Comparison of the time histories of pressure at two probes when $\theta_0 = 8^\circ$.

stability. However, as shown in the previous section, when simulating the violent free surface flows, the preliminary model would attain predictions which deviate from the benchmark solutions to some extent. This indicates that the numerical stability achieved by adopting the first-order upwind scheme in the preliminary model may be based on a compromise of accuracy. In this section, inspired by introducing the smoothing zone into the Level-Set technique, which also aims to reduce the numerical instability when dealing with the sharp change of the fluid properties, an investigation on the effects of smoothing band is performed. It is found that with a relatively larger smoothing band, the sharp gradient between the air and water is mitigated a bit and satisfactory numerical results are achieved. According to this finding, the intermediate model with a 10% limitation on the the size of the smoothing band is developed. Validation is performed with three sloshing cases excited by motions in different directions. Good agreement with the published experimental measurements and benchmark solutions indicates the intermediate model is accurate and applicable.

4.4 The final model: implementation of high-resolution convection schemes

As stated earlier, the smoothing zone is a numerical technique used to attain the stable solutions but it does not physically exist. Therefore, the application of the increased smoothing band is not quite general even though the 10% limitation is followed. Additionally, there are some cases when one of the two dimensions is very small. Take, for example, a simulation of a free surface flow in a very long tank. The vertical mesh size compared with the horizontal mesh size is quite small. Thus, the smoothing band is relatively limited to a small size. We can increase the vertical mesh size to a certain extent for such a case in order to apply the intermediate model with a properly increased smoothing band. However, the accompanying computational effort would be huge and undesirable in our study. Thus, we are looking for alternative ways to improve the accuracy of our numerical model for simulation of free surface flows.

One viable option is to replace the first-order upwind scheme by a convection scheme with a higher-order of accuracy. Most studies (Gu et al., 2005; Wang et al., 2011) using the Level-Set scheme with the smoothing band concept to solve free surface flows apply the second-order or even lower order convection schemes based on finite difference or finite volume approximations. The third-order Quadratic Upstream Interpolation for Convective Kinematics (QUICK) scheme of Leonard (1979) has been applied to the fluid solver with the Level-Set technique to capture the interface by Yang and Stern (2009). But unlike the aforementioned studies, they adopted the ghost-fluid method proposed by Kang et al. (2000), which does not smooth the fluid properties but handles them in a sharp manner. Thus, in this section, we try to incorporate a higher-order convection scheme into our current numerical model, which can retain the smoothing zone of the Level Set Method.

4.4.1 Highly-accurate and bounded convection schemes

The numerical approximation for the convective term of hyperbolic conservation laws and transport equations has been one of the critical challenges in computational fluid dynamics. Many researchers have devoted efforts to devising a perfect convection scheme, which would be accurate, stable and bounded. However, there is a conflicting issue in meeting all these requirements. Achieving high levels of stability and boundedness requires some kind of diffusive smoothing mechanism which would definitely lead to a compromise of the scheme's accuracy. Among the different convection

schemes developed in the past which have often been applied in practical engineering applications, the classical first-order upwind scheme and the hybrid central/upwind scheme are highly stable and unconditionally bounded, but highly diffusive in certain circumstances. The second-order upwind scheme and the skew-up upwind scheme have been proposed as alternative higher-order schemes and have been successful in increasing the accuracy of the solution. In particular, the third-order QUICK scheme, which has the very attractive properties of no numerical diffusion, low dispersion and inherent convective stability, has been widely applied. However, even though QUICK is robust and reliable under many conditions, it has a shortcoming: under highly convective conditions (such as sharp changes in gradients and jump discontinuities), it has the tendency to produce overshoots and undershoots, displaying unphysical oscillations near regions of steep gradients. These oscillations can be sufficiently serious and lead to numerical instabilities eventually.

To retain QUICK's desirable attributes (third-order accuracy and good stability) while eliminating unphysical oscillations, Leonard (1988) modified the QUICK scheme slightly and proposed the resulting Simple High-Accuracy Resolution Program (SHARP), which can produce solutions without undershoots and overshoots. This is a significant advance in the modeling of highly convective flows. More importantly, Leonard (1988) introduced the concept of variable normalization and the normalized variable diagram (NVD), which is a plot of the locally normalized convected control-volume face variable with respect to the normalized adjacent upstream node variable. Using the NVD plane, standard convection methods, such as first- and second-order upwind, second-order central difference and third-order QUICK, can be represented by various straight lines. In addition, based on this frame, researchers can construct various convection schemes by combining different classical convection methods within certain constraints. A brief introduction of the NVD is given in the following section.

4.4.1.1 Normalized Variable Diagram

As shown in Fig. 4.15, we consider the variation of a convected scalar Φ along a direction normal to a control-volume (CV) face. According to the convecting velocity shown in Fig. 4.15, three adjacent nodes U, C, D are labeled as the upstream, central and downstream nodes around the CV face (denoted by the dotted line). To model the Φ value of the CV face, some or all of the Φ values at the three U, C, D nodes are applied to perform the interpolation depending on different convection schemes. Note that the choice of the nodes of Φ_U , Φ_C and Φ_D depends on the direction of

the normal velocity. As indicated in Fig. 4.16, variable normalization of the same information is performed, and the locally normalized variable is thus defined by,

$$\tilde{\Phi} = \frac{\Phi - \Phi_U}{\Phi_D - \Phi_U}. \quad (4.5)$$

According to the definition, the normalized variables for the upstream and downstream values are $\tilde{\Phi}_U = 0$ and $\tilde{\Phi}_D = 1$ respectively.

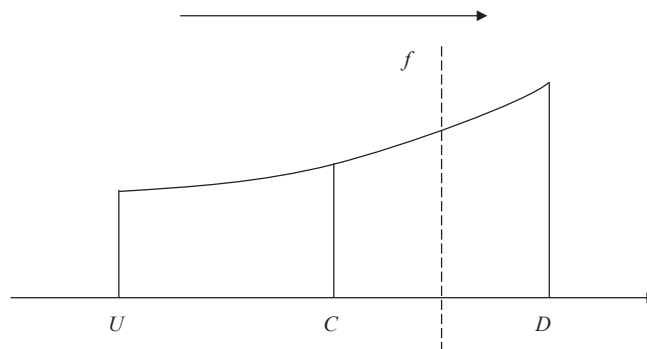


Figure 4.15: Node variables in a general form.

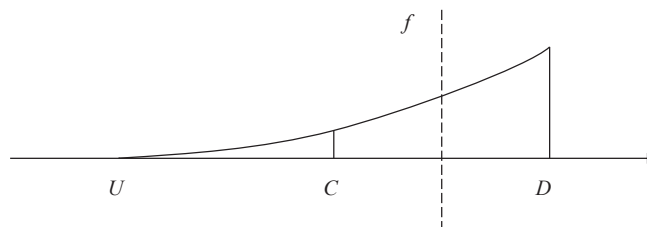


Figure 4.16: Node variables in a normalized form.

Before applying variable normalization, the Φ value at the CV face is basically the function of the Φ values at the U, C and D nodes, denoted as $\Phi_f = F(\Phi_U, \Phi_C, \Phi_D)$. But in terms of the normalized variables, the value at the CV face is only related to the adjacent upstream node, which means $\tilde{\Phi}_f = f(\tilde{\Phi}_C)$. Thus, the NVD frame presents the relationship between the normalized value at the CV face and its adjacent upstream normalized value. In other words, the NVD concept offers a plane where standard convection schemes can be greatly simplified and easily investigated.

Applying variable normalization and present notations (which consider the same CV face and normal velocity direction), the classical convection schemes can be re-defined.

First-order upwind scheme

When applying the first-order upwind scheme to compute the Φ value at the CV face, the equation based on usual variables is,

$$\Phi_f = \Phi_C. \quad (4.6)$$

Based on the normalized variables, it becomes,

$$\tilde{\Phi}_f = \tilde{\Phi}_C. \quad (4.7)$$

Second-order central difference scheme

Similarly, using the second-order central difference scheme based on usual variables, the Φ value at the CV face is calculated by,

$$\Phi_f = \frac{1}{2} (\Phi_D + \Phi_C). \quad (4.8)$$

Using the normalized variables, it becomes,

$$\tilde{\Phi}_f = \frac{1}{2} (1 + \tilde{\Phi}_C) = 0.75 + 0.5 (\tilde{\Phi}_C - 0.5). \quad (4.9)$$

Second-order upwind scheme

Based on the linear upwind-biased extrapolation, the equation given by the second-order upwind scheme in terms of usual variables is,

$$\Phi_f = \frac{1}{2} (3\Phi_C - \Phi_U). \quad (4.10)$$

Using variable normalization, it is written as,

$$\tilde{\Phi}_f = \frac{3}{2} \tilde{\Phi}_C = 0.75 + 1.5 (\tilde{\Phi}_C - 0.5). \quad (4.11)$$

QUICK scheme

Finally, using the widely applied **QUICK** scheme to predict the Φ value at the CV face, the equation based on usual variables is,

$$\Phi_f = \frac{1}{8} (3\Phi_D + 6\Phi_C - \Phi_U), \quad (4.12)$$

In terms of the normalized variables, it is expressed as,

$$\tilde{\Phi}_f = \frac{1}{8} (3 + 6\tilde{\Phi}_C) = 0.75 + 0.75 (\tilde{\Phi}_C - 0.5). \quad (4.13)$$

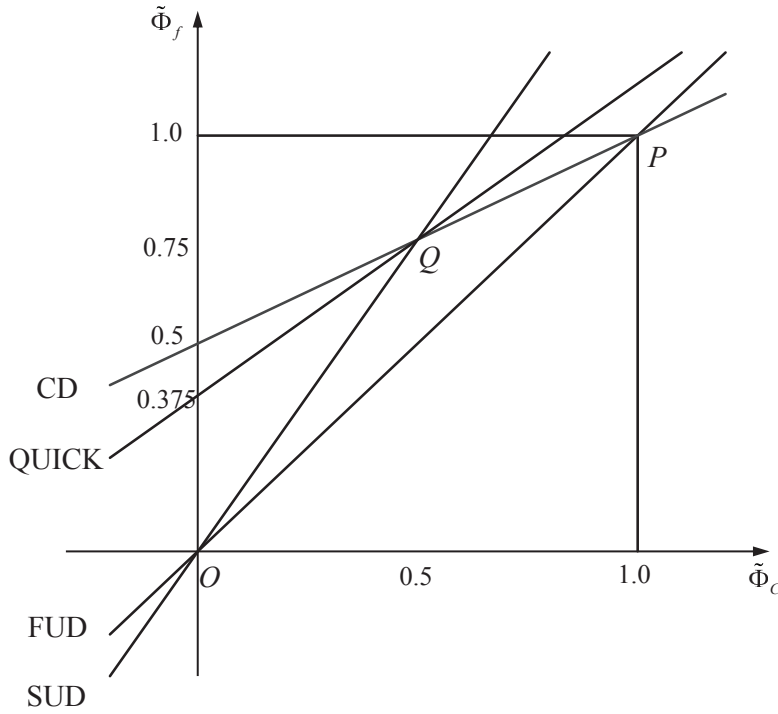


Figure 4.17: Classic convection schemes on NVD.

Based on Eqs. (4.7), (4.9), (4.11) and (4.13), the standard convection schemes can be represented by different straight lines as shown in Fig. 4.17, which is the Normalized Variable Diagram. As previously stated, the relation between the normalized value at the CV face $\tilde{\Phi}_f$ and the value of its adjacent upstream node $\tilde{\Phi}_C$ can be easily plotted and expressed for different convection schemes in this diagram. More

importantly, it should be noted that other than the first-order upwind scheme, the other three characteristics all pass through point $(0.5, 0.75)$, labeled as Q in Fig. 4.17. In particular, the characteristics of the first-order upwind scheme passes through the origin O and the point $(1, 1)$ labeled as P. Thus, characteristics passing through Q can be written as,

$$\tilde{\Phi}_f = 0.75 + S \left(\tilde{\Phi}_C - 0.5 \right), \quad (4.14)$$

where S is the slope of the line. Going back to the un-normalized variables with the upwind-weighted curvature, the original value at the CV face becomes,

$$\Phi_f = 0.5 (\Phi_D + \Phi_C) - CF (\Phi_D - 2\Phi_C + \Phi_U), \quad (4.15)$$

where CF is the curvature factor, and clearly,

$$CF = \frac{1}{2}S - \frac{1}{4}. \quad (4.16)$$

In terms of the normalized variables, Eq. (4.15) can be written as,

$$\tilde{\Phi}_f = 0.5 \left(1 + \tilde{\Phi}_C \right) - CF \left(1 - 2\tilde{\Phi}_C \right). \quad (4.17)$$

It should be noted that applying the curvature factor CF , which is taken to be a function of $\tilde{\Phi}_C$ rather than a constant, Eq. (4.17) is more general such that any functional relationship (linear and nonlinear) between $\tilde{\Phi}_f$ and $\tilde{\Phi}_C$ passing through Q can be written in this form. This also forms the basis for the development of the convection schemes that produce nonlinear characteristics in the NVD frame. In addition, by applying Taylor series expansions about the CV face locations, Leonard (1988) draws two basic conclusions: for any characteristic in the NVD frame,

1. Passing through Q is necessary and sufficient for second-order accuracy.
2. Passing through Q with a slope of 0.75 is necessary and sufficient for third-order accuracy.

This corresponds with the observations of Fig. 4.17 based on Eqs. (4.7), (4.9), (4.11) and (4.13), which shows that the third-order QUICK scheme passes through Q with a slope of 0.75, whereas the second-order schemes have different S values. According to Leonard (1988), linear characteristics in the NVD frame that pass through the second quadrant would produce unphysical oscillations in the steady

one-dimensional convection. Others that pass below the origin O are artificially diffusive. In addition, based on numerical experiments, characteristics passing above point P would lead to overshoots and undershoots in two dimensions. Thus, to develop a convection scheme similar to QUICK without producing oscillations based on the NVD frame, Leonard (1988) summarized the above constraints and proposed a criterion:

The nonlinear NVD characteristic should pass through O , P and Q , with a slope of 0.75 at Q .

Based on this criterion, they introduced the third-order SHARP scheme, which is capable of convective modeling of discontinuities.

4.4.1.2 The Convection Boundedness Criterion

Almost at the same time, Gaskell and Lau (1988) proposed their own bounded convection algorithm, Sharp and Monotonic Algorithm for Realistic Transport (SMART), based on the same variable normalization concept. More importantly, they introduced a different perspective on boundedness constraints from the previous criterion summarized by Leonard (1988), and proposed the Convection Boundedness Criterion (CBC). Together with the NVD frame, CBC becomes the basis for the development of many convection schemes. The details regarding CBC are given as follows.

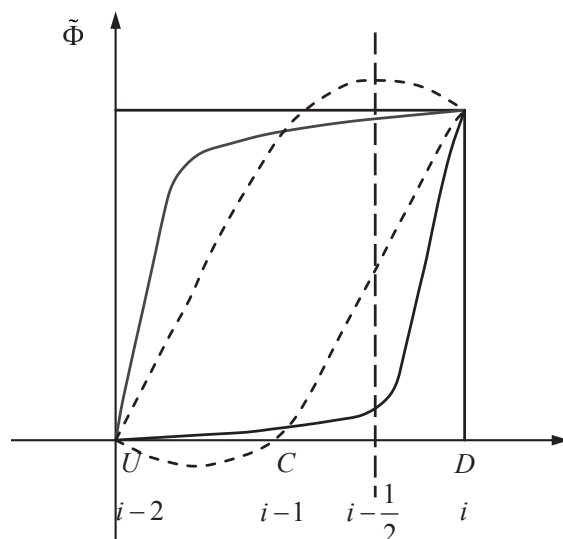


Figure 4.18: An illustration of interpolative boundedness.

The original idea starts with a diagram which plots the normalized variable $\tilde{\Phi}$ related to x when $\tilde{\Phi}_{i-1} \approx 1$ or 0 . As shown in Fig. 4.18, quadratic profiles that pass through $(0, 0)$, $(\Delta x, \tilde{\Phi}_{i-1})$ and $(2\Delta x, 1)$ clearly violate the boundedness. For example, when $\tilde{\Phi}_{i-1} \approx 1$, if the value of $\tilde{\Phi}_{i-1/2}$ exceeds 1 as shown, the value at i must increase (overshoot), enhancing the convective flux at $i + 1/2$, in order to balance the high (unphysical) influx to the CV centered at i . By contrast, monotonic profiles make the value of $\tilde{\Phi}_{i-1/2}$ bounded by $\tilde{\Phi}_{i-1}$ and either 1 or 0, with the largest variation in $\tilde{\Phi}$ occurring over a thin layer located upstream $x \approx 0$, or downstream $x \approx 2\Delta x$, respectively. This kind of violation is referred to as the lack of ‘interpolative boundedness’ in Gaskell and Lau (1988), which would lead to the unphysical oscillations, and is found inherent in some higher-order convection schemes, like, for instance, the second-order upwind scheme. Thus, to make a convection scheme bounded, the following two conditions need to be satisfied:

1. When $\tilde{\Phi}_{i-1} \in (-\infty, 1]$, $\tilde{\Phi}_{i-1/2} \in (\tilde{\Phi}_{i-1}, 1]$;
2. When $\tilde{\Phi}_{i-1} \in [1, \infty)$, $\tilde{\Phi}_{i-1/2} \in [1, \tilde{\Phi}_{i-1})$.

Among all the aforementioned classical schemes, only the first-order upwind and the central difference scheme satisfy the interpolative boundedness. However, the second-order central difference scheme is not known as a boundedness-preserving algorithm. Thus, it is obvious that guaranteeing interpolative boundedness does not necessarily result in ‘computed boundedness’, which requires that the numerical solution should not contain any unphysical overshoots or undershoots while remaining bounded with respect to the adjacent values. Therefore, Gaskell and Lau (1988) concluded that interpolative boundedness is only a necessary, but not sufficient condition, for a convection scheme to attain computed boundedness.

To further investigate the sufficient conditions for a computed bounded convection scheme from a physical point of view, Gaskell and Lau (1988) considered the general convection-diffusion equation for the scalar Φ :

$$\frac{\partial(u_i\Phi)}{\partial x_i} = \frac{\partial}{\partial x_i} \left(\mu \frac{\partial \Phi}{\partial x_i} \right) + S \quad (4.18)$$

where S is the source term. Combined with the notations in the previous NVD (U: $i - 2$, C: $i - 1$ and D: i), the integral form of Eq. (4.18) over the CV centered at C based on variable normalization can be written as,

$$\tilde{\Phi}_{i-1/2} - \tilde{\Phi}_{i-3/2} = \frac{\Phi_{i-1/2} - \Phi_{i-3/2}}{\Phi_i - \Phi_{i-2}} = \tilde{S}^*, \quad (4.19)$$

where \tilde{S}^* is the net effective normalized source term, and,

$$\tilde{S}^* = \frac{\left[\left(\mu \frac{\partial \Phi}{\partial x} \right)_{i-1/2} - \left(\mu \frac{\partial \Phi}{\partial x} \right)_{i-3/2} \right] + \int_{i-3/2}^{i-3/2} S dx}{u_0(\Phi_i - \Phi_{i-2})}, \quad (4.20)$$

which consists of the diffusion and source terms.

Physical considerations lead to the conclusion that the normalized values at the CV center $\tilde{\Phi}_{i-1}$ must be positive if the normalized source term \tilde{S}^* is greater than 0, and vice versa. Thus, it is straightforward to obtain the following constraints:

$$\text{for } \tilde{S}^* > 0, \tilde{\Phi}_{i-1} > 1, \quad 1 < \tilde{\Phi}_{i-1/2} \leq \tilde{\Phi}_{i-1}, \quad (4.21)$$

$$\text{for } \tilde{S}^* \leq 0, 0 \leq \tilde{\Phi}_{i-1} \leq 1, \quad 0 \leq \tilde{\Phi}_{i-3/2} \leq \tilde{\Phi}_{i-1} < \tilde{\Phi}_{i-1/2} \leq 1, \quad (4.22)$$

$$\text{for } \tilde{S}^* < 0, \tilde{\Phi}_{i-1} < 0, \quad \tilde{\Phi}_{i-1} \leq \tilde{\Phi}_{i-1/2} < \tilde{\Phi}_{i-1/3} < 0, \quad (4.23)$$

which are consistent with Eq. (4.19) and the physical expectations. In addition, they also include the previously introduced interpolative boundedness. Thus, satisfaction of the three constraints can be both necessary and sufficient to ensure the computed boundedness.

Based on the three constraints, Gaskell and Lau (1988) proposed the convection boundedness criterion (CBC). Here, combined with the NVD frame, the CBC is slightly modified by replacing $\tilde{\Phi}_{i-1/2}$ and $\tilde{\Phi}_{i-1}$ with $\tilde{\Phi}_f$ and $\tilde{\Phi}_C$, respectively, while the face value is only related to the adjacent upstream value as $\tilde{\Phi}_f = f(\tilde{\Phi}_C)$ in the NVD plane. Thus, a finite difference approximation to Φ_f is bounded if:

1. f should be a continuous increasing function or union of piecewise continuous increasing functions;
2. for $\tilde{\Phi}_C \in [0, 1]$, f is bounded by the function $\tilde{\Phi}_f = \tilde{\Phi}_C$ and $\tilde{\Phi}_f = 1$ ($\tilde{\Phi}_C \leq \tilde{\Phi}_f \leq 1$);
3. for $\tilde{\Phi}_C \notin [0, 1]$, f is equal to $\tilde{\Phi}_C$ ($\tilde{\Phi}_f = \tilde{\Phi}_C$).

Based on the NVD frame, the CBC is illustrated diagrammatically in Fig. 4.19, where the line $\tilde{\Phi}_f = \tilde{\Phi}_C$ and the shaded area are the region over which the CBC is valid.

The proposed CBC is a necessary and sufficient condition for guaranteeing computed boundedness if at most three neighboring nodes are applied to approximate face values. This is not a problem for the schemes based on the NVD frame since the NVD concept also applies at three nodes surrounding the CV. From Fig. 4.17,

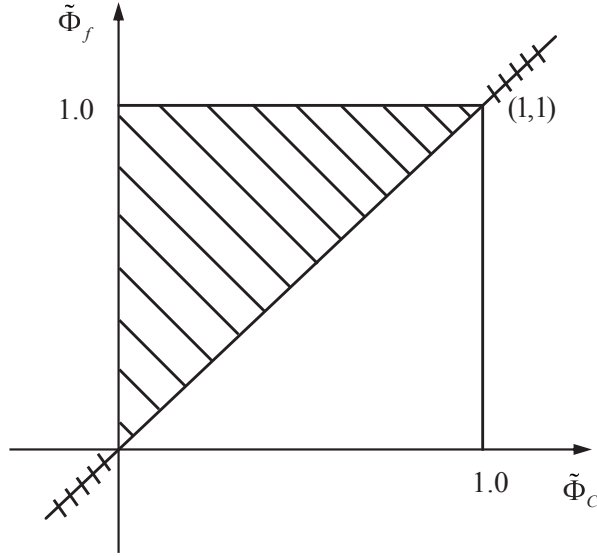


Figure 4.19: An illustration of the convection boundedness criterion.

it can be seen that only the first-order upwind scheme unconditionally satisfies the CBC, while the other three classical schemes violate the CBC outside the range of $\tilde{\Phi}_C \in [0, 1]$. This is consistent with the experience that these schemes would exhibit spurious undershoots and overshoots, especially for highly convective conditions.

4.4.1.3 Composite schemes

From the previous discussions, it is straightforward to conclude that it is impossible for a single linear scheme in the NVD plane to satisfy both high-order accuracy and CBC conditions. Thus, applying the composite forms to construct a bounded convection scheme with higher-order accuracy is unavoidable. In the NVD frame, within the region of $\tilde{\Phi}_C \in [0, 1]$, the characteristic of the desired scheme must pass through the origin O (0,0), point Q (0.5, 0.75) and P (1, 1). Different combinations of the piecewise lines that connect the three points would lead to different composite schemes. Heretofore, the development of perfect convection schemes has presented a continuing challenge.

Various composite schemes have been proposed. Most of them have quite similar forms but few of them have been applied to free surface flows, not to mention applied with the Level-Set technique. Thus, in the current stage of our study, we only

select some popular composite schemes and incorporate them into our intermediate numerical model. The details of the four selected schemes are given as follows. It is worth mentioning that some of the convection schemes developed based on the NVD frame with the CBC constraints are essentially the same as some schemes based on the Total Variational Diminishing flux limiters (TVD), which are widely applied in numerical simulation of compressible flows. For instance, one of the schemes applied in our study, the composite Second-Order Upwind-Central differencing-first-order Upwind scheme (SOUCUP) proposed by Zhu and Rodi (1991) is essentially equivalent to the minimum modulus (MINMOD) scheme of Roe (1986). Thus, the MINMOD here represents the SOUCUP scheme in the NVD frame.

MINMOD (SOUCUP)

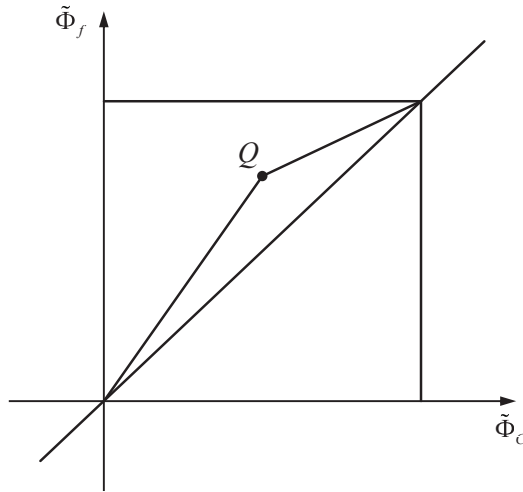


Figure 4.20: MINMOD in the NVD frame.

Following the CBC constraints, Zhu and Rodi (1991) noticed that in the NVD frame, the second-order upwind and the central difference schemes pass through points O (0,0) and P (1,1), respectively and intersect at point Q (0.5,0.75) located in the shaded area defined in Fig. 4.19. Thus, they made a straightforward choice to employ a union of piecewise-linear characteristics that connect the three points by simply combining the second-order upwind and the central difference scheme in the region of $0 \leq \tilde{\Phi}_c \leq 1$, outside which, the first-order upwind scheme is applied. Thereby, they proposed the composite SOUCUP (MINMOD) scheme, which is given based on normalized variables as follows:

$$\tilde{\Phi}_f = \begin{cases} \frac{3}{2}\tilde{\Phi}_C & 0 \leq \tilde{\Phi}_C \leq \frac{1}{2} \\ \frac{1}{2}(1 + \tilde{\Phi}_C) & \frac{1}{4} \leq \tilde{\Phi}_C \leq 1 \\ \tilde{\Phi}_C & \text{otherwise.} \end{cases} \quad (4.24)$$

Fig. 4.20 shows the MINMOD scheme in the NVD plane. According to the criteria of Leonard (1988), since its characteristics pass through point Q (0.5, 0.75) with a slope not equal to 0.75, the MINMOD scheme is second-order accurate.

MUSCL

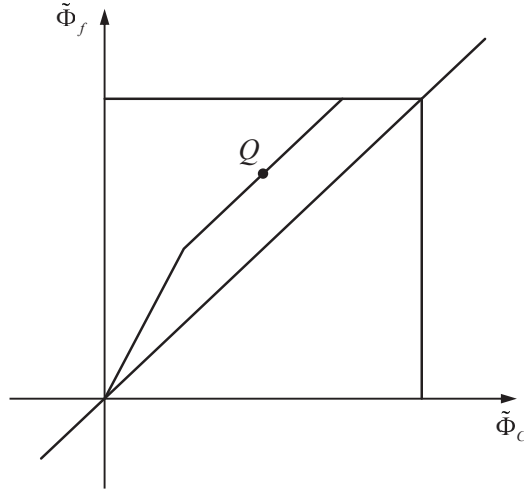


Figure 4.21: MUSCL in the NVD frame.

The monotonic upwind scheme for conservation law (MUSCL), proposed by Van Leer (1979) is the first high-order scheme based on the total variation diminishing with a second-order accuracy. Applying variable normalization, Lien and Leschziner (1993) rewrote the MUSCL scheme to approximate the turbulence convection as,

$$\tilde{\Phi}_f = \begin{cases} 2\tilde{\Phi}_C & 0 \leq \tilde{\Phi}_C \leq \frac{1}{4} \\ \frac{1}{4} + \tilde{\Phi}_C & \frac{1}{4} \leq \tilde{\Phi}_C \leq \frac{3}{4} \\ 1 & \frac{1}{4} \leq \tilde{\Phi}_C \leq 1 \\ \tilde{\Phi}_C & \text{otherwise.} \end{cases} \quad (4.25)$$

As shown in Fig. 4.21, the slope of the characteristics of the MUSCL scheme at point Q is 1.0, not 0.75. Therefore, it is still second-order accurate, consistent with the accuracy obtained in the TVD form.

SMART

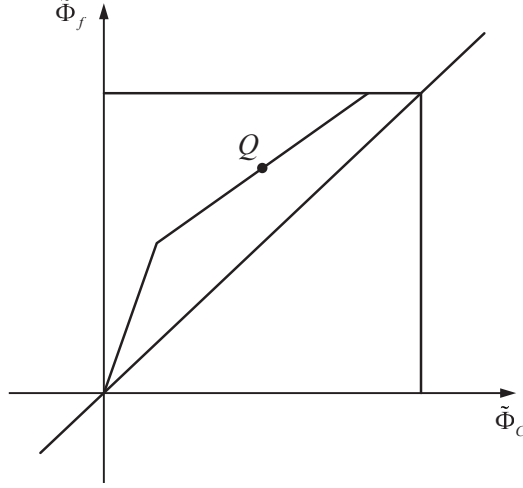


Figure 4.22: SMART in the NVD frame.

After applying the Taylor series expansion, Gaskell and Lau (1988) obtained a similar equation to Eq. (4.17) by ignoring the higher-order terms and introducing the upstream curvature with an undermined variable α^- :

$$\Phi_f = \frac{1}{8}(6\Phi_D + 3\Phi_C - \Phi_U) - \alpha^- (\Phi_D - 2\Phi_C + \Phi_U). \quad (4.26)$$

The difference is that Eq. (4.26) is clearly comprised of the QUICK scheme and the upstream curvature, while Eq. (4.17) applies the central difference and the curvature. Following their own CBC constraints, Gaskell and Lau (1988) determined the values of curvature variable α^- within different regions of $\tilde{\Phi}_C$ and proposed the SMART scheme. Applying normalized variables, SMART can be written as,

$$\tilde{\Phi}_f = \begin{cases} 3\tilde{\Phi}_C & 0 \leq \tilde{\Phi}_C \leq \frac{1}{6} \\ \frac{3}{8} + \frac{3}{8}\tilde{\Phi}_C & \frac{1}{6} \leq \tilde{\Phi}_C \leq \frac{5}{6} \\ 1 & \frac{5}{6} \leq \tilde{\Phi}_C \leq 1 \\ \tilde{\Phi}_C & \text{otherwise.} \end{cases} \quad (4.27)$$

From the above description and the normalized equations, it is evident that the SMART scheme is mainly based on the QUICK scheme, though revised slightly in order to obey the CBC. This can also be observed in Fig. 4.22, in which the slope of the characteristics at point Q is 0.75, same as the QUICK scheme. Thus, the SMART scheme is third-order accurate.

COPLA

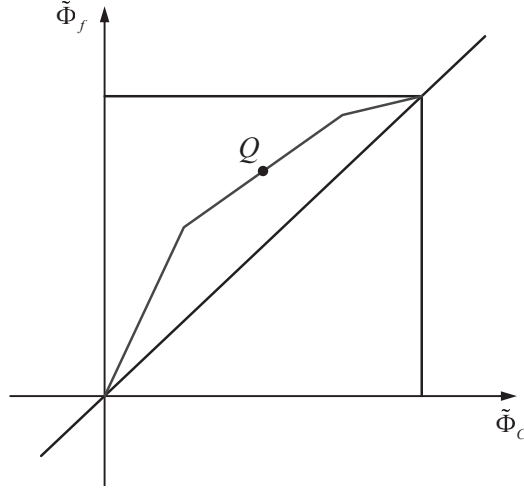


Figure 4.23: COPLA in the NVD frame.

Numerical experiments led by Zhu (1992) ascertained that the SMART scheme needed a relatively large amount of computer storage to overcome the oscillatory convergence behavior. Thus, Choi et al. (1995) modified the SMART scheme slightly without deteriorating the accuracy of the original scheme. Their proposed combination of piecewise linear approximations (COPLA) scheme is as follows:

$$\tilde{\Phi}_f = \begin{cases} 2.25\tilde{\Phi}_C & 0 \leq \tilde{\Phi}_C \leq \frac{1}{4} \\ \frac{3}{8} + \frac{3}{8}\tilde{\Phi}_C & \frac{1}{4} \leq \tilde{\Phi}_C \leq \frac{3}{4} \\ \frac{3}{4} + \frac{1}{4}\tilde{\Phi}_C & \frac{3}{4} \leq \tilde{\Phi}_C \leq 1 \\ \tilde{\Phi}_C & \text{otherwise.} \end{cases} \quad (4.28)$$

Fig. 4.23 shows that the piecewise lines of COPLA pass through point Q with a slope of 0.75, which is consistent with the previous statement that its order of accuracy remains the same as that of SMART.

The four schemes described above represent a kind of convection scheme, which is clearly computed bounded and highly accurate. To distinguish them from other higher-order schemes (QUICK, Third-order Upwind), this kind of convection scheme is named as high-resolution schemes.

Application in the present model

In Chapter 2, the development of the preliminary numerical model was described in detail. The convective terms of the Navier-Stokes equations are discretized by the first-order upwind scheme on a staggered variable arrangement, applying the velocity value at the cell faces directly. As stated earlier, the NVD concept is built based on the use of the control volume. Thus, to apply the aforementioned high-resolution convection schemes, a new variable Φ is introduced as a velocity component into the preliminary numerical model.

Taking term $u \frac{\partial u}{\partial x}$ as an example, the discretization for $u(i-1/2, j)$ can be rewritten as,

$$u \frac{\partial u}{\partial x} = \frac{1}{\Delta x} (\Phi(i, j)u(i, j) - \Phi(i-1, j)u(i-1, j)), \quad (4.29)$$

where $u(i, j)$ and $u(i-1, j)$ are obtained by the interpolation using the calculated velocity components at the cell faces, i.e.:

$$u(i, j) = \frac{1}{2}(u(i-1/2, j) + u(i+1/2, j)) \quad (4.30)$$

$$u(i-1, j) = \frac{1}{2}(u(i-3/2, j) + u(i-1/2, j)). \quad (4.31)$$

Applying variable normalization, if $u(i-1/2, j) > 0$, we have,

$$\left\{ \begin{array}{l} \Phi_U = u(i-3/2, j), \\ \Phi_C = u(i-1/2, j), \\ \Phi_D = u(i+1/2, j), \\ \tilde{\Phi}_C = \frac{u(i-1/2, j) - u(i-3/2, j)}{u(i+1/2, j) - u(i-3/2, j)}. \end{array} \right. \quad (4.32)$$

Going back to the un-normalized variables, the value of $\Phi(i, j)$ in the newly introduced CV can be approximated by the four selected high-accuracy bounded schemes in our numerical model as follows:

MINMOD

$$\Phi(i, j) = \Phi_f = \left\{ \begin{array}{ll} 1.5u(i-1/2, j) - 0.5u(i-3/2, j) & 0 \leq \tilde{\Phi}_C \leq \frac{1}{2} \\ 0.5u(i+1/2, j) + 0.5u(i-1/2, j) & \frac{1}{2} \leq \tilde{\Phi}_C \leq 1 \\ u(i-1/2, j) & \text{otherwise.} \end{array} \right. \quad (4.33)$$

MUSCL

$$\Phi(i, j) = \Phi_f = \begin{cases} 2.0u(i - 1/2, j) - u(i - 3/2, j) & 0 \leq \tilde{\Phi}_C \leq \frac{1}{4} \\ 0.25u(i + 1/2, j) + u(i - 1/2, j) - 0.25u(i - 3/2, j) & \frac{1}{4} \leq \tilde{\Phi}_C \leq \frac{3}{4} \\ u(i + 1/2, j) & \frac{3}{4} \leq \tilde{\Phi}_C \leq 1 \\ u(i - 1/2, j) & \text{otherwise.} \end{cases} \quad (4.34)$$

SMART

$$\Phi(i, j) = \Phi_f = \begin{cases} 3.0u(i - 1/2, j) - 2.0u(i - 3/2, j) & 0 \leq \tilde{\Phi}_C \leq \frac{1}{6} \\ 0.375u(i + 1/2, j) + 0.75u(i - 1/2, j) - 0.125u(i - 3/2, j) & \frac{1}{6} \leq \tilde{\Phi}_C \leq \frac{5}{6} \\ u(i + 1/2, j) & \frac{5}{6} \leq \tilde{\Phi}_C \leq 1 \\ u(i - 1/2, j) & \text{otherwise.} \end{cases} \quad (4.35)$$

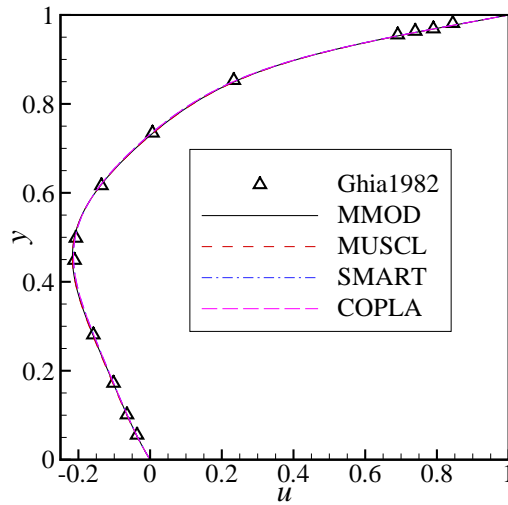
COPLA

$$\Phi(i, j) = \Phi_f = \begin{cases} 2.25u(i - 1/2, j) - 1.25u(i - 3/2, j) & 0 \leq \tilde{\Phi}_C \leq \frac{1}{4} \\ 0.375u(i + 1/2, j) + 0.75u(i - 1/2, j) - 0.125u(i - 3/2, j) & \frac{1}{4} \leq \tilde{\Phi}_C \leq \frac{3}{4} \\ 0.25u(i - 1/2, j) + 0.75u(i + 1/2, j) & \frac{3}{4} \leq \tilde{\Phi}_C \leq 1 \\ u(i - 1/2, j) & \text{otherwise.} \end{cases} \quad (4.36)$$

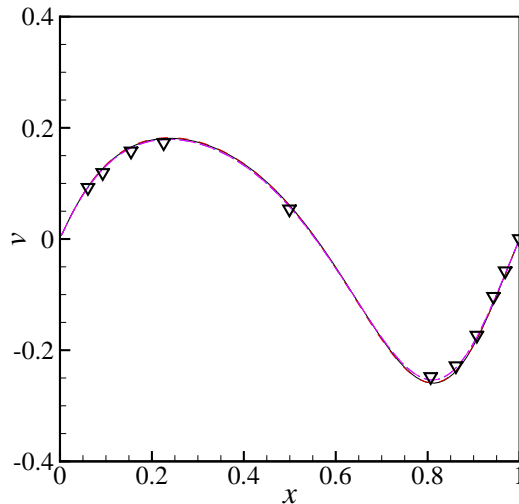
4.4.2 Validation: lid-driven flow

Prior to applying the newly incorporated high-resolution convection schemes to solve the free surface flows, the validation of the fluid solver is conducted first. Here, the well-known test case, the lid-driven cavity problem, is again considered. The detailed setup of this case can be found in Section 2.3.2. In this section, only $Re = 100$ and $Re = 1000$ are considered. After the grid convergence test, the mesh size of 160×160 is applied.

Fig. 4.24 shows the numerical results for the $Re = 100$ case given by the four schemes. The velocities in the x - and y -directions are plotted along the vertical



(a) u along the vertical centerline

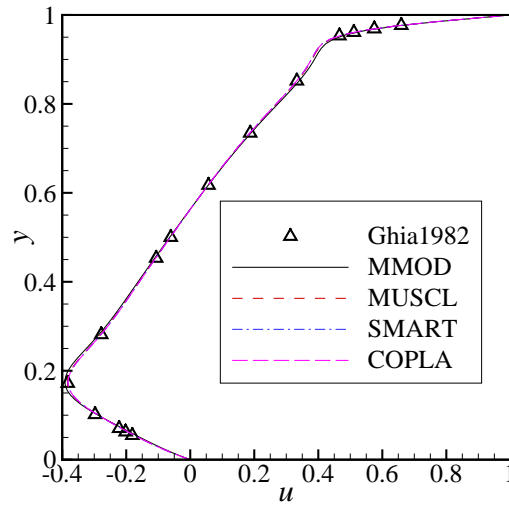


(b) v along the horizontal centerline

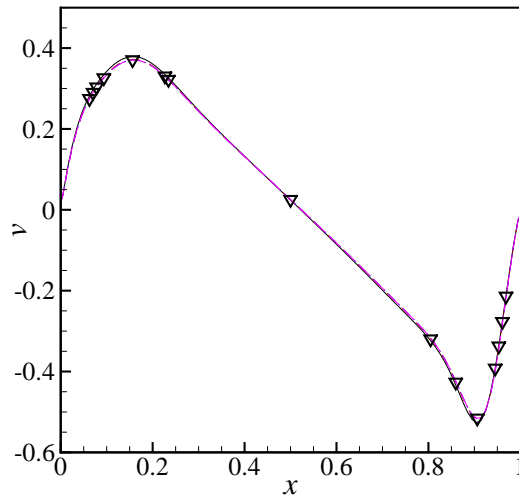
Figure 4.24: Comparison between solutions given by the high-resolution convection schemes and the benchmark solution for $Re = 100$.

and horizontal centerlines. To validate the newly added convection schemes, the benchmark solution of Ghia et al. (1982) is also given, for comparison with the present results. It can be seen that the four schemes predict almost identical results for both directions and agree well with the benchmark solutions.

Further comparison is made for the $Re = 1000$ case, as shown in Fig. 4.25. Clearly, for a higher Reynolds number, at the steady state, the velocity gradients along the centerline become larger. In this case, identical results are also obtained by the four schemes with a slight discrepancy between the result of MINMOD and those of the



(a) u along the vertical centerline



(b) v along the horizontal centerline

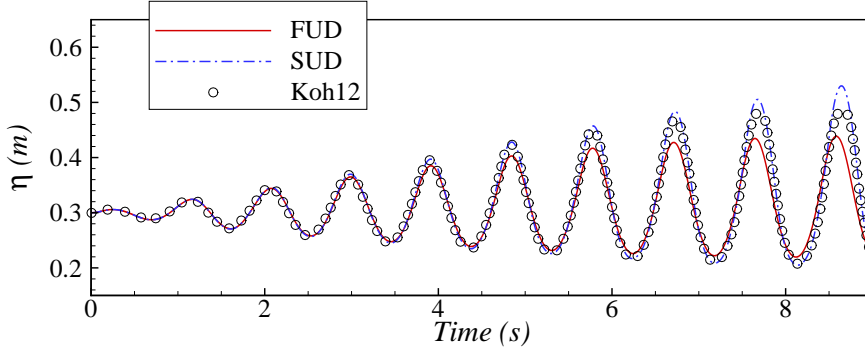
Figure 4.25: Comparison between solutions given by the high-resolution convection schemes and the benchmark solution for $Re = 1000$.

other three schemes. Overall, the four convection schemes achieve accurate results against the benchmark solution. Thus, we can move on to combine the new fluid solver with the Level-Set technique to solve the free surface flows.

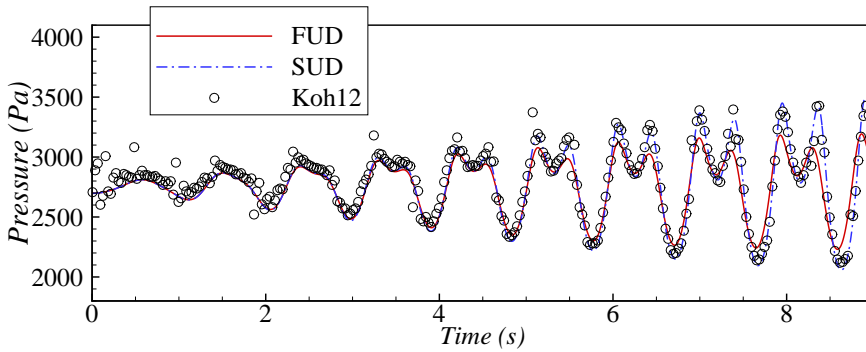
4.4.3 Sloshing under surge motions

Again, the experiment conducted by Koh et al. (2012) to investigate liquid sloshing in a two-dimensional rectangular tank is reproduced numerically. The description of

the experiment setup can be found in Section 3.2.1.



(a) Time histories of free surface displacement at point $H1$

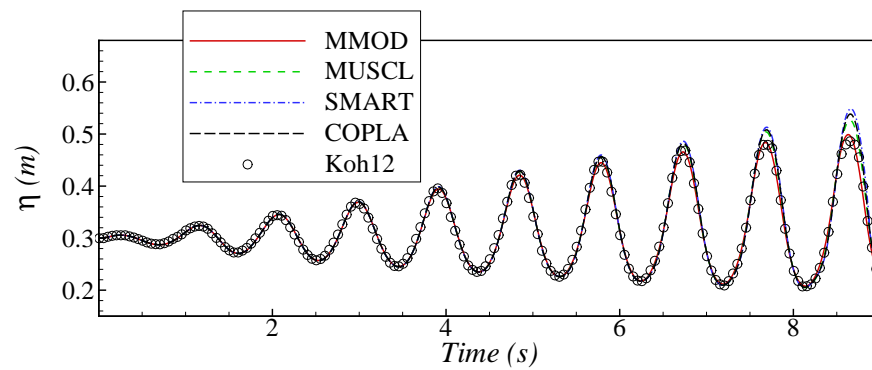


(b) Time histories of pressure at point $P1$

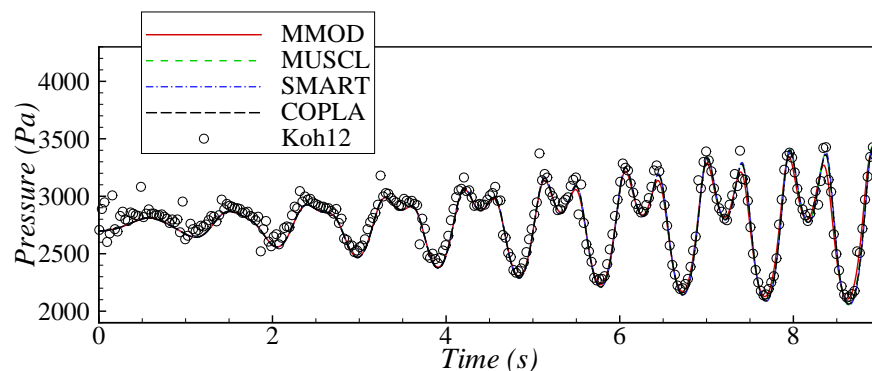
Figure 4.26: Comparison between numerical results based on classical upwind schemes and Koh's experimental data.

The mesh size of 120×120 and a time interval of 0.001 s are applied first to test the performance of all the schemes. The size of the smoothing band is set as $s = 2$. In Fig. 4.26, the wave elevation and pressure obtained by the classical upwind schemes are compared with the experimental data. Achieving higher wave elevation and pressure results indicates that the second-order upwind scheme does alleviate the numerical dissipation. In addition, from 6 s to 8 s for the surface displacement, the second-order upwind scheme can also predict a closer trough to the experimental measurements than the first-order upwind scheme. This indicates that a higher-order convection scheme does improve on the accuracy of the current numerical model. However, Fig. 4.26 also shows that the second-order upwind scheme over-predicts results from 7 s to 9 s. This means that it is necessary for us to consider high-resolution convection schemes in stead of the classical upwind schemes in our final model.

The application of high-resolution convection schemes produces promising results, as shown in Fig. 4.27. All the pressure predictions given by high-order schemes are quite identical to each other, as well as being close to the experimental recordings. In the time history of the surface displacement, a discrepancy can be observed but it is not apparent. In order to better investigate the effects of different convection schemes, an error study is conducted by comparing the numerical results with the experimental data from Koh et al. (2012).



(a) Time histories of free surface displacement at point $H1$



(b) Time histories of pressure at point $P1$

Figure 4.27: Comparison between numerical results based on high-resolution convection schemes and Koh's experimental data.

As shown in the previous figures, pressure discrepancies are less evident than those shown in the surface displacement results. Thus, this error study is based on comparison of the surface displacement value at specified time steps. In order to quantify the discrepancy in surface displacement history, the following standard deviation is defined:

$$\sigma = \sqrt{\frac{1}{N} \left[\sum_{i=1}^N \left(\frac{\eta_i - \eta_{0i}}{\eta_{0i}} \right)^2 \right]}, \quad (4.37)$$

where N is the total number of data from the experimental measurements of Koh et al. (2012), η_i is the i th surface displacement given by the numerical model at a certain time instant, and η_{0i} is the corresponding experimental result. In the experiment conducted by Koh et al. (2012), the wave elevation (surface displacement) data captured by the wave gauge are outputted every 0.005 s. The whole experiment runs up to 9 seconds. For our comparison, we selected the data at corresponding time steps by using a 0.005 filter, since we applied the 0.001 s time interval in our simulations.

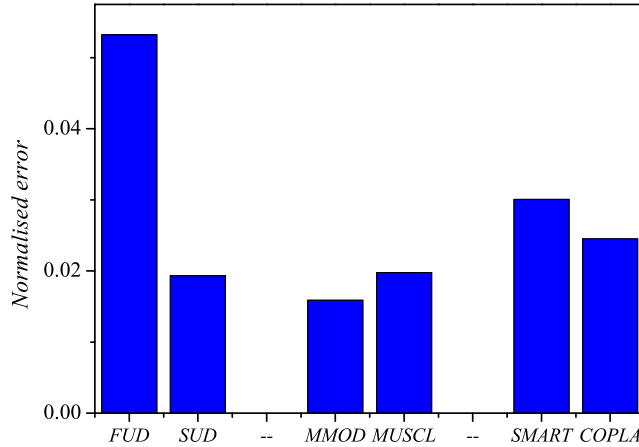


Figure 4.28: Results of the error study for the selected convection schemes.

As shown in Fig. 4.28, the six convection schemes are categorized into three groups: classical upwind schemes, second-order high-resolution schemes, third-order high-resolution schemes. The results given by the first-order upwind scheme deviate most from the experimental measurements. This is consistent with the observation we get from the time history of the surface displacement. In addition, all the discrepancies between the experimental data and the results obtained by the higher-order convection schemes are below 3%. This again indicates that the preliminary model using higher-order schemes to handle the convective terms will have the capability to simulate free surface flows accurately.

Furthermore, with the mesh size of 120×120 and the smoothing band $s = 2$, results predicted by the present numerical model using the convection schemes with a second-order accuracy have relatively smaller deviations: they are all below 2%. However, when the convection schemes with a third-order accuracy are employed with the same mesh and the same sized smoothing band, smaller deviations than those given by the second-order schemes are not obtained as expected. This is also captured in Fig. 4.27, especially in the surface displacement result which shows that the third-order schemes over-predict the surface displacement as time elapses. From 6 s to 9 s, the over-estimation becomes increasingly apparent. However, the two solutions given by the third-order schemes lie quite close to each other, suggesting they are convergent to a certain value. Considering the findings from the previous parametric study on the effects of the smoothing band, we can say that, with the size of the smoothing band chosen to be $s = 2$, the selected convection schemes with the second-order accuracy obtain optimal numerical results when compared with the experimental data. Based on the fact that the first-order upwind scheme obtains optimal results with $s = 4$, while the second-order schemes require the smaller size $s = 2$, we conduct a further investigation to see if a smaller smoothing size could also achieve satisfactory results with third-order convection schemes.

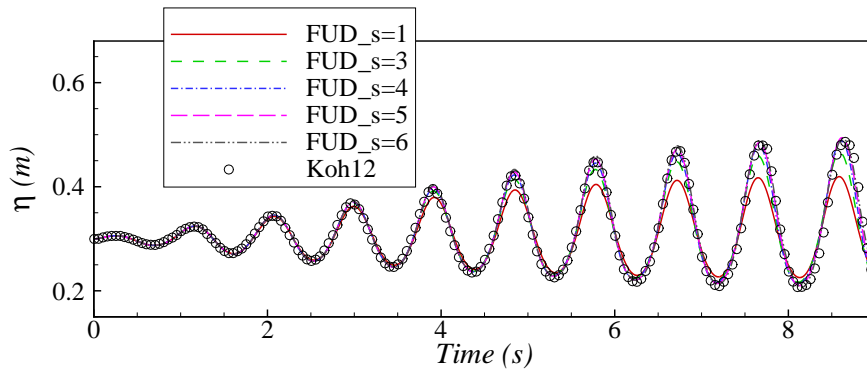


Figure 4.29: Time histories of surface displacement predicted by first-order upwind scheme with different s values.

To validate our idea, we choose the second-order MINMOD scheme and the third-order COPLA scheme, both of which achieve the better results with smaller deviations in their own category; see Fig. 4.28. The first-order upwind scheme is also applied for a comprehensive comparison. We still adopt the mesh size of 120×120 and the time interval of 0.001s in this investigation. Thus, according to the 10% limitation, we test the size of the smoothing band from $s = 1$ to $s = 6$ with interval $\Delta s = 1$. Just like the

error study, the investigation is based on the comparison of the surface displacement. First, Fig. 4.29 shows the results obtained by the first-order upwind scheme with different s values. Similar to the tendency we observe in the previous investigation on the smoothing band, by increasing the size of the smoothing band, more accurate numerical results that are closer to the experimental data can be obtained. From $s = 1$ to $s = 4$, evident improvement is captured. From $s = 4$ to $s = 6$, the obtained surface displacement results lie close to each other, suggesting that a convergence is nearly achieved. This also corresponds to the phenomena we observe with the intermediate model.

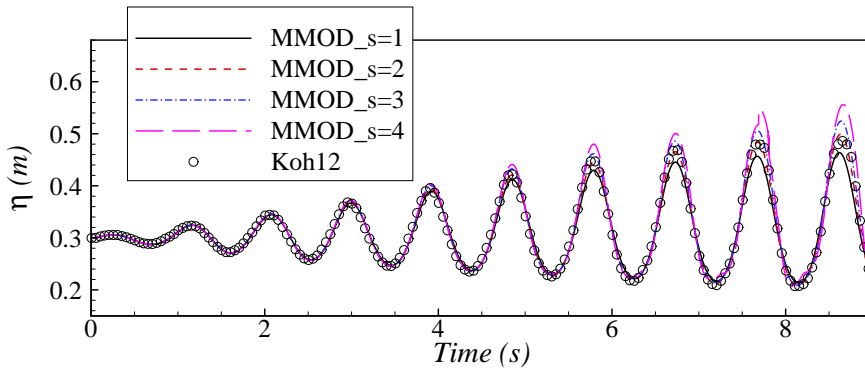


Figure 4.30: Time histories of surface displacements predicted by MINMOD with different s values.

Figs. 4.30 and 4.31 show the solutions obtained by the MINMOD and COPLA schemes respectively. Apparently, even with smaller s values, both high-resolution schemes still predict the surface displacement accurately. Note that in Fig. 4.30, the maximum size of the smoothing band applied in this case is only $s = 4$. Around $t = 7.6$ s, the long dash line, which is the surface displacement result given by $s = 4$, forms an abnormal wave peak. As well as this, the predicted data has clearly deviated from the experimental recordings. A possible explanation for both scenarios is that the numerical model with the second-order MINMOD scheme starts to simulate a different case here when the smoothing band $s = 4$ or larger is applied. Therefore, we end this case by not increasing the s value further. Similar scenarios can be observed in Fig. 4.31 which shows the simulation results obtained by COPLA. This supports our explanations. More importantly, an abnormal wave peak is captured around $t = 7.6$ s by the third-order COPLA scheme with the size of the smoothing band being only $s = 3$. This suggests that the higher-order scheme may require a smaller smoothing zone to simulate real situations. With a higher-order and stable

convection scheme, the numerical model can solve the free surface flow accurately by using a smaller smoothing band. To further show the effects of the size of the smoothing band with various convection schemes, following the same method as the previous error study, an investigation is performed.

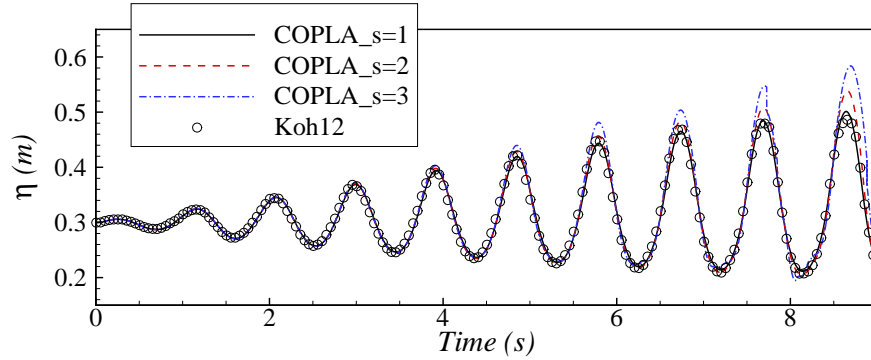


Figure 4.31: Time histories of surface displacements predicted by COPLA with different s values.

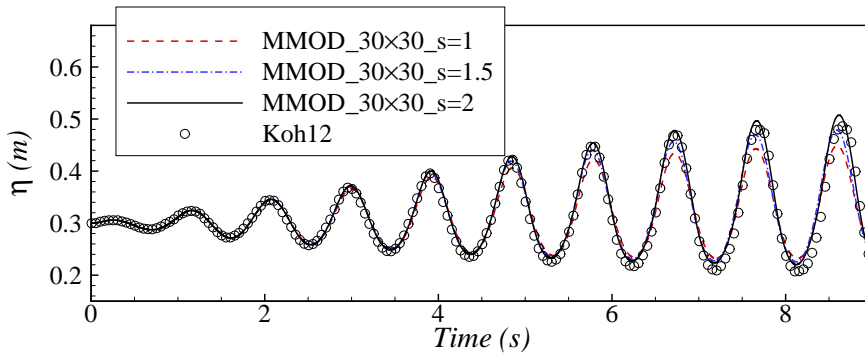
In Table 4.1, We can see that the results given by the error study are in agreement with our observations. In addition, we note that the convergent predictions are achieved around $s = 2$ to $s = 3$ for MINMOD, and $s = 1$ to $s = 2$ for COPLA respectively.

Table 4.1: Results of the error study for the three convection schemes with different s values.

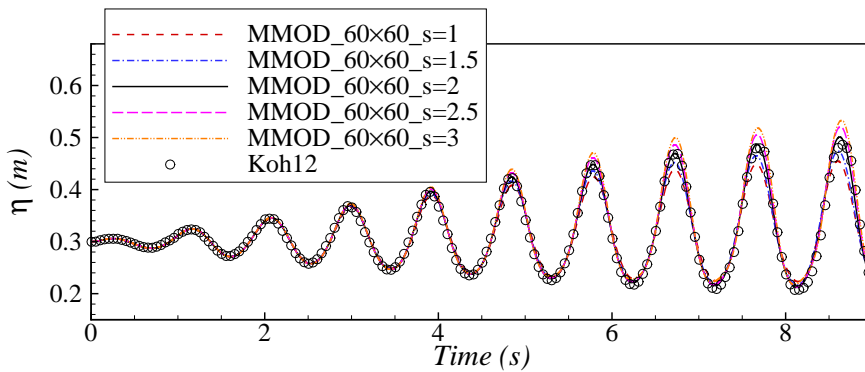
	FUD	MINMOD	COPLA
$s = 1$	6.28%	3.19%	2.08%
$s = 2$	5.32%	1.59%	2.45%
$s = 3$	4.14%	2.03%	6.06%
$s = 4$	3.06%	4.29%	
$s = 5$	2.34%		
$s = 6$	2.21%		

To find out more about the effect of the smoothing band combined with the convection schemes, a further investigation is conducted by applying three different mesh sizes with corresponding s values. Besides 120×120 , the meshes 60×60 and 30×30 are applied. Based on the 10% limitation, the maximum s value should be $s = 3$ and $s = 1.5$ respectively. To find the optimal size of the smoothing band, $s = 2$, which is found to be best for the MINMOD scheme, is applied as the maximum value

for 30×30 . A smaller interval $\Delta s = 0.5$ is applied to see if there is an intermediate optimal value between $s = 2$ and $s = 3$ for MINMOD, and between $s = 1$ and $s = 2$ for COPLA scheme. Just like the previous study, the time history of the surface displacement is compared first, as shown in Fig. 4.32 and 4.33. Even with coarse meshes, we can see that satisfactory results are achieved with a smaller smoothing band for both convection schemes. The displacement predictions lie close to each other in each case for various s values.



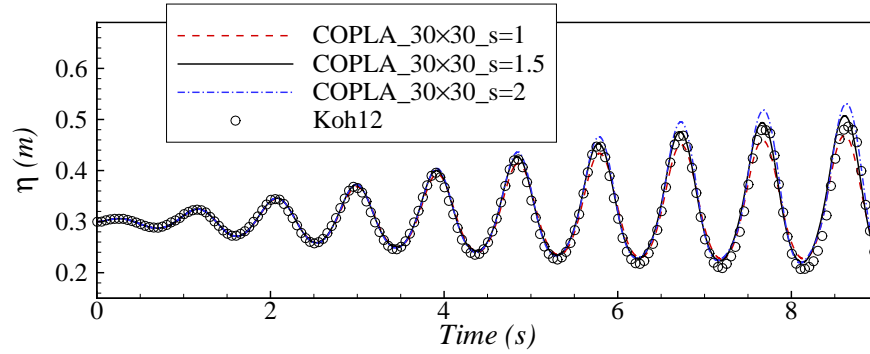
(a) MINMOD with 30×30



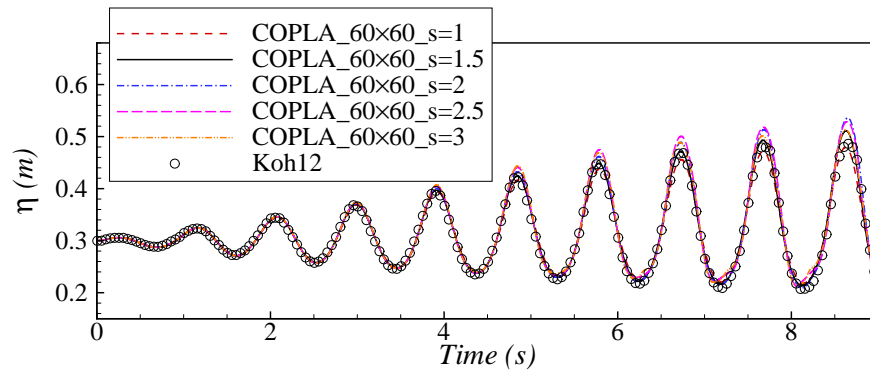
(b) MINMOD with 60×60

Figure 4.32: Comparison of time histories of surface displacement between different s values with two different mesh sizes based on MINMOD.

A further error study is still required to find the optimal s value. Following the previous method, Table 4.2 provides the results by comparing the numerical solutions with experimental measurements. It reveals that for the second-order MINMOD scheme, the optimal value is $s = 2$. For the third-order COPLA scheme, $s = 1.5$ can produce the closest predictions to the experimental recordings. In addition, this s value is the best for each scheme in all cases, no matter what mesh size is applied. Thus, we can say that, with a higher-order convection scheme applied in



(a) COPLA with 30×30



(b) COPLA with 60×60

Figure 4.33: Comparison of time histories of surface displacement between different s values with two different mesh sizes based on COPLA.

our intermediate numerical model, the free surface flow problems could be solved accurately even with quite a small smoothing band. Additionally, as the order of accuracy for a convection scheme increases, the optimal size of the smoothing band becomes smaller.

Table 4.2: Results of the error study for MINMOD and COPLA with different mesh sizes.

	MINMOD			COPLA		
	30×30	60×60	120×120	30×30	60×60	120×120
$s = 1.0$	5.59%	4.37%	3.19%	4.33%	2.97%	2.08%
$s = 1.5$	5.03%	3.39%	2.43%	3.94%	2.10%	1.65%
$s = 2.0$	3.85%	2.17%	1.59%	4.05%	2.42%	2.45%
$s = 2.5$		2.47%	1.60%		3.49%	3.87%
$s = 3.0$		3.30%	2.03%		3.42%	6.06%

4.4.4 Wave generation in a wave tank

To further validate the final numerical model of the present study, the experimental study performed by Gao (2003) to investigate wave generation and propagation in a tank is simulated. In this test, regular waves are generated in a 8.75 m long wave tank with a still water depth of 0.28 m. Free surface elevations at three different stations $x = 0.55$ m, $x = 3.55$ m and $x = 5.45$ m in the wave tank are recorded by the wave gauge. The wave paddle is set at the left side of the wave tank and its motion is governed by a sinusoidal displacement. In our co-moving system, to attain the same conditions, we set the velocity of the left wall to be the same as the velocity of the wave paddle measured in the experiment, as shown in Fig. 4.34. To begin with, the preliminary model with the first-order upwind scheme and $s = 2$ is employed to perform the mesh size convergence test.

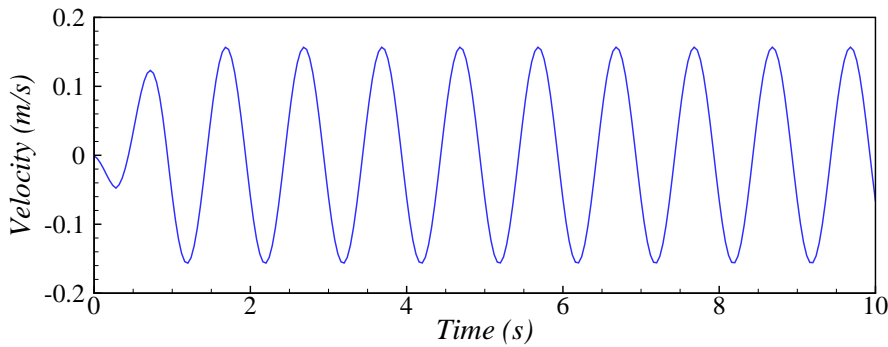
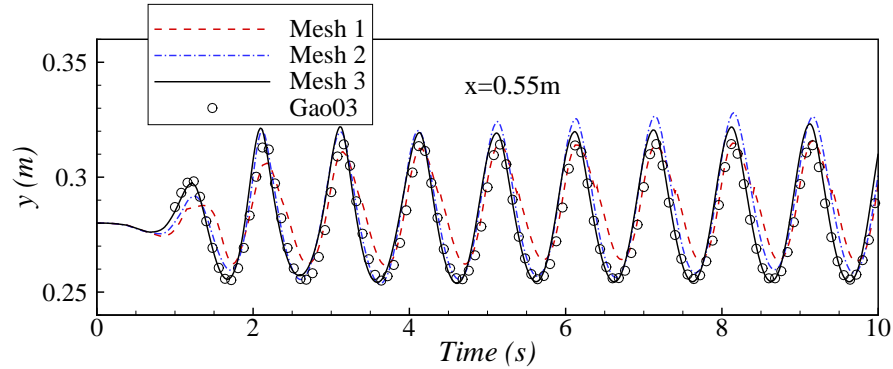


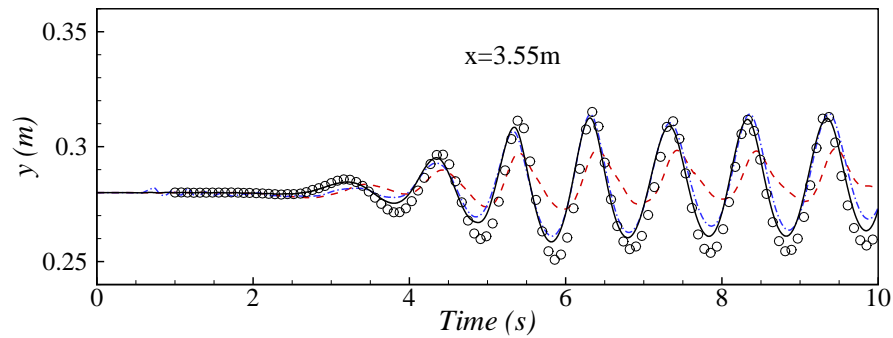
Figure 4.34: Time history of the velocity of the wave paddle recorded in Gao's experiment.

Three mesh sizes with cells numbers 200×10 , 400×20 and 800×40 are tested respectively with a time interval of 0.001 s. In Fig. 4.35, time histories of the free surface elevations at the three stations obtained by the three mesh sizes are compared with the corresponding experimental results. We can see that with the finer mesh applied, the numerical results gradually approach the experimental data. This trend is apparent in the predictions at $x = 0.55$ m, especially in the first 2 seconds when the first wave peak is formed. As the distance from the wave paddle increases, larger differences between the coarse mesh and the two finer meshes appear in the results. This discrepancy is mainly due to the accumulation of numerical errors caused by the coarse mesh. Conversely, solutions given by Mesh 2 (400×20) and Mesh 3 (800×40) lie close to each other at all three stations, suggesting that a grid-convergent solution

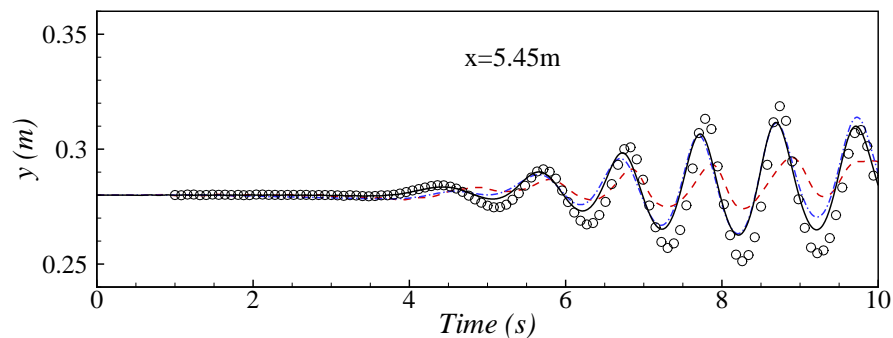
is achieved. Therefore, Mesh 3 is adopted to perform the following simulations in this test.



(a) $x = 0.55$ m



(b) $x = 3.55$ m



(c) $x = 5.45$ m

Figure 4.35: Comparison of time histories of wave elevation between numerical results with different mesh sizes and Gao’s experimental data.

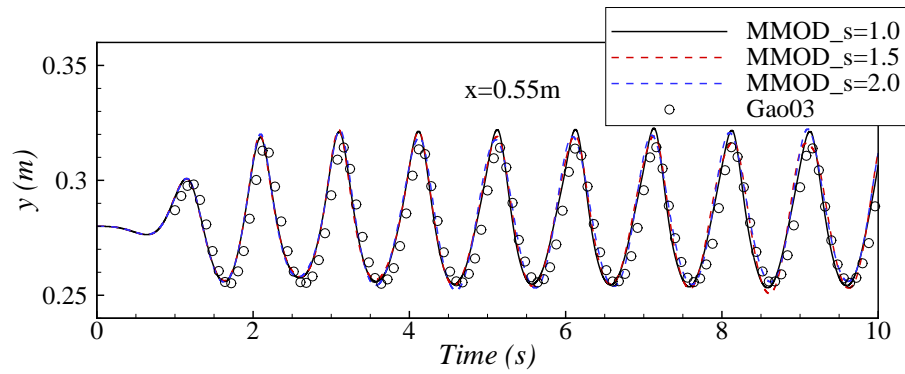
Take a further look at the solid lines in Fig. 4.35. At $x = 0.55$ m, except for some over-estimations of the wave peak value, fair agreement is achieved between the preliminary numerical model and the experimental recordings. At $x = 3.55$ m, the

over-estimations of the wave peak are barely observed. So far, the preliminary numerical model is still capable of repeating the wave generation case accurately. However, the time series of the wave elevations at $x = 5.45$ m predicated by the preliminary model suffers apparent discrepancies from the experimental measurements around at 8 to 9 s, when forming two wave peaks. This indicates that the preliminary model, which uses the first-order upwind scheme and the smoothing band $s = 2$, is not accurate enough to solve this wave generation problem.

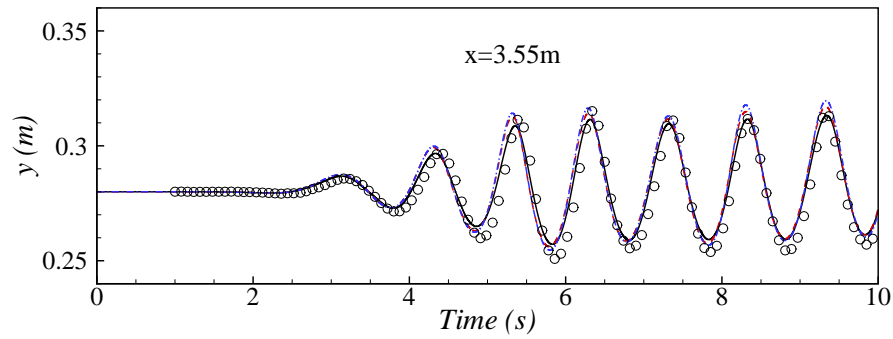
As discussed in the previous section, the intermediate model, which applies the first-order upwind scheme and a larger smoothing band than $s = 2$, may achieve a satisfactory result. However, since we adopted mesh 800×40 to perform these simulations, the maximum size of the smoothing band should be limited to $s = 2$. As shown in the earlier mesh size tests, the numerical model using the first-order upwind scheme with $s = 2$ is not able to accurately repeat the wave generation and propagation experiments. Therefore, in the following simulations we are going to apply the final model based on high-resolution convection schemes directly.

The second-order MINMOD scheme and the third-order COPLA scheme are applied to calculate the convective terms in the Navier-Stokes equations respectively. The size of the smoothing band varies from $s = 1.0$ to $s = 2.0$ with an interval $\Delta s = 0.5$.

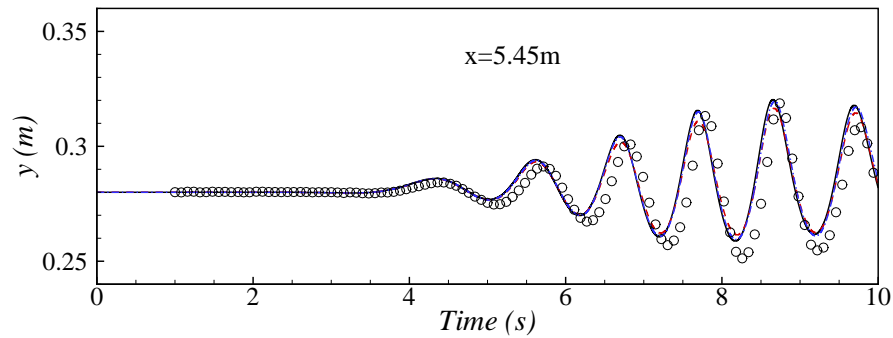
In Fig. 4.36, the time histories of the wave elevations obtained by the final model with MINMOD and various s values are compared with the experimental results. We can see that all three results predicted with different s values lie quite close to each other at $x = 0.55$ m. But it should also be noted that for the two wave peaks around 8 to 9 seconds, $s = 1.5$ predicts the closet result to the experiment. For the two further stations, an obvious phase shift can be observed. The reason for this discrepancy might be that in the numerical simulation, the wave is generated by inputting the velocity of the wave paddle at the inlet where a fixed wall is applied as the boundary condition. But in the experiment, the wave is generated by a moving paddle at the inlet, rather than a fixed wall. Thus, this may cause a very small phase difference at the beginning, and this shift is amplified as the distance increased from the inlet boundary. This also explains why the shift is not evident in the predictions obtained at $x = 0.55$ m. In addition, the dash line given by $s = 1.5$ at $x = 5.45$ m again agrees best with the experimental recordings while the other two results are almost identical. Thus, in this case, we can say that the optimal size of the smoothing band is $s = 1.5$ when the final model adopts the MINMOD scheme.



(a) $x = 0.55$ m



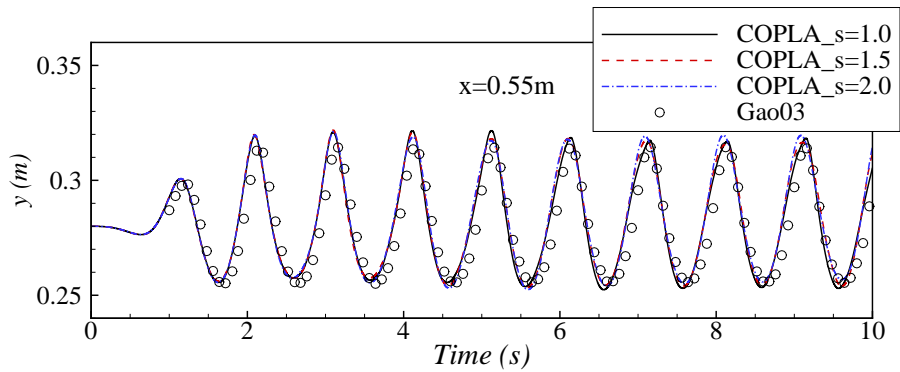
(b) $x = 3.55$ m



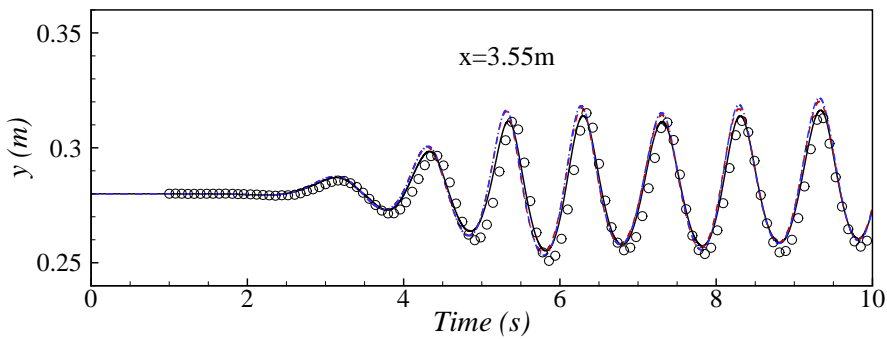
(c) $x = 5.45$ m

Figure 4.36: Comparison of time histories of wave elevation between MINMOD results with different s values and Gao's experimental data.

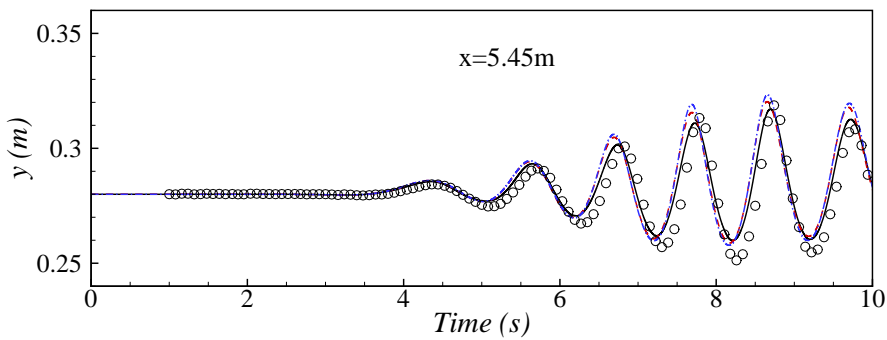
Fig. 4.37 shows the wave elevations predicted by the present numerical model with the third-order COPLA scheme at the three stations. At $x = 0.55$ m, all three results achieved by different s values lie quite close to each other and agree fairly well with the experimental measurements. However, at $x = 3.55$ m, discrepancies between the numerical predictions can be observed. It should be noted first that a



(a) $x = 0.55$ m



(b) $x = 3.55$ m



(c) $x = 5.45$ m

Figure 4.37: Comparison of time histories of wave elevation between COPLA results with different s values and Gao's experimental data.

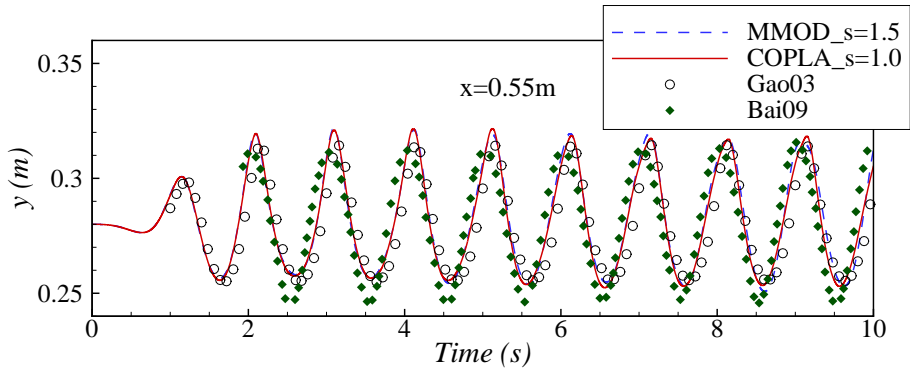
phase difference appears between the solid line ($s = 1.0$) and the other two lines. Another difference is that around 5 to 9 seconds, the wave peaks captured by the two larger smoothing bands are almost identical but clearly larger than the experimental recordings.

As the distance increases from the wave paddle, at $x = 5.45$ m, the discrepancies

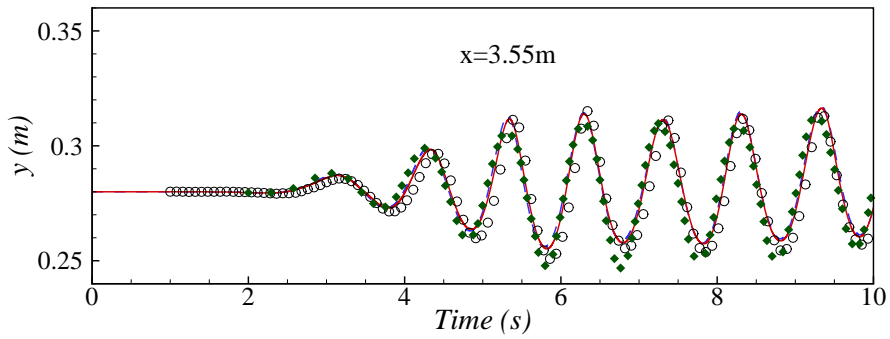
between the three numerical solutions by three s values become more apparent. It can be seen that larger smoothing bands result in larger deviations from the experimental recordings, especially when predicting the wave peaks around 9.7 s. Additionally, a phase discrepancy between numerical and experimental results is also captured. This should be caused by the same reason explained in the previous MINMOD test. Except for some local discrepancies and the phase shift, the numerical solution given by the final model, based on COPLA and the smoothing band $s = 1$, achieves good agreement with the experimental measurements.

To support our explanation of the phase difference between the experimental results and the numerical predictions, we further compare our numerical results with those predicted by a numerical model based on the finite volume approximation with the cut cell approach proposed by Bai et al. (2009). In this comparison, the two optimal combinations of MINMOD with $s = 1.5$ and COPLA with $s = 1.0$ are employed, as well as the experimental results by Gao (2003) as a reference. Fig. 4.38 shows the final comparison at the three stations. In general, all numerical results agree well with the experimental data. The only discrepancy is that, compared with Gao's experimental recordings, our numerical solution over-predicts the wave peaks, while Bai's solution over-predicts the wave troughs. But more importantly, the numerical solutions by the present final model and the model of Bai et al. (2009) have a similar phase difference from the experimental measurements. This phenomenon become more palpable at the two stations farther from the wave paddle. This supports our previous explanation.

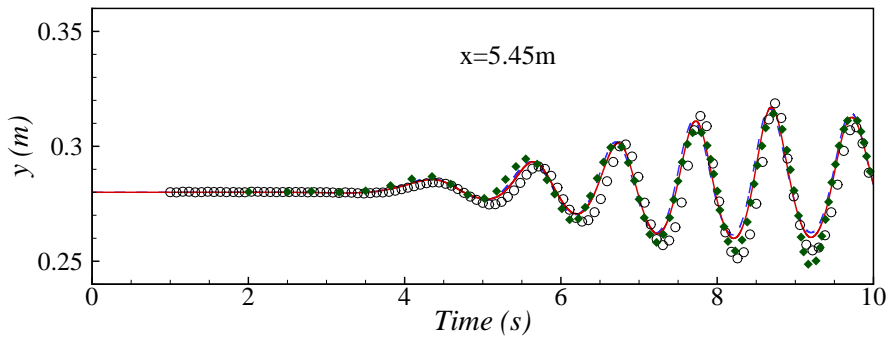
In addition, it should be pointed out that the optimal combinations (the second-order MINMOD scheme with $s = 1.5$ and the third-order COPLA scheme with $s = 1.0$) again validate our previous statements. With a higher-order convection scheme applied, a smaller smoothing band can be adopted to attain a satisfactory result. This is quite important because, for a wave generation case like this, with only 40 cells in the vertical direction, a smaller smoothing band is more reasonable. Moreover, the smoothing band is an artificial technique to achieve a stable numerical solution. A smaller smoothing zone more accurately reflects the real-world situations. Thus, for the present numerical model, the third-order COPLA scheme is adopted to solve the convective terms.



(a) $x = 0.55$ m



(b) $x = 3.55$ m



(c) $x = 5.45$ m

Figure 4.38: Comparison of time histories of wave elevation among the present numerical results, Bai's numerical solutions and Gao's experimental data.

4.5 Summary

In this chapter, an improved numerical model for the simulation of free surface flows was developed.

First, the numerical dissipation issue of the preliminary numerical model was reported. The preliminary model can produce acceptable results for modeling non-resonant sloshing flows. However, when dealing with the resonant sloshing case, the preliminary model under-predicts the wave elevations.

To improve performance of our numerical model, the intermediate model was developed based on the findings of the parametric study regarding the size of the smoothing band in Level-Set technique. It was found that with finer mesh sizes and a relatively larger smoothing band, even though the physical smoothing region is the same, the numerical prediction with the larger smoothing band matches the published experimental data better.

Finally, considering the dissipation nature of the first-order upwind scheme applied in the preliminary model, the final model was built by implementing high-resolution convection schemes to solve the Navier-Stokes equations. The bases for the development of high-resolution convection schemes, the Normalized Variable Diagram and the Convection Boundedness Criterion, were introduced. The expressions of the high-resolution convection schemes applied in the present model were also formulated. To validate the final model, the error study regarding convection schemes and smoothing band was performed. It was found that with a higher-order convection scheme applied, a smaller optimal smoothing band is required to achieve satisfactory results. This finding is of great importance: it indicates that the final numerical model with the implementation of high-resolution convection schemes utilizes the smallest artificial smoothing zone to achieve accurate solutions.

Chapter 5

NUMERICAL STUDY ON COUPLING OF SLOSHING AND SHIP MOTIONS

This chapter presents the numerical study on the coupling of sloshing and ship motions. First, we briefly introduce the numerical model developed by Bai and Eatock Taylor (2006), which solves the ship motions in waves based on nonlinear potential flow theory. Then the methodology of coupling the numerical models for ship motions and sloshing motions is developed. After that, a preliminary validation of the COUPLED numerical model is performed by reproducing a benchmark experiment conducted by Rognebakke and Faltinsen (2003). Finally, a parametric study with regard to wave amplitude, frequency and the filling level in the water tank is conducted.

5.1 Numerical modeling of ship motions in waves

To model nonlinear ship motions, nonlinear potential flow theory is applied. The problem is formulated as an initial boundary value problem and solved by the boundary element method in the time domain. It should be pointed out that at this stage, the barge is considered as the LNG carrier in this study in order to simplify the numerical modeling.

5.1.1 Mathematical formulation

5.1.1.1 Model description

Following the work of Feng and Bai (2015), the circular numerical wave tank (NWT) is used to investigate the ship motion in waves. Fig. 5.1 shows the top view of the NWT model. As well as the circular tank, the barge is also illustrated with the free water surface and a damping zone on the free surface near the tank side wall. The origin of the three-dimensional coordinate system $Oxyz$ is placed at the center of the barge (also the center of the circular wave tank) on the plain water surface. The z -axis points vertically upward. β is the direction of the incident wave which is defined from the positive x -axis. The length of the damping zone is set equal to one wavelength. It should be noted that all the following simulations are under head sea conditions, since the liquid sloshing is simulated inside a two-dimensional tank.

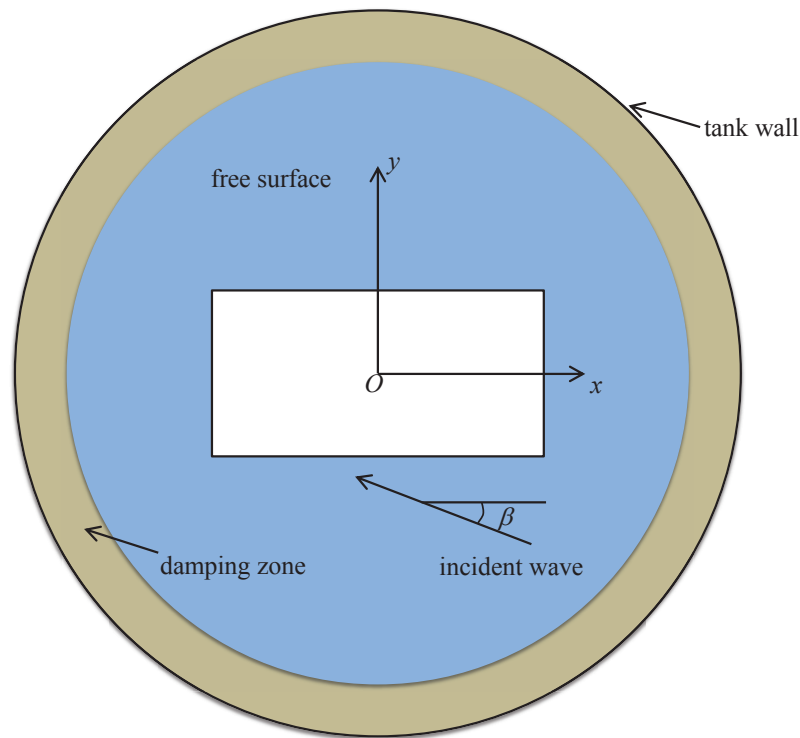


Figure 5.1: A schematic view of the circular numerical wave tank.

5.1.1.2 Governing equations and boundary conditions

Assumptions are made that the fluid is incompressible and inviscid, and the flow is irrotational. Based on potential flow theory, ship motions in waves can be formulated

in terms of a velocity potential $\phi(x, y, z, t)$. Then in the fluid domain, the velocity can be described by the gradient of this potential function as,

$$u = \nabla\phi = \frac{\partial\phi}{\partial x}\vec{i} + \frac{\partial\phi}{\partial y}\vec{j} + \frac{\partial\phi}{\partial z}\vec{k}. \quad (5.1)$$

According to the continuity equation, the velocity potential ϕ satisfies Laplace's equation in the fluid domain Ω ,

$$\nabla^2\phi = 0, \quad (5.2)$$

and is also subject to other boundary conditions on all surfaces S in the whole domain.

Boundary condition on the free surface

In order to update the free surface location and the associated velocity potential on the free surface, the kinematic and dynamic conditions on the free water surface S_F need to be satisfied. In the Lagrangian description, they can be written as,

$$\frac{D\mathbf{X}}{Dt} = \nabla\phi \quad (5.3)$$

$$\frac{D\phi}{Dt} = -gz + \frac{1}{2}\nabla\phi \cdot \nabla\phi \quad (5.4)$$

where D/Dt is the usual total derivative, \mathbf{X} is the position of points on the free surface, and g is the gravitational acceleration. In Eq. (5.4), the atmospheric pressure on the free surface is set equal to zero.

As can be seen, the free surface boundary conditions are nonlinear in nature. The exact application of these nonlinear boundary conditions result in a nonlinear problem which is impossible to solve analytically. Hence, difficulties arise when incorporating the nonlinear effect of these boundary conditions into the solution procedure; special techniques need to be applied to solve these difficulties. There are a few such special methods available to deal with above mentioned problems. Among these methods, the Mixed Eulerian-Lagrangian (MEL) time stepping approach is found to be widely accepted and thus is applied in this numerical model.

Boundary condition on solid surface

Generally, the boundary condition on the solid faces (the floating barge, the tank wall, the sea bed) can be expressed as,

$$\frac{\partial \phi}{\partial \mathbf{n}} = \mathbf{V}_{\mathbf{n}}, \quad (5.5)$$

where \mathbf{n} is the outward unit normal vector from the solid to the fluid surface and $\mathbf{V}_{\mathbf{n}}$ is the normal velocity of the body surface. Assuming the rotational motions of the rigid body (the floating barge) are not significant, the motions of the body about its center of mass $\mathbf{X}_{\mathbf{g}} = (x_g, y_g, z_g)$ can be written in terms of six components. Thus, the following expression can be obtained:

$$\mathbf{V}_{\mathbf{n}} = (\dot{\boldsymbol{\xi}} - \dot{\boldsymbol{\alpha}} \times (\mathbf{X} - \mathbf{X}_{\mathbf{g}})) \cdot \mathbf{n}, \quad (5.6)$$

where $\boldsymbol{\xi} = (\xi_1, \xi_2, \xi_3)$ is the vector representing the displacements of surge, sway and heave motions and $\boldsymbol{\alpha} = (\alpha_1, \alpha_2, \alpha_3)$ is the rotational vector denoting the angles of roll, pitch and yaw about the center of mass $\mathbf{X}_{\mathbf{g}}$ in an anticlockwise direction.

To be more specific, the boundary conditions for the fixed rigid body (the tank wall and the seabed) can be simplified from Eq. (5.6) to the impermeability condition,

$$\frac{\partial \phi}{\partial \mathbf{n}} = 0. \quad (5.7)$$

Initial condition

Since the model is simulated in the time domain, an initial condition must be imposed for the time step marching. The simulation usually starts from calm water conditions, thus the velocity potential and wave elevation are set as,

$$\phi = 0, \quad z = 0 \quad \text{when} \quad t \leq 0. \quad (5.8)$$

5.1.1.3 Higher-order boundary element method

Because the boundary element method can reduce the dimensions of the boundary value problem (BVP) to be solved by one, it is widely used to solve the BVP and perform the numerical simulation of the nonlinear waves.

In this method, to formulate the BVP, a Rankine source is adopted as the Green's function G . Then a boundary integral equation for the potential ϕ over the whole

boundary S can be derived. Applying Green's second identity, the original potential flow problem can be expressed by,

$$C(\mathbf{x}_0)\phi(\mathbf{x}_0) = \iint_S \left[G(\mathbf{x}, \mathbf{x}_0) \frac{\partial \phi(\mathbf{x})}{\partial \mathbf{n}} - \phi(\mathbf{x}) \frac{\partial G(\mathbf{x}, \mathbf{x}_0)}{\partial \mathbf{n}} \right] ds, \quad (5.9)$$

where $C(\mathbf{x}_0)$ denotes the solid angle at the field point \mathbf{x}_0 and \mathbf{n} is measured from the source point \mathbf{x} . As mentioned above, only head sea conditions are considered in this study, thus the simulations are symmetric about the $x - z$ plane. Assuming the seabed in all the simulations is horizontal, the simple Rankine source and its image with respect to the symmetry plane and the horizontal seabed can be chosen as the Green's function. In this way, the Green's function can be expressed as

$$G(\mathbf{x}, \mathbf{x}_0) = \frac{1}{4\pi} \left(\frac{1}{R_1} + \frac{1}{R_2} + \frac{1}{R_3} + \frac{1}{R_4} \right), \quad (5.10)$$

where

$$\begin{aligned} R_1 &= \sqrt{(x - x_0)^2 + (y - y_0)^2 + (z - z_0)^2} \\ R_2 &= \sqrt{(x - x_0)^2 + (y + y_0)^2 + (z - z_0)^2} \\ R_3 &= \sqrt{(x - x_0)^2 + (y - y_0)^2 + (z + z_0 + 2d)^2} \\ R_4 &= \sqrt{(x - x_0)^2 + (y + y_0)^2 + (z + z_0 + 2d)^2}. \end{aligned} \quad (5.11)$$

Following the work in Bai and Eatock Taylor (2006), the higher-order boundary element method is applied to discretize the surface over which the integral is performed. Two kinds of quadratic isoparametric elements, the six-node triangular element and the eight-node quadrilateral element are employed in this study. To obtain desired variables (position coordinate, velocity potential etc.), shape functions are introduced within every element. Due to its easy description, a local intrinsic coordinate system (ξ, η) is applied to define the shape function. Based on this local coordinate system, the shape functions for the six-node element are expressed as follows:

$$\begin{aligned} N_1(\xi, \eta) &= (1 - \xi - \eta)(1 - 2\xi - 2\eta) \\ N_2(\xi, \eta) &= \xi(2\xi - 1) \\ N_3(\xi, \eta) &= \eta(2\eta - 1) \\ N_4(\xi, \eta) &= 4\xi(1 - \xi - \eta) \\ N_5(\xi, \eta) &= 4\xi\eta \\ N_6(\xi, \eta) &= 4\eta(1 - \xi - \eta) \end{aligned} \quad (5.12)$$

where $N_j(\xi, \eta)$ is the shape function at the j th node in an element.

Similarly, the shape function for the eight-node element can be constructed in the local intrinsic coordinate system by,

$$\begin{aligned}
N_1(\xi, \eta) &= 0.25(1 - \xi)(1 - \eta)(1 + \xi + \eta) \\
N_2(\xi, \eta) &= 0.5(1 - \xi^2)(1 - \eta) \\
N_3(\xi, \eta) &= 0.25(1 + \xi)(1 - \eta)(\xi - \eta - 1) \\
N_4(\xi, \eta) &= 0.5(1 + \xi)(1 - \eta^2) \\
N_5(\xi, \eta) &= 0.25(1 + \xi)(1 + \eta)(\xi + \eta - 1) \\
N_6(\xi, \eta) &= 0.5(1 - \xi^2)(1 + \eta) \\
N_7(\xi, \eta) &= 0.25(1 - \xi)(1 + \eta)(\xi - \eta + 1) \\
N_8(\xi, \eta) &= 0.5(1 - \xi)(1 - \eta^2).
\end{aligned} \tag{5.13}$$

After introducing the shape functions into each element, the position coordinate, velocity potential and its derivatives within an element in terms of the nodal values can be found by,

$$\mathbf{x}(\xi, \eta) = \sum_{j=1}^K N_j(\xi, \eta) \mathbf{x}_j, \tag{5.14}$$

$$\phi(\xi, \eta) = \sum_{j=1}^K N_j(\xi, \eta) \phi_j, \tag{5.15}$$

$$\frac{\partial \phi(\xi, \eta)}{\partial \xi} = \sum_{j=1}^K \frac{N_j(\xi, \eta)}{\partial \xi} \phi_j, \tag{5.16}$$

$$\frac{\partial \phi(\xi, \eta)}{\partial \eta} = \sum_{j=1}^K \frac{N_j(\xi, \eta)}{\partial \eta} \phi_j, \tag{5.17}$$

where K is the number of nodes in the element, i.e.: six for the triangular element and eight for the quadrilateral element. x_j and ϕ_j are the nodal positions and potentials respectively. By putting these expressions back into Eq. (5.9), the BIE is transformed to a discretized form as,

$$\begin{aligned}
C(\mathbf{x}_0) \phi(\mathbf{x}_0) &= \sum_{n=1}^N \sum_{m=1}^M \left\{ G(\mathbf{x}_m, \mathbf{x}_0) \left[\sum_{j=1}^K N_j(\xi, \eta) \left(\frac{\partial \phi}{\partial n} \right)_j \right] \right. \\
&\quad \left. - \frac{\partial G(\mathbf{x}_m, \mathbf{x}_0)}{\partial n} \left[\sum_{j=1}^K N_j(\xi, \eta) \phi_j \right] \right\} w_m |J_m(\xi, \eta)|,
\end{aligned} \tag{5.18}$$

where M is the number of sampling points in the standard Gauss-Legendre method, w_m denotes the integral weight at m th sampling point, $J_m(\xi, \eta)$ represents the Jacobian transformation from the local to the global coordinate and N is the number of elements.

To solve Eq. (5.18), the undetermined solid angle $C(\mathbf{x}_0)$ in Eq. (5.9) needs to be solved. Inspired by the fact that a uniform potential applied over a closed domain would not generate any flux, Wu and Eatock Taylor (1989) specified that $\phi = \text{constant} \neq 0$ over the entire integral boundary S in a uniform field. Following them, Eq. (5.9) leads to,

$$C(\mathbf{x}_0) = - \iint_S \frac{\partial G(\mathbf{x}, \mathbf{x}_0)}{\partial n} ds. \quad (5.19)$$

In this expression, the solid angle can be directly computed by the influence coefficients.

To sum up, the discretized equation can be finally organized in the matrix form as,

$$\begin{bmatrix} \mathbf{A}^{(11)} & \mathbf{A}^{(12)} \\ \mathbf{A}^{(21)} & \mathbf{A}^{(22)} \end{bmatrix} \begin{bmatrix} \mathbf{X}^{(1)} \\ \mathbf{X}^{(2)} \end{bmatrix} = \begin{bmatrix} \mathbf{B}^{(1)} \\ \mathbf{B}^{(2)} \end{bmatrix} \quad (5.20)$$

where,

$$\begin{aligned} \mathbf{X}^{(1)} &= \{\phi_1, \phi_2, \dots, \phi_{N_n}\} \\ \mathbf{X}^{(2)} &= \left\{ \left(\frac{\partial \phi}{\partial n} \right)_1, \left(\frac{\partial \phi}{\partial n} \right)_2, \dots, \left(\frac{\partial \phi}{\partial n} \right)_{N_p} \right\} \end{aligned} \quad (5.21)$$

$$\begin{aligned} A_{i,j}^{(11)} &= C(\mathbf{x}_i) + A_{i,j}^{(21)} \\ A_{i,j}^{(21)} &= \sum_{n=1}^{N_n} \sum_{m=1}^M \left[\frac{\partial G(\mathbf{x}_m, \mathbf{x}_i)}{\partial n} N_j(\xi, \eta) \omega_m |J_m(\xi, \eta)| \right] \end{aligned} \quad (5.22)$$

$$\begin{aligned} A_{i,j}^{(12)} &= A_{i,j}^{(22)} \\ A_{i,j}^{(22)} &= - \sum_{n=1}^{N_p} \sum_{m=1}^M \left[G(\mathbf{x}_m, \mathbf{x}_i) N_j(\xi, \eta) \omega_m |J_m(\xi, \eta)| \right] \end{aligned} \quad (5.23)$$

$$\begin{aligned}
B_i^{(1)} &= \sum_{n=1}^{N_n} \sum_{m=1}^M \left[G(\mathbf{x}_m, \mathbf{x}_i) \frac{\partial \phi(\mathbf{x}_m)}{\partial n} \omega_m |J_m(\xi, \eta)| \right] \\
&\quad - \sum_{n=1}^{N_n} \sum_{m=1}^M \left[\frac{\partial G(\mathbf{x}_m, \mathbf{x}_i)}{\partial n} \phi(\mathbf{x}_m) \omega_m |J_m(\xi, \eta)| \right] \\
B_i^{(2)} &= -C(\mathbf{x}_i) + B_i^{(1)}
\end{aligned} \tag{5.24}$$

In the above expressions, N_n and N_p are the numbers of elements on the Neumann and Dirichlet boundaries, respectively.

After assembling the above equations for each node on the whole integral surface, a set of linear algebraic equations are attained. Since either the potential or its derivative on the boundary is known from the corresponding boundary conditions, the set of linear algebraic equations can be solved to obtain the solution of the mixed boundary value problem.

5.1.1.4 Hydrodynamic forces

After the velocity potential is obtained by solving the mixed boundary value problem, the pressure on the floating barge can be found by the Bernoulli equation,

$$p = -\rho(\phi_t + \frac{1}{2} \nabla \phi \cdot \nabla \phi + gz) \tag{5.25}$$

where ρ is the density of the fluid, and ϕ_t is the time derivative of the potential. By integrating the pressure over the body surface,

$$f_i = - \iint_{S_B} p n_i ds \tag{5.26}$$

the hydrodynamic forces $\mathbf{F} = (f_1, f_2, f_3)$ and moments $\mathbf{M} = (f_4, f_5, f_6)$ can be computed. Here, n_i denote the six components of the normal unit vector \mathbf{n} defined in Eq. (5.5). Thus, to compute the hydrodynamic forces, the pressure given in Eq. (5.25) needs to be determined first. The only concern here is the evaluation of the temporal derivative of potential ϕ_t .

Following Wu and Eatock Taylor (2003), ϕ_t is represented by another boundary value problem. Additional auxiliary functions ψ_i which satisfy Laplace's equation in the fluid domain are introduced. They are also subject to the following boundary conditions. On the free water surface, the auxiliary functions satisfy,

$$\psi_i = 0. \tag{5.27}$$

On the body surface, they are specified by,

$$\frac{\partial \psi_i}{\partial n} = n_i. \quad (5.28)$$

For other boundaries, the Neumann condition is used and it defines the auxiliary functions by,

$$\frac{\partial \psi_i}{\partial n} = 0. \quad (5.29)$$

Based on Green's identity, the following relationship between ψ_i and ϕ_t is developed to obtain the hydrodynamic forces through the auxiliary functions:

$$\iint_S (\phi_t \frac{\partial \psi_i}{\partial n} - \psi_i \frac{\partial \phi_t}{\partial n}) = 0. \quad (5.30)$$

Eq. (5.30) can be simplified based on the boundary conditions for ψ_i and ϕ_t . This leads to expressions for the hydrodynamic forces as,

$$f_i = -c_{i,j} \ddot{\xi}_j + Q_i, \quad (5.31)$$

where ξ_j denotes the body displacement in the j th generalized direction, $c_{i,j}$ is equivalent to an added mass coefficient (computed from the auxiliary functions), and Q_i represents a complex expression involving the auxiliary functions, the potential, and the components of displacement. See Wu and Eatock Taylor (2003) for more details.

Thus, computing the auxiliary functions can lead to the solution of the hydrodynamic forces. It should be noted that the second mixed boundary value problem for ψ_i has the same boundary condition as the first one for the velocity potential ϕ . Therefore, these two problems have the same influence coefficient matrix, which saves computational effort to calculate the hydrodynamic forces by the auxiliary function approach.

Since the freely floating barge is considered in this study, the equation of motion needs to be solved to predict the position of the barge at each time step. Following Bai and Eatock Taylor (2009), based on the transformed representation of the force and Newton's second law, the following expression is obtained:

$$\sum_{j=1}^6 (m_{i,j} + c_{i,j}) \ddot{\xi}_j = Q_j + m_b g \delta_{i,3}. \quad (5.32)$$

Here, $m_{i,j}$ is the element of the mass matrix, m_b indicates the body mass and,

$$\begin{aligned} \delta_{i,j} &= 1 & \text{if } i = j \\ \delta_{i,j} &= 0 & \text{if } i \neq j \end{aligned} \quad (5.33)$$

After obtaining the potential and the auxiliary functions, the acceleration of the floating barge can be solved directly based on the formula above. In this way, the position of the barge can be updated.

5.1.2 Numerical implementation

5.1.2.1 Mesh generation

In the present study, the boundary integral equations Eqs. 5.20-5.24 are discretized using two kinds of quadratic elements as introduced in the previous section. It should be noted that the entire boundary in the computational domain is not continuous and smooth due to the presence of the floating barge and the free water surface. Thus, it is necessary to introduce continuous patches into the discretized surfaces, over which the mesh generation is carried out.

Based on the two kinds of quadratic elements defined by Eqs. 5.12 and 5.13, there are two types of patches correspondingly introduced in this model. Since it is easy to generate quadrilateral meshes on the vertical boundaries like the side wall, this structured type of mesh is applied under this condition. The corner nodes are distributed exponentially in the z direction with a view to approaching the vertical decay of the velocity potential. Therefore, the vertical coordinates are calculated as,

$$z_{i,j} = z_{1,j} - (z_{1,j} + D) \cdot \frac{1 - \exp[\gamma(z_{i,j} + D)(M_z + 1 - i)/M_z]}{1 - \exp[\gamma(z_{1,j} + D)]}, \quad (5.34)$$

with i varying from 1 to $M_z + 1$. Here $z_{1,j}$ denotes the coordinate of the point where the wave intersects the vertical surface, M_z is the number of elements in the z direction and D represents the water depth or the draft of the barge. The parameter γ determines the mesh size near the free surface.

Due to the fact that a triangular mesh is applicable in complex geometries, this unstructured type of mesh is used on the free surface and the truncated bottom of the body. To generate triangular meshes, the Delaunay triangulation method is applied in this model. See Subramanian et al. (1994) for details. Fig. 5.2 provides an example of the mesh generation in this study.

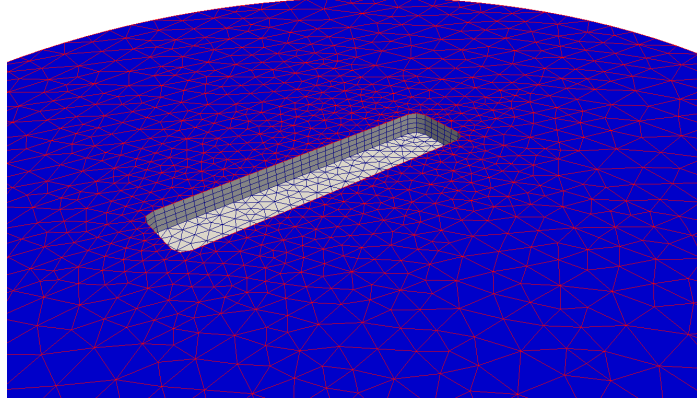


Figure 5.2: An example of mesh generated on the barge and the free surface.

5.1.2.2 Artificial damping layer

As shown in Fig. 5.1, an artificial damping layer is adopted to absorb the scattered wave energy on the outer annulus of the circular tank. To model the damping layer, the kinematic and dynamic free surface boundary conditions in Eq. (5.3) and Eq. (5.4) are simply modified by adding a damping term over a finite length of the free surface. The expressions are given as,

$$\frac{D\mathbf{X}}{Dt} = \nabla\phi - \nu(r)(\mathbf{X} - \mathbf{X}_e) \quad (5.35)$$

$$\frac{D\phi}{Dt} = -gz + \frac{1}{2}\nabla\phi \cdot \nabla\phi - \nu(r)\phi, \quad (5.36)$$

where r denotes the distance from the barge, $\nu(r)$ is the damping coefficient and $\mathbf{X}_e = (x_e, y_e, 0)$ is the reference value specifying the condition when the water surface is still. For practical application, the damping coefficient is imposed to be continuous and tuned to a characteristic excitation frequency ω of the wave motion. Here, it is defined by,

$$\nu(r) = \begin{cases} \omega \left(\frac{r-r_0}{\lambda} \right)^2 & \text{if } r \geq r_0 = r_D - \lambda \\ 0 & \text{if } r < r_0 \end{cases}, \quad (5.37)$$

where λ denotes the representative wavelength corresponding to the excitation, r_D is the radius of the outer circular computational domain.

5.1.2.3 Time stepping scheme

After solving the mixed boundary value problem by the higher-order boundary element method, the geometry of the free surface and the potential are to be updated for the calculation at the next time step. To realize this, the fourth-order Runge-Kutta scheme is adopted to conduct the integration of the nonlinear free surface boundary conditions in time.

The particle velocities on the surface need to be calculated before the time stepping integration of the free surface boundary conditions. From the solution of the boundary value problem and the corresponding boundary conditions, the potential and its derivatives in the whole domain are known. Thus they can be applied to calculate the particle velocities by the following expression:

$$\begin{bmatrix} \frac{\partial \phi}{\partial x} \\ \frac{\partial \phi}{\partial y} \\ \frac{\partial \phi}{\partial z} \end{bmatrix} = \begin{bmatrix} \frac{\partial x}{\partial \xi} & \frac{\partial y}{\partial \xi} & \frac{\partial z}{\partial \xi} \\ \frac{\partial x}{\partial \eta} & \frac{\partial y}{\partial \eta} & \frac{\partial z}{\partial \eta} \\ n_x & n_y & n_z \end{bmatrix}^{-1} \begin{bmatrix} \frac{\partial \phi}{\partial \xi} \\ \frac{\partial \phi}{\partial \eta} \\ \frac{\partial \phi}{\partial n} \end{bmatrix}. \quad (5.38)$$

As there is always more than one element surrounding a node, the velocity at each node is determined by averaging the values of the above equation applied within every element surrounding this node. Now, based on the boundary conditions, the surface position and velocity potential at the next time step can be updated. In this manner, the time is marching forward until the stopping criteria are satisfied.

5.1.2.4 Algebraic equation solver

The solution of the full and asymmetric influence matrix from the mixed boundary value problem at each time step is of great importance to the present study. The efficiency of the numerical model mainly depends on the solution scheme applied. There are a number of options for solving the matrix system. But the efficiency of most schemes is unfortunately case-dependent. The generalized minimum residual (GMRES) iterative scheme with a diagonal preconditioner, which is widely used for similar problems and found to be very effective by Bai and Eatock Taylor (2006), is adopted in this present study.

5.2 A COUPLED numerical model for simulation of the interaction between sloshing and ship motions

As described in Chapter 1, prior to studying the coupling effects between sloshing and ship motions, the two distinct sub-problems need to be computed accurately. In previous chapters, the Level-Set based free surface flow solver has proved its capability in accurate simulation of sloshing flows, even with breaking waves. The HOBEM based ship motion solver has also been well validated in the work of Bai and Eatock Taylor (2006, 2009). Thus in this section, the COUPLED numerical model, which combines both solvers, is developed and validated.

5.2.1 Mathematical formulation

Here, to consider the interactions between the sloshing and the ship motions, the coupling mechanism of Kim (2002) is adopted. First, external ship motions induce liquid sloshing in the internal tank from the start of the coupling process. Therefore, the external force in Eq. (3.1) for the sloshing flows is modified as,

$$\mathbf{f}_e = \mathbf{g} - \frac{d^2 \boldsymbol{\xi}_{\mathbf{1}, \mathbf{3}}}{dt^2} - \frac{d \boldsymbol{\alpha}_{\mathbf{5}}}{dt} \times (\mathbf{r} - \mathbf{R}) - \boldsymbol{\alpha}_{\mathbf{5}} \times [\boldsymbol{\alpha}_{\mathbf{5}} \times (\mathbf{r} - \mathbf{R})] - 2 \boldsymbol{\alpha}_{\mathbf{5}} \times \frac{d(\mathbf{r} - \mathbf{R})}{dt} \quad (5.39)$$

where $\boldsymbol{\xi}_{\mathbf{1}, \mathbf{3}}$ denotes the translational vectors of surge and heave, $\boldsymbol{\alpha}_{\mathbf{5}}$ indicates the velocity vector of pitch motion and the other terms use the same definition as in Eq. (3.1). In addition, the center of rotation is defined at the same position as the center of gravity of the barge.

At the same time, the sloshing flow inside the tank will generate forces and moments on the tank which will act on the ship in return. Therefore, the hydrodynamic force defined in Section 5.1.1.4 should consider the sloshing-induced forces and moments before updating the position of the freely floating barge at the next time step. Here, Eq. (5.32) is modified as,

$$\sum_{j=1}^6 (m_{i,j} + c_{i,j}) \ddot{\xi}_j = Q_j + m_b g \delta_{i,3} + F_{si}, \quad (5.40)$$

where F_{si} consists of the force on the horizontal tank wall (F_{s1}), the force on the vertical tank wall (F_{s3}) and the induced moments (F_{s5}). It should be pointed out

again, that the sloshing model is two-dimensional and the ship motion model is three-dimensional. Therefore, in order to include the sloshing effects into the COUPLED model, a length of 0.02 m along the y -direction is considered when computing the forces and moments defined above. In this way, the two numerical models are combined together and developed into the final COUPLED model applied in the present study.

5.2.2 Numerical implementation

The fully COUPLED numerical model is built based on the modification of the Level-Set based free surface flow solver and the HOBEM based ship motion solver. Here, a complete computational cycle within one time step is summarized as follows.

1. Read the input file and set up the initial conditions for the circular wave tank.
2. Define the vertical patches and horizontal patches. Generate elements accordingly on the water surface, the barge surface, the tank wall, etc. at the initial time step.
3. According to the updated value, regenerate the elements on the surfaces except at the initial time step.
4. Solve the mixed boundary value problem by the higher-order boundary element method for ship motions in waves.
5. Calculate the derivatives of potential on the free water surface and the body surfaces.
6. Go to the sloshing cycle.
7. Set up the initial conditions for the computational domain in the internal water tank.
8. Solve the Level-Set evolution equation to capture the free surface.
9. Reinitialize the Level-Set function by the fast marching technique.
10. Based on the interface captured, define the fluid properties in the whole water tank by the Heaviside function.

11. Take the fluid properties into the Navier-Stokes equations. At the same time, introduce the velocities and accelerations of the barge into the Navier-Stokes equations to induce the sloshing flow.
12. Rewrite the Navier-Stokes equations with a two-step scheme and obtain the source term for the Poisson equation.
13. Solve the Poisson equation and update the velocity field.
14. Based on the computed pressure, obtain the force and moments on the tank wall by integration.
15. Jump out of the sloshing cycle.
16. Calculate the hydrodynamic force on the barge.
17. Combine the obtained force and the sloshing-induced force. Add them into the motion equation.
18. Solve the motion equation and update the position of the barge at the next time step.
19. Update the position and potential on the free surface at the next time step.
20. Go back to Step 3. Repeat the computational cycle until the desired time is reached.

5.2.3 A preliminary validation of the COUPLED model

To validate the COUPLED model, the two-dimensional experimental work of Rognebakke and Faltinsen (2003) has been reproduced numerically. In this case, a box-shaped hull section is allowed to move in the sway direction only. It is excited by regular waves and contains two identical water tanks. In order to prevent the model from drifting off, a system of springs with total stiffness 30.9 N/m is added. Fig. 5.3 shows the dimensions of the section.

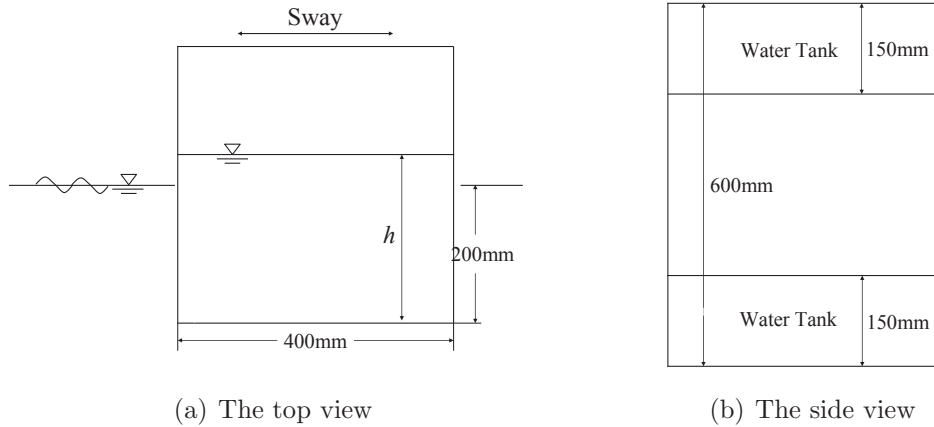


Figure 5.3: A schematic view of box-shaped hull section used in Rognebakke’s experiment.

Here, the two filled tanks series and the empty tank series are studied at different wave frequencies. 20 wave periods are applied as the total simulation time. Fig. 5.4 shows the results of the sway amplitude for empty tanks and two filled tanks.

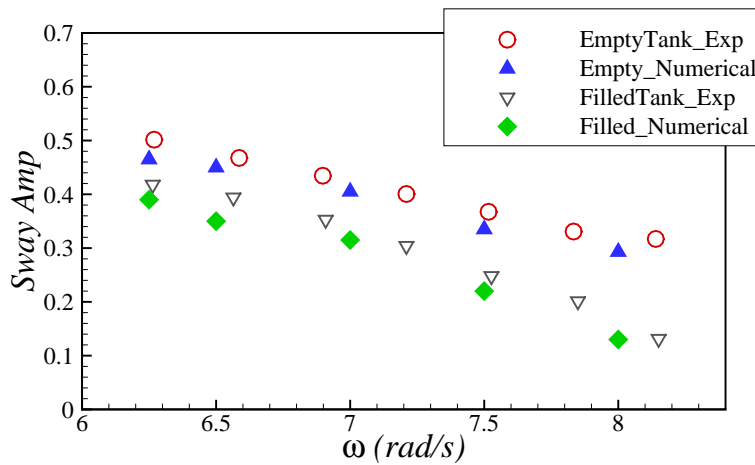


Figure 5.4: Comparison of sway amplitude for empty tanks and two tanks filled with $h = 0.186$ m between the present numerical results and Rognebakke’s experimental data.

As can be seen in Fig. 5.4, the overall trends of motion RAOs show close agreement between the numerical results and the experimental data. However, it is observed that the present numerical results have slightly smaller values. One possible reason is that the amplitude applied in the numerical simulation is 0.012 m in order to avoid introducing numerical instability in the HOBEM model, while in the

experiment it is 0.015 m. In addition, it can be seen that the difference between numerical and experimental results for the empty tank is close to that for the filled tank. This indicates that the accuracy of the COUPLED model is mainly determined by the HOBEM model. The numerical error due to the interchange of data between the Level-Set based sloshing model and the HOBEM model might be quite limited. It should also be noted that there is an apparent reduction in the sway motion when tanks are filled with water. This suggests that the internal sloshing flow would have a significant impact on the external ship motions. In general, the capability of the COUPLED model is validated by the good agreement with the experimental recordings.

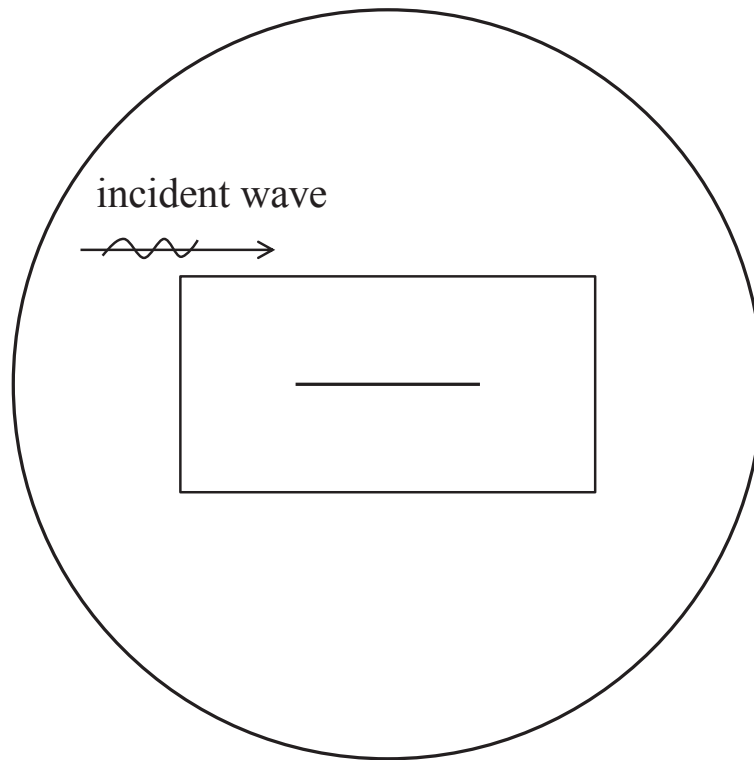
5.3 A parametric study on the coupling effects between sloshing and ship motions

In this section, the COUPLED model is adopted to perform a numerical simulation of the interaction between sloshing and ship motions. A systematic parametric study regarding wave amplitude, frequency and filling conditions of the water tank is carried out.

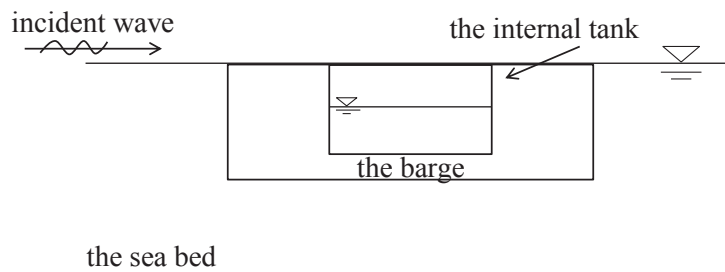
As shown in Fig. 5.5, a circular wave tank with a radius of 4 m, and a water depth of 3 m is adopted. At the center of the circular wave tank, a barge with a length of 2.47 m, a breadth of 0.6 m and a draft of 0.18 m, which has been used in the work of Molin et al. (2009), is placed, considering its shape, size and feasibility. Inside the barge, an internal sloshing tank is set at the middle position. It measures 0.6 m, 0.18 m in the horizontal and vertical directions respectively. To achieve stable numerical results, the total simulation time is set as 20 times of the wave period. It should be noted that the surge motion shown in the following cases includes the drift of the barge. Also note that the Level-Set based free surface flow solver is only applicable to two-dimensional flows. Thus, head sea conditions, which only induce surge, heave and pitch motions, are considered in this study.

5.3.1 Effects of wave amplitude

In this section, four wave amplitudes from $A = 0.005$ m to 0.014 m with an increment of 0.003 m are employed with the wave frequency $f = 5.0$ rad/s. The water tank is filled to 50% of the tank height.



(a) The top view

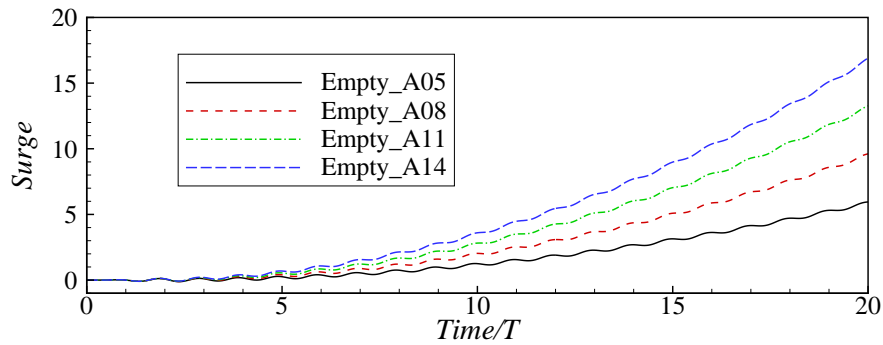


(b) The side view

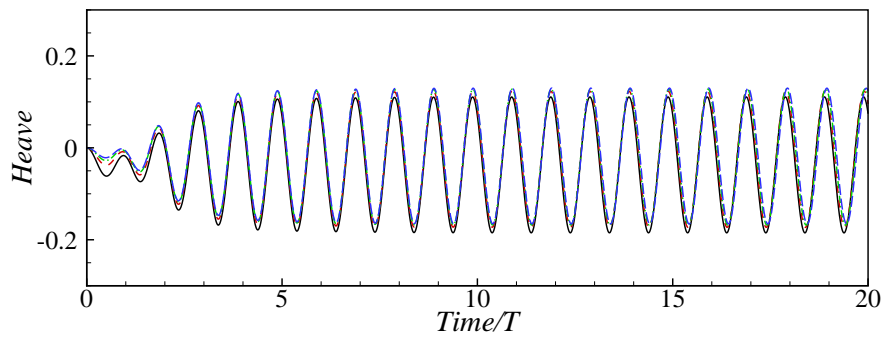
Figure 5.5: A schematic view of the COUPLED model used in this study.

First, to better illustrate the effects of sloshing in the water tank, the HOBEM model is used to simulate the freely floating barge with an empty tank (no internal sloshing). Fig. 5.6 and Fig. 5.7 plot the corresponding normalized motions and the hydrodynamic forces on the barge.

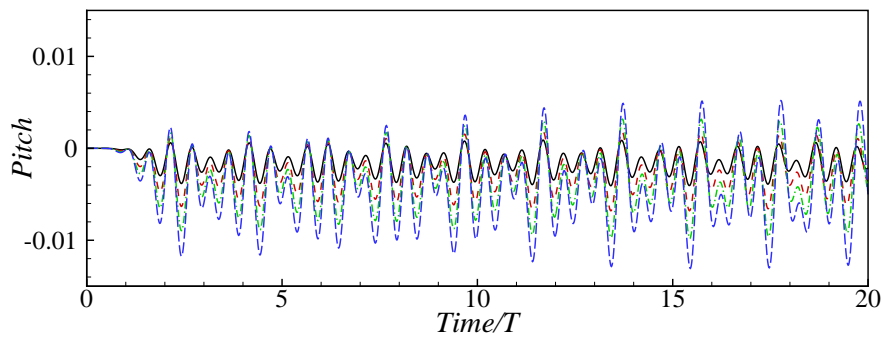
From Fig. 5.6, one can see that the motion response of the barge generally becomes larger as the wave amplitude increases. To be more specific, due to the inclusion of



(a) surge



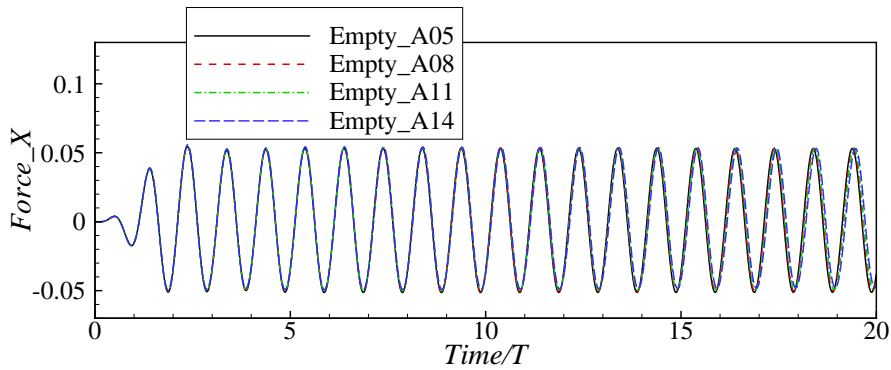
(b) heave



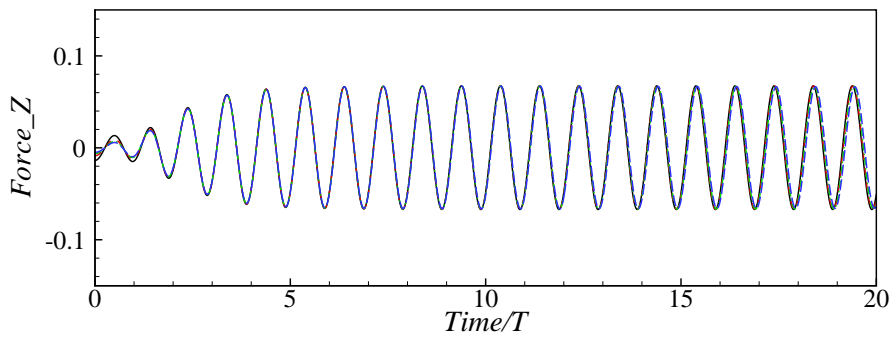
(c) pitch

Figure 5.6: Time histories of the motion RAOs of the barge with an empty tank for different wave amplitudes.

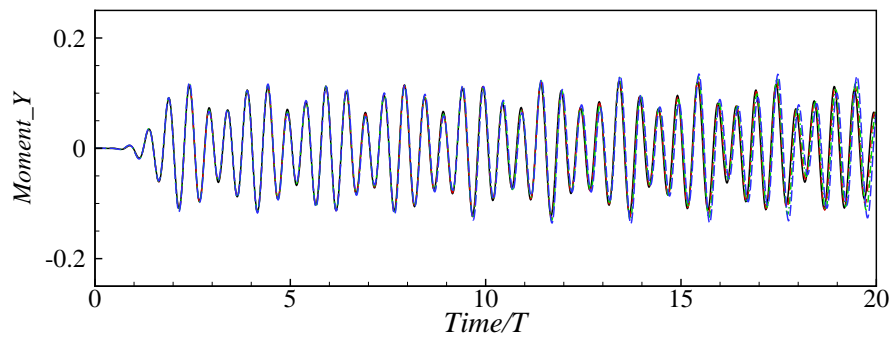
drift, surge motions are proportionally raised with the enlarged wave amplitudes. The normalized heave motions are close to each other with almost identical amplitudes and small shifts of the mean heave displacements. This suggests that the heave motion is probably linear with respect to the wave amplitude. Similar to the surge motions, Fig. 5.6(c) shows that the normalized pitch motions are enlarged as the



(a) force_x



(b) force_z

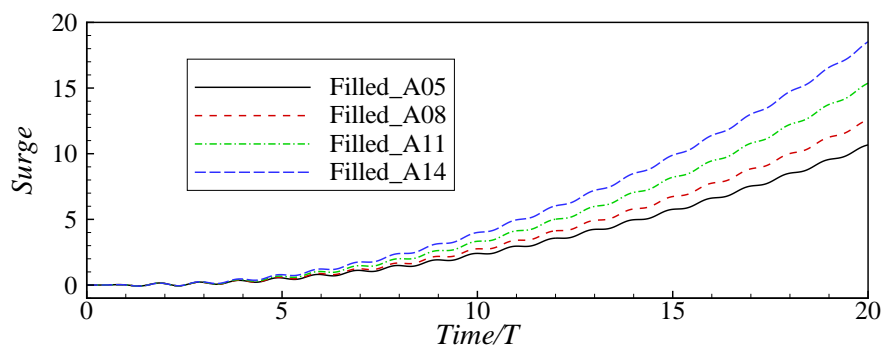


(c) moment_y

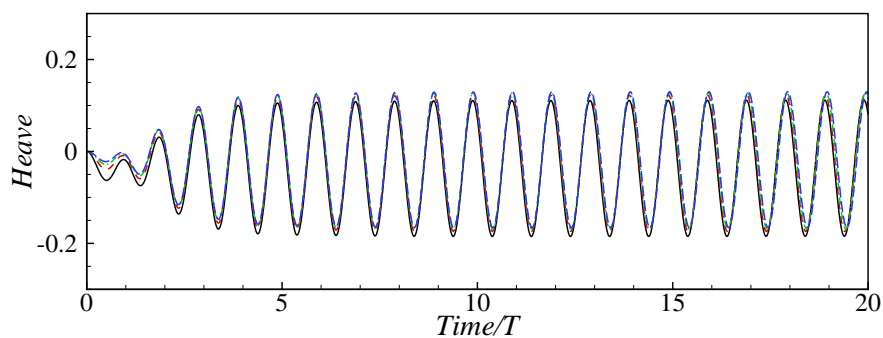
Figure 5.7: Time histories of the wave forces on the barge with an empty tank for different wave amplitudes.

wave amplitude increases. In Fig. 5.7, the normalized translational forces for various wave amplitudes are almost identical. This supports our explanations for almost identical heave motions and enlarged surge motions due to drift. This also indicates that translational motions are proportional to the wave amplitudes. Furthermore, the difference in the moments about the y direction for different wave amplitudes can

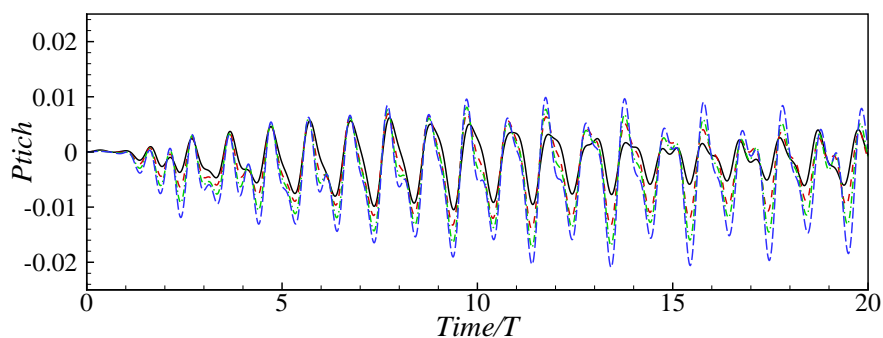
be observed from $t = 10T$. The difference becomes larger over time and clearly lead to the increase in the rotational motions of the barge. Therefore, this phenomenon validates our previous statement and indicates that the pitch motions are not linear to the wave amplitude.



(a) surge



(b) heave



(c) pitch

Figure 5.8: Time histories of the motion RAOs of the barge with a filled tank for different wave amplitudes.

Fig. 5.8 and Fig. 5.9 display the displacements and hydrodynamic forces of the

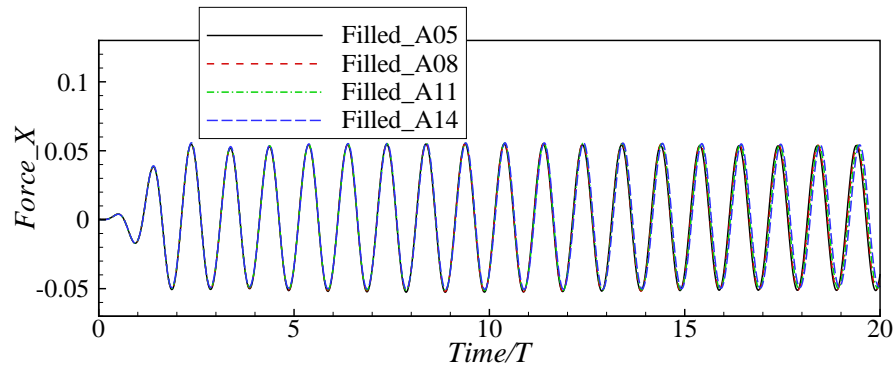
barge given by the COUPLED model, which considers the internal water tank with a 50% filling level. In both figures, similar tendencies to those obtained without internal sloshing can be observed. The normalized surge motions increase as the wave amplitude increases. The obtained results of heave motions lie quite close to each other. The pitch motions are also visibly more violent as the wave amplitude increases.

Additionally, the translational forces are almost the same, while the moments vary from different wave amplitudes. However, we can see that most of the values from the time series achieved by the COUPLED model for the barge with a filled tank are larger than those obtained by the HOBEM model for the barge with an empty tank without the effects of internal sloshing. Furthermore, in Fig. 5.8(c), from $t = 10T$, the results obtained by the larger wave amplitudes tend to represent a slightly different pattern from that obtained by $A = 0.005$ m. This should be mainly due to the influence of the sloshing motion.

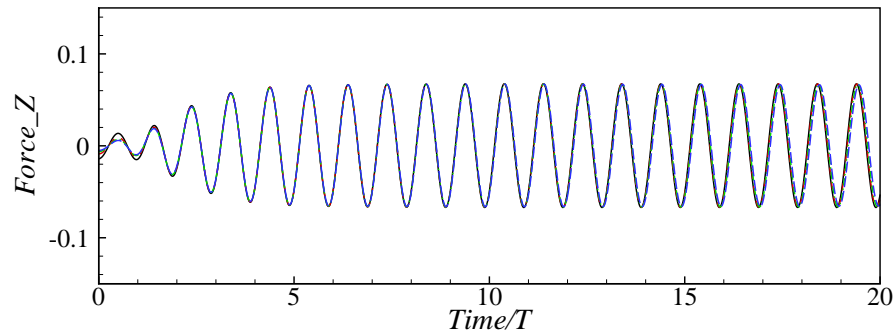
Thus, to better illustrates the effects of internal sloshing on barge motions, the difference of the normalized motions are plotted by using the time history obtained by the COUPLED model to minus that from the HOBEM model. Fig. 5.10 shows the difference of motion due to the coupling effects.

Evidently, the differences of the three components due to internal sloshing exhibit different patterns from the previous time histories of the normalized barge motions. First, the previous surge solutions from both models become larger due to the larger wave amplitudes. However, the difference of the surge components decreases as the wave amplitude increases. In addition, in the time history of sloshing effects on the surge motions of the barge, the peaks and troughs are barely noticeable. Considering both points, the presence of internal sloshing might counteract the effects of the wave amplitude on the surge motions (mainly on the drift). In other words, the increment of surge motions due to the larger wave amplitude is reduced because of the effects of sloshing motion.

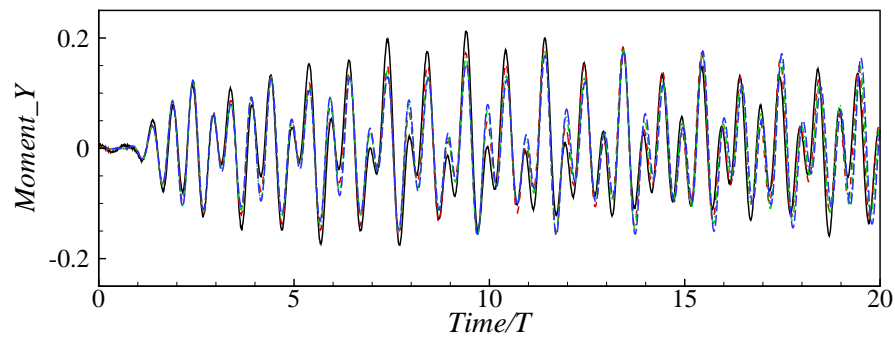
Second, the previous heave solutions become stable beyond a certain time instant, while the differences of the heave components intensify over time, indicating that the effects of sloshing on the heave motions are amplified with time. Obvious shifts in the results for various wave amplitudes can be observed. However, it should be noted that the highest shift is achieved with $A = 0.005$ m, while the lowest one is obtained with $A = 0.008$ m. Thus, the heave motion shifts do not follow a monotonic relation with respect to the wave amplitudes.



(a) force_x



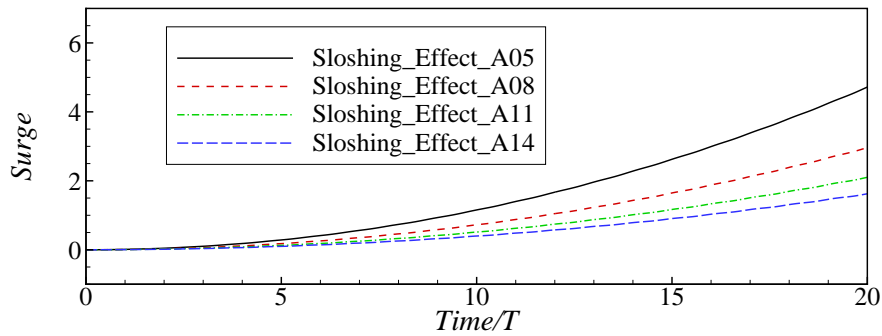
(b) force_z



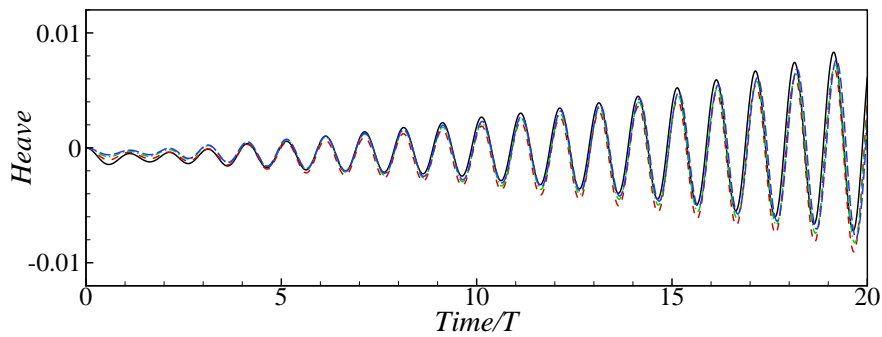
(c) moment_y

Figure 5.9: Time histories of the wave forces on the barge with a filled tank for different wave amplitudes.

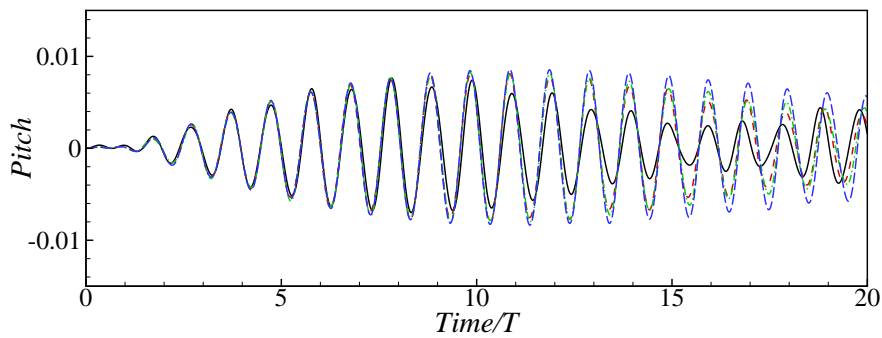
Finally, as shown in Fig. 5.10(c), the differences of the normalized pitch motions are symmetrical to the initial position (i.e.: there is no rotation angle). This again supports our previous conclusion that internal sloshing has a greater influence on the pitch motions than the drift motions. In addition, after $t = 10T$, the differences between each of the pitch results with varying wave amplitudes become larger over



(a) surge



(b) heave



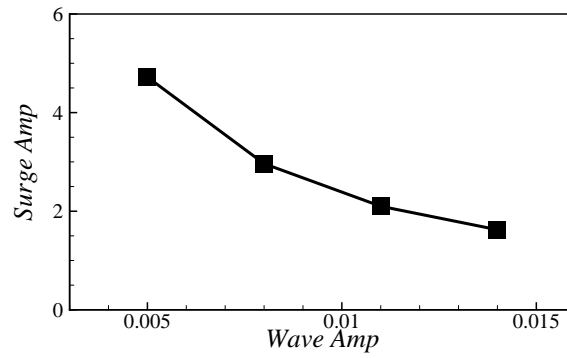
(c) pitch

Figure 5.10: Time histories of the slushing effects on the barge motions for different wave amplitudes.

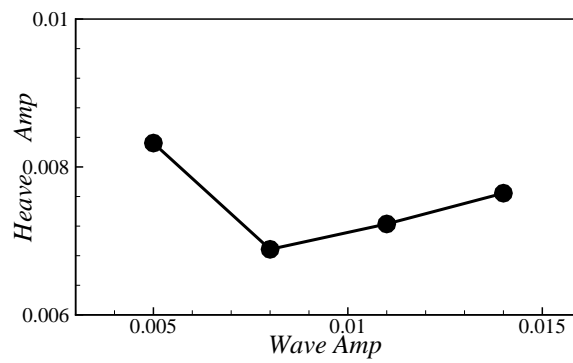
time. A different beating phenomenon of the $A = 0.008$ m result is observed. This indicates that the larger wave amplitude leads to a different pattern of pitch motions due to the presence of internal slushing. Therefore, we can conclude that the effects of slushing on the pitch motions of the barge are not proportional to the wave amplitude.

Fig. 5.11 records the maximum motion differences during the whole simulation.

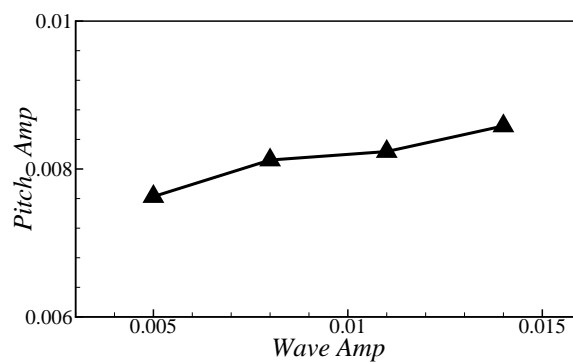
It concurs with the previous discussion. The effects of internal sloshing reduce the increment of surge motions due to the increase in the wave amplitude, while they intensify the increment of pitch motions. The sloshing influence on heave responses is not monotonic to the wave amplitudes.



(a) surge



(b) heave



(c) pitch

Figure 5.11: Maximum sloshing effects on ship motions under different wave amplitudes.

As studied in Chapter 3, higher wave amplitudes induce stronger sloshing flows inside the water tank. To better understand the effects of ship motions on the sloshing motions, the surface displacements at the left of the water tank wall are plotted for different wave amplitudes.

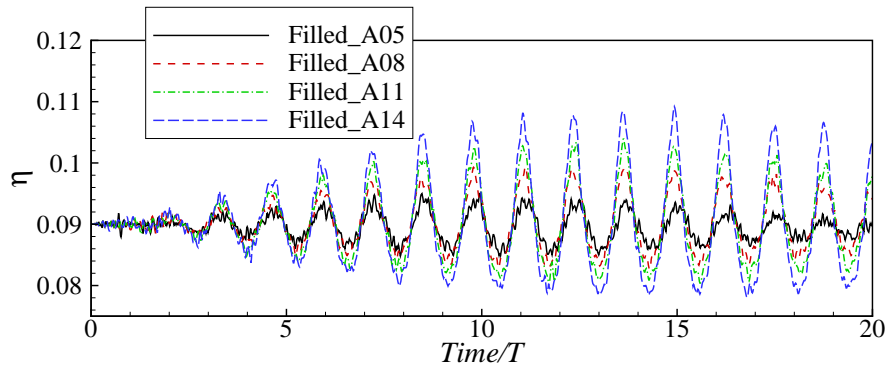


Figure 5.12: Time histories of the surface displacement at the left wall for different wave amplitudes.

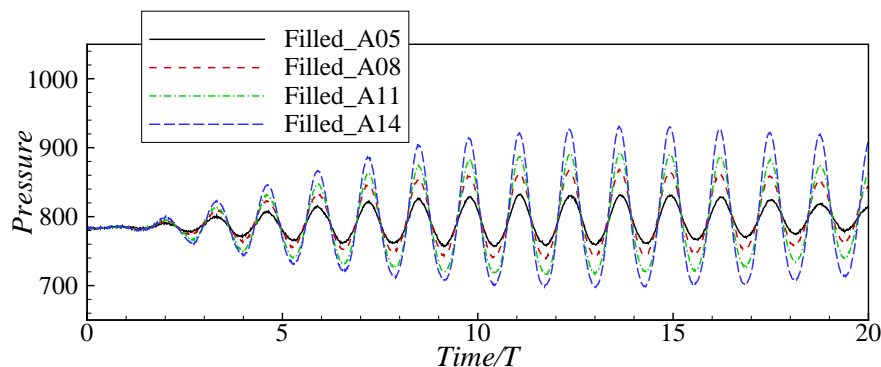


Figure 5.13: Time histories of pressure at the left wall for different wave amplitudes.

As shown in Fig. 5.12, it is clear that the surface displacements become larger as the wave amplitude increases. More specifically, the time series of the surface displacement achieved with $A = 0.005$ m is almost symmetrical to the initial water depth ($d = 0.09$ m). However, with a larger wave amplitude applied, for example, $A = 0.014$ m, larger peaks and relatively smaller troughs are observed, and the surface displacement is no longer symmetrical to the still water line.

The time history of the pressure at the left wall 0.01 m above the tank bottom is recorded in Fig. 5.13. Similar patterns to the surface displacement are obtained.

As the wave amplitude increases, the pressure results gradually become asymmetric. From both figures, we can conclude that with larger wave amplitudes applied, nonlinear sloshing flows are generated inside the water tank by the COUPLED model.

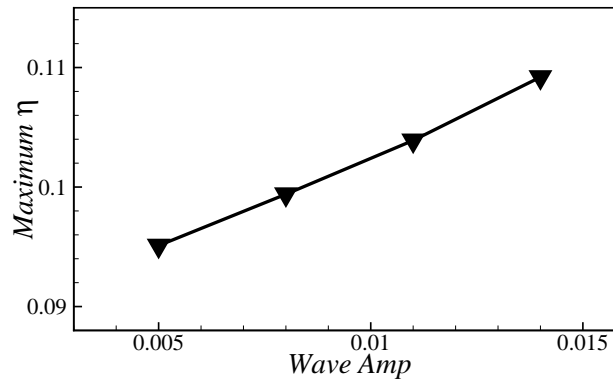


Figure 5.14: Maximum surface displacements under different wave amplitudes.

Fig. 5.14 shows the maximum wave elevation recorded at the left wall of the water tank for each wave amplitude. A nearly linear relation between the sloshing flow and the wave amplitude can be observed. However, Fig. 5.15 shows that the maximum pressure changes nonlinearly with the variation of the wave amplitude. Thus, one can conclude that the sloshing motions inside the tank are not proportional to the wave amplitude.

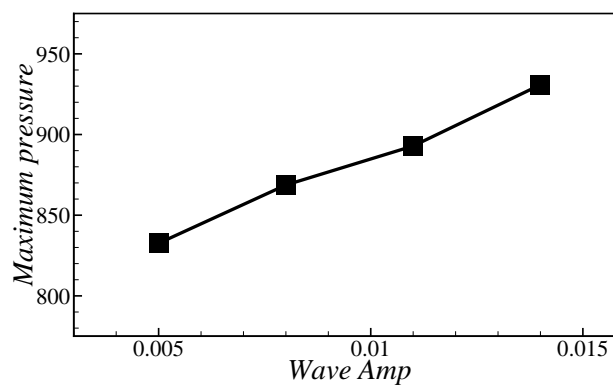


Figure 5.15: Maximum pressure under different wave amplitudes.

5.3.2 Effects of wave frequency

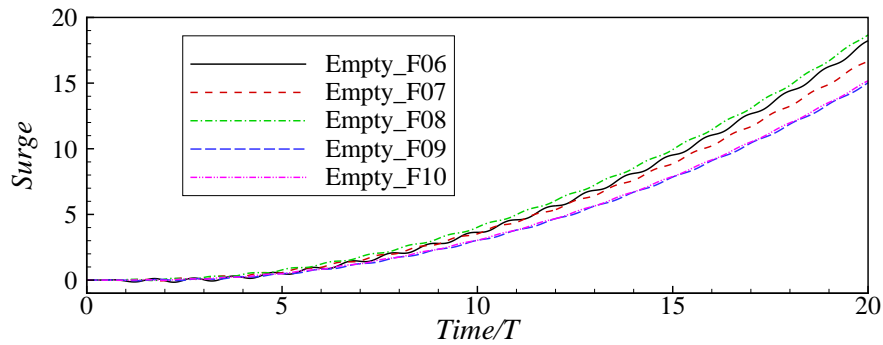
Based on the previous section, a critical wave amplitude of $A = 0.014$ m is chosen to perform the following simulations. In this section, the coupling effects under various wave frequencies from $f = 6$ to 10 rad/s with a interval of 1 rad/s are studied. It should be mentioned that the hydrodynamic forces which are obviously less affected by the coupling effects as shown in the previous section, are not a concern in the following cases.

Following the same steps from the previous section, first, the HOBEM model is used to simulate the freely floating barge with an empty tank (no internal sloshing) at different wave frequencies. The numerical results are given in Fig. 5.16.

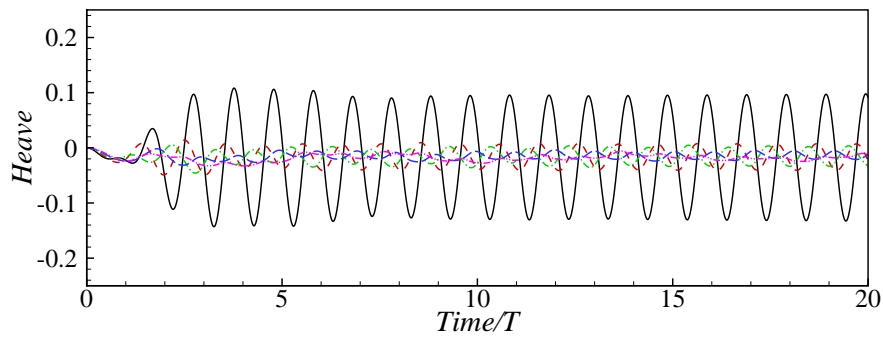
As shown in Fig. 5.16(a), it is easily observed that the time series of the surge motions are not monotonic to the variation of the wave frequencies. The main reason for this might be that the surge motion (including the drift) is not significantly influenced by the variation of the wave frequencies when the same wave amplitude is applied. In addition, the noticeable peaks and troughs in the time series are only found at frequency $f = 6$ rad/s. This suggests that larger motion responses are induced at this value than at other frequencies. Fig. 5.16(b) shows the time series of the heave motions. The outstanding result of the heave motion is obtained at wave frequency $f = 6$ rad/s, as expected. Furthermore, in contrast to the surge component, the time histories of the heave motion seem monotonic to the wave frequencies. As the wave frequency increases, the value of the heave motions drops. From Fig. 5.16(c), interesting phenomena can be observed in the time histories of the pitch motions. Various wave frequencies result in different shapes of beating phenomena. It should be noted that the value of the pitch motion at $f = 7$ rad/s is obviously larger than those at other frequencies.

Taking the 50% filled water tank into account, numerical results obtained by the COUPLED model are shown in Fig. 5.17. Barge motions predicted by the COUPLED model are similar to those computed by the HOBEM model. The time histories of the three components given by both models have the same tendencies. The frequency $f = 6$ rad/s leads to the largest heave motions, while the frequency $f = 7$ rad/s can generate strong pitch motions.

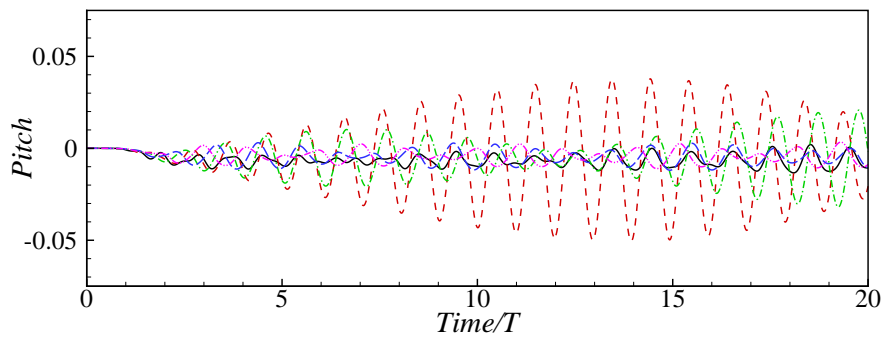
Since differences between the results of the two models can barely be observed, the effects of internal sloshing are represented by using the time history obtained by the COUPLED model to minus that from the HOBEM model. As shown in Fig. 5.18(a), the differences show a different pattern from that of the two time histories of the surge motions. Unlike the non-monotonic relation, the increment of surge motions



(a) surge



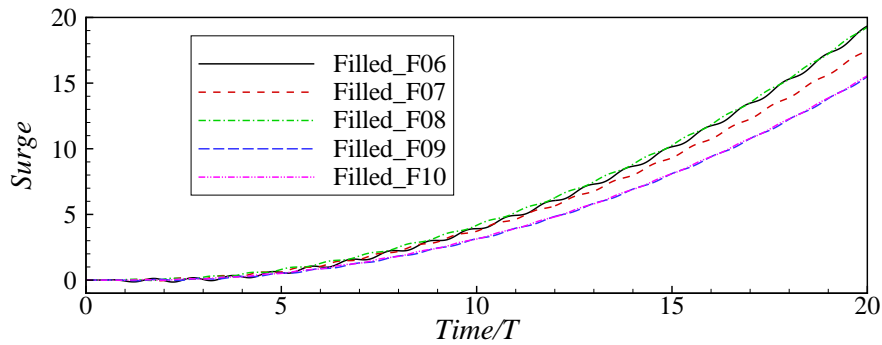
(b) heave



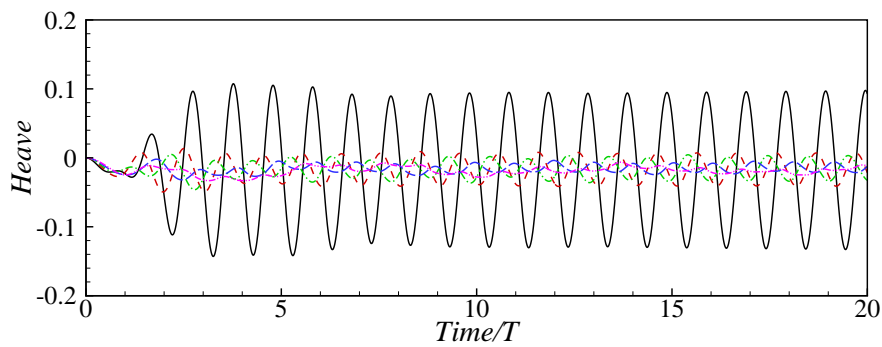
(c) pitch

Figure 5.16: Time histories of the motion RAOs of the barge with an empty tank at different wave frequencies.

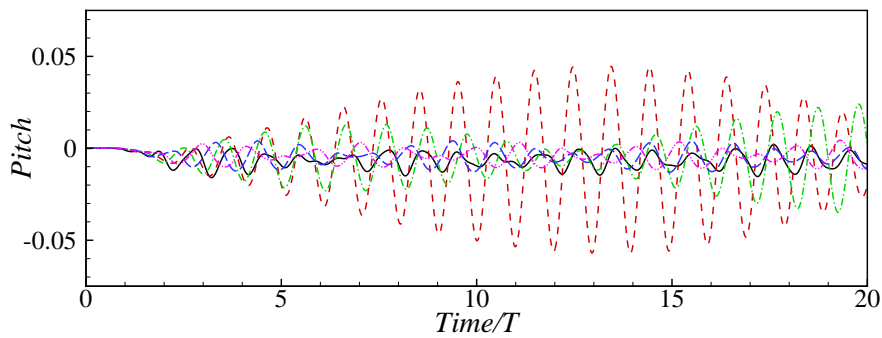
due to the sloshing presence is reduced as the wave frequency increases. Fig. 5.18(b) shows the differences of the heave motions at various wave frequencies. Just as with the surge component, the increase in the wave frequency leads to the decrease in difference. It should also be noted that the value for each time history is gradually amplified, indicating the sloshing effects become larger with time. Similar to the



(a) surge



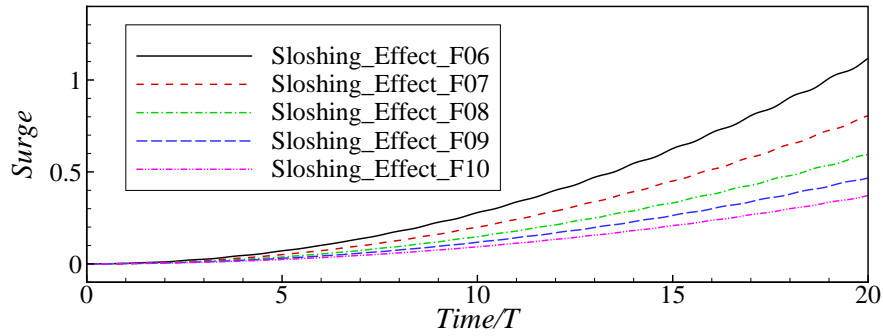
(b) heave



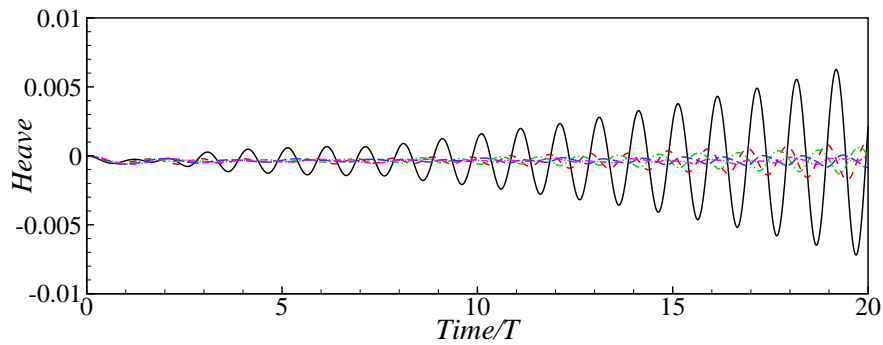
(c) pitch

Figure 5.17: Time histories of the motion RAOs of the barge with a filled tank at different wave frequencies.

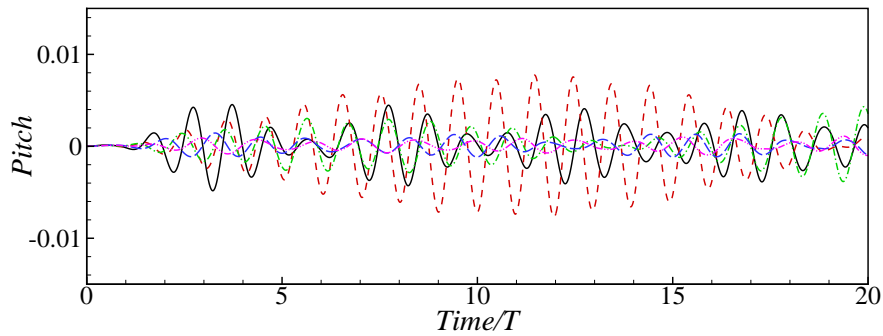
previous two pitch results, Fig. 5.18(c) shows that different beating phenomena are formed, and the outstanding result with $f = 7$ rad/s can be observed. However, there is one major difference: the value of the difference at $f = 6$ rad/s is relatively closer to those at $f = 8$ rad/s and is much greater than those at $f = 9$ and 10 rad/s. In the two original pitch results (by HOBEM and COUPLED), the predictions at $f = 6$



(a) surge



(b) heave

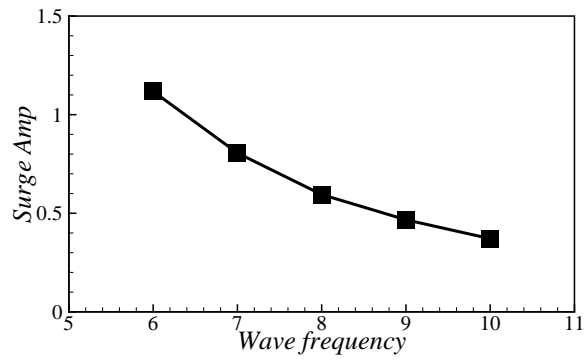


(c) pitch

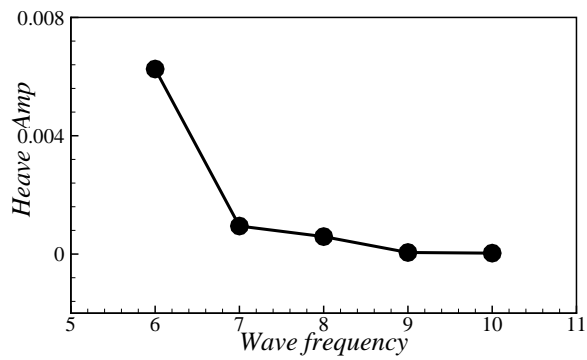
Figure 5.18: Time histories of the sloshing effects on the barge motions at different wave frequencies.

rad/s are closed to those at $f = 9$ and 10 rad/s and are much smaller than those at $f = 8$ rad/s. This could be caused by the relatively larger sloshing effects on the pitch motion at $f = 6$ rad/s, suggesting a more severe sloshing flow would be induced at this frequency.

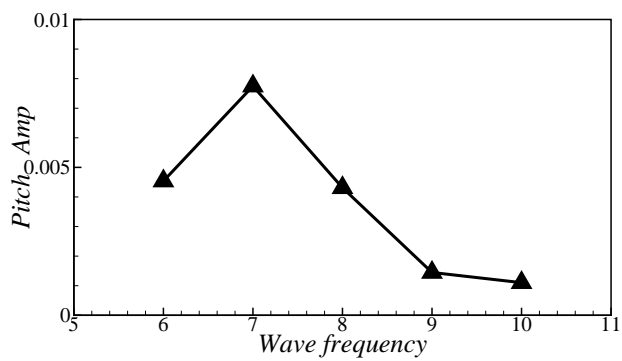
Fig. 5.19 records the maximum value of the differences during the simulation. It



(a) surge



(b) heave



(c) pitch

Figure 5.19: Maximum sloshing effects on ship motions at different wave frequencies.

can be seen that as the wave frequency increases, the increment of surge and heave motions due to the internal sloshing decreases. For the pitch motion, a non-monotonic trend can be observed, while maximum effects due to internal sloshing are caused at $f = 7$ rad/s.

As discussed in Chapter 3, the influence of the wave frequency on the sloshing

flow is complicated. Two factors need to be considered. The first one is the ratio of the wave frequency to the natural frequency of the sloshing system. The other is the body response at the given wave frequency. For example, a smaller body response might lead to a more violent sloshing flow if the wave frequency is closer to the natural frequency of the sloshing system.

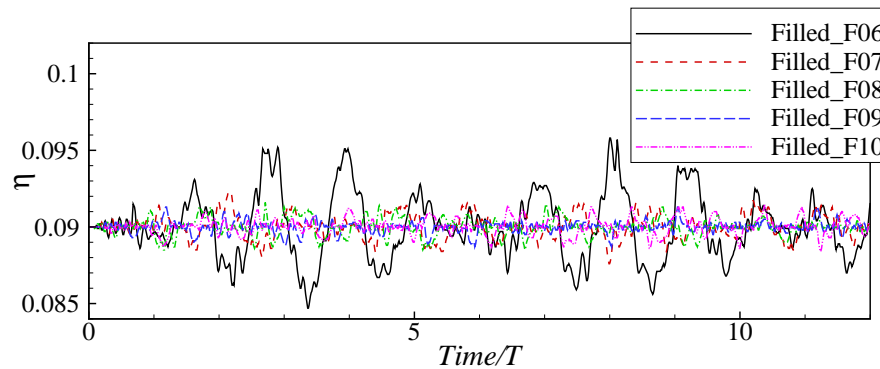


Figure 5.20: Time histories of the surface displacement at the left wall at different wave frequencies.

Here, Fig. 5.20 shows the time series of the free surface displacement at various wave frequencies. The sloshing flow excited by $f = 6$ rad/s is much stronger than those excited by other frequencies. This is partially due to the larger surge and heave motions obtained at this frequency. However, the outstanding pitch motion at $f = 7$ rad/s doesn't result in a strong sloshing flow inside the water tank. Thus, to explain this scenario, one should take the ratio of the wave frequency to the natural frequency into account. According to Eq. (3.3), the natural frequency of this sloshing system is 4.7497 rad/s. Clearly, $f = 6$ rad/s is closest to the critical value. Thus, as the wave frequency increases, the sloshing flow becomes smaller. This indicates that in this case, the ratio of the wave frequency to the natural frequency of the sloshing system has greater effects on the induced sloshing than the barge motions.

Fig. 5.21 indicates the time history of the pressure recorded at the left wall 0.01 m above the tank bottom. A similar trend to the surface displacement result is achieved. This also suggests that hydrostatic pressure is dominant in these cases.

Fig. 5.22 and Fig. 5.23 record the maximum surface displacement and pressure against the wave frequency. The decreasing trend supports our previous description.

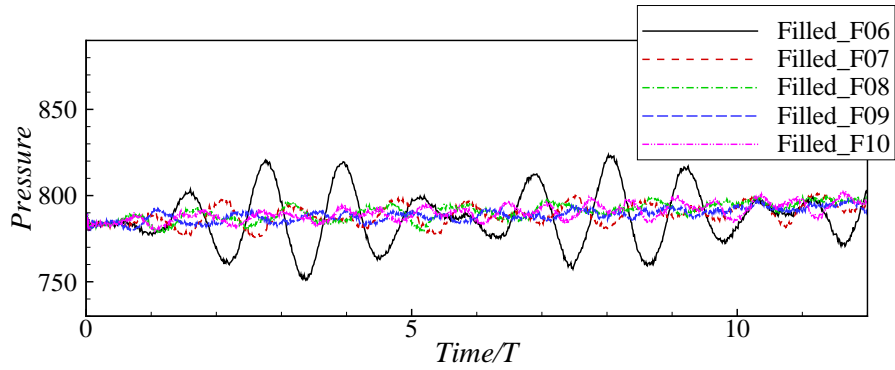


Figure 5.21: Time histories of pressure at the left wall at different wave frequencies.

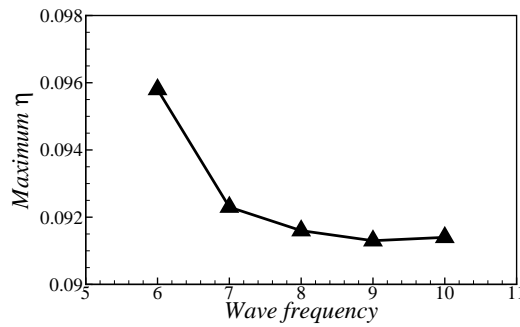


Figure 5.22: Maximum surface displacements at different wave frequencies.

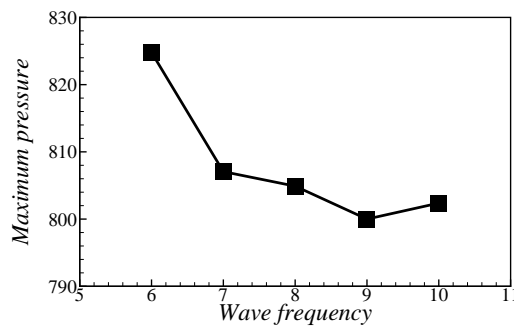


Figure 5.23: Maximum pressure at different wave frequencies.

5.3.3 Effects of the filling level in the water tank

In this section, the influence of the filling level in the water tank on the coupling effects is investigated. To begin with, the three usual filling levels 20%, 50% and 80% are adopted, with the chosen amplitude $A = 0.014$ m and frequency $f = 5.0$ rad/s.

Fig. 5.24 shows the motions predicted by the COUPLED model under the three

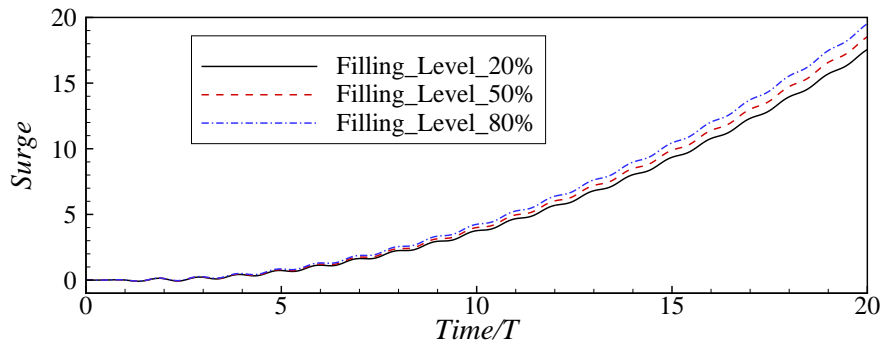
filling levels. It can be seen that as the filling level increases, the surge motions (including the drift) become larger with time. However, with various filling levels, the heave motions are almost identical. Finally, an interesting scenario can be found in Fig. 5.24(c): the time histories of the pitch motion are not monotonic to the variation of the filling level inside the water tank. The most critical condition is found when the internal tank is 50% filled.

To better illustrate the effects of the internal sloshing, just as in the previous sections, the difference of the time series of barge motions is given by using the results obtained by the COUPLED model for the three filling levels to minus the time history of the barge motions with an empty tank computed by the HOBEM model for $A = 0.014$ m and $f = 5$ rad/s (shown in Fig. 5.6). As displayed in Fig. 5.25, the motion differences display a similar trend to the previous results from the COUPLED model. The increment of the surge motions is enlarged as the tank is filled with more water. The mid filling level results in the largest increase in the pitch motions. However, unlike the identical results of the heave component from the COUPLED model, the presence of the sloshing increases the differences in heave motions over time.

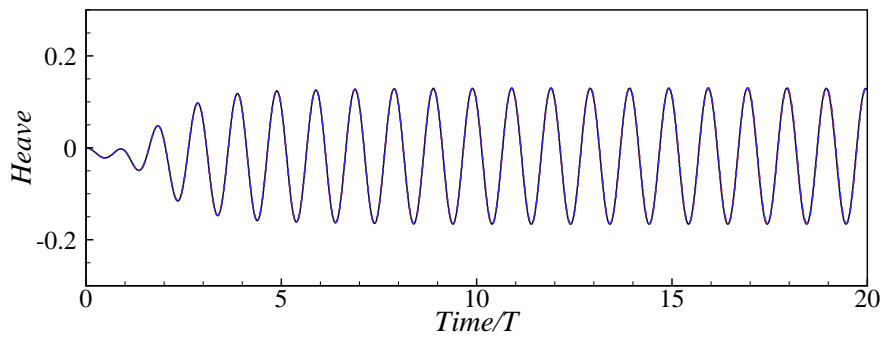
As discussed in Chapter 3, the lower filling condition has gained a lot of attention since in such conditions, greater nonlinear characteristics of the sloshing flow could be observed. Thus, in this section, three additional lower filling levels, 10%, 15% and 25% are further considered.

To illustrate the effects of the lower filling levels directly, the original motions by the COUPLED model are not shown here. The corresponding differences of the time series of motions for the four lower filling levels are plotted in Fig. 5.26. Similar to those results for the usual filling levels, the increment of surge and heave motions would be amplified as the filling level increases. However, unlike the non-monotonic relation between the effect on pitch motions and the usual filling levels, for the lower filling conditions, the sloshing effects on pitch motions are intensified as the tank is filled with more water. This suggests that the mid filling level might induce quite violent sloshing flow.

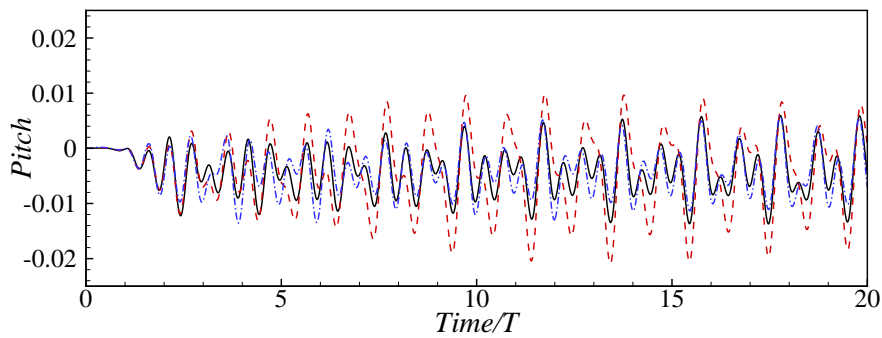
In addition, there is another scenario that needs to be noted. For the usual filling levels, as shown in Fig. 5.25, the increment of the differences in the surge and heave motions are almost proportional to the increase in the filling level. However, as shown in Fig. 5.26, the increment changes nonlinearly with the variation of the lower filling levels. This again suggests that the nonlinearity of sloshing is more evident under lower filling conditions.



(a) surge



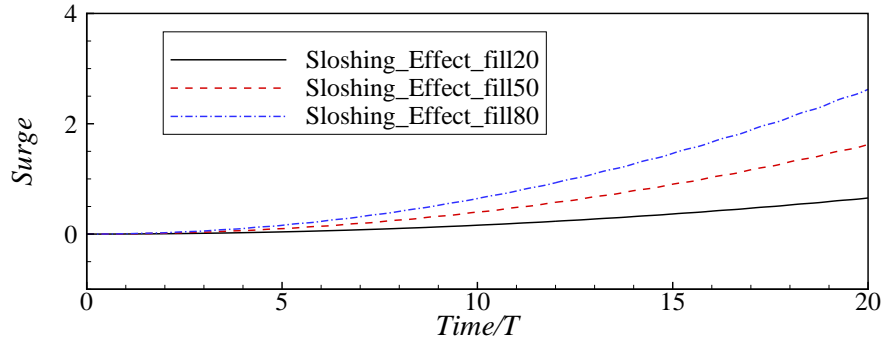
(b) heave



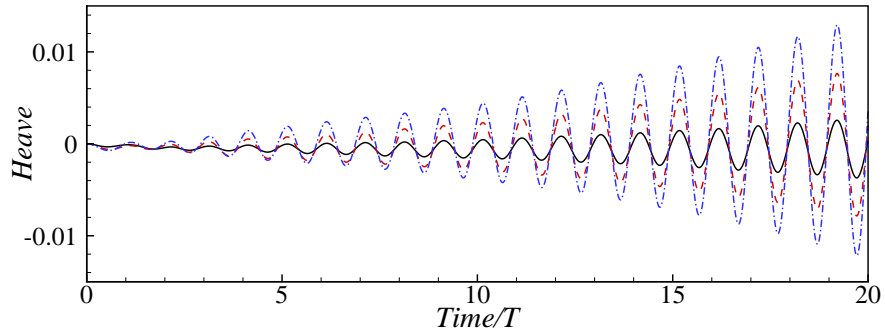
(c) pitch

Figure 5.24: Time histories of the barge motions obtained by the COUPLED model under different filling conditions.

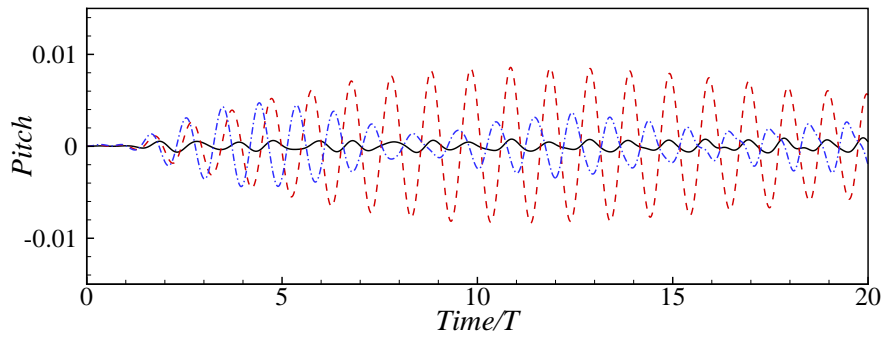
Fig. 5.27 shows the maximum difference value against the filling level. Except for the pitch component, the surge and heave motions are amplified as the tank is filled with more water. Maximum sloshing effects on pitch motions are generated at the 50% filling level at the given wave frequency and amplitude. The nonlinear relation between the lower filling level and the motion differences due to sloshing can also be



(a) surge



(b) heave

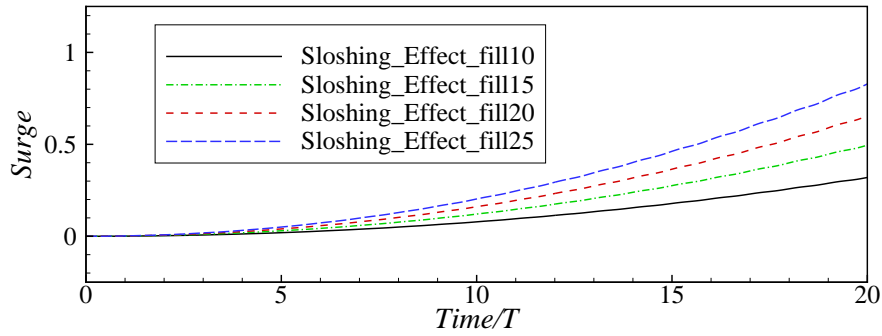


(c) pitch

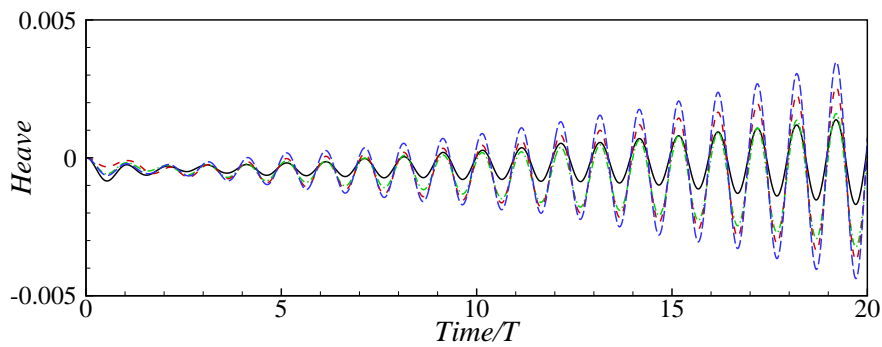
Figure 5.25: Time histories of the sloshing effects on barge motions under different filling conditions.

observed in Fig. 5.27.

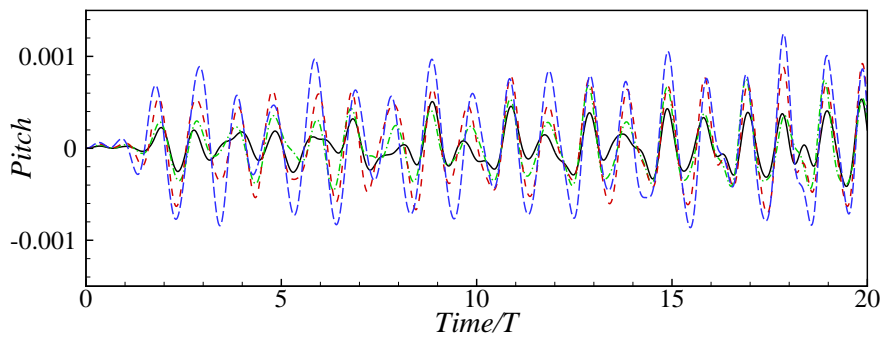
To further investigate the influence of the filling level on internal sloshing, the surface elevations at the left tank wall are plotted for the three usual filling levels in Fig. 5.28. It can be observed that the mid filling level clearly induces the most violent sloshing flow while achieving the highest surface elevation. This accords with



(a) surge



(b) heave

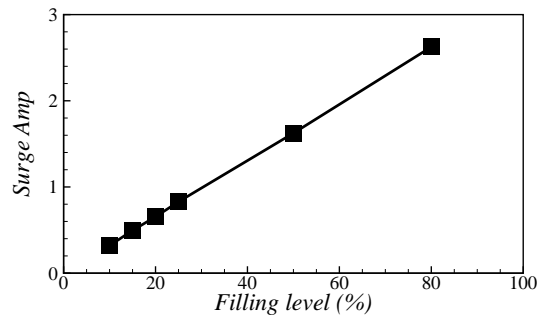


(c) pitch

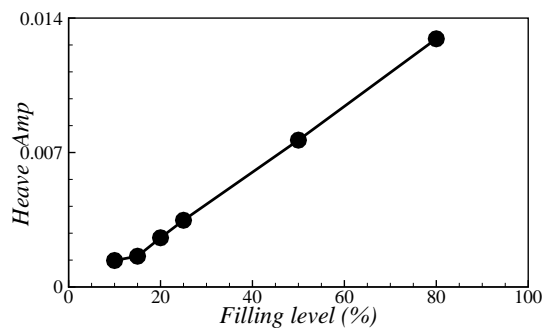
Figure 5.26: Time histories of the sloshing effects on barge motions under low filling conditions.

the previous discussion on pitch motions.

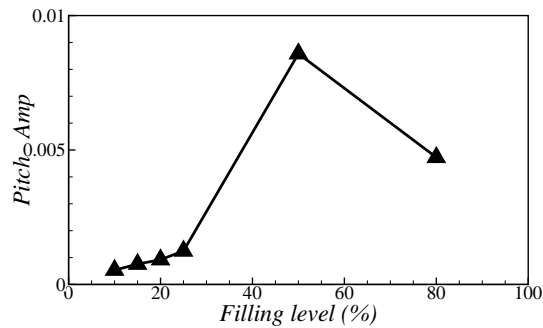
As discussed in Section 5.3.2, the ratio of the wave frequency to the natural frequency of the sloshing system is one major reason leading to the different internal sloshing flows. In this section, according to Eq. (3.3), the natural frequencies for the 20%, 50% and 80% filling levels are $f = 3.0933$, 4.7497 and 5.7224 rad/s respectively.



(a) surge



(b) heave



(c) pitch

Figure 5.27: Maximum sloshing effects on barge motions under different filling conditions.

With the given wave frequency $f = 5.0$ rad/s and fixed wave amplitude, it is clear that the 50% filling level would induce most severe sloshing motions, since its natural frequency is closest to the given value. Accordingly, the sloshing at the 80% filling level would lie between the mid filling level and the lower 20% filling level. In Fig. 5.29, which records the time history of the pressure at the left wall, this explanation is validated. It should be noted that the initial hydrostatic pressure is deducted for

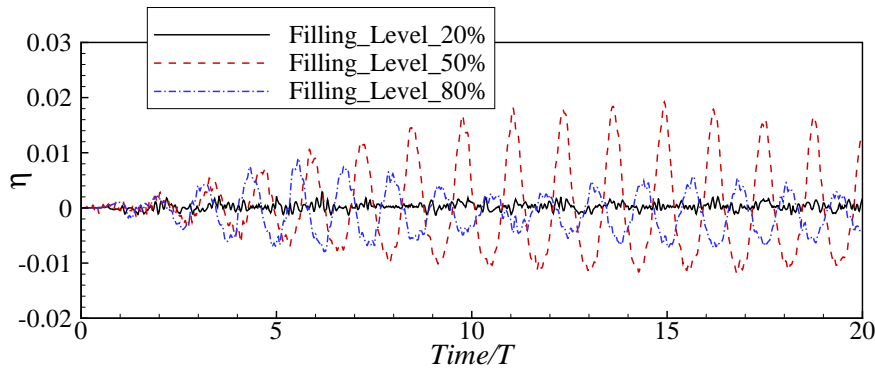


Figure 5.28: Time histories of the surface elevation at the left wall under different filling conditions.

better comparison. Similar trends to the surface elevation are achieved, indicating the influence of the natural frequency is significant here.

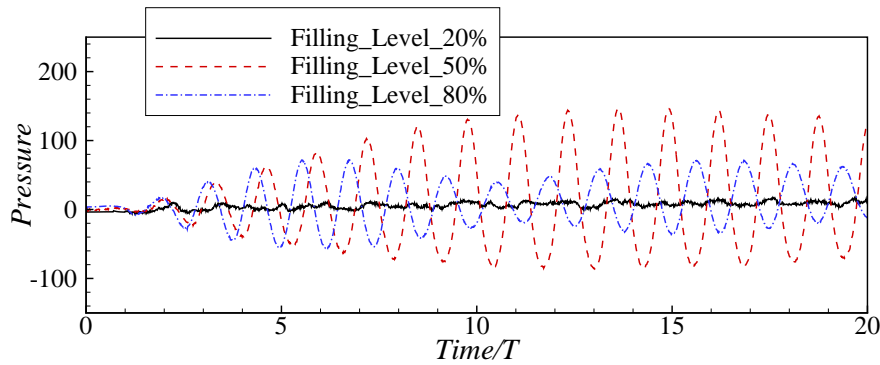


Figure 5.29: Time histories of pressure at the left wall under different filling conditions.

Maximum surface elevations are recorded and plotted against the filling level in Fig. 5.30. It accords with the observations from the time histories and suggests that the mid filling level would lead to the most violent sloshing in the tank. However, it should be noted there is a tiny peak observed at the 20% filling level. This might be caused by both the lower filling nonlinear effects and the corresponding barge motions, consistent with the detailed discussion in Section 3.3.3.

Fig. 5.31 plots the pressure distributions on the left tank wall at the moment when the maximum wave elevations are captured for three filling conditions. We can see that the three pressure distributions are almost linear along the tank wall. This suggests that the sloshing flows generated under the three filling conditions are not

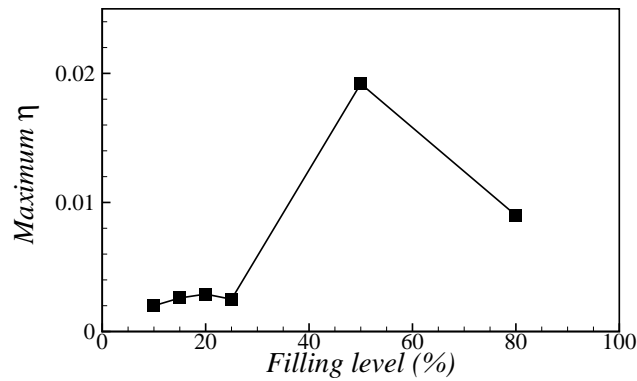


Figure 5.30: Maximum surface elevations under various filling conditions.

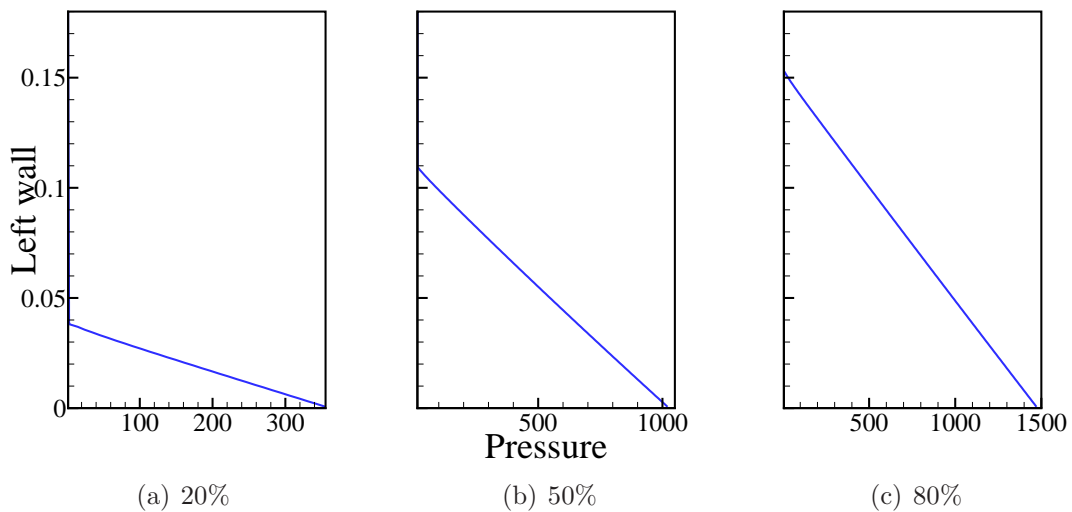


Figure 5.31: Pressure distribution at the left wall under three different filling conditions.

strong.

5.4 Summary

In this chapter, the numerical model based on nonlinear potential flow theory to simulate the ship motions was introduced. The boundary value problem was described and the higher-order boundary element formulation of this problem was presented. The numerical implementation of this model was also given in detail.

To study the interaction between sloshing and ship motions, the methodology of coupling the two numerical models was developed by applying the ship motions as the excitations of the sloshing, and combining the sloshing-induced forces into the external wave forces as the total forces acting on the ship. A preliminary test was conducted by reproducing the experimental work of Rognebakke and Faltinsen (2003) numerically. Good agreement between the numerical results and the experimental recordings validated the capability of the developed COUPLED model.

By applying the COUPLED model, a parametric study regarding wave amplitude, wave frequency and the filling level in the tank was performed. The following conclusions could be made:

1. The variations of ship motions obtained with and without the presence of the sloshing motion are both nonlinear to the change of the wave amplitude.
2. The increase in the wave amplitude would reduce the sloshing effects on the surge motion but amplify the sloshing effects on the pitch motion.
3. Unlike wave amplitude, the increasing wave frequency generally leads to a decrease in ship motions, with or without the influence of sloshing flow.
4. Similar to the wave amplitude, the motion variation changes nonlinearly with the wave frequency. It is clear that the ratio of the wave frequency to the resonant frequency of the ship/the sloshing system is the dominant factor in determining the ship motions/sloshing flows.
5. With regard to filling levels, the higher the filling level, the larger the surge and pitch motions. However, note that the mid filling level results in the most significant effect on the pitch motions.
6. Correspondingly, the most severe sloshing flow is generated under the 50% filling condition. This is due to the given wave frequency being the closest to the natural frequency of the sloshing system under the mid filling level. This also indicates that, the internal sloshing flow affects the rotational motions of the ship most significantly at the prescribed condition.

Based on the parametric study, the wave frequency and its related resonant phenomena of ship/sloshing motions should be the main concern in the design of LNG carriers and tanks.

Chapter 6

CONCLUSIONS AND RECOMMENDATIONS

6.1 Conclusion

The main objective of this research is to develop a nonlinear coupled numerical model and investigate the liquid sloshing in LNG tanks coupled with ship motions. To achieve this, the following work has been done successively.

Firstly, in order to model nonlinear viscous sloshing flows, a free surface flow solver based on the finite difference approximation was developed. The fluid solver and interface tracker of the preliminary model were validated separately by successful reproduction of benchmark test cases. The performance of the preliminary model was assessed by carrying out the non-resonance and resonance sloshing cases. Satisfactory results were obtained for the non-resonance case. However, numerical dissipations were found in the resonance case. To solve this dissipative issue, two improvements have been made to the preliminary model:

- The first improvement was applying a larger size of the smoothing band in the Level-Set technique of the preliminary model than the conventional size, based on which, the intermediate model was developed.
- The second improvement was incorporating high-resolution convection schemes into the intermediate model. Thus, the final model of the free surface flow solver was developed.

Different free surface flow problems with and without breaking waves have been studied. Good agreement with published data was achieved. Results also show that:

- The size of smoothing band in the Level Set Method would have significant effects on the performance of current free surface flow solver.
- With higher-order convection schemes used in the fluid solver, a smaller smoothing band than the conventional size could be employed in the current model.
- $s = 4$, $s = 2$ and $s = 1$ are recommended smoothing sizes for the Level-Set based free surface solver with first-order Upwind scheme, second-order MINMOD scheme and third-order COPLA scheme respectively.

Secondly, to study the effects of ship motions, an investigation of sloshing flows in a full-scale LNG tank was conducted. A co-moving coordinate system was adopted to simulate sloshing waves in a rectangular tank excited randomly by three-degrees-of-freedom motions. It is found that:

- In the head sea condition, the random initial phase difference between surge and pitch motions has a significant effect on the induced sloshing waves, and the phase difference of 180° can cause the most violent sloshing.
- The most severe sloshing wave is generated when the sea wave frequency approaches the natural frequency of the sloshing system, at which both the pressure and free surface elevation reach the maximum value.
- The free surface elevation excited by each resonant frequency decreases as the filling depth increases, due to the corresponding smaller RAOs applied. In lower filling level conditions, the nonlinear characteristics of sloshing wave are more evident than those in mid and higher filling conditions, such as 50% and 80%.

Next, in order to investigate coupling effects between nonlinear viscous sloshing flows and nonlinear ship motions, a COUPLED numerical model in time domain was developed:

- A numerical model based on nonlinear potential wave theory was adopted to solve ship motions in waves.
- In order to use ship motions to induce sloshing, the free surface flow solver was modified, and employed the accelerations and velocities obtained from the potential flow model into the Navier-Stokes equations as the external excitations.

- To consider the sloshing effects, pressure results obtained by the sloshing model were integrated along tank walls. The equation of motions in the ship model was modified accordingly by incorporating the sloshing-induced forces and moments.
- A preliminary validation of the COUPLED model was conducted by numerically reproducing a benchmark experiment. Good agreement validated the applicability of the COUPLED model.

Finally, a parametric study regarding wave amplitude, wave frequency and the filling level in the water tank was performed. Results show that:

- Variations of the ship motions obtained with and without the presence of sloshing motions were both nonlinear to the change of wave amplitude.
- The increase in wave amplitude would reduce the effects of sloshing on surge motions but amplify the effects of sloshing on pitch motions.
- A more nonlinear sloshing would be generated when a larger wave amplitude was used. The variations of sloshing flows were not proportional to the change of wave amplitudes.
- The increase in wave frequency would generally lead to the decrease in ship motions, with or without the influence of sloshing flow. It is clear that the ratio of the wave frequency to the natural frequency of ship/sloshing system is the dominant factor to determine ship/sloshing motions.
- As the tank was filled with more water, larger surge and pitch motions would be induced. The mid filling level would result in the most significant effect on the pitch motion. Correspondingly, the most severe sloshing flow was generated under the 50% filling condition. This is due to the given wave frequency being closest to the natural frequency of the sloshing system under this mid filling level.

Thus, further conclusions could be drawn:

- Wave frequencies and amplitudes have a substantial effect on liquid sloshing and its interaction with ship motions.
- Internal sloshing flows would significantly affect surge and pitch motions. In addition, in the current study, sloshing would most influence the rotational motions of the ship.

- The dimension of LNG tanks should be designed to avoid the corresponding natural frequency coinciding with the prominent ocean wave frequency and falling into the frequency range in which a large motion RAO of the LNG carrier would be generated.

6.2 Recommendations for future research

In traditional LNG industry, LNG carriers are usually required to be empty or fully loaded during transportation. During offloading process, when the tank would be partially filled and sloshing could be induced, the coupling of ship motions and sloshing may arise, even though a mooring system would be used to stabilize LNG carriers considering the sloshing effect. In addition, as mentioned in Chapter 1, with the growing demand for LNG, the newly designed LNG carriers needs to meet the requirement of a wide range of filling levels. This suggests that LNG carriers may transport partially filled tanks under certain circumstances. In such situations, the interaction between ship motions and liquid sloshing is of great concern. The proposed nonlinear COUPLED model may provide an important means for investigation of this kind of problem. To make the COUPLED model more applicable, the following aspects are recommended for future research.

One possible avenue for future work is the extension of the two-dimensional sloshing model to three dimensions for a deeper investigation of the sloshing phenomena. This is necessary since different kinds of sloshing waves may be found when excited by real sea waves in three dimensions besides the already known kinds excited by earthquakes (Wu and Chen, 2009). A three-dimensional sloshing model would also be much more applicable and useful when coupled with the three-dimensional nonlinear potential flow model for ship motions. As described earlier, only head sea conditions are considered in this study due to the two-dimensional sloshing model. After the extension, more factors could be considered in the study of coupling effects. The influence of angle of the incident wave on the interaction between sloshing and ship motions can be analyzed. The effects of the position and size of water tanks in the LNG carrier could also be figured out. There have already been several three-dimensional Level-Set model applied in other areas, such as image processing, compute graphics and material engineering. Therefore, it should be feasible to extend the current sloshing model to three dimensions.

Considering large sloshing-induced loads on the LNG tanks, recent studies have also been interested in suppressing the sloshing motions with internal structures (Wu

et al., 2012; Jung et al., 2012; Akyildiz et al., 2013; Koh et al., 2013; Molin and Remy, 2013; Jin et al., 2014). Based on the extended three-dimensional sloshing model, additional technique needs to be taken into account due to the presence of the structure (baffles, perforated screens). One of the popular method to study the interaction between free surface flows and marine structures is the Immersed Boundary Method (IBM), which introduces a body force to the momentum equation to enforce the boundary condition of the structure in the fluid. Due to its easy grid generation, inherent simplicity to study moving bodies on fixed grids and straightforward calculation of the forces on the body, the IBM has been widely adopted (Fadlun et al., 2000; Mittal et al., 2005; Zhang et al., 2010). A similar two-dimensional IBM Level-Set combined numerical model (Bai and Huo, 2013) has been developed and well validated in simulations of fluid structure interaction (FSI). Therefore, it would be applicable to incorporate the IBM to the three-dimensional sloshing model (if extended). Studies on the sloshing-suppressing structures could be performed consequently. More complicated interactions between free surface flows and submerged moving structures could be investigated. In addition, considering the possibly introduced breaking waves in the process of FSI, the turbulence model could be incorporated in the future.

Publication

Journal paper:

1. Bai, W., Liu, X. and Koh, C.G. (2015). Numerical study of violent LNG sloshing induced by realistic ship motions using level set method. *Ocean Engineering*. 97, 100-113.

Conference paper:

1. Liu, X., Bai, W. and Koh, C.G. (2013). Numerical study of sloshing waves in a 2D tank by level set method. The twenty-sixth KKHTCNN symposium on Civil Engineering, 18-19 November, Singapore

Bibliography

- Abramson, H., 1966. The dynamic behavior of liquids in moving containers. NASA SP 106.
- Abramson, H., Bass, R., Faltinsen, O., Olsen, H., 1974. Liquid slosh in LNG carriers. In 10th Symp. Naval Hydrodynamics, MIT, Cambridge, MA.
- Akyildiz, H., Erdem Ünal, N., Aksoy, H., 2013. An experimental investigation of the effects of the ring baffles on liquid sloshing in a rigid cylindrical tank. *Ocean Engineering* 59, 190–197.
- Akyildiz, H., Ünal, E., 2005. Experimental investigation of pressure distribution on a rectangular tank due to the liquid sloshing. *Ocean Engineering* 32 (11), 1503–1516.
- Antuono, M., Bouscasse, B., Colagrossi, A., Lugni, C., 2012. Two-dimensional modal method for shallow-water sloshing in rectangular basins. *Journal of Fluid Mechanics* 700, 419–440.
- Arai, M., Cheng, L., Inoue, Y., Sasaki, H., Yamagishi, N., 1992. Numerical analysis of liquid sloshing in tanks of FPSO. In *Proceedings of 2nd ISOPE*, San Francisco 3, 383–390.
- Archer, P., Bai, W., 2011. The applicability of the particle level set method for the simulation of breaking waves. In *Proceedings of 21st International Offshore (Ocean) and Polar Engineering Conference (ISOPE)*, Maui, USA.
- Bai, W., Eatock Taylor, R., 2006. Higher-order boundary element simulation of fully nonlinear wave radiation by oscillating vertical cylinders. *Applied Ocean Research* 28 (4), 247–265.
- Bai, W., Eatock Taylor, R., 2009. Fully nonlinear simulation of wave interaction with fixed and floating flared structures. *Ocean engineering* 36 (3), 223–236.

- Bai, W., Mingham, C. G., Causon, D. M., Qian, L., 2009. Finite volume simulation of viscous free surface waves using the cartesian cut cell approach. *International Journal for Numerical Methods in Fluids* 63 (1), 69–95.
- Bass, D. W., 1991. Roll stabilization for small fishing vessels using paravanes and anti-roll tanks. *Marine Technology* 35 (2), 74–84.
- Bass, R., Bowles, E., Trudell, R., Navickas, J., Peck, J., Yoshimura, N., Endo, S., Pots, B., 1985. Modeling criteria for scaled lng sloshing experiments. *Journal of Fluids Engineering* 107 (2), 272–280.
- Bosch, J. v. d., Vugts, J., 1966. Roll damping by free surface tanks. Tech. Rep. 83S, Shipbuilding Laboratory of the Technical University of Delft.
- Buchner, B., van Ballegoyen, G., 1997. Joint industry project: F (p) so green water loading. A, B and C, MARIN report (13644-1).
- Celebi, M., Akyildiz, H., 2002. Nonlinear modeling of liquid sloshing in a moving rectangular tank. *Ocean Engineering* 29 (12), 1527–1553.
- Chen, B., Nokes, R., 2005. Time-independent finite difference analysis of fully non-linear and viscous fluid sloshing in a rectangular tank. *Journal of Computational Physics* 209 (1), 47–81.
- Chen, Y., Price, W., 2009. Numerical simulation of liquid sloshing in a partially filled container with inclusion of compressibility effects. *Physics of Fluids* 21, 112105.
- Chen, Z., Zong, Z., Li, H., Li, J., 2013. An investigation into the pressure on solid walls in 2D sloshing using SPH method. *Ocean Engineering* 59, 129–141.
- Cho, J., Lee, H., 2004. Non-linear finite element analysis of large amplitude sloshing flow in two-dimensional tank. *International Journal for Numerical Methods in Engineering* 61 (4), 514–531.
- Choi, S. K., Nam, H. Y., Cho, M., 1995. Evaluation of a higher-order bounded convection scheme: three-dimensional numerical experiments. *Numerical Heat Transfer, Part B Fundamentals* 28 (1), 23–38.
- Colagrossi, A., Lugni, C., Brocchini, M., 2010. A study of violent sloshing wave impacts using an improved SPH method. *Journal of hydraulic research* 48, 94–104.

- Colagrossi, A., Lugni, C., Greco, M., Faltinsen, O., 2004. Experimental and numerical investigation of 2D sloshing with slamming. In Proceedings of 19th IWWWFB, Cortona, Italy.
- Colicchio, G., Greco, M., Faltinsen, O., 2006. A bem-level set domain-decomposition strategy for non-linear and fragmented interfacial flows. *International journal for numerical methods in engineering* 67 (10), 1385–1419.
- Colicchio, G., Landrini, M., Chaplin, J., 2005. Level-set computations of free surface rotational flows. *Journal of fluids engineering* 127 (6), 1111–1121.
- Cordonnier, J., 1994. Numerical simulation of sloshing in tanks. *Marine, offshore and ice technology*, 197.
- Dillingham, J., 1981. Motion studies of a vessel with water on deck. *Marine technology* 18, 38–50.
- Dodge, F., Green, S., Cruse, M., 1991. Analysis of small-amplitude low gravity sloshing in axisymmetric tanks. *Microgravity Science and Technology* 4, 228–234.
- Faltinsen, O., 1978. A numerical nonlinear method of sloshing in tanks with two-dimensional flow. *Journal of Ship Research* 22 (3).
- Faltinsen, O., Timokha, A., 2001. An adaptive multimodal approach to nonlinear sloshing in a rectangular tank. *Journal of Fluid Mechanics* 423 (1), 167–200.
- Faltinsen, O., Timokha, A., 2012. On sloshing modes in a circular tank. *Journal of Fluid Mechanics* 695, 467–477.
- Faltinsen, O., Timokha, A., 2013. Multimodal analysis of weakly nonlinear sloshing in a spherical tank. *Journal of Fluid Mechanics* 719, 129–164.
- Fekken, G., 1998. Numerical simulation of green water loading on the foredeck of a ship. Preprint of the Department of Mathematics, University of Groningen, 55.
- Feng, G., 1973. Dynamic loads due to moving liquid. *AIAA Paper* (73-409), 11.
- Feng, X., Bai, W., 2015. Wave resonances in a narrow gap between two barges using fully nonlinear numerical simulation. *Applied Ocean Research* 50, 119–129.
- Foss, M., 2012. Introduction to lng. Center for Energy Economics, Bureau of Economic Geology, Jackson School of Geosciences, University of Texas at Austin.

- Frandsen, J. B., 2004. Sloshing motions in excited tanks. *Journal of Computational Physics* 196 (1), 53–87.
- Gao, F., 2003. An efficient finite element technique for free surface flow. Ph.D. Thesis, Brighton University, U.K.
- Gaskell, P., Lau, A., 1988. Curvature-compensated convective transport: SMART, a new boundedness-preserving transport algorithm. *International Journal for Numerical Methods in Fluids* 8 (6), 617–641.
- Ghia, U., Ghia, K. N., Shin, C., 1982. High-re solutions for incompressible flow using the navier-stokes equations and a multigrid method. *Journal of computational physics* 48 (3), 387–411.
- Gingold, R., Monaghan, J., 1977. Smoothed particle hydrodynamics-theory and application to non-spherical stars. *Monthly notices of the royal astronomical society* 181, 375–389.
- Gotoh, H., Khayyer, A., Ikari, H., Arikawa, T., Shimosako, K., 2014. On enhancement of incompressible sph method for simulation of violent sloshing flows. *Applied Ocean Research* 46, 104–115.
- Gu, H., Li, Y., Lin, P., 2005. Modeling 3D fluid sloshing using level set method. *Modern Physics Letters B* 19 (28n29), 1943–1746.
- Harlow, F. H., Welch, J. E., et al., 1965. Numerical calculation of time-dependent viscous incompressible flow of fluid with free surface. *Physics of fluids* 8 (12), 2182.
- Harten, A., Engquist, B., Osher, S., Chakravarthy, S. R., 1987. Uniformly high order accurate essentially non-oscillatory schemes, iii. *Journal of computational physics* 71 (2), 231–303.
- Hinatsu, M., Tsukada, Y., Fukasava, R., Tanaka, Y., 2001. Experiments of two-phase flows for the joint research. In: *Proceedings of the SRI-TUHH Mini-Workshop on Numerical Simulation of Two-Phase Flows*.
- Hirt, C., Nichols, B., 1981. Volume of fluid (VOF) method for the dynamics of free boundaries. *Journal of computational physics* 39 (1), 201–225.
- Hirt, C., Nichols, B., Romero, N., 1975. SOLA: a numerical solution algorithm for transient fluid flows. NASA STI/Recon Technical Report N 75, 32148.

- Huang, S., Duan, W.-y., Zhu, X., 2010. Time-domain simulation of tank sloshing pressure and experimental validation. *Journal of Hydrodynamics, Ser. B* 22 (5), 556–563.
- Ibrahim, R. A., 2005. *Liquid sloshing dynamics: theory and applications*. Cambridge University Press.
- Ikeda, T., Ibrahim, R. A., Harata, Y., Kuriyama, T., 2012. Nonlinear liquid sloshing in a square tank subjected to obliquely horizontal excitation. *Journal of Fluid Mechanics* 700, 304–328.
- Ikeda, Y., Yoshiyama, T., 1991. A study on flume-type anti-rolling tank. *Journal of the Kansai society of naval architects* 216, 111.
- Ji, Y. M., Shin, Y. S., Park, S. J., Hyun, M. J., 2012. Experiments on non-resonant sloshing in a rectangular tank with large amplitude lateral oscillation. *Ocean Engineering* 50, 10–22.
- Jiang, G., Peng, D., 2000. A boundary condition capturing method for multiphase incompressible flow. *SIAM Journal on Scientific computing* 21 (6), 2126–2143.
- Jin, H., Liu, Y., Li, H.-J., 2014. Experimental study on sloshing in a tank with an inner horizontal perforated plate. *Ocean Engineering* 82, 75–84.
- Journée, J., 1997. *Liquid cargo and its effect on ship motions*. TU Delft.
- Jung, J., Yoon, H., Lee, C., Shin, S., 2012. Effect of the vertical baffle height on the liquid sloshing in a three-dimensional rectangular tank. *Ocean Engineering* 44, 79–89.
- Kang, M., Fedkiw, R., Liu, X., 2000. A boundary condition capturing method for multiphase incompressible flow. *Journal of Scientific Computing* 15 (3), 323–360.
- Khezzar, L., Seibi, A., Goharzadeh, A., 2009. Water sloshing in rectangular tanks—an experimental investigation & numerical simulation. *International Journal of Engineering (IJE)* 3 (2), 174.
- Kim, J., Moin, P., 1985. Application of a fractional step method to Navier-Stokes equations. *Journal of Computational Physics* 59 (2), 308–323.

- Kim, J., Sim, I., Shin, Y., Kim, Y., Bai, K., 2003. A three-dimensional finite element computation for the sloshing impact pressure in LNG tank. In Proceedings of 13th ISOPE, Honolulu.
- Kim, Y., 2001. Numerical simulation of sloshing flows with impact load. *Applied Ocean Research* 23 (1), 53–62.
- Kim, Y., 2002. A numerical study on sloshing flows coupled with ship motion—the anti-rolling tank problem. *Journal of Ship Research* 46 (1), 52–62.
- Kim, Y., Kim, K., Song, M.J. and Kim, M., Sun, J., Song, K., Shin, K., Yang, J., 2008. Comparative study on time-domain analysis of ship motions and structural loads in waves. In Proceedings of 18th ISOPE, Canada 3, 335–340.
- Kim, Y., Kim, S., Ahn, Y., Kim, K., 2013. Experimental analysis on sloshing loads for lng cargo design. In: Proceed. PRADS2013, Changwon City, Korea. pp. 881–891.
- Kim, Y., Nam, B., Kim, D., Kim, Y., 2007. Study on coupling effects of ship motion and sloshing. *Ocean Engineering* 34 (16), 2176–2187.
- Kim, Y., Shin, Y., Lee, K., 2004. Numerical study on slosh-induced impact pressures on three-dimensional prismatic tanks. *Applied Ocean Research* 26 (5), 213–226.
- Koh, C., Gao, M., Luo, C., 2012. A new particle method for simulation of incompressible free surface flow problems. *International Journal for Numerical Methods in Engineering* 89 (12), 1582–1604.
- Koh, C., Luo, M., Gao, M., Bai, W., 2013. Modelling of liquid sloshing with constrained floating baffle. *Computers & Structures* 122, 270–279.
- Koshizuka, S., Oka, Y., 1996. Moving-particle semi-implicit method for fragmentation of incompressible fluid. *Nuclear science and engineering* 123 (3), 421–434.
- Landrini, M., Grytøyr, G., et al., 1999. A b-spline based bem for unsteady free-surface flows. *Journal of ship research* 43 (1), 13–24.
- Lee, D., Kim, M., Kwon, S., Kim, J., Lee, Y., 2007a. A parametric sensitivity study on LNG tank sloshing loads by numerical simulations. *Ocean Engineering* 34 (1), 3–9.
- Lee, D. Y., Choi, H. S., 1999. Study on sloshing in cargo tanks including hydroelastic effects. *Journal of marine science and technology* 4 (1), 27–34.

- Lee, S., Kim, M., Lee, D., Kim, J., Kim, Y., 2007b. The effects of lng-tank sloshing on the global motions of lng carriers. *Ocean Engineering* 34 (1), 10–20.
- Lee, S., Lee, Y., Jeong, K., 2011. Numerical simulation of three-dimensional sloshing phenomena using a finite difference method with marker-density scheme. *Ocean Engineering* 38 (1), 206–225.
- Leonard, B., 1988. Simple high-accuracy resolution program for convective modelling of discontinuities. *International Journal for Numerical Methods in Fluids* 8 (10), 1291–1318.
- Leonard, B. P., 1979. A stable and accurate convective modelling procedure based on quadratic upstream interpolation. *Computer methods in applied mechanics and engineering* 19 (1), 59–98.
- Lien, F., Leschziner, M., 1993. Approximation of turbulence convection with a tvd scheme. *Proc. 5th Int. Sym. on Refined Flow Modelling and Turbulence Measurements*, Paris, France, 183–190.
- Lin, P., Li, C., 2002. A σ -coordinate three-dimensional numerical model for surface wave propagation. *International journal for numerical methods in fluids* 38 (11), 1045–1068.
- Liu, D., Lin, P., 2008. A numerical study of three-dimensional liquid sloshing in tanks. *Journal of Computational Physics* 227 (8), 3921–3939.
- Liu, X.-D., Osher, S., Chan, T., 1994. Weighted essentially non-oscillatory schemes. *Journal of computational physics* 115 (1), 200–212.
- Losasso, F., Fedkiw, R., Osher, S., 2006. Spatially adaptive techniques for level set methods and incompressible flow. *SIAM Journal on Scientific computing* 35 (10), 995–1010.
- Madarame, H., Okamoto, K., Iida, M., 2002. Self-induced sloshing caused by an upward round jet impinging on the free surface. *Journal of fluids and structures* 16 (3), 417–433.
- Malenica, S., Zalar, M., Chen, X., 2003. Dynamic coupling of seakeeping and sloshing. In: *13th International Offshore and Polar Engineering Conference, ISOPE*, Honolulu, HI, May. pp. 25–30.

- Mikelis, N., Journee, J., 1984. Experimental and numerical simulations of sloshing behaviour in liquid cargo tanks and its effect on ship motions. In: National Conference on Numerical Methods for Transient and Coupled Problems, Venice, July. pp. 9–13.
- Mitra, S., Wang, C., Reddy, J., Khoo, B., 2012. A 3d fully coupled analysis of non-linear sloshing and ship motion. *Ocean Engineering* 39, 1–13.
- Moiseev, N., 1958. On the theory of nonlinear vibrations of a liquid of finite volume. *Journal of Applied Mathematics and Mechanics* 22 (5), 612–621.
- Molin, B., Remy, F., 2013. Experimental and numerical study of the sloshing motion in a rectangular tank with a perforated screen. *Journal of Fluids and Structures* 43, 463–480.
- Molin, B., Remy, F., Camhi, A., Ledoux, A., 2009. Experimental and numerical study of the gap resonances in-between two rectangular barges. In: 13th Congress of Intl. Maritime Assoc. of Mediterranean IMAM.
- Molin, B., Remy, F., Rigaud, S., De Jouette, C., 2002. Lng fpsos: Frequency domain, coupled analysis of support and liquid cargo motion. In: Proceedings of the 10th International Maritime Association of the Mediterranean (IMAM) Conference, Rethymnon, Greece.
- Nakayama, T., Washizu, K., 1980. Nonlinear analysis of liquid motion in a container subjected to forced pitching oscillation. *International Journal for Numerical Methods in Engineering* 15 (80), 1207–1220.
- Nakayama, T., Washizu, K., 1981. The boundary element method applied to the analysis of two-dimensional nonlinear sloshing problems. *International Journal for Numerical Methods in Engineering* 17 (11), 1631–1646.
- Nam, B., Kim, Y., Kim, D., Kim, Y., 2009. Experimental and numerical studies on ship motion responses coupled with sloshing in waves. *Journal of Ship Research* 53 (2), 68–82.
- Newman, J., 2005. Wave effects on vessels with internal tanks. In: Proceedings of the 20th Workshop on Water Waves and Floating Bodies, Spitsbergen, Norway.
- Ockendon, J., Ockendon, H., 1973. Resonant surface waves. *Journal of Fluid Mechanics* 59 (02), 397–413.

- Okamoto, T., Kawahara, M., 1990. Two-dimensional sloshing analysis by lagrangian finite element method. *International Journal for Numerical Methods in Fluids* 11 (5), 453–477.
- Olsen, H., 1970. Unpublished sloshing experiments at the technical university of delft. Delft, The Netherlands.
- Olsen, H., Johnsen, K., 1975. Nonlinear sloshing in rectangular tanks. a pilot study on the applicability of analytical models.
- Osher, S., Fedkiw, R., 2006. Level set methods and dynamic implicit surfaces. Vol. 153. Springer Science & Business Media.
- Osher, S., Sethian, J., 1988. Fronts propagating with curvature-dependent speed: algorithms based on Hamilton-Jacobi formulations. *Journal of Computational Physics* 79 (1), 12–49.
- Osher, S., Shu, C.-W., 1991. High-order essentially nonoscillatory schemes for hamilton-jacobi equations. *SIAM Journal on numerical analysis* 28 (4), 907–922.
- Peregrine, D., 2003. Water-wave impact on walls. *Annual Review of Fluid Mechanics* 35 (1), 23–43.
- Pérez, T., Blanke, M., 2002. Simulation of ship motion in seaway. Department of Electrical and Computer Engineering, The University of Newcastle, Australia, Tech. Rep. EE02037.
- Pistani, F., Thiagarajan, K., 2012. Experiments on non-resonant sloshing in a rectangular tank with large amplitude lateral oscillation. *Ocean Engineering* 52, 60–74.
- Roe, P., 1986. Characteristic-based schemes for the euler equations. *Annual review of fluid mechanics* 18 (1), 337–365.
- Rognebakke, O., Faltinsen, O., 2003. Coupling of sloshing and ship motions. *Journal of Ship Research* 47 (3), 208–221.
- Sethian, J., 1996. A fast marching level set method for monotonically advancing fronts. *Proceedings of the National Academy of Sciences* 93 (6), 1591–1595.
- Shao, J., Li, H., Liu, G., Liu, M., 2012. An improved SPH method for modeling liquid sloshing dynamics. *Computers & Structures* 100, 18–26.

- Shu, C., Osher, S., 1988. Efficient implementation of essentially non-oscillatory shock-capturing schemes. *Journal of Computational Physics* 77 (2), 439–471.
- Shu, C.-W., Osher, S., 1989. Efficient implementation of essentially non-oscillatory shock-capturing schemes, ii. *Journal of Computational Physics* 83 (1), 32–78.
- Solass, F., 1995. Analytical and numerical studies of sloshing in tanks. Ph.D. thesis, Norwegian Institute of Technology, NTH, Trondheim, Norway.
- Souto-Iglesias, A., Delorme, L., Pérez-Rojas, L., Abril-Pérez, S., 2006. Liquid moment amplitude assessment in sloshing type problems with smooth particle hydrodynamics. *Ocean Engineering* 33 (11), 1462–1484.
- Souto Iglesias, A., Pérez Rojas, L., Zamora Rodríguez, R., 2004. Simulation of anti-roll tanks and sloshing type problems with smoothed particle hydrodynamics. *Ocean Engineering* 31 (8), 1169–1192.
- Stoker, J., Lindsay, R., 1958. Water waves. *Physics Today* 11, 28.
- Subramanian, G., Raveendra, V., Gopolakrishna, K., 1994. The coupled finite element and boundary element analysis of nonlinear interactions between waves and bodies. *Int J Numer Meth Eng* 37, 1779–89.
- Sumner, I., 1965. Experimentally determined pendulum analogy of liquid sloshing in spherical and oblate-spheroidal tanks. NASA TN D-2737.
- Sussman, M., Fatemi, E., Smereka, P., Osher, S., 1998. An improved level set method for incompressible two-phase flows. *Journal of Computational Physics* 27 (5), 663–680.
- Sussman, M., Smereka, P., Osher, S., 1994. A level set approach for computing solutions to incompressible two-phase flow. *Journal of Computational Physics* 93 (4), 1591–1595.
- Tsai, S., Hsu, S., Chien, H., Chou, C., Malenica, S., Chen, X., 2013. Numerical study on seakeeping-sloshing coupling effect of container ship for sea trial purpose. In: *Proceed. PRADS2013, Changwon City, Korea*. pp. 509–514.
- Van Daalen, E., Kleefsman, K., Gerrits, J., Luth, H., Veldman, A., 2000. Anti roll tank simulations with a volume of fluid (vof) based navier-stokes solver. In: *23rd Symposium on Naval Hydrodynamics*.

- Van Leer, B., 1979. Towards the ultimate conservative difference scheme. v. a second-order sequel to godunov's method. *Journal of computational Physics* 32 (1), 101–136.
- Vasta, J., Gidding, A. J. and Taplin, A., Stilwell, J. J., 1961. Roll stabilization by means of passive tanks. *Transactions of Society of Naval Architects and Marine Engineers* 69, 411.
- Wang, C., Khoo, B., 2005. Finite element analysis of two-dimensional nonlinear sloshing problems in random excitations. *Ocean Engineering* 32 (2), 107–133.
- Wang, C., Teng, J., Huang, G., 2011. Numerical simulation of sloshing motion inside a two dimensional rectangular tank by level set method. *International Journal of Numerical Methods for Heat & Fluid Flow* 21 (1), 5–31.
- Wang, X., Gu, X., Hu, J., Xu, C., 2012. A study of sloshing influence on wave induced responses of a lng ship by experimental method. In: *Proceedings of Hydroelasticity in Marine Technology*, Tokyo, JAPAN. pp. 21–30.
- Watts, P., 1883. On a method of reducing the rolling of ships at sea. *Transactions of the Institution of Naval Architects* 24, 165–191.
- Watts, P., 1885. The use of water chambers for reducing the rolling of ships at sea. *Transactions of the Institution of Naval Architects*, 30.
- Wu, C.-H., Faltinsen, O. M., Chen, B.-F., 2012. Numerical study of sloshing liquid in tanks with baffles by time-independent finite difference and fictitious cell method. *Computers & Fluids* 63, 9–26.
- Wu, G., Eatock Taylor, R., 1989. The numerical solution of the motions of a ship advancing in waves. In: *Proceedings of the 5th proc int conf on numerical ship hydrodynamics*. pp. 386–394.
- Wu, G., Eatock Taylor, R., 2003. The coupled finite element and boundary element analysis of nonlinear interactions between waves and bodies. *Ocean Engineering* 30 (3), 387–400.
- Wu, G., Ma, Q., Eatock Taylor, R., 1998. Numerical simulation of sloshing waves in a 3D tank based on a finite element method. *Applied Ocean Research* 20 (6), 337–355.

- Yang, J., Stern, F., 2009. Sharp interface immersed-boundary/level-set method for wave–body interactions. *Journal of Computational Physics* 228 (17), 6590–6616.
- Yoon, H., Koshizuka, S., Oka, Y., 1999. A particle-gridless hybrid method for incompressible flows. *International Journal for Numerical Methods in Fluids* 30, 407–424.
- Yue, W., Lin, C., Patel, V., 2003. Numerical simulation of unsteady multidimensional free surface motions by level set method. *International Journal for Numerical Methods in Fluids* 42 (8), 852–884.
- Zhao, W., Yang, J., Hu, Z., Tao, L., 2014. Coupled analysis of nonlinear sloshing and ship motions. *Applied Ocean Research* 47, 85–97.
- Zhu, J., 1992. On the higher-order bounded discretization schemes for finite volume computations of incompressible flows. *Computer Methods in Applied Mechanics and Engineering* 98 (3), 345–360.
- Zhu, J., Rodi, W., 1991. A low dispersion and bounded convection scheme. *Computer Methods in Applied Mechanics and Engineering* 92 (1), 87–96.